Nonlinear dynamics and fluctuations in biological systems

Kumulative Habilitationsschrift

im Fach
Theoretische Physik

vorgelegt
der Fakultät Mathematik und Naturwissenschaften
der Technischen Universität Dresden
von

Dr. rer. nat. Benjamin Friedrich
geboren am 22.07.1979 in Rostock

eingereicht am 30.05.2016;
Wissenschaftlicher Vortrag und Aussprache am 11.12.2017

Gutachter:
Prof. Dr. Eberhard Bodenschatz
Prof. Dr. Erwin Frey
Prof. Dr. Stephan Grill

Technische Universität Dresden

TECHNISCHE UNIVERSITÄT DRESDEN

Die Habilitationsschrift wurde in der Zeit von Oktober 2011 bis Mai 2016
am Max-Planck-Institut für Physik komplexer Systeme in Dresden angefertigt.

Table of Contents

Abstract

The present habilitation thesis in theoretical biological physics addresses two central dynamical processes in cells and organisms: (i) active motility and motility control and (ii) self-organized pattern formation. The unifying theme is the nonlinear dynamics of biological function and its robustness in the presence of strong fluctuations, structural variations, and external perturbations.

We theoretically investigate motility control at the cellular scale, using cilia and flagella as ideal model system. Cilia and flagella are highly conserved slender cell appendages that exhibit spontaneous bending waves. This flagellar beat represents a prime example of a chemo-mechanical oscillator, which is driven by the collective dynamics of molecular motors inside the flagellar axoneme. We study the nonlinear dynamics of flagellar swimming, steering, and synchronization, which encompasses shape control of the flagellar beat by chemical signals and mechanical forces. Mechanical forces can synchronize collections of flagella to beat at a common frequency, despite active motor noise that tends to randomize flagellar synchrony. In Chapter 2, we present a new physical mechanism for flagellar synchronization by mechanical self-stabilization that applies to free-swimming flagellated cells. This new mechanism is independent of direct hydrodynamic interactions between flagella. Comparison with experimental data provided by experimental collaboration partners in the laboratory of J. Howard (Yale, New Haven) confirmed our new mechanism in the model organism of the unicellular green alga *Chlamydomonas*. Further, we characterize the beating flagellum as a noisy oscillator. Using a minimal model of collective motor dynamics, we argue that measured non-equilibrium fluctuations of the flagellar beat result from stochastic motor dynamics at the molecular scale. Noise and mechanical coupling are antagonists for flagellar synchronization.

In addition to the control of the flagellar beat by mechanical forces, we study the control of the flagellar beat by chemical signals in the context of sperm chemotaxis. We characterize a fundamental paradigm for navigation in external concentration gradients that relies on active swimming along helical paths. In this helical chemotaxis, the direction of a spatial concentration gradient becomes encoded in the phase of an oscillatory chemical signal. Helical chemotaxis represents a distinct gradient-sensing strategy, which is different from bacterial chemotaxis. Helical chemotaxis is employed, for example, by sperm cells from marine invertebrates with external fertilization. We present a theory of sensorimotor control, which combines hydrodynamic simulations of chiral flagellar swimming with a dynamic regulation of flagellar beat shape in response to chemical signals perceived by the cell. Our theory is compared to three-dimensional tracking experiments of sperm chemotaxis performed by the laboratory of U. B. Kaupp (CAESAR, Bonn).

In addition to motility control, we investigate in Chapter 3 self-organized pattern formation in two selected biological systems at the cell and organism scale, respectively. On the cellular scale, we present a minimal physical mechanism for the spontaneous self-assembly of periodic cytoskeletal patterns, as observed in myofibrils in striated muscle cells. This minimal mechanism relies on the interplay of a passive coarsening process of crosslinked actin clusters and active cytoskeletal forces. This mechanism of cytoskeletal pattern formation exemplifies how local interactions can generate large-scale spatial order in active systems.

On the organism scale, we present an extension of Turing's framework for self-organized pattern formation that is capable of a proportionate scaling of steady-state patterns with system size. This new mechanism does not require any pre-pattering clues and can restore proportional patterns in regeneration scenarios. We analytically derive the hierarchy of steady-state patterns and analyze their stability and basins of attraction. We demonstrate that this scaling mechanism is structurally robust. Applications to the growth and regeneration dynamics in flatworms are discussed (experiments by J. Rink, MPI CBG, Dresden).

Zusammenfassung [Abstract in German]

Das Thema der vorliegenden Habilitationsschrift in Theoretischer Biologischer Physik ist die nichtlineare Dynamik funktionaler biologischer Systeme und deren Robustheit gegenüber Fluktuationen und äußeren Störungen. Wir entwickeln hierzu theoretische Beschreibungen für zwei grundlegende biologische Prozesse: (i) die zell-autonome Kontrolle aktiver Bewegung, sowie (ii) selbstorganisierte Musterbildung in Zellen und Organismen.

In Kapitel 2, untersuchen wir Bewegungskontrolle auf zellulärer Ebene am Modelsystem von Zilien und Geißeln. Spontane Biegewellen dieser dünnen Zellfortsätze ermöglichen es eukaryotischen Zellen, in einer Flüssigkeit zu schwimmen. Wir beschreiben einen neuen physikalischen Mechanismus für die Synchronisation zweier schlagender Geißeln, unabhängig von direkten hydrodynamischen Wechselwirkungen. Der Vergleich mit experimentellen Daten, zur Verfügung gestellt von unseren experimentellen Kooperationspartnern im Labor von J. Howard (Yale, New Haven), bestätigt diesen neuen Mechanismus im Modellorganismus der einzelligen Grünalge *Chlamydomonas*. Der Gegenspieler dieser Synchronisation durch mechanische Kopplung sind Fluktuationen. Wir bestimmen erstmals Nichtgleichgewichts-Fluktuationen des Geißel-Schlags direkt, wofür wir eine neue Analyse-Methode der Grenzzykel-Rekonstruktion entwickeln. Die von uns gemessenen Fluktuationen entstehen mutmaßlich durch die stochastische Dynamik molekularen Motoren im Innern der Geißeln, welche auch den Geißelschlag antreiben. Um die statistische Physik dieser Nichtgleichgewichts-Fluktuationen zu verstehen, entwickeln wir eine analytische Theorie der Fluktuationen in einem minimalen Modell kollektiver Motor-Dynamik. Zusätzlich zur Regulation des Geißelschlags durch mechanische Kräfte untersuchen wir dessen Regulation durch chemische Signale am Modell der Chemotaxis von Spermien-Zellen. Dabei charakterisieren wir einen grundlegenden Mechanismus für die Navigation in externen Konzentrationsgradienten. Dieser Mechanismus beruht auf dem aktiven Schwimmen entlang von Spiralbahnen, wodurch ein räumlicher Konzentrationsgradient in der Phase eines oszillierenden chemischen Signals kodiert wird. Dieser Chemotaxis-Mechanismus unterscheidet sich grundlegend vom bekannten Chemotaxis-Mechanismus von Bakterien. Wir entwickeln eine Theorie der senso-motorischen Steuerung des Geißelschlags während der Spermien-Chemotaxis. Vorhersagen dieser Theorie werden durch Experimente der Gruppe von U.B. Kaupp (CAESAR, Bonn) quantitativ bestätigt.

In Kapitel 3, untersuchen wir selbstorganisierte Strukturbildung in zwei ausgewählten biologischen Systemen. Auf zellulärer Ebene schlagen wir einen einfachen physikalischen Mechanismus vor für die spontane Selbstorganisation von periodischen Zellskelett-Strukturen, wie sie sich z.B. in den Myofibrillen gestreifter Muskelzellen finden. Dieser Mechanismus zeigt exemplarisch auf, wie allein durch lokale Wechselwirkungen räumliche Ordnung auf größeren Längenskalen in einem Nichtgleichgewichtssystem entstehen kann. Auf der Ebene des Organismus stellen wir eine Erweiterung der Turingschen Theorie für selbstorganisierte Musterbildung vor. Wir beschreiben eine neue Klasse von Musterbildungssystemen, welche selbst-organisierte Muster erzeugt, die mit der Systemgröße skalieren. Dieser neue Mechanismus erfordert weder eine vorgegebene Kompartimentalisierung des Systems noch spezielle Randbedingungen. Insbesondere kann dieser Mechanismus proportionale Muster wiederherstellen, wenn Teile des Systems amputiert werden. Wir bestimmen analytisch die Hierarchie aller stationären Muster und analysieren deren Stabilität und Einzugsgebiete. Damit können wir zeigen, dass dieser Skalierungs-Mechanismus strukturell robust ist bezüglich Variationen von Parametern und sogar funktionalen Beziehungen zwischen dynamischen Variablen. Zusammen mit Kollaborationspartnern im Labor von J. Rink (MPI CBG, Dresden) diskutieren wir Anwendungen auf das Wachstum von Plattwürmern und deren Regeneration in Amputations-Experimenten.

Acknowledgement

Foremost, I thank Stephan Grill for being the mentor for my habilitation. He made it possible that I could offer lectures on hydrodynamics, elasticity theory and nonlinear dynamics at the Technical University of Dresden in the years 2014-2016. Furthermore, I wholeheartedly thank Frank Jülicher for his continuous support and many inspiring scientific discussions.

I am strongly indebted to a large number of experimental collaboration partners, who generously shared primary data as well as their expert knowledge of biological model systems. Specifically, for the publications selected in this thesis, I had the pleasure to work with Luis Alvarez, Veikko F. Geyer, Jonathon Howard, U. Benjamin Kaupp, Jochen C. Rink, and Tom Stückemann. In several occasions, experimental collaboration partners performed experiments that were proposed by me and directly aimed to test theoretical ideas, for which I am most grateful.

I had and still have the privilege to work with three great PhD students, Steffen Werner, Gary S. Klindt, and André Scholich. Most of our joint results are not yet included in this thesis. I also thank all colleagues and friends at the Max Planck Institute for the Physics of Complex Systems, as well as at the Max Planck Institute for Molecular Cell Biology and Genetics in Dresden, for generating a thriving research environment. A special 'thank you' goes to Johannes Baumgart, Veikko Geyer, and Rabea Seyboldt for their critical reading of this thesis. Marius Asal helped formatting the bibliography.

I thank my wife Elisabeth Fischer-Friedrich, herself a scientist, for her constructive feedback and practical advice over many years. In fact, she is co-author of one publication in this thesis.

Finally, I gratefully acknowledge funding from the Max Planck Society and the German Science Foundation.

1 Introduction

1.1 Overview of the thesis

In this habilitation thesis, we present systems-level theoretical descriptions of motility control and self-organized pattern formation in cells and tissues. The overarching theme is the nonlinear dynamics of biological function and its robustness in the presence of strong fluctuations, structural variations, and external perturbations. As examples of biological function, we focus on two central dynamical processes in cells and organisms: (i) active motility and motility control of motile cells and (ii) self-organized pattern formation in cells and tissues. Cell motility and motility control is studied in the model system of cilia and flagella, a highly conserved motile cell appendage of eukaryotic cells[1–3], which is regulated by chemical and mechanical cues. This flagellar control facilitates flagellar synchronization[4-6] and navigation of flagellated swimmers[7–9]. The second theme, pattern formation, is studied both at the sub-cellular scale in the context of self-organization of cytoskeletal filaments into regular myofibrillar patterns[10], and at the organism scale. There, we present a new mechanism for the dynamic scaling of self-organized Turing patterns[11].

Cell motility and motility control. We study the nonlinear dynamics of the eukaryotic flagellum, a slender cell appendage capable of spontaneous bending waves, which propels cellular microswimmers and pumps fluids in the human body. The rhythmic beat of eukaryotic flagella represents a prime example of a chemo-mechanical biological oscillator. In publication 2.1, we study the emergent dynamics that arises from the interactions between several flagella. We identified a novel mechanism of synchronization in pairs of beating flagella, which applies to free-swimming, bi-flagellated cells. This synchronization mechanism relies on a closed feedback loop between flagellar dynamics and self-motion of the cell. This novel synchronization mechanism of mechanical self-stabilization is different from a previous mechanism that had been widely discussed in the field. This alternative mechanism proposed direct hydrodynamic interactions between flagella as the primary cause of flagellar synchronization. We show that both mechanisms can synchronize pairs of flagella, yet the new mechanism is predicted to dominate in free-swimming cells.

In publication 2.2, we extend the conceptual theoretical description of flagellar synchronization developed in the previous publication towards a full quantitative description of flagellar swimming and synchronization in the model system of a swimming unicellular alga, *Chlamydomonas*. For that aim, we combine a minimal description of flagellar beat dynamics that coarse-grains active processes inside the flagellum in terms of an active driving force with a full hydrodynamic treatment of cellular swimming. We present a one-to-one comparison between theoretical results and experimental measurements that have been conducted by our collaboration partners in the Howard laboratory (now Yale University, New Haven). Using our quantitative description, we were able to quantitatively predict the swimming dynamics as well as a force-velocity relation of flagellar oscillations. Of note, the description is free from adjustable parameters: it had been fully parameterized by one set of experimental data (of synchronized beating), allowing us to make quantitative predictions that we could test against a second, complementary set of data (of desynchronized beating). The comparison of theory and experiment validates the theory and highlights the predictive power of theory, which in this case preceded the experiments.

In publication 2.3, we characterize the beating flagellum as a noisy oscillator. We present direct measurements of flagellar phase and amplitude fluctuations. These fluctuations are of active nature and

surpass the contribution from thermal noise by orders of magnitude. Active fluctuations are a hallmark of active dynamics far from thermal equilibrium. In addition to this analysis of experimental data, which was guided by theoretical concepts of a noisy Hopf oscillator, we provide a theory of noisy motor oscillations. Thereby, we are able to explain the observed active fluctuations as the result of small-number fluctuations in the activity of molecular motors. Specifically, we study a minimal model of collective dynamics of molecular motors, which gives rise to spontaneous oscillations by a dynamic instability, similar to the rhythmic flagellar beat. We demonstrate how small-number-fluctuations arising from the stochastic dynamics of individual molecular motors result in active fluctuations of collective motor oscillations, similar to those of the flagellar beat. Hence, using the flagellar beat as a model system, we demonstrate that stochastic dynamics at the molecular scale can yield to measurable implications for mesoscopic dynamics at the cellular scale. We show that flagellar amplitude fluctuations introduce stochasticity in the swimming paths of flagellated swimmers such as sperm cells. Phase fluctuations disturb flagellar synchronization, which implies a competition between active fluctuations and any mechanical coupling that tends to stabilize flagellar synchrony.

In publication 2.4, we address the control of flagellar motility by chemical signals. We characterize a chemotaxis strategy along helical paths, which is employed by sperm cells to find the egg, *e.g.* in marine invertebrates with external fertilization. There, sperm cells are able to sense signaling molecules released by the egg and to steer their swimming paths upwards a concentration gradient of these molecules. We previously postulated a generic mechanism for helical chemotaxis that relies on a closed feedback loop of sensorimotor control, linking temporal chemical signals and flagellar steering responses. This helical chemotaxis represents a distinct gradient-sensing strategy that is different from the well-studied chemotaxis of bacteria along biased random walks. Recently, a close theory-experiment collaboration with the experimental laboratory of Prof. Kaupp (CAESAR, Bonn, Germany), allowed the validation of our theory on a quantitative level. In publication 2.4, we present the results of this theory-experiment collaboration, including a comprehensive theoretical description of flagellar swimming and steering. In particular, our theory accounts for the hydrodynamics of flagellar swimming for a flagellar beat whose shape is dynamically regulated by a cellular signaling cascade. This theory, which encompasses only a small set of dynamic rules, can quantitatively account for apparently complex steering behaviors of sperm cells as observed in experiments. This includes dynamic decision making of sperm cells between two distinct steering modes in a situation-specific manner.

Self-organized pattern formation in cells and tissues. In addition to motility control, we study pattern formation at the cell and organism level as a second example of nonlinear dynamics in biological systems.

In publication 3.1, we address the self-assembly process of a complex motor-filament system, the myofibril, which is the key force generator in striated and cardiac muscle cells. We present a minimal mechanism by which actin filaments and bipolar myosin filaments inside a one-dimensional bundle self-organize into periodic spatial patterns, similar to those found in myofibrils. This minimal mechanism demonstrates that local interactions between micrometer-sized ‘active building blocks’ are capable of generating spatial order on large scales. We discuss how the polydispersity of filament lengths and the stochasticity of kinetic interactions impacts on the regularity of the emergent periodic patterns.

In publication 3.2, we study pattern formation at the organism scale. We account for a remarkable biological phenomenon, the spontaneous emergence of self-organized patterns that scale with organism size. We present a minimal model for perfect pattern scaling of a head-tail gradient in the absence of pre-patterning cues. This minimal model comprises three interacting chemical species subject to a reaction-diffusion dynamics. We analytically derive a hierarchy of self-organized and self-scaling patterns. We analyze the stability of steady-state patterns, their basin of attraction, and relaxation

dynamics. For this, we apply the theory of dynamical systems to a pattern formation problem. Our theory provides a conceptual framework for pattern scaling and regeneration as observed *e.g.* in flatworms. Flatworms exhibit astonishing capabilities of reversible growth and regeneration, which are studied by our experimental collaboration partners in the Rink laboratory (MPI CBG, Dresden, Germany). Our minimal theory highlights a generic mechanism that predicts signatures of self-organized pattern scaling that can be tested in experiments conducted by our collaboration partners.

These selected publications exemplify our approach of complexity reduction in complex biological systems and the quantitative comparison of theory and experiment. In all publications, we use theoretical physics to understand the nonlinear dynamics of biological function and its robustness in the presence of non-equilibrium fluctuations.

1.2 What is biological physics?

While biology is traditionally concerned with the study of life, including the structure, development, and behavior of living organisms and their molecular underpinnings, physics studies fundamental interactions of energy and matter, and their motion in space and time. The subject of biological physics, living matter, constitutes a common intersection between these two natural sciences. Living matter displays novel physical phenomena with unconventional features, which are not commonly recognized in equilibrium systems. These include active motility[12], non-equilibrium fluctuations[13,14], adaptive dynamics[15–17], and self-organized pattern formation[18,19]. Biological physics studies the physical principles that underlie these phenomena. On a methodological side, biological physics comprises tools from different fields of physics: dynamical systems theory, statistical physics, and computational physics, see Figure 1.

Biological systems represent complex dynamical systems, where local interactions give rise to emergent dynamics on the system's level[20]. As a prominent example, inside cells, interacting cytoskeletal filaments self-assemble into regular structures, such as stress fibers or myofibrils characterized by nematic and smectic order[21,22]. Ensembles of molecular motor proteins exhibit collective dynamics, which drives active cell motility. On the scale of tissues, chemical and mechanical communication between cells orchestrates tissue development and homeostasis. In these examples, system-scale dynamics arises from local interactions. The description of this emergent dynamics is the realm of statistical physics, yet three practical differences between the statistical physics of living and non-living condensed matter should be noted.

- First, living systems are by definition out of equilibrium[20]. Even the maintenance of a steady-state is characterized by a continuous flux of energy and mass. Dynamics far from equilibrium implies that active fluctuations can surpass thermal fluctuations[13,14].
- Second, the number of interacting constituents in living matter are often in the range of $N = 10^2 - 10^6$, not $N \approx 6 \times 10^{23}$ as in a mole of ideal gas. Examples of such constituents include individual cytoskeletal filaments inside an animal cell that form its cytoskeleton. The comparatively small number of interacting constituents implies that small-number fluctuations proportional to $N^{1/2}$ give rise to substantial deviations from mean field dynamics.
- Third, there is not a single division line between what defines the small scale and the large scale in a biological system, see Figure 1. Rather, there is a hierarchy of coarse-graining levels: from molecules to subcellular processes to cellular dynamics to tissues to organisms and even ecological systems, see Figure 1. It is the challenge of biological physics to develop appropriate effective theoretical descriptions for a specific coarse-graining level, which can bridge from one level to the next higher level[23].

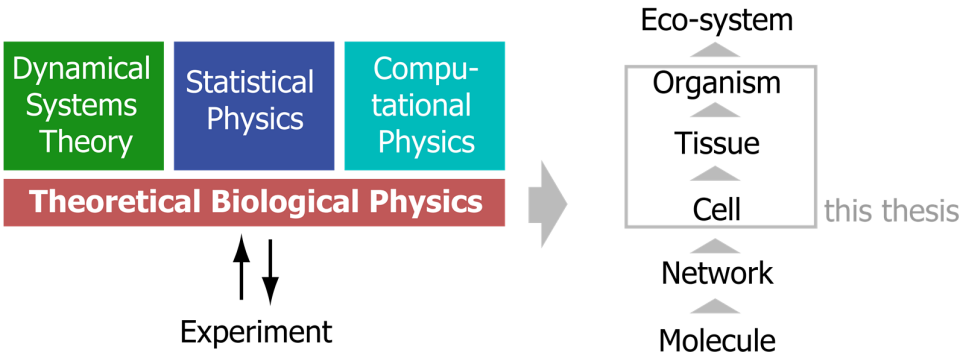

Figure 1. *The toolbox of theoretical biological physics.* Theoretical biological physics draws from different fields of physics. First, dynamical systems theory is indispensable to analyze effective theories of biological dynamics. Such effective theories coarse-grain dynamic processes at smaller scales and usually comprise effective degrees of freedom, *e.g.* system-level activity states. Second, statistical physics provides the framework to derive such effective theories of mesoscopic dynamics from interactions at the micro-scale. Third, computational physics enables the analysis of theoretical descriptions of biological processes at different levels of detail and complexity, which are not amenable to analytical treatment anymore. Computational methods are further needed to analyze experimental data and to quantitatively compare theory and experiment. This toolbox of theoretical biological physics is applied to identify physical mechanisms of biological function at different coarse-graining levels and length scales, ranging from subcellular dynamics up to the interactions between organisms. In this thesis, we focus on the intermediate scale of cells and organisms.

In this thesis, we employ an approach of minimality that seeks to identify those degrees of freedom of a biological system, which are absolutely needed to understand the physical principle behind a specific phenomenon, thus following the principle of Occam's razor. It is understood that any theoretical description represents an idealization of nature's complexity. We nonetheless strive for a quantitative comparison of theory and experiment. In fact, it is often only through the use of a theoretical description with a minimal number of adjustable parameters that the successful determination of parameters becomes feasible. The same applies to the falsifiability of a proposed physical mechanism of biological function. A bottom-up molecular description of biological processes is often not feasible due to the complexity of the system under study, as well as a result of our limited knowledge of its components and interactions. Even if this quantitative information were available, it is often desirable to complement bottom-up approaches by coarse-grained effective descriptions that highlight generic principles, one at a time, as studied in this thesis. We consider the crucial determinants of a theoretical description of biological system to be this choice of coarse-graining level and the choice of effective degrees of freedom, together with falsifiable assumptions on their dynamic relationships. In contrast, the actual mathematical framework used to formulate the theoretical description can often be chosen by practical considerations. Common choices include ordinary and partial differential equations, stochastic differential equations, finite difference equations, agent-based simulations, Markov models, Boolean networks, and cellular automata. Thus, the same physical idea may be cast into different specific mathematical formulations, which can often be considered equivalent on a conceptual level. The theoretical descriptions in this thesis employ stochastic nonlinear differential equations, both ordinary and partial, as well as agent-based simulations.

We apply this methodological toolbox to two central dynamical processes of biological systems: (i) cell motility and motility control, and (ii) self-organized pattern formation inside cells and organisms.

Thereby, we seek to understand physical mechanisms that ensure robust biological function in the presence of non-equilibrium fluctuations, structural variations, and external perturbations.

1.3 Nonlinear dynamics and control

Active biological systems such as cells, tissues, and organisms continuously convert chemical energy into work and heat to facilitate *e.g.* directed motility and information processing[24]. Additionally, these systems are able to form ordered spatial patterns at the cell, tissue, and organism level by means of self-organization[20]. In both cases, nonlinear feedback loops control biological dynamics. This nonlinear control ensures robust function in the presence of fluctuations and perturbations. In addition to external perturbations, internal fluctuations arising from non-equilibrium molecular processes and small-number fluctuations in biochemical reactions can be substantial and impact the dynamics on mesoscopic scales.

Nonlinear dynamics. We can characterize biological systems in terms of mesoscopic variables. These variables may refer to classical biological variables such as the expression of specific genes or protein concentrations, as well as physical variables such as forces and fluxes, or spatial order parameters. A combination of positive and negative feedbacks between these mesoscopic variables gives rise to a rich nonlinear dynamics, whose features include excitability, bistability, and spontaneous oscillations[25–28]. These features enable responses to external stimuli and cellular decision making[27,29,30].

Excitability has been well characterized in the context of neuronal dynamics[25]. In publication 3.1, we will encounter an example of excitability in a pattern formation system. Bistability allows cells to dynamically switch between two cellular programs, *e.g.* modes of metabolic activity, in an adaptation to environmental conditions[31]. We will encounter an example of dynamic switching between two different steering modes in the context of chemotaxis of sperm cells in publication 2.4.

Oscillations are paramount in biology: they are observed *e.g.* in cellular signaling systems. In these systems, closed feedback loops with a temporal delay represent a generic design paradigm for spontaneous oscillations[32]. A well-studied example of a biological oscillator is the circadian clock, which sets day-night rhythms of biological activity[33]. In the circadian clock, signaling proteins regulate their own concentrations in a closed feedback loop with delays, resulting in oscillations with an intrinsic oscillation period of about $24\,\mathrm{h}$. These spontaneous oscillations become entrained to the daily rhythm of light exposure, providing an example of synchronization. Generally, signaling systems that harbor an internal oscillator can serve as a bandpass filter that actively amplifies oscillations of a sensory input signal at a certain frequency. An example is provided by hair cells of the inner ear that detect sound waves[34,35]. Some swimming cells process oscillatory light or chemical stimuli while navigating along chiral paths[7,8,36,37], which we address in publication 2.4.

Spontaneous oscillations occur also in chemo-mechanical oscillators. An important example are motile cilia and flagella, which represent slender cell appendages of eukaryotic (non-bacterial) cells[1–3]. Cilia and flagella exhibit self-organized regular bending waves with typical frequencies in the range of $10-100\,\mathrm{Hz}$. This flagellar beat pumps fluids and propels cellular swimmers in a liquid. Flagellar bending waves result from the collective dynamics of molecular motors inside the flagellum. A closed feedback loop, where elastic deformations of the flagellum control spatial profiles of motor activity inside the flagellum, gives rise to a dynamic instability and self-organized oscillations[38,39]. These chemo-mechanical oscillations do not depend on inertia, as motion is highly overdamped at the relevant length and time-scales. Instead, a combination of positive feedback and negative feedback with delay is sufficient to drive oscillations[32]. Positive feedbacks are a result of active processes and have been termed negative friction in the context of collective motor dynamics.

In addition to temporal dynamics, closed feedback loops also account for spatial patterns. Bidirectional, local interactions between two spatial fields $A(x)$ and $B(x)$ can give rise to the self-organized formation of spatial patterns[40,41], as discussed in section 1.3.2. These spatial fields can correspond to local concentrations of signaling molecules, or also local mechanical stress[40,42,43]. In publication 3.2, we will present a generic mechanism for self-organized pattern formation, whose patterns adapt to system size by nonlinear feedback control[11].
The nonlinear dynamics of biological system facilitates adaptation to external perturbations, and robust function in the presence of strong fluctuations. These are discussed in the following.

Adaptation. Cells and tissues can adapt to external conditions that change in time. A prototypical example is provided by sensory adaptation, where the sensitivity towards an extracellular stimulus is dynamically adjusted in response to slow changes of the stimulus base-level[15,17]. Sensory adaptation allows the detection of relative changes of a stimulus on a time-scale faster than a time-scale τ of adaptation. For sake of illustration, we consider a minimal model of sensory adaptation that has been abstracted by Barkai and Leibler from the more complex signaling dynamics of the chemotactic response of the bacterium *Escherichia coli* as[17]

$$\tau \dot{p} = 1 - ps. \tag{1}$$

Here, a single nonlinearity, the product of the external stimulus $s(t)$ and a dynamic sensitivity $p(t)$, ensures that the system's output $a = ps$ is independent of the stimulus level for constant stimulus, $s(t) = s_0$, yet faithfully tracks relative changes of the stimulus on time-scales faster than τ. We will employ an extension of this minimal model of sensory adaptation in a theoretical description of sperm chemotaxis in publication 2.4.
In addition to the dynamic adaptation of sensitivity levels, even functional spatial structures can adapt to external perturbations. For example, in cells that mechanically interact with an elastic substrate, the spatial organization of the cytoskeleton and its rheological properties change as a function of substrate stiffness[44,45] (see also theoretical work by the author on this topic[46–48]). On the tissue and organ level, examples of structural adaptation include the growth of muscle in response to exercise, or the thickening of bones in response to mechanical load[49,50]. Complex tissues such as the liver adapt to changes in metabolic load. These examples highlight the dynamic adaptation of form to function in biological systems. This dynamic adaptation requires a reverse feedback of functional characteristics on the structures that generated this function in the first place. Adaptation represents a specific case of information processing in biological systems. We now turn to another instance of cellular information processing, motility control, which offers the unique opportunity to directly observe the output of cellular signaling in the form of cellular motility responses.

Motility control. The control of cell motility requires closed feedback loops that link motility and sensory input. During chemotactic navigation of cells reviewed in section 1.4.3, external chemical stimuli are transduced by the cell to control the dynamics of the cytoskeleton of the cell, and thus cellular motility. Conversely, the active motion of a cell in a spatial field of a stimulus determines the temporal stimuli perceived by the cell. This general principle, by which a motile agent structures the sensory input it receives by its own motion has gained recent attention in the field of control theory as the principle of *information self-structuring*[51]. Steering responses of a cell represent a direct read-out of the output of the signaling cascades that control motility. Thus, cellular motility control represents a convenient model system to study the nonlinear dynamics of cellular information processing.

Robustness. An important aspect of dynamic feedback control in biological systems is the robustness of biological function to external perturbations and internal fluctuations[52,53]. At the mesoscopic scale of the cell, thermal noise, non-equilibrium fluctuations, and molecular shot noise can be substantial and interfere with biological function. For example, small-number fluctuations of signaling molecules introduce a substantial element of stochasticity into biological information processing. In section 1.4.3, we review three different chemotaxis strategies employed by single cells, each of which allows to detect extracellular concentration gradients of signaling molecules in a different way. We argue that these different mechanisms represent an adaptation to different levels of noise, both in motility and sensing[8]. Occasionally, fluctuations can play also a beneficial role: some cells harness noise to facilitate a spectrum of heterogeneous responses despite their otherwise identical setup, the most prominent example being the adaptive immune system[54]. Theoretical descriptions of biological function as pursued here allow to assess the reliability of control mechanisms with respect to external perturbations and intrinsic fluctuations. In addition to robustness with respect to intrinsic and extrinsic fluctuations, biological control designs often exhibit structural robustness.

Structural robustness defines the property of a system to function reliably, even if parameters of the system, or even its design, are varied. Such variability can be the result of genotypic heterogeneity, or of external perturbations and internal fluctuations that occurred during the development of the system. Control mechanisms that require fine-tuning of parameters would lack structural robustness. Theoretical descriptions of biological function allow to delineate the parameter region of reliable function. We will discuss examples of parameter robustness in chapters 2 and 3 in the context of motility control and pattern formation, respectively. Structural robustness relates also to the very design of the control mechanism itself. One common design paradigm for structural robustness is redundancy, where important functional elements operate in duplicate. Redundancy applies for example at the level of proteins, where several proteins often perform similar functions, and can partly substitute for one another, if one protein were absent. Similar, complex signaling networks often have redundant network topologies that can compensate for the failure of individual signaling links. Another design paradigm ensuring structural robustness are control mechanisms that depend only on qualitative features of functional relations between state variables (*e.g.* monotonic dependence of one variable on another) as compared to strict quantitative relations (*e.g.* linear dependence). In publication 3.2, we will explicitly discuss a generic pattern forming system that scales self-organized patterns proportional to system size, whenever a number of qualitative conditions are met[11].

In the following, we review selected aspects of nonlinear dynamics and feedback control with a focus on cell motility and self-organized pattern formation.

1.3.1 Mechanisms of cell motility

Cells employ a great variety of energy-dependent mechanisms for locomotion, including swimming, crawling, and twitching as discussed below[55]. A common feature of these different mechanisms is the non-equilibrium dynamics of the cytoskeleton of the cell[12]. Active shape changes allow motile bacteria and flagellated eukaryotic cells such as sperm to propel themselves in a liquid[56–58]. In these examples, molecular motors interact with cytoskeletal filaments to drive motility. Other cells such as macrophage immune cells crawl on a substrate by harnessing active polymerization forces of cytoskeletal filaments, which push their cell front forward[59,60]. This crawling motility requires partial adhesion to a substrate in order to constrain backward motion due to reaction forces.

Directed motion requires a structural polarity of the cell. Cell polarity can be static, as in the case of sperm cells with a defined head-tail morphology. Static cell polarity implies that cells have to actively rotate during steering responses. Other cells, such as macrophages with crawling motility, display a

dynamic polarity, associated with a continuous remodeling of their cytoskeleton[61,62]. Multiple sensory cues including chemical and mechanical stimuli control the direction of cell motility.

The molecular machinery of cell motility. We first review key components of the cytoskeleton, whose non-equilibrium dynamics drives the different locomotion strategies of single cells: these components comprise structural biopolymeric filaments and force-generating molecular motors, see Figure 2.
Three classes of cytoskeletal filaments in eukaryotic cells. Inside cells, monomers of cytoskeletal proteins polymerize into filaments that constitute the cytoskeleton of the cell[3,63]. The cytoskeleton defines the mechanical properties and morphology of cells, especially in cells that lack a cell wall, such as animal cells. In eukaryotic cells, three classes of cytoskeletal filaments are found: actin filaments, microtubules, and intermediate filaments.
- *Actin filaments:* Actin is the most abundant intracellular protein in the eukaryotic (non-bacterial) cell, constituting 1-5% of its total protein content. Actin monomers (G-actin) polymerize into semiflexible actin filaments (F-actin), which have a persistence length of about $10\,\mu\mathrm{m}$ [63]. Actin filaments are structurally polar, with a designated plus-end (also named: barbed end) and minus-end (also: pointed end). In a typical eukaryotic cell, actin filaments form a crosslinked meshwork with gel-like properties that fills intracellular space. Additionally, actin filaments form a dense cortical network beneath the cell membrane of animal cells, the actin cortex. Turn-over of the actin cytoskeleton is fast, with a time-scale of $1-10\,\mathrm{s}$ measured for the actin cortex[64].
Polymerization dynamics of actin filaments is coupled to the hydrolysis of Adenosine triphosphate (ATP)[3,63]. This renders actin polymerization a non-equilibrium phenomenon that breaks detailed balance. Generally, polymerization kinetics is faster at the structural plus-end of an actin filament compared to its minus-end. Polymerizing actin filaments can exert active polymerization forces[65], which underlie the mechanism of crawling motility of cells[59].
The structure of the actin cytoskeleton is tightly regulated by the cell[3]. Specifically, the length of actin filaments is fine-tuned by capping proteins that cap filament ends to regulate actin polymerization dynamics. Severing proteins can bind at any position along an actin filament, inducing filament breakage at the binding position. Actin binding proteins can crosslink and bundle actin filaments. In addition to these 'passive' actin binding proteins, actin filaments interact with molecular motors of the myosin family that generate active forces[3]. The structural polarity of actin filaments with a designated plus- and minus-end sets a direction of motor motion. Conventional myosin motors walk towards the actin plus-end. Further, actin filaments, myosin motor proteins, and actin binding proteins can assemble into spatially ordered structures inside cells. For example, non-motile animal cells adhered to a substrate can form stress fibers of bundled actin filaments, thus representing a case of nematic order. In striated and cardiac muscle cells, actin filaments and myosin filaments are arranged in myofibrils of almost crystalline regularity, thus representing an example of smectic order of the cytoskeleton[22].
- *Microtubules:* The second major class of cytoskeletal filaments are microtubules, which are polymerized out of stable dimers of the protein tubulin. Microtubules are comparatively stiff hollow tubes of diameter $24\,\mathrm{nm}$ with a persistence length of about $1\,\mathrm{mm}$ [63]. Microtubules serve as tracks for kinesin and dynein motor proteins and play a major role in directed intracellular transport.
Microtubules can assemble into cell-scale ordered structures. One prominent example is the mitotic spindle, a bipolar cytoskeletal scaffold that serves for partitioning the two copies of the chromosomes to the two prospective daughter cells before cell division[3]. A second microtubule-based structure is the flagellar axoneme, which forms the cytoskeletal core of cilia and flagella. The axoneme comprises a cylindrical arrangement of 9 doublet microtubules, which are connected by dynein molecular motors (and additional proteins ensuring structural integrity)[66]. The collective dynamics of these motors drives regular bending waves of motile flagella[2], see Figure 4.

- *Intermediate filaments:* As a third class, intermediate filaments represent a heterogeneous family of filaments that serve as structural elements, *e.g.* in neurons and muscle cells. Special intermediate filaments form the hairs and nails of animals[3].
In bacteria, cytoskeletal filaments homologous to those of eukaryotic cells are found, which play important roles for cell motility and cell division[67].

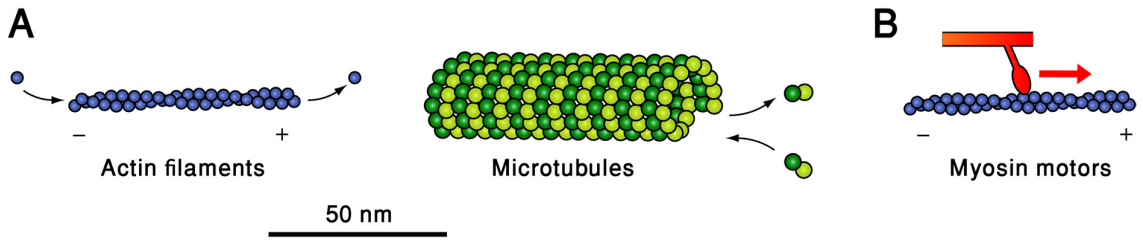

Figure 2: *Elements of the cytoskeleton.* **A.** Eukaryotic (non-bacterial) cells contain actin filaments and microtubules as key elements of their cytoskeleton, which defines mechanical properties of the cell. These biopolymers are highly dynamic and continuously undergo non-equilibrium polymerization dynamics. Actin filaments and microtubules are structurally polar, with distinct polymerization dynamics at their structural plus- and minus-end, respectively. **B.** Actin filaments and microtubules serve as tracks with defined directionality for molecular motor proteins, such as myosin motors. Myosin motors undergo chemo-mechanical cycles, which couple the energy-favorable hydrolysis of ATP molecules and a conformational change, which can generate piconewton forces and perform mechanical work.

Non-equilibrium polymerization dynamics. Polymerization of cytoskeletal filaments is a non-equilibrium process that is coupled to the hydrolysis of ATP in the case of actin filaments and GTP in the case of microtubules[3,63]. We briefly review non-equilibrium polymerization dynamics for the case of actin filaments[63]. Each actin monomer tightly binds either an ATP or ADP molecule. We thus refer to T-state and D-state monomers, respectively. Free monomers in the cytosol are mainly in T-state, while the monomers within an actin filament rapidly switch to D-state by hydrolysis of their bound ATP. An actin filament will elongate by polymerization at its tip, whenever the concentration of free monomers exceeds the critical concentration of the polymerization reaction. The critical concentrations for T-state and D-state monomers are different due to different values of ΔG for the respective polymerization reactions. For intermediate concentrations of free actin monomers, there can be net polymerization of T-state monomers at the structural plus-end of an actin filament, and net depolymerization of D-state monomers at the structural minus-end. As a result, a dynamic steady state can form that is characterized by net elongation at the plus-end and net shrinkage at the minus-end. During this actin treadmilling, actin monomers 'flow' through the filament. This mechanism requires that the rate at which new T-state monomers are added at the plus-end is faster than the rate of hydrolysis, such that the plus-end-tip of the filament will remain in T-form. The treadmilling of individual actin filaments captures essential aspects of crawling cell motility, which is driven by the non-equilibrium polymerization dynamics of a structurally polarized actin cytoskeleton[68]. In publication 3.1, we further discuss a possible role of actin treadmilling for the formation of periodic cytoskeletal patterns[10].
Actin filaments and microtubules serve as tracks for molecular motors, which we review in the next paragraph.

Molecular motors convert chemical energy into work and heat. Directed transport processes inside cells, cell locomotion, and contraction of muscle all rely on the activity of motor proteins at the

molecular scale. The common working principle of a molecular motor is a tight coupling between an energy-favorable chemical reaction and a conformational change of the motor protein itself. This conformational change can perform mechanical work (with a typical order of magnitude of $1-10\,\mathrm{pN}\,\mu\mathrm{m}$ per chemo-mechanical cycle).

Different classes of molecular motors exist in bacterial and eukaryotic cells. In the cell membrane of bacteria such as *Escherichia coli*, a rotary motor is driven by a proton-gradient[56]. This rotary motor rotates helical filaments for cell propulsion[69]. In eukaryotic cells, molecular motors move along actin filaments and microtubules to transport cargo and generate active mechanical forces[63]. Important motor families include myosin motors, which move along actin filaments, and kinesins and dyneins, which move along microtubules. In their function as motor tracks, actin filaments and microtubules provide a periodic lattice of motor binding sites with a lattice constant of a few nanometers, which is set by the size of their respective monomers. The structural polarity of actin filaments and microtubules with a designated plus-end and minus-end defines a direction of motor motion. Most members of the kinesin motor family walk towards the structural plus-end of microtubules, whereas most dyneins walk towards the minus-end. Conventional myosin motors move towards the plus-end of microtubules. Molecular motors undergo periodic chemo-mechanical cycles, during which the motors bind and unbind from their track to take a single step, while one ATP molecule is hydrolyzed. We review this chemo-mechanical cycle for the example of skeletal myosin[63]: In the most common reaction path, a free myosin motor domain binds an ATP molecule, which is subsequently hydrolyzed into Adenosine diphosphate (ADP) and a phosphate group. The release of the reaction products constitutes the rate limit step of the ATPase activity of free myosin. Binding of myosin to an actin filament accelerates this release at least 200-fold. The release of ADP and phosphate is accompanied by a conformational change of the myosin motor domain, which causes a motion of the myosin backbone relative to the actin filament with a working distance of about $5\,\mathrm{nm}$. The myosin is then ready to bind a new ATP-molecule. This triggers the unbinding of myosin from the actin filament to restart the cycle.

Single molecular motors such as myosin and kinesin exert typical forces in the piconewton range. For example, conventional kinesin motors can exert forces up to $6\,\mathrm{pN}$, while taking $8\,\mathrm{nm}$ steps along their microtubule track. This corresponds to a mechanical work of $10\,k_BT$ per step. This represents a considerable fraction of the difference in Gibbs free energy of $\Delta G = 20-25\,k_BT$ associated with the hydrolysis of a single ATP molecule during each step[63]. Kinesin is a processive motor that takes a sequence of steps before it detaches from its track. Such processive molecular motors exhibit effective force-velocity relationships[70]: an applied external force reduces their velocity, until their motion comes to a halt at a critical stall force. For conventional kinesin, the stall force is about $6\,\mathrm{pN}$.

We note that for a single molecular motor, the principle of microscopic reversibility holds: for each reaction step of the chemo-mechanical cycle, both the forward and the backward reaction are possible. Thus, there is a finite probability that a molecular motor takes a step backwards. At physiological conditions, the high chemical potential of ATP breaks detailed balance of the cycle and favors forward motion. Backward stepping of molecular motors has been observed experimentally, especially under high load forces. As a side note, ATP-synthesis in mitochondria relies exactly on this microscopic reversibility: the F_0-F_1-ATPase protein complex couples a proton-driven and an ATP-driven rotary motor. In the presence of a strong proton gradient generated by glycolosis across the mitochondrial membrane, the proton-driven F_0 motor spins the ATP-driven F_1-motor backwards[71,72]. As a result, the F_1-motor serves as a dynamo that synthesizes its own fuel in the form of high-energy ATP molecules.

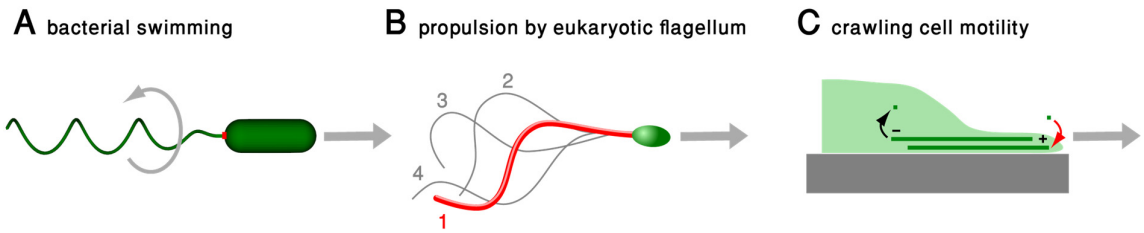

Figure 3: *Mechanisms of cell motility.* **A.** Bacteria such as *Escherichia coli* propel themselves in a liquid by rotating a passive helical filament, the prokaryotic flagellum. The rotation of this prokaryotic flagellum is driven by a rotary motor in the cell membrane, which draws its energy from a proton gradient across the cell membrane. Some bacterial strains are multi-flagellated with several prokaryotic flagella that can synchronize their rotations and form stable bundles. **B.** Eukaryotic (non-bacterial) cells such as sperm cells can swim in a liquid by virtue of regular bending waves of one or several eukaryotic flagella. Eukaryotic flagella are active filaments. Their bending waves emerge from the collective dynamics of a large number ($10^4 - 10^5$) of molecular dynein motors distributed along the length of the eukaryotic flagellum. **C.** Eukaryotic cells, such as macrophages of the immune system, harness polymerization forces of numerous actin filaments to crawl on a substrate. Propagation of a leading front termed lamellipodium is driven by polymerization forces of a structurally polarized actin cytoskeleton. Additional motility mechanisms are mentioned in the text.

Bacteria swim by rotating passive helical filaments. One of the best-studied examples of cell motility is the swimming of the bacterium *Escherichia coli*. This bacterium employs a rotary molecular motor in its cell wall to rotate a passive helical filament, termed the prokaryotic flagellum[56]. The prokaryotic flagellum is physically connected by a flexible hook to the rotor of the motor complex, which in turn can rotate freely inside a stator that is anchored to the cell wall. A proton gradient across the cell membrane drives a counter-rotation of rotor and stator[73]. This rotary motor has been a model system of biological physics, and its macro-molecular structure and mechanical function have been studied in great detail. The rotation of the rotary motor spins the helical filament and thereby propels the bacterium in a liquid[69], see Figure 3.

Bacterial motility control. Bacterial swimming represents a model system of motility control that has been studied extensively at the level of individual motors, of individual filaments, and at the level of the cell. Classic experiments revealed an operational load characteristic of the rotary motor with a rotation frequency that decreases with the applied load[74]. Such force-velocity relationships represent a general characteristic of molecular motors.

The prokaryotic flagellum itself is a passive filament. It is polymerized out of a single type of monomer, the protein flagellin. The prokaryotic flagellum forms a tubular polymer with 11 protofilaments. The helical shape of this filament is the result of a cooperative conformational change of flagellin monomers within a defined sub-set of its protofilaments. This heterogeneous conformational switch minimizes an intrinsic eigenstrain of the protein lattice in the flagellum[75–78]. Mechanical load can induce a cooperative conformational switching of all flagellins in one protofilament and thus a dynamic transition of the entire filament to a different polymorphic helical state. Most of the 11 theoretically possible polymorphic states have been observed in experiments.

In bacteria with multiple flagellar filaments, hydrodynamic interactions between rotating helical filaments results in the synchronization of filament rotation of the different filaments and the formation a stable bundle[79,80]. This flagellar bundling enhances propulsion efficiency. During bacterial swimming

and navigation, flagellar bundling is tightly controlled by an intracellular signaling pathway[69]. Specifically, chemical signals can reverse the rotation direction of one or several rotary motors, which destabilizes the flagellar bundle and induces a transition of one or several flagella to a different polymorphic state of different handedness. The net result of this transient dynamics is a random reorientation event of the cell. A dynamic regulation of the frequency of these stochastic reorientation events facilitates chemotactic navigation in chemical gradients along a 'run-and-tumble' biased random walk[81]. This bacterial chemotaxis strategy is discussed in more detail in section 1.4.3.
While the bacterial flagellum is a passive filament, eukaryotic (non-bacterial) cells employ active filaments, termed cilia and flagella, which we discuss next.

The eukaryotic flagellum is an actively bending filament. Many eukaryotic (non-bacterial) cells are equipped with slender cell appendages termed cilia or flagella[1]. Cilia and flagella perform multiple sensory, signaling, and motility functions[82,83]. We will use the term eukaryotic flagellum for both cilia and flagella (where the main difference between cilia and flagella are their length and minor structural details). The eukaryotic flagellum is not to be confused with the prokaryotic flagellum of bacterial cells. While the prokaryotic flagellum is a passive protein polymer, the eukaryotic flagellum is an active filament.
The eukaryotic flagellum is a membrane-enclosed cell appendage of typical length $10-100\,\mu\mathrm{m}$ and diameter of about $500\,\mathrm{nm}$ that contains a highly regular cytoskeletal core, the axoneme[3], see Figure 4. The axoneme is composed out of 9 doublet microtubules in equidistant cylindrical arrangement, see figure 3. Additionally, a central pair of microtubules in the center of this cylinder may be present or not, corresponding to the sub-types of 9+2 and 9+0-axonemes. More than 250 accessory proteins ensure structural integrity and function of the axoneme[66]. The axoneme of motile eukaryotic flagella contains dynein motors[66,84], which render the eukaryotic flagellum a mechanically active filament[85].

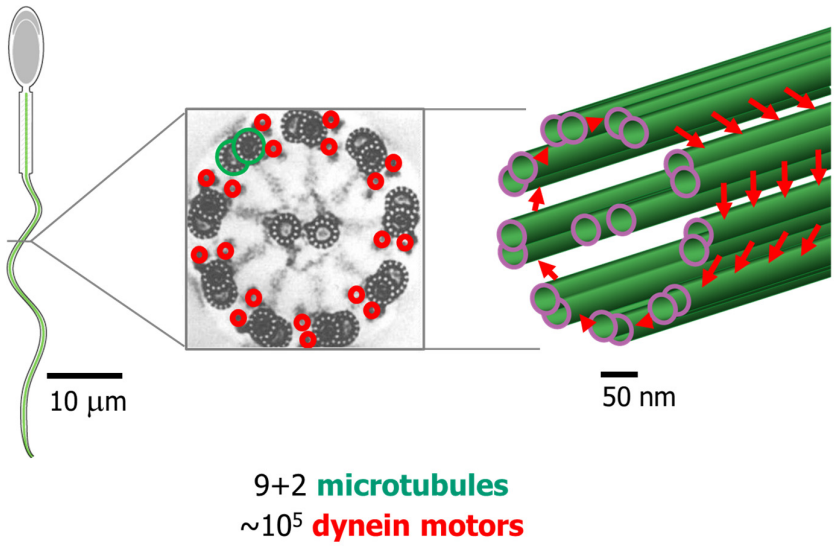

Figure 4: The eukaryotic flagellum contains a highly conserved cytoskeletal core, the axoneme. The axoneme comprises a cylindrical arrangement of 9 doublet microtubules, which are connected by dynein molecular motors. The collective dynamics of these dynein motors drives regular bending waves of cilia and flagella. *Left:* Schematic of flagellated sperm cell, *middle:* cross-section of the flagellar axoneme, *right:* schematic of axonemal architecture. Electron micrography from ref.[86] with permission.

It is remarkable that the highly regular structure of the axoneme is found in all 5 kingdoms of eukaryotic life, including amoeba, plants, and animals[87]. This evolutionary highly conserved structure appeared early after the chiasm between prokaryotes (bacteria and archaea) and eukaryotes. It has been speculated that the axoneme evolved from the cytoskeletal cell division machinery in eukaryotic cells, the mitotic spindle, by means of re-dedication to a new function[87].

Collective motor dynamics drives flagellar bending waves. Some cilia and flagella are motile. Inside their axonemes, neighboring doublet microtubules are connected by dynein molecular motors[66,84]. The axoneme has a chiral architecture: dyneins are tightly bound to one doublet and exert forces on the neighboring doublet in clockwise sense (when viewed from the basal end of the axoneme).

We review the mechanism of active flagellar bending by motor-induced filament sliding[2,3]. The activity of dynein motors slides neighboring doublet microtubules relative to each other[88,89]. Free sliding is partially constrained, both at the basal end of the axoneme as well as by nexin protein links distributed along the flagellar length. These constraints convert the shearing forces generated by the dynein motors into bending moments that bend the axoneme. Bending in one direction requires that motors on one side of the axoneme are preferentially active at a given time. Spontaneous oscillations in motor activity drives regular bending waves of the flagellum. The bending rigidity of the flagellum is highly anisotropic for many flagella[90], favoring bending in a plane. This results in planar flagellar beat patterns in many cells, including important flagellated model swimmers such as marine invertebrate sperm or the green alga *Chlamydomonas*. A small chirality of flagellar bending waves results in helical swimming paths of defined handedness of these flagellated swimmers[91–93], which has implications for cellular navigation[7–9,94].

The control of dynein activity and the emergence of oscillatory motor activity represents an instance of self-organized collective dynamics in an ensemble of molecular motors[95]. One of the most-striking experiments demonstrating this self-organization is the re-activation of demembranated axonemes isolated from flagellated cells[96–98]. Upon provision of ATP, these isolated axonemes resumed regular bending waves, independent of any cellular control circuits.

Self-organized flagellar bending waves are the result of a closed feedback loop between the spatial activity profile of dynein motors inside the axoneme and geometric deformations of the axoneme, which gives rise to a dynamic instability[99,100]. Specifically, local motor activity deforms the axoneme, which again changes motor activity in a defined spatial range. As a result, travelling waves of motor activity emerge, which propagate along the flagellar length[39,100–102]. The shape of the resultant flagellar bending waves is sensitive to boundary conditions[100]. We have been general in refereeing to the geometric deformation of the axoneme on purpose. The precise nature of the control of motor activity by deformations of the axoneme is still open. Three major theories are discussed. In one of the earliest theories, Brokaw proposed that the local curvature of the axoneme constitutes the key regulator of motor activity[99]. Other authors objected that the local deformation resulting from typical curvatures are negligibly small on the length-scale of individual molecular motors[39]. Lindemann *et al.* proposed that bending of the axoneme causes splay, *i.e.* an increase of the inter-doublet spacing, which potentially could regulate motor activity[102]. Finally, Jülicher *et al.* considered a theoretical description in which the local sliding displacement of neighboring microtubules controls motor activity[39]. While the last model could quantitatively account for the waveform of the sperm flagellar beat, recent experiments with shorter flagella of the green alga *Chlamydomonas* challenges the sliding control model[103,104]. It is possible that control mechanisms of the flagellar beat are less conserved as previously anticipated. A major bottle-neck in uniquely identifying the mechanism of motor control of the beating axoneme is the simplicity of flagellar bending waves, which can be characterized by a small number of waveform parameters. Thus, different mechanisms relying on different microscopic assumptions can reproduce the observed waveforms equally well, provided the parameters of these models are chosen

appropriately. Our research presented in this thesis provides additional characterizations of the flagellar beat in terms of (i) an active mechano-response of the flagellar beat in response to changes in hydrodynamic load[5] and (ii) active fluctuations of the flagellar beat due to motor noise[14]. We anticipate that such additional characterizations can contribute to the discrimination between the different proposed theories on the origin of the flagellar beat.

Moving in fluids. Flagellar bending waves propel cellular swimmers such as sperm cells[1,58], swimming alga[105], and pathogens (*e.g.* Trypanosomes[106], which cause sleeping sickness, and certain life cycle stages of Malaria parasites[107]). At the length and time-scales of cellular microswimmers, viscous forces dominate over inertial effects[108–110]. The relative magnitude of inertial forces compared to viscous forces for a swimmer with periodic shape dynamics is characterized by the dimensionless Reynolds number of oscillatory motion

$$\mathrm{Re} = \frac{\rho\,\omega_0 A\,d}{\eta}. \tag{2}$$

Here, ρ and η denote the density and dynamic viscosity of the fluid, respectively, while ω_0 and A denote frequency and amplitude of the periodic swimming stroke. Finally, d denotes a characteristic length-scale of the swimmer. A low Reynolds number implies that viscous forces dominate over inertial forces at the relevant time and length-scales. For example, for a beating flagellum of diameter $d = 0.4\,\mu\mathrm{m}$, beat amplitude $A = 5\,\mu\mathrm{m}$, beat frequency $\omega_0 = 30\,\mathrm{Hz}$, we estimate $\mathrm{Re} \sim 10^{-4}$. Note that it is the diameter of the flagellum, not its length, that sets the magnitude of maximal fluid stresses[111].
In the limit of zero Reynolds number, the Navier-Stokes equation governing fluid flow simplifies to the linear Stokes equation,

$$0 = \nabla p - \eta \nabla^2 \mathbf{v}, \tag{3}$$

where p and $\mathbf{v}$ denotes pressure and flow field of the fluid. The Stokes equation is linear. Thus, its solutions obey a superposition principle. General solutions of the Stokes equation can be found as superposition of its fundamental solution, the Stokeslet $v_i = G_{ij}F_j$, which describes the flow resulting from a point force $F_j\delta(\mathbf{r})$ acting on the fluid. Here, $G_{ij}(\mathbf{r}) = (8\pi\eta)^{-1}(1/r + r_i r_j/r^3)$ denotes the Oseen tensor. This superposition principle has been exploited to derive analytical results for the motion of minimal model swimmers, see *e.g.* references[112–116]. This superposition principles further underlies efficient algorithms to solve the Stokes equation in complex geometries numerically[117].
The second general feature of the Stokes equation is its invariance under time-reversal. This time-reversal symmetry has important functional consequences for swimming and hydrodynamic synchronization at low Reynolds number. Time-reversibility implies that the swimming path of a low Reynolds number swimmer depends only on the sequence of shapes it attains as a function of time, but is independent of the rate of shape change. In particular, a reciprocal swimming stroke with a backward stroke that traces a forward stroke exactly backwards in time will produce a periodic motion, but zero net displacement. This phenomenon is known under the colloquial name of the *Scallop theorem*[108]. The name was coined following an illustrative example of an idealized scallop presented in a popular lecture by Purcell: a two-leg-swimmer with a single joint that opens and closes periodically. A corollary of the scallop theorem is that any swimming stroke with amplitude A, where A is small compared to a size L of the swimmer, will result in a net swimming speed $\overline{v}$ that scales quadratically with A, *i.e.*

$$\overline{v} \sim A^2 \omega_0 / L. \tag{4}$$

Here, ω_0 is the frequency of the swimming stroke. One may denote this relation the *quadratic law of low Reynolds number propulsion*[115]. Formally, the net swimming speed $\overline{v}$ is independent of fluid viscosity η. However, this argument assumes that the swimming stroke will not be altered by an increase in hydrodynamic load associated with an increase in η. In real systems, the active processes that drive the swimming stroke will generally display a force-velocity relationship, *i.e.* slow down under increased load. Such force-velocity relationships have been measured for beating flagella both in response to an increase in fluid viscosity[96,118,119] as well as in response to a dynamically varying load[5].

The mathematical beauty of self-propulsion at low Reynolds numbers has attracted a continuous stream of theoretical studies, following an early exposition by Taylor in 1951[4]. We briefly mention a geometric interpretation by Shapere and Wilczek, who identified self-propulsion at low Reynolds numbers as a connection of an $SE(3)$-fiber bundle on a space S of admissible shapes of a swimmer[120]. Here, the special Euclidean group $SE(3)$ denotes the Lie group of rigid body transformation in 3-dimensional space. Any trajectory $s(t)$ in shape space S lifts to a trajectory $[s(t), \mathbf{G}(t)]$ in this fiber bundle $S \times SE(3)$. This trajectory characterizes the translational and rotational motion of a shape-changing low Reynolds number swimmer that is free from external forces and torques in terms of a time-dependent rigid body transformation $\mathbf{G}(t) \in SE(3)$ of a material frame of the swimmer. For periodic shape changes of small amplitude A, the net motion $\mathbf{G}(T)^{-1}\mathbf{G}(0)$ after one swimming stroke of period T is proportional to A^2, see equation (4). The proof relies on the argument that any swimming stroke of infinitesimal amplitude can be written as the superposition of several reciprocal shape modes. As a consequence of the scallop theorem, none of these reciprocal shape modes alone can result in any net motion of the swimmer. However, nonlinear cross-terms between different reciprocal modes result in net displacement, which thus scales with A^2. As an example, we note that flagellar bending waves can be approximately described as traveling bending waves. A traveling bending wave can be written as the superposition of two standing waves phase-shifted by $\pi/2$ by elementary trigonometry. Each standing wave alone would provide zero net propulsion, while their superposition allows for flagellar self-propulsion[121].

We conclude that the time-reversal symmetry of the Stokes equation prompts non-reciprocal swimming strokes that explicitly break time-reversal symmetry to allow for net propulsion. Similarly, we will find that hydrodynamic synchronization at low Reynolds numbers is only possible if specific symmetries are broken[110,115,122], see also section 1.4.2.

Flagellated microswimmers represent a model system for motility control. Cilia and flagella are a best-seller of nature. Virtually all animal cells display one or more of these slender cell appendages, which serve for motility and sensing[1,123]: non-motile primary cilia facilitate our senses of smell, vision, and, in some species, hearing, and gauge blood flow to regulate blood pressure. Motile cilia and flagella propel sperm cells, green algae, and disease-causing protists, such as Trypanosomes (responsible for sleeping sickness) or plasmodia (which cause malaria) in a fluid[124]. Sensory input controls flagellar beating in these microswimmers and enables them to actively steer their path in response to environmental cues[7–9]. On epithelial surfaces, carpets of short flagella termed cilia synchronize their beat to pump fluids, such as mucus in mammalian airways[125] and cerebrospinal fluid in the brain[126]. Chiral flagellar beating plays a crucial role in the establishment of the left-right body axis during embryonic development[127,128].

Flagellar swimming, steering, and synchronization. The flagellar beat − itself a manifestation of microscopic dynamics of dynein motors inside the flagellar axoneme − facilitates swimming and

steering in flagellated microswimmers. The asymmetric shape of the flagellar beat determines the chiral swimming paths of these cellular swimmers. A dynamic regulation of beat shape underlies steering in response to chemical signals, light, and possibly temperature. Finally, speed and shape of the flagellar beat are susceptible to external mechanical forces. This flagellar load response is a prerequisite for the remarkable phenomenon of beat synchronization by mechanical coupling in collections of beating flagella.

Flagellar bending waves are chiral. In sperm cells and green alga, flagellar beat patterns resemble planar bending waves that propagate along the flagellum, from its proximal to its distal tip[1]. These flagellar bending waves commonly display a pronounced in-plane asymmetry, characterized by a static mean curvature of the flagellar shape. This mean flagellar curvature K_0 is a result of active processes inside the flagellum. Experiments with reactivated flagellar axonemes revealed that K_0 depends on ATP concentration[98]. This finding is consistent with the notion that flagellar asymmetry is generated by static motor activity inside the flagellum. Changes in the viscosity of the surrounding fluid reduced the mean flagellar curvature K_0 [119]. During chemotactic steering responses of sperm cells, an intraflagellar signaling cascade dynamically regulates flagellar asymmetry K_0 [129,130]. The microscopic origin of flagellar beat asymmetry remains insufficiently understood.

In addition to the static and dynamic component of flagellar curvature, the flagellum is also twisted. This results in non-planar beat patterns that break chiral symmetry[93,131,132]. Flagellar twist is small in the green alga *Chlamydomonas*, as well as the beat of the flagellar beat in sperm of many model species. In mouse and humans, a pronounced flagellar twist gives rise to conical flagellar waves[133]. Flagellar twist is also pronounced for cilia on epithelial surfaces, whose beat pumps fluids. These cilia move backward during their recovery stroke in close proximity to the surface in a highly twisted configuration.

The chiral flagellar beat controls swimming and steering. Chiral flagellar beat patterns result in chiral swimming paths of flagellated swimmers such as circles, twisted ribbons, and helices[93,119,134]. These chiral swimming paths form the basis of dedicated sampling strategies of cellular navigation[7–9], which are reviewed in section 1.4.3. Far from boundary surfaces, sperm from marine invertebrates swim along helical paths[91–93]. From hydrodynamic simulations, we could estimate the flagellar twist required to account for the observed helicity of swimming paths[93]. This flagellar twist is surprisingly small and corresponds to an out-of-plane component of the planar flagellar bending waves of less than a micrometer. In the vicinity of boundary surfaces, sperm cells localize close to the interface[135], where they swim in circles with defined sense of rotation relative to the surface normal[119]. It has been proposed that the chirality of the flagellar beat contributes to this surface accumulation of sperm in addition to pure hydrodynamic effects[136–138].

Swimming of sperm cells along circular and helical paths represents a stereotypic form of exploratory motion, which forms the basis of a dedicated navigation strategy. Sperm from marine species perform helical chemotaxis[8,93,139–142] to steer their swimming path up chemical gradients of signaling molecules to find the egg[143,144]. In the unicellular green alga *Chlamydomonas*, a small out-of-plane component of the beat of the its two flagella causes a self-rotation of the cell around its swimming axis at a frequency of about $2\,\mathrm{Hz}$ (which is much slower than the beat frequency of $50\,\mathrm{Hz}$)[105]. This slow rotation allows this green alga to detect directed light stimuli as cell rotation periodically exposes a light-sensitive eye spot to incident light. A simple steering feedback allows these cells to steer their swimming path relative to the direction of incident light[9,94,145].

Finally, during embryonic development, the chiral beat of flagella generates leftward flow of fluid, which determines the left-right-body axis in the developing embryo[146]. The broken chiral symmetry of the flagellar beat results neither from a spontaneous symmetry breaking, nor does it depend on physical laws that explicitly break chiral symmetry. Instead, the chiral flagellar beat is a result of the chiral

architecture of the flagellar axoneme[131], which in turn is rooted in the chirality of the proteins it is built of. Chiral flagellar beat patterns represent an example of homo-chirality that propagates from the molecular scale all the way up to the scale of cells, tissues and organisms.

Mechanical control of flagellar motility. The beating flagellum exerts active forces on the surrounding liquid. Conversely, external mechanical forces affect the swimming path of flagellar microswimmers. Additionally, external forces change the speed and shape of the flagellar beat itself. This mechanical control of the flagellar beat is important for flagellar mechano-taxis and flagellar synchronization in collections of flagella, as reviewed below.

Interactions with flows and structures. Fluid-structure interactions control flagellated motility in a number of functional contexts. It had been noticed already by Rothschild that sperm cells localize near a glass-water interface, where sperm cells swim in a plane[135]. This phenomenon can be explained as a pure hydrodynamic effect. The chirality of the flagellar beat of sperm cells induces a thrust component normal to the interface that brings cells closer to the interface until a critical distance is reached, where short range repulsion sets in[136,138]. At least two additional hydrodynamic effects stabilize swimming at the interface. First, the leading order singularity of the time-averaged flow field generated by a swimming sperm is that of a pusher, with an inward flow component along the normal of the beat plane. This induces a hydrodynamic attraction the wall[109]. Second, swimming at a small distance d to the wall, which is less than the flagellar length L, effectively suppresses rotational diffusion of the cell, thereby prolonging residence times close to the interface[137].

A second instance of flagellar motility control by mechanical forces is the active upstream migration of sperm cells, termed rheotaxis[147,148]. In the presence of walls, local shear flows rotate swimming sperm like a weather van such that the vector of their net swimming direction points upstream[149]. It has been proposed that this rheotaxis serves as a sperm guidance mechanism in the mammalian oviduct, where post-coitus oviductal flows are sufficiently strong to align sperm[148].

As a final example of microswimmer-structure interactions, flagellated trypanosomes were found to swim more efficiently in the presence of obstacles, whose size matches the radius of curvature of flagellar bending waves[150]. This has been interpreted as an adaption to the crowded environment of the blood stream, where red blood cells represent semi-rigid obstacles.

Active mechano-responses. Self-organized flagellar bending waves exhibit active mechano-responses with a flagellar wave form that depends on applied external forces. Early experiments by Brokaw have shown that an increase in the viscosity of the swimming medium reduces both the frequency and the amplitude of the flagellar beat[96,118]. Similar experiments using local micropipette-generated flows or swimming sperm in a visco-elastic fluid gave qualitatively similar results[151,152].

The flagellar beat is an emergent phenomenon of collective dynamics in an ensemble of dynein molecular motors working against both intra-flagellar forces and hydrodynamic friction forces, which result from moving the surrounding fluid. It is thus to be expected that changes in these external forces change the shape of the flagellar beat. The waveform compliance of the flagellar beat provides a rough estimate of the relative importance of intraflagellar friction forces and hydrodynamic friction forces. In publication 2.2, we theoretically derive a force-velocity relationship of the flagellar beat[5]. The corresponding effective theory coarse-grains active motor dynamics in the flagellar axoneme in terms of a phase-dependent active driving force. Our theoretical predictions are compared to a dynamic measurement of this force-velocity relationship in the green alga *Chlamydomonas*. We provide an analysis of experimental data that shows how the phase speed of the flagellar beat changes in response to rotations of the cell, which imparts known hydrodynamic friction forces on the flagellum, allowing us to infer how the beating flagellum responds to external fluid forces.

Recent experiments suggest that the ATP consumption of flagellar beating is rather insensitive to mechanical load[153]. This experimental finding resonates with a theoretical description that employs a fixed phase-dependent flagellar driving force to represents the active dynamics inside the axoneme that makes the flagellum beat. Accordingly, any increase in load is compensated by a reduction in speed, not an increase in fuel consumption.

For single processive motors such as kinesin force-velocity curves have been measured in single-molecule experiments[70]. Analogous measurements for non-processive axonemal dynein are not known, let alone their collective dynamics. Analysis of the flagellar beat under different load conditions provides a means to measure this force-velocity relationship.

Flagellar synchronization. The force-velocity relationship of the flagellar beat is an essential prerequisite for the striking phenomenon of beat synchronization by mechanical coupling. It had been observed already by Gray almost 100 years ago that pairs of sperm cells swimming in close proximity can synchronize their flagellar beat[1,154]. Similarly, sperm held in vibrating micropipettes or exposed to oscillatory flows entrain to the frequency of external driving[155,156]. Flagellar synchronization plays an important role for the collective dynamics in ciliar carpets, for example on the surface of unicellular *Paramecium* or the epithelial surfaces of mammalian airways[125]. Emergent metachronal waves enable fast swimming and efficient fluid pumping[127,157,158]. It has been proposed already by Taylor in 1951 that a mechanical coupling between several flagella can synchronize their beat[4]. Obviously, such a mechanical coupling requires a dependence of the speed of the flagellar beat on mechanical forces. In publication 2.2, we could identify a mechanism of flagellar synchronization in free-swimming *Chlamydomonas* cells. The unicellular green alga *Chlamydomonas* swims like a breast-stroke swimmer with two flagella that can beat in synchrony[5,159–161]. Synchronized beating is important for *Chlamydomonas* to swim fast and straight[5,162]. Flagellar synchronization relies on a force-velocity relation of the flagellar beat, which we predict theoretically and characterize experimentally by analyzing experimental data[5].

Mutual interactions between flagellated swimmers can even give rise to dynamic pattern formation in collections of microswimmers. In dense suspensions of sperm cells, swimming in circles close to a boundary surface, sperm organized into vortices of about 5 cells each[163]. Inside each vortex, sperm flagella phase-locked their individual flagellar waves into a fixed phase-relationship. Vortices organized into regular hexagonal patterns, presumably due to an effective repulsion between neighboring vortices.

Chemical control of flagellar motility. During flagellar swimming, the shape of the flagellar beat is under tight control of intracellular signaling. This chemical beat control facilitates in particular flagellar steering responses during chemotaxis[129,130,164], phototaxis[94,165], and mechanotaxis[166]. For example, sperm cells from marine invertebrates dynamically regulate the asymmetry of their flagellar beat to steer their path up a concentration gradient of chemoattractant[129,130]. The bi-flagellated green alga *Chlamydomonas* can switch from normal forward swimming to backward swimming upon exposure to strong, potentially harmful light stimuli[7,94,165]. During these photoshock responses, the asymmetry of the flagellar beat is greatly diminished in both flagella. In weak light conditions, a differential regulation of beat amplitude causes a yawing motion of the cell to facilitate phototaxis towards the direction of incoming light[165]. Mammalian sperm cells switch from travelling flagellar bending waves to a state of vigorous flagellar motility termed 'hyperactivation' during a ripening process inside the oviduct[143,167].

The intraflagellar calcium is a key regulator of the flagellar beat. Classic experiments by Brokaw in reactivated, demembranated axonemes have shown that an increase of calcium concentration increased the asymmetry of the flagellar beat in a gradual manner[168]. Studying the relationship of intraflagellar calcium and beat asymmetry in intact flagella is challenging, as methods for simultaneous manipulation and monitoring of calcium concentration are required. Recently, sea urchin sperm cells served as a versatile experimental model to address this question. Specifically, changes in intraflagellar calcium

were evoked by activation of the chemotactic signaling cascade. Intraflagellar calcium concentration can be monitored using calcium-dependent fluorescent dyes. In these experiments, the instantaneous curvature of sperm swimming paths has been used as a proxy for a time-dependent flagellar asymmetry. These dynamic measurements revealed a dynamic relationship between fluorescence signal and path curvature that was well approximated by a smooth time-derivative[169]. This finding suggests that the transfer function from intraflagellar calcium to beat asymmetry is a band pass filter. Such a control design would serve as an additional layer of sensory adaptation in the chemotactic control of the flagellar beat during chemotaxis[8]. Measurement of fluctuations of the flagellar beat in the green alga *Chlamydomonas* revealed unusually long correlation times of seconds, which is much longer than the chemo-mechanical cycle times of molecular motors[151]. It has been proposed that these slow flagellar fluctuations are caused by fluctuations of intraflagellar calcium concentration.
It is not known by which molecular mechanism intraflagellar calcium regulates the shape of the flagellar beat. Axonemal dynein has several calcium binding domains and it is likely that calcium regulates motor activity[170]. Alternatively, it has been proposed that calcium control is indirect, mediated by calcium binding proteins such as calmodulin or calaxin[171,172]. Interestingly, *in vitro* motility assays with reactivated dynein suggests an indispensable role of calaxin for motor control[172]. In addition to calcium, the shape of the flagellar beat is also regulated by cAMP concentration and possibly pH[173].

Other motility mechanisms of single cells. We will only briefly mention alternative motility mechanisms employed by single cells. Despite their diversity, all these mechanisms rely on the non-equilibrium dynamics of the cellular cytoskeleton in one way or the other.
Bacterial twitching motility. Some bacteria use depolymerization forces for locomotion. For example, bacteria, such as *Neisseria gonorrhoeae*, extends passive protein filaments termed type IV pili, which adhere to neighboring cells or a substrate[174]. Active depolymerization at the cell-facing end of these pili generates forces of up to $100\,\mathrm{pN}$, rendering type IV pili the strongest molecular machines characterized so far[175,176]. Active pili retraction pulls the cells forward at speeds $v \lesssim 1\,\mu\mathrm{m\,s^{-1}}$ [174,177]. This twitching motility of bacterial cells plays an important role in biofilm formation.
Crawling motility of eukaryotic cells. Crawling motility of eukaryotic cells on a substrate depends to a large extent on polymerization forces. This locomotion strategy is employed *e.g.* by immune cells such as marcophages, and has been extensively studied in the model organism *Dictyostelium*, a slime mold[60,178]. These cells comprise a cytoskeleton of cross-linked actin filaments. Polymerization of actin monomers into actin filaments is a non-equilibrium process. Notably, net polymerization can occur even when the plus-end of the filament is pushing against an obstacle such as the cell membrane. In this case, each elongation of the filament by one monomer performs mechanical work[65]. The concerted action of an ensemble of polymerizing actin filaments results in a net forward propagation of the cell front, the lamellipodium. This crawling motility requires a self-polarization of the actin cytoskeleton that establishes a structural polarization of the cytoskeleton, to set the direction of motion. Signaling cues can bias the polarization direction, *e.g.* during chemotaxis of cells in external chemical concentration gradients[61].
After this short review of active cell motility and its dynamic control, we now turn to self-organized pattern formation as a second instance of spatio-temporal biological dynamics.

1.3.2 Self-organized pattern formation in cells and tissues

In systems far from equilibrium, such as living matter, local interactions between constituents can give rise to large-scale ordered patterns that represent dynamic steady states. Examples range from self-organized pattern formation inside cells, *e.g.* in the cytoskeleton, to the robust development of complex tissues and organisms with specific spatial order adapted to their function[179]. In Chapter 3, we will

present two publications that address self-organized pattern formation at the cytoskeleton and at the organism level, respectively.

Self-assembly of macro-molecular structures. Inside cells, functional marco-molecular complexes self-assemble from individual molecules such as interacting proteins. Self-assembly can be passive as for the bacterial rotary motor, where more than 20 different proteins assemble stator and rotor of the motor complex[73,180]. Self-assembly of larger structures often involves active processes. For example, for the assembly of the prokaryotic flagellum, an active excretion system exports flagellin monomers, inserting them at the proximal end of the hollow flagellum, from where the monomers diffuse to the assembly site at the distal end[181]. The axoneme of the eukaryotic flagellum contains a bidirectional transport system known as intra-flagellar transport[182,183]. Therein, kinesin motors transport cargo, including the proteins that built the axoneme, towards the distal tip of the axoneme, whereas mobile dynein motors transport cargo back towards the proximal end, resulting in a stable steady state.
The interaction of cytoskeletal filaments and molecular motors gives rise to a variety of pattern formation phenomena, both *in vitro* and *in vivo*. This includes bundles of nematically aligned actin filaments, asters, stable swirling patterns[184–186], and even 'artificial cilia'[187]. A case of almost crystalline order of the cytoskeleton is found in myofibrils in striated muscle cells and cardiomyocytes[3]. Myofibrils are acto-myosin bundles characterized by a periodic arrangement of actin filaments of defined structural polarity and bipolar myosin filaments, which are organized in sarcomeric unit cells, see figure 5-C. In publication 3.1, we present a minimal mechanism for the self-assembly of periodic cytoskeletal patterns as observed in myofibrils[10]. This minimal mechanism relies on active force generation, such as active polymerization forces of treadmilling actin filaments.

Pattern formation in ensembles of active particles. Self-organized dynamic patterns naturally evolve in suspensions of actively moving particles. Cytoskeletal filaments interacting with a large number of surface-bound molecular motors give rise to dynamic bundle formation and stable swirling patterns[185,186]. In dense suspensions of motile bacteria, chaotic low-Reynolds-number flows have been observed on a mesoscopic scale, a phenomenon termed 'bacterial turbulence'[188,189]. Dense suspensions of swimming sperm cells at a glass-water interface can self-organize into vortex arrays with hexagonal order (spatial order), where additionally the sperm cells in each vortex phase-lock their flagellar oscillations (temporal order)[163]. The study of dynamic pattern formation in ensembles of active colloids and groups of organisms such as fish schools or bird swarms represents a sub-field of its own[190–193].

Pattern formation in reaction-diffusion systems far from equilibrium. A classical mechanism for the spontaneous formation of spatially inhomogeneous patterns are chemical reactions of diffusible molecules in spatially extended domains. This pattern formation requires a closed feedback loop between at least two reaction partners with different diffusion coefficients. Alan Turing proposed spontaneous pattern formation by reaction-diffusion-dynamics as a generic mechanism for the establishment of spatial patterns during the morphogenesis of organisms[40]. Recent experiments indeed revealed Turing mechanisms in a number of developmental processes[18], including pattern formation in the bacterial cytoskeleton[194], and the formation of digits during development[195], or the formation of stripe patterns in zebrafish[196,197].
The generic pattern formation mechanism of Turing patterns can be paraphrased as a principle of local activation and long-ranged inhibition[41]. A positive feedback amplifies the local concentration of an activator, where the activator concentration exceeds a certain threshold set by the concentration of an inhibitor. Fast diffusion of this inhibitor results in a long-ranged inhibitory effect that sets the size of activation regions. This mechanism can account for both stationary and dynamic patterns. A well-studied *in vitro* realization of this principle is the Beluzov-Zhabotinsky reaction, where cross-reacting

and diffusing chemical species give rise to travelling wave patterns and rotating spirals in the presence of topological defects[198]. Obviously, the Beluzov-Zhabotinsky reaction represents a non-equilibrium system. Generalization of this mechanism, where spatial fields of active stresses, strains, or fluxes play the role of either activator or inhibitor had been already contemplated by Turing[40], with specific realizations proposed recently[42,43].

Inside cells: self-assembly of cytoskeletal patterns. Non-equilibrium dynamics in the cytoskeleton gives rise to the self-assembly of functional structures such as stress fibers or myofibrils on cellular scales. Below, we review selected examples of cytoskeletal pattern formation by local interactions inside cells. We will put special focus on myofibrillogenesis, *i.e.* the assembly of the almost crystalline acto-myosin bundles with sarcomeric periodicity in striated muscle cells.

Regular patterns of the actin cytoskeleton. Actin filaments can spontaneously form spatial patterns, both *in vitro* and inside living cells. Reconstituted actin filaments form stable bundles and asters as a result of passive depletion and active motor forces as well as entropic effects[199–202]. The interaction of actin filaments, crosslinkers, and myosin molecular motors results in dynamic patterns, including pulsatile myosin foci[203] and stable swirling patterns[185], revealing the rich dynamics of cytoskeletal pattern formation far from equilibrium.

Inside cells, actin filaments, actin-binding-proteins and myosin motors self-assemble into functional structures. A crosslinked meshwork of actin filaments with gel-like properties fills the intracellular space in animal cells and defines its rheological properties[204]. Myosin motors interact with actin filaments in a polarity-specific manner and exert microscopic force dipoles. As a result, myosin activity confers active contractility to the actin meshwork. We note that acto-myosin contractility is an emergent property of ensembles of interacting actin filaments and bipolar myosin motor filaments. A single myosin may either contract or expand a pair of parallel aligned actin filaments, depending on two possible configurations of structural polarity[205,206]. Specific physical mechanisms that effectively break the symmetry between expansion and contraction have been proposed, which result in a net compressive effect. These mechanisms include prolonged residence of myosin at the plus-end of actin filaments, filament rotation, and buckling of actin filaments under compressive load[205–207]. A thin and dense acto-myosin-meshwork beneath the cell membrane of animal cells constitutes the actin cortex. This actin cortex sets an effective surface tension and represents a major determinant of cell shape.

In cells that mechanically interact with an elastic substrate, actin filaments and myosin motor filaments form dense bundles, termed stress fibers[21]. These stress fibers generate contractile forces on a length-scale of cellular dimensions. Contractile actin-bundles also form the cell division ring that constricts animal cells during cytokinesis, the final stage of cell division. Contractile actin bundles can even span across multiple cells and exert contractile forces on the tissue scale[208]. In the stress fibers of certain cell types, such as fibroblast connective tissue cells, actin-crosslinkers and myosin motors are not distributed homogeneously along the fiber, but display periodic patterns with alternating localization with a characteristic periodicity of $1-2\,\mu\mathrm{m}$ [209]. The periodic patterns in these striated stress fibers are reminiscent of the sarcomeric arrangement of actin-crosslinkers and myosin in myofibrils, to be discussed in more detail below. We speculate that similar physical mechanisms of self-organized pattern formation account for the self-assembly of periodic patterns both in striated stress fibers and myofibrils[10]. Maturation processes that regularize initial periodic patterns may be lacking in striated stress fibers.

In summary, self-organized pattern formation of the actin cytoskeleton results in a diverse set of functional structures that are characterized by different types of spatial order. These include (figure 5)

- isotropic symmetry, *e.g.* in crosslinked actin meshworks and the actin cortex[202]
- nematic order, *e.g.* in stress fibers[21]
- smectic order, *e.g.* in striated stress fibers and myofibrils with sarcomeric periodicity[22].

Actin binding proteins. Actin filaments interact with a large number of actin-binding-proteins. Capping proteins regulate polymerization dynamics at the structural plus- and minus-end in a differential manner, and thus control filament length and treadmilling dynamics. Severing proteins such as gelsolin bind along the length of actin filaments and sever filaments at the binding position. Since their net rate of binding depends on filament length, severing represents a simple, yet effective mechanism of filament length control[210]. Crosslinking proteins promote the formation of crosslinked meshworks of actin filaments and the formation of actin bundles with nematically aligned filaments. Inside myofibrils, structural proteins such as tropomyosin decorate actin filaments for stability. Additional proteins provide structural support and elastic linkage inside sarcomeres. This includes the 'giant proteins' titin and nebulin, which scan span $0.5\,\mu\mathrm{m}$ in their extended configuration[211].

Regular patterns of microtubules. Microtubules interact with the actin cytoskeleton and have been proposed to represent tension-bearing structural elements[212]. During cell division, microtubules self-assemble the mitotic spindle[213], which constitutes part of the cell division machinery that distributes the chromosomes to the prospective daughter cells. This self-assembly process is driven by active motor forces and continuous turn-over of polymerizing and depolymerizing microtubules. Spindle assembly is orchestrated by two microtubule nucleation centers, which are located at opposite poles of the spindle. Each of these microtubule nucleation centers usually contains a centriole, a regular structure of triplet microtubules that the bears the same nine-fold symmetry as the microtubule-based axoneme of the eukaryotic flagellum. In fact, centrioles also serve as templates for axoneme assembly. Many cells, including the green alga *Chlamydomonas*, possess exactly two centrioles, which are used to assemble either a mitotic spindle during cell division, or to assemble and anchor up to two flagella. This shared use of centrioles implies that cell division and flagellar motility cannot occur at the same time in these cells[214]. The shared use of centrioles also point at a common evolutionary origin of the mitotic spindle and the flagellar axoneme[87].

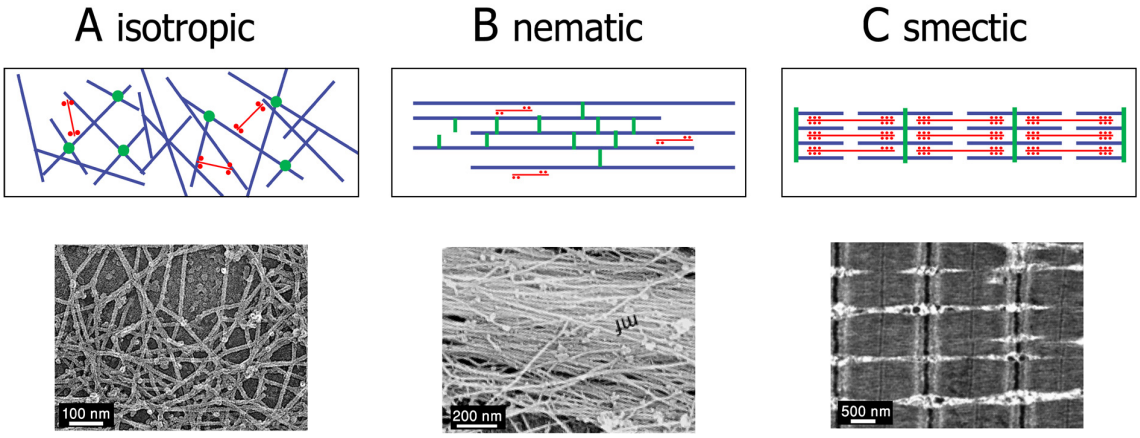

Figure 5: *Pattern formation in the actin cytoskeleton.* **A.** Actin filaments form dense crosslinked meshworks with isotropic symmetry, *e.g.* in lamellipodia or the actin cortex of animal cells. **B.** Actin filaments can organize into bundles of aligned filaments, representing a case of nematic order, *e.g.* in connective tissue cells. **C.** Inside striated muscle cells and cardiomyocytes, actin and myosin filaments are arranged in myofibrils of almost crystalline regularity. Myofibrils are characterized by periodic patterns of sarcomere units and represent a case of smectic order in the cytoskeleton. Micrographs from ref.[215,216] with permission.

Example of cytoskeletal pattern formation: Self-assembly of myofibrils. Myofibrils are the active force generator inside striated muscle cells and the cardiomyocytes of the heart[3]. Upon activation by calcium signals, myofibrils actively contract by the concerted activity of millions of myosin molecular motors inside. Myofibril contractions underlie all voluntary movements of higher animals and the rhythmic beat of the heart. The *de novo* assembly of myofibrils serves as a model system to study the general question how large scale patterns can emerge from local interactions in non-equilibrium systems.

Myofibrils are highly regular macro-molecular structures that are characterized by a periodic repetition of unit cells termed sarcomeres, see Figure 5-C. Sarcomeres are composed of actin filaments, myosin motor filaments, and additional structural proteins. Their regular spatial organization inside myofibrils represents a case of cytoskeletal order with almost crystalline regularity. Myofibrils measure $100-1000\,\mu\mathrm{m}$ in length; their functional and structural unit, the sarcomere, displays typical lengths of $1-2\,\mu\mathrm{m}$. The major constituents of the sarcomere are actin and myosin filaments, the latter being polymerized out of individual muscle-specific myosin molecular motors. The structural plus ends of the actin filaments are anchored in a crosslinking region termed Z-band, with the actin-binding protein α-actinin as an important constituent. During myofibril contraction, myosin filaments slide relative to the actin myosin filaments towards the actin plus-end, resulting in shortening of each sarcomere. This generation of active forces relies on the defined structural polarity of filaments inside each sarcomere. In addition to the three proteins named, actin, myosin, and α-actinin, several hundred different proteins ensure the structural integrity and regulation of sarcomeric force generation. Interestingly, some of the largest known proteins are found inside myofibrils, such as the giant protein titin that spans half a sarcomeres length and serves as an elastic element[211]. Maximal force generation by myofibrils requires a dense and regular packing of myosin molecular motors and their actin tracks. In fact, the arrangement of proteins inside myofibrils are crystalline and result in distinct X-ray diffraction patterns[217].

It is an open question, how myofibrils are assembled. It has been proposed that existing myofibrils can grow by an epitaxy-like mechanism or serve as templates for the assembly of additional myofibrils. Additionally, precursor structures named premyofibrils, which already have a periodic structure, may be assembled first. These premyofibrils can then serve as template for mature myofibrils[218,219]. There is partial experimental evidence for the premyofibril hypothesis in at least some cell types. Yet, the fundamental question remains open: How do micrometer-sized building blocks such as actin filaments, myosin filaments, and titin assemble periodic structures, whether these are striated stress fibers, premyofibrils, or nascent myofibrils? It can be considered certain that giant scaffolding proteins such as titin and obscurin serve as a molecular templates for the assembly and structural organization of single sarcomeres[211,220]. However, it is unclear if these scaffolding proteins are involved already in the early establishment of periodic patterns in initially unstriated acto-myosin bundles. The proposition that that a periodic arrangement of titin molecules directs myofibrillogenesis would require a yet unknown mechanism by which titin molecules become arranged in periodic patterns first. We emphasize that the diffusion coefficients of large molecules such as titin or actin and myosin filaments are extremely low, which renders their passive sorting into periodic patterns kinetically impossible. We thus argue that active, force-generating processes should be required for myofibrillogenesis. This hypothesis is consistent with recent experimental findings that emphasize the importance of active tension for myofibrillar pattern formation, and the requirement for attachment to support structures, such as tendons, which can resist active forces[221].

Myosin motor forces are an obvious source of active force generation inside nascent myofibrils. Yet, these forces cannot explain self-assembly. In myofibrils, myosin filaments are localized near the structural minus-end of actin filaments, despite their tendency to slide towards the plus-end. We speculate that strong myosin forces can disrupt nascent myofibrils. Interestingly, it has indeed been

found that myosin force generation is up-regulated only after the initial stages of myofibril assembly. In some cells, myofibril precursors are assembled with non-muscle myosin filaments that generate less force, which are replaced by muscle-myosin only at later stages. These findings are consistent with a potentially destructive role of myosin forces during myofibril assembly. Different physical mechanisms have been proposed for the source of forces that sort actin and myosin filaments in place in nascent myofibrils. Zemel *et al.* proposed a sorting mechanism that depends on a second, hypothetical motor, which is minus-end directed[222]. This model could indeed account for the spontaneous emergence of periodic structures with polarity-sorted filaments. However, the involvement of such a hypothetical minus-end directed motor needs yet to be demonstrated. Yoshinaga *et al.* proposed a Turing-like mechanisms with a mutual coupling of fields of local active stress and actin polarity[42]. This generic mechanism predicts the emergence of periodic polarity patterns, yet its coarse-grained nature does not inform about underlying molecular mechanisms. In publication 3.1, we present a minimal model for the self-assembly of periodic cytoskeletal patterns as observed in myofibrils from local interactions between three constituents: actin filaments, bipolar myosin filaments, and a plus-end actin crosslinker[10].

Inside tissues and organisms: self-organized morphogen gradients. Inside tissues and organisms, concentration gradients of signaling molecules regulate growth and developmental patterning[223]. Important examples include the proteins Bmp[224], Dpp[225], and Wnt[224], which establish concentration gradients along principal body axes during embryonic development. Signaling molecules that spatially orchestrate cell differentiation during morphogenesis are termed morphogens, a term first coined as a theoretical concept by Turing[40]. A more biological view defines morphogens as signaling molecules that are secreted in localized source regions and form long-ranged concentration gradients that determine discrete cell fates in a concentration-dependent manner[223,226] (although this definition may disqualify some signaling molecules such as Wnt as classical morphogens[227]).
In a minimal description, a morphogen is secreted at a point source located at $x = 0$, and diffuses with effective diffusion coefficient D in a spatial domain of size L, while being subject to degradation with degradation rate k

$$\dot{c} = p\delta(x) - kc + D\nabla^2 c. \tag{5}$$

Note the effective diffusion term can account also for undirected active transport, *e.g.* by cellular transport processes of endocytosis and exocytosis[228], in addition to passive diffusion. Equation (5) implies an exponential concentration profile $c(x) \sim \exp(-x/\lambda)$, where the pattern length-scale λ is set by a competition of diffusion and degradation

$$\lambda = \sqrt{D/k}. \tag{6}$$

Remarkably, scaling of concentration profiles with system size L, characterized by $\lambda \sim L$, has been observed in a number of biological systems, including the developing fly wing[229–231]. In the fly wing, it was shown that pattern scaling results from a dynamic regulation the morphogen degradation rate according to system sizes, $k \sim L^{-2}$ [229]. Several theoretical mechanisms for self-regulated pattern scaling have been proposed[232–234], which still need to be experimentally confirmed.
These theoretical mechanisms of pattern scaling are challenged in systems with regeneration capabilities. For example, small amputation fragments of the flatworm *Schmidtea mediterranea* can regenerate into a miniature version of the original worm with a proportional body plan proportionally scaled according to the size of the amputation fragments[235]. This re-patterning occurs within weeks. Additionally, flatworms can scale their body plan by a factor of 20 in length during growth and active

degrowth, depending on feeding conditions[235]. Long-range gradients of gene expression patterns of signaling molecules such as Wnt are known to pattern the anterior-posterior-axis in flatworms[236]. Regeneration capabilities as observed in flatworms require de-novo formation of a morphogen source after amputation. Mechanisms of self-organized pattern formation such as Turing mechanisms can account for the formation and positioning of a new morphogen source[40,41]. However, classical Turing mechanisms are characterized by fixed intrinsic pattern length-scales, which are again set by a competition of diffusion and degradation of patterning molecules, compare equation (6). In publication 3.2, we present a general mechanism for self-organized pattern formation that generates spatial patterns that scale with system size[11]. This minimal mechanism displays structural robustness and can cope with parameter variations and fluctuations. We review different sources of fluctuations in biological systems.

1.4 Fluctuations and biological robustness

Life relies on stochastic processes[237]. Thermal noise enables diffusive transport and biochemical reactions at the molecular scale. Small-number fluctuations cause stochastic dynamics at the scale of cells and organisms. Even biological evolution relies on fluctuations: stochastic events during gene duplication generate genotypic variations. Here, we will focus on cell motility, which is driven by stochastic non-equilibrium dynamics of its cytoskeleton. This implies measurable active fluctuations at the mesoscopic scale of the cell that violate the fluctuation-dissipation theorem. A common phenomenological description of active fluctuations in terms of an effective temperature T_{eff} above the thermodynamic temperature T can provide a first, rough approximation only. Effective descriptions of noise in biological systems, which coarse-grain chaotic out-of-equilibrium dynamics at the microscopic scale, are researched actively[13,14].

1.4.1 Sources of fluctuations in biological systems

Any chemical reaction between molecules requires that Brownian motion first brings the reaction partners into close contact. Thermal fluctuations are also required to overcome energetic barriers of the chemical reaction. In consequence, each reaction step is a stochastic event, which can often be described as a Poisson jump process[238]. Small-number fluctuations of chemical reactions do not necessarily average out at the scale of the cell. One simple reason for this is that copy numbers inside cells can be as low as a few tens or hundreds[239]. Thus, mean field description may miss important aspects of cellular dynamics. As an important aspect, nonlinear feedback loops can amplify small-number fluctuations, thereby propagating fluctuations from the molecular scale to the mesoscopic scale of the cell. For example, the stochastic binding of a single transcription factor to a specific DNA binding site can initiate the transcription of a particular gene and result in its translation into many copies of the corresponding protein. Such stochastic gene expression can lead to different gene expression profiles in cells of identical genetic setup[240]. Signaling systems that implement bistable switches with long hysteresis can amplify this effect. In fact, some bacterial colonies harness stochastic gene expression to induce phenotypic heterogeneity within the population, which can provide a competitive advantage in a time-varying environment[241]. In addition to intracellular noise, cells are subject to external perturbations. These external perturbations include fluctuations in nutrient levels and physical parameters such as light, pH, and temperature, each of which affects the dynamical state of the cell.

Thermal fluctuations. Free energy differences of biochemical reactions are commonly on the order of a few $k_B T$, where the thermal energy $k_B T \approx 4 \times 10^{-21} J$ at room temperature. For example, the Gibbs free energy difference for the hydrolysis of a single ATP molecule equals $20 - 25\, k_B T$ [63]. Unfavorable reactions inside cells that result in high-energy reaction products, a local reduction of entropy, or which perform mechanical work, are coupled to the hydrolysis of triphosphate nucleosides such as ATP, which

breaks detailed balance of reaction cycles[3,24,63]. Such reactions include the chemo-mechanical cycles of molecular motors[242]. As a specific example, single kinesin molecular motors take directed $8\,\mathrm{nm}$ steps on a microtubule per chemo-mechanical cycle, which corresponds to mechanical work of $10\,k_BT$ at full $5\,\mathrm{pN}$ load force. Molecular motors that show on average directed motion will occasionally take a backward step due to thermal fluctuations.

Molecular shot noise and small-number fluctuations. Inside cells or subcellular compartments, copy numbers of proteins are often in the range of hundreds. For example, the volume of an *E. coli* bacterium comprises just a few femto-liters, which implies that a concentration of one micro-molar corresponds to just a few thousand molecules. This is a typical order of magnitude for the most abundant bacterial proteins. Eukaryotic cells can be much larger than bacteria, yet important signaling processes are often spatially confined to sub-cellular regions of femto-liter volume, such as the nucleus or a flagellum. Low copy numbers imply substantial small-number fluctuations of chemical reactions and thus introduce noise in cellular signaling. Inside tissues, communication between cells is subject to the same sources of noise inherent to chemical reactions[243].

Sensory perception at the physical limit. Fluctuations are paramount in sensory perception of weak stimuli. Many sensory organelles can operate at the physical limit[244]. For example, rod photoreceptors in the retina of the eye can detect single photons[245–247]. Hair bundles in the inner ear respond to faint vibrations that carry an energy of only a few k_BT per oscillation cycle[244]. Specialized olfactory sensory neurons can detect single odorant molecules[248], likewise sperm respond to single chemoattractant molecules[249]. Such signaling events are inherently stochastic in nature.
In addition to this quantized nature of single molecule detection, thermal fluctuations impact on sensation at the physical limit: the absorption of a single photon or the binding of a single ligand molecule to a receptor induces a conformational change in the receptor proteins, which then activates down-stream signaling cascades. Thermal noise can induce the same conformational change as a detection event, and thus limits the precision of cellular signal detection[250,251].

Active motor fluctuations. Individual molecular motors progress through their mechano-chemical cycles in an inherently stochastic manner. Single-molecule experiments allow to detect discrete steps of single molecular motors and the stochastic timing of their stepping[252]. The collective dynamics in ensembles of molecular motors gives rise to active contractility, directed transport, but also to non-equilibrium fluctuations. A hallmark of non-equilibrium fluctuations is the violation of the fluctuation-dissipation theorem. At thermal equilibrium, the fluctuation-dissipation theorem relates the fluctuation spectrum $\langle |A(\omega)|^2 \rangle$ of a degree of freedom A to its response function $\chi_A(\omega)$, which characterizes the response to an external perturbation[253]

$$\langle |A(\omega)|^2 \rangle = \frac{2k_BT}{\omega}\,\mathrm{Im}\,\chi_A(\omega). \tag{7}$$

Violations of the fluctuation-dissipation theorem have been experimentally observed in fluctuation spectrum of the cell membrane of red blood cells[254], fluctuations of the cytoskeleton[255–257], or the hair bundles of auditory sensory neurons in the inner ear[258]. These non-equilibrium fluctuations have been attributed to the stochastic collective dynamics of molecular motors.
The beat of the eukaryotic flagellum exhibits active fluctuations as well. Previous studies reported Fourier peaks of finite width in power spectra of flagellar dynamics, which provides a signature of phase fluctuations. Goldstein *et al.* conducted an indirect measurement of these phase fluctuations by examining the frequency of phase-slips in pairs of synchronized flagella[160,259,260]. In publication 2.3, we

present a method to measure phase and amplitude fluctuations of the flagellar beat directly. Specifically, our method maps high-precision measurements of flagellar bending waves on a generic description of a limit cycle oscillator with phase and amplitude noise, the normal form of a Hopf bifurcation with complex noise term,

$$\dot{Z} = i(\omega_c - \omega_1|Z|^2)Z + \mu(\Lambda - |Z|^2)Z + (\xi_A + i\xi_\varphi)Z. \tag{8}$$

Here, $Z = Ae^{i\varphi}$ is a complex oscillator variable and ξ_A and ξ_φ denote amplitude and phase noise terms, respectively. In publication 2.3, we further consider a minimal model of stochastic collective motor dynamics and show that emergent noisy motor oscillations can be likewise mapped on equation (8) of a noisy Hopf oscillator.

Stochastic motor dynamics has been studied in a number of systems, ranging from stochastic oscillations of hair bundles of auditory sensory neurons in the inner ear[34], bi-directional transport of actin filaments that interact with a surface coated with myosin motors in motility assays[261,262], to oscillations in in vitro system of myosin motors and actin filaments[263] and 'artificial cilia' consisting of microtubule bundles interacting with kinesin motors[187]. These measurements of non-equilibrium fluctuations in mesoscopic systems provide a way to observe signatures of the stochastic dynamics of molecular motors.

1.4.2 Example of stochastic dynamics: synchronization of noisy oscillators

Since the observation of phase-locked pendulum clocks by van Huygens, it is known that active oscillators can synchronize by virtue of a weak coupling, despite effects of noise or a mismatch of intrinsic oscillation frequencies[264]. In the middle of the 20th century, work on generators of radio signals, and phase-locked electronic oscillators in particular, motivated the development of a general theory of synchronization[265,266]. Synchronization is also observed in biological systems: examples include synchronization of the walking gaits of pedestrians[268], coupling of the 'segmentation clock' genetic oscillators that orchestrate somatogenesis during embryonic development[267], and last but not least synchronization in collections of beating flagella as studied in this thesis. Synchronization of oscillators implies the emergence of a common oscillation frequency and a fixed phase relation. We first review the Adler equation, a generic description for the synchronization of a pair of coupled noisy oscillators in the next paragraph and then turn to the synchronization in pairs of beating flagella in the remainder of this section.

The stochastic Adler equation of coupled oscillators. The stochastic Adler equation provides a generic description for the synchronization of a pair of noisy, active oscillators. The dynamics of the phase difference $\delta = \varphi_1 - \varphi_2$ between the two phase oscillators with respective phases φ_1 and φ_2 can be idealized by[265]

$$\dot{\delta} = \Delta\omega - \lambda \sin\delta + \xi. \tag{9}$$

Here, $\Delta\omega = \omega_1 - \omega_2$ denotes the mismatch between the intrinsic frequencies of the two oscillators, λ is an effective coupling strength and $\xi(t)$ denotes a Gaussian white noise term with $\langle \xi(t)\xi(t')\rangle = 2D\,\delta(t-t')$. The Adler equation, equation (9), captures key dynamical features of synchronization, which we discuss below. Many specific systems of coupled oscillators can be approximately mapped on the Adler equation. This includes a description of flagellar swimming and flagellar synchronization in free-swimming *Chlamydomonas* cells presented in publication 2.2. The dynamics given by equation (9) can be interpreted as that of an overdamped particle in a tilted periodic

potential $U(\delta) = -\Delta\omega\delta - \lambda\cos\delta$ [269]. For zero frequency mismatch, $\Delta\omega = 0$, steady states of equation (9) correspond to in-phase synchronization with $\delta = 0$, and anti-phase synchronization with $\delta = \pi$. For positive synchronization strength $\lambda > 0$, in-phase synchronization is stable, while anti-phase synchronization represents a meta-stable steady state, see figure 6-A,B. Noise induces stochastic phase slips at a frequency $G = D/|2\pi I_0(\lambda/D)|^2$ [266], where I_0 denotes the modified Bessel function of the first kind. In case of a frequency mismatch $\Delta\omega \neq 0$, the two oscillators will synchronize with a phase-lag $\delta^* = \sin^{-1}(\Delta\omega/\lambda)$ at steady-state, provided $|\Delta\omega| < |\lambda|$. If the frequency mismatch becomes too large, the system undergoes a saddle-node bifurcation and no steady state exists anymore for $|\Delta\omega| > |\lambda|$. In this case, the dynamics is characterized by phase drift, see figure 6-D. Many analytic results for the stochastic Adler equation are known, see *e.g.* the book by Stratonovich[266].

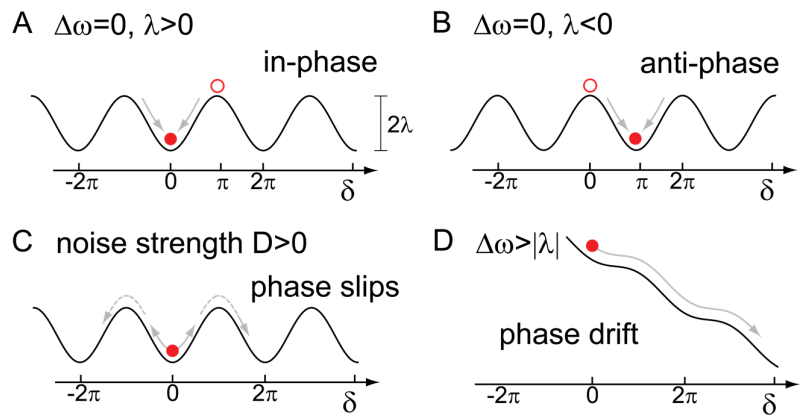

Figure 6: *Dynamic regimes of the stochastic Adler equation.* The dynamics of the phase difference δ is equivalent to the overdamped motion of a particle in a tilted periodic potential. **A.** For positive coupling strength $\lambda > 0$, the in-phase synchronized state is stable, while the state of anti-phase synchronization is meta-stable. **B.** For negative synchronization strength $\lambda < 0$, stability is reversed. **C.** In the presence of noise, d exhibits stochastic transitions between adjacent stable states, so-called phase slips. **D.** If the mismatch $\Delta\omega$ between the intrinsic frequencies of the two coupled oscillators becomes too large, no synchronization occurs, and the phase difference will increase monotonically, corresponding to a regime of phase drift. Modified from[273].

Flagellar synchronization and the Adler equation. All dynamic regimes predicted by the Adler equation have been observed for pairs of beating flagella, including in-phase[159,160,270] and anti-phase synchronization[271], stable phase-lags[160,161], phase slips[159,160,259] and phase drift[5,272]. Synchronization of beating flagella have been proposed to result from a mechanical coupling between flagella, *e.g.* by direct hydrodynamic interactions[4]. The symmetry of the Stokes equation, equation (3), which governs hydrodynamics at the cellular scale, prompts systems that explicitly break either time-reversal symmetry or spatial symmetries to facilitate such hydrodynamic synchronization.

Hydrodynamic synchronization requires broken symmetries. Already in 1951, Taylor proposed that the remarkable phenomenon of flagellar synchronization arises from a mechanical coupling between flagella, such as direct hydrodynamic interactions[4]. Only recently was flagellar synchronization by direct hydrodynamic interactions unequivocally demonstrated in experiments. Using pairs of flagellated cells held in separate micro-pipettes at a distance, it was found that flagellar synchronized with a distance-dependent synchronization strength[6]. Synchronization by direct hydrodynamic interactions

was additionally studied in systems of artificial actuators such as colloids driven by oscillating magnetic fields, or 'light-mill' micro-rotors driven by laser-light[274–278].

Similar to the problem of self-propulsion at low Reynolds numbers, hydrodynamic synchronization requires broken symmetries to overcome the symmetries of the Stokes equation and to provide a net coupling between oscillators. For illustration, we consider the idealized example of two spheres revolving around circular trajectories. Each sphere is driven by a constant tangential force and would thus assume a constant angular speed $d\varphi/dt = \omega_0$ if the other sphere were absent. The motion of one sphere generates a long-ranged flow field whose strength decays with inverse distance. This flow field exerts a hydrodynamic interaction force on the second sphere, which changes the phase speed $d\varphi/dt$ of this sphere. Although, these hydrodynamic interactions indeed couple the phase dynamics of the two spheres, the resultant net coupling strength λ is zero. This can be seen from symmetry arguments[122]: a spatial mirror operation and time-reversal will both result in the same dynamics, since the Stokes equation is invariant under these operations. While the spatial mirror operation does not change the stability of any synchronized state, stability is reversed under time-reversal. We conclude that any synchronized state can be neither stable nor unstable, hence $\lambda = 0$.

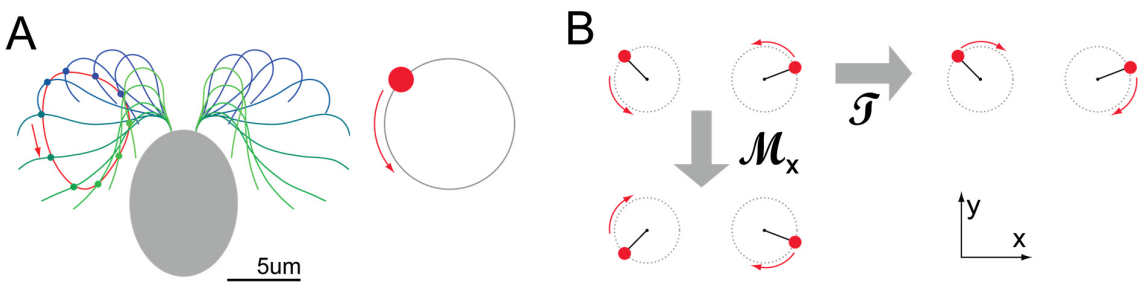

Figure 7: *Lack of hydrodynamic synchronization in a minimal model with symmetries.* **A.** In an idealized model, a beating flagellum is represented by a sphere that moves in a viscous fluid along a circle, being driven by a constant tangential force [112]. This model is inspired by the observation that each point on a beating flagellum moves on a circular orbit. **B.** Direct hydrodynamic interactions between the two rotating spheres couple their motion. However, the net synchronization effect is zero, as a consequence of symmetries: A reflection $\mathcal{M}_x$ of the system at the x-axis is dynamically equivalent to a time-reversal $\mathcal{T}$. As the time-reversal reverses the stability of synchronized states, while a reflection does not, we conclude that any synchronized states is neutrally stable[112,115,122].

Different physical mechanisms have been proposed for synchronization by direct hydrodynamic interactions, all of which break spatio-temporal symmetry in one way or the other, which we review now.

Amplitude compliance. In a generalization of the two sphere model considered by Lenz *et al.*, the radii of the circular tracks are not constant, but are considered as elastic degrees of freedom with an effective stiffness k [279]. This amplitude compliance breaks the time-reversal symmetry of the equation of motion. It is found that both spheres can synchronize their motion with an effective synchronization strength that scales inversely with the amplitude stiffness, $\lambda \sim 1/k$.

Phase-dependent driving forces. Golestanian *et al.* proposed a different symmetry-breaking mechanism that relies on phase-dependent driving forces[280,281]. Thereby, the two sphere system is not invariant anymore under a spatial mirror operation, thus facilitating net synchronization.

Other means to break symmetry. Additionally, Theers *et al.*, considered the effect of small, non-zero Reynolds number[282]. The effect of unsteady acceleration at finite Reynolds numbers breaks time-reversal symmetry and results in net synchronization with a synchronization strength $\lambda \sim \mathrm{Re}^{1/2}$. In the original formulation of the two sphere model by Vilfan *et al.*, a no-slip boundary close to the two spheres was introduced, which breaks spatial mirror symmetry[112].

The beat of real cilia and flagella is characterized by both phase-dependent driving forces and a finite compliance of the flagellar wave forms[118,151]. Thus, time-reversal symmetry is broken, which allows for flagellar synchronization by direct hydrodynamic interactions. It should be noted that the symmetry breaking can be weak, thus resulting in a weak synchronization strength[5,156]. In publication 2.1, we present an alternative synchronization mechanism that operates independently of direct hydrodynamic interactions[283]. Instead, this mechanism relies on a closed feedback loop between flagellar dynamics and swimming motion. In publication 2.2, we demonstrate that this synchronization mechanism is important in free-swimming *Chlamydomonas* cells[5]. Synchronized beating of its two flagella is a prerequisite for this cell to swim fast and straight.
Purposeful motion further requires a control of swimming direction in response to environmental cues. In the next section, we review navigation mechanisms for directed motion in external concentration gradients.

1.4.3 Cellular navigation strategies reveal adaptation to noise

We review three distinct strategies employed by single cells for navigation in external concentration gradients[8]. Any cellular gradient-sensing strategies must cope with noise, such as motility fluctuations, or molecular shot noise of chemosensation at dilute concentrations. We argue that the three different chemotaxis strategies employed by single cells represent an adaptation to the respective strength of motility and sensing noise encountered by these cells.

Physical limits to chemo-sensation. Cells constantly monitor extracellular concentrations of signaling molecules. This sensory input controls *e.g.* chemotaxis in chemical gradients or cell fate decisions during development. Berg and Purcell made seminal contributions to our understanding of the physical limits of chemosensation[284]. Their work was later re-derived in the framework of statistical physics by Bialek *et al.*[250]. Specifically, many cells measure the extracellular concentration c of a signaling molecule by counting binding events of individual molecules to cognate surface receptors. In the idealized limit of maximal uptake, characterized by high receptor density and irreversible binding, the mean number $\langle N \rangle$ of binding events in a time window of duration τ is given by[250,284]

$$\langle N \rangle = 2\pi L \cdot Dc \cdot \tau, \tag{10}$$

where D denotes the diffusion coefficient of the molecule. The geometric factor $2\pi L$ corresponds to a cellular geometry of a perfect sphere of diameter L; generally it will scale with the longest dimension of the cell[285]. Individual binding events will be uncorrelated to good approximation, and thus the actual number N of binding events will be a Poissonian random variable with mean $\langle N \rangle$ and variance $\langle N \rangle$. Cellular concentration measurements are thus prone to molecular shot noise: at physiological pico-molar concentrations, only a few molecules per second will diffuse to the cell. Hence, cells face trade-off choices between the accuracy of concentration measurements and the temporal resolution for sensing time-varying concentrations, which has implications for cellular chemotaxis strategies.
For chemotaxis, the maximal integration time τ for local concentration measurements is set by the time it takes the cell to move one body length, $\tau \sim L/v$, where v and L denote speed and size of the cell. As

a numeric example, we find $N \approx 500$ from equation (10) using typical values for a bacterial cell ($L \approx 3\,\mu\mathrm{m},\ L \approx 50\,\mu\mathrm{m\,s^{-1}},\ D \approx 700\,\mu\mathrm{m^2\,s^{-1}},\ c = 1\,\mathrm{nM}$). Thus, concentration measurements are inherently unreliable at the cellular scale. This constrains the range of potential chemotaxis strategies for a given cell.

Motility noise. Motility noise comprises contributions from both thermal fluctuations and active motility fluctuations. For the smallest cells, such as bacteria, the contribution from thermal fluctuations can be substantial. In particular, effective rotational diffusion will randomize the swimming direction of a cell. We can estimate the effect of thermal fluctuations on a passive particle of same shape as the cell, which provides a lower bound for the effective rotational diffusion coefficient. For such a passive particle, the rotational diffusion coefficient is given by an Einstein-Stokes relation, $D_{\mathrm{rot}} = k_B T/\gamma_{\mathrm{rot}}$, where γ_{rot} denotes the hydrodynamic friction coefficient for rotational motion. The rotational friction coefficient typically scales as $\gamma_{\mathrm{rot}} \sim L^3$, where L denotes a typical size of the cell. Hence,

$$D_{\mathrm{rot}} \sim L^{-3}. \tag{11}$$

As a numerical example, we find $D_{\mathrm{rot}} = 0.1\,\mathrm{s}^{-1}$, for a spherical particle of radius $a = 1$, for which $\gamma_{\mathrm{rot}} = 8\pi\eta a^3$. This estimate implies that the correlation time $\tau = 1/D_{\mathrm{rot}}$ of persistent directional swimming is just a few seconds for a micron-sized bacterium. For typical swimming speeds of a bacterium, $v \approx 10\,\mu\mathrm{m\,s^{-1}}$, the resultant swimming path will be a persistent random walk (even in the absence of active tumbling) with persistence length of $l_p = v/(2D_{\mathrm{rot}}) \approx 50\,\mu\mathrm{m}$ [286,287]. It was argued that active motility would not pay off for the smallest bacteria, which measure less than a micron in size[288]: for these cells, directional persistence of motion would be so low that net locomotion becomes impossible and active motility would increase only the effective translational diffusion coefficient of the cell, $D_{\mathrm{eff}} = D_{\mathrm{trans}} + v^2/(6D_{\mathrm{rot}})$. Interestingly, most cells that measure less than a micron are indeed immotile[288].

Motile cells, such as swimming bacteria, often show chemotaxis, *i.e.* the directed motility upwards a concentration gradient, such as a gradient of nutrient concentration. Rotational diffusion restricts the gradient sensing strategies available to these cells. During a time span on the order of τ, the information gathered by swimming bacteria such as *E. coli* is not sufficient for directed steering responses in the direction of the gradient. Instead, these bacteria employ a stochastic navigation strategy, where only the frequency of random re-orientation events is adjusted. This steering strategy results in a biased random walk with net drift up the gradient as detailed in the next section.

Three cellular strategies of gradient sensing. Motility control of motile cells is an ideal test case to study the adaptation of cellular signaling to dynamic and noisy environments. Pioneering work by Howard Berg unraveled the stochastic control logic of chemotaxis in bacteria upwards concentration gradients of nutrients[81]. Motile bacteria such as *E. coli* perform a biased random walk to move up a chemical gradient. We enjoy a rather comprehensive understanding of chemotactic signaling in bacteria today[289,290]. Eukaryotic (*i.e.* non-bacterial) cells, however, employ fundamentally distinct navigation strategies of helical chemotaxis[140,291] and spatial comparison[61,292], which are reviewed below. For eukaryotic chemotaxis, many questions regarding the underlying sensorimotor feedback logic, and its adaptation to dynamic chemoattractant fields are still open. Below, we elaborate the hypothesis that different chemotaxis strategies of bacteria and eukaryotic cells actually represent adaptations to different regimes of noise in sensing and motility[8]. We emphasize that molecular shot noise makes renders measuring a concentration gradient accurately a non-trivial task at the cellular scale.

Measuring a concentration gradient requires the comparison of local concentration measurements $c_1 = c(\mathbf{r}_1, t_1)$ and $c_2 = c(\mathbf{r}_2, t_2)$ at different positions in space and possibly different times. The most

direct method of gradient-sensing would be to measure local concentrations at different positions $\mathbf{r}_1$ and $\mathbf{r}_2$ of the cell at the same time $t_1 = t_2$, which amounts to a mechanism of *spatial comparison*. However, recalling that cells detect a number N of binding events as a proxy for local concentration c with $\langle N \rangle \sim c$, see equation (10), we are led to compare the difference in the expectation values of two measurements $\Delta N = \langle N_1 - N_2 \rangle$, to the uncertainty σ in its measurement, which provides a signal-to-noise ratio[284]

$$\frac{\Delta N}{\sigma} \sim L^2 \sqrt{\frac{Dc}{v}} \frac{\nabla c}{c}. \tag{12}$$

From this equation, we find that spatial comparison is a viable strategy only for relatively large and slowly moving cells. For fast-swimming bacteria and sperm cells, one finds that the signal-to-noise ratio of spatial comparison would be too low to allow for reliable steering. Instead, these cells employ different strategies of *temporal comparison*[8,293], for which these cells rely on their active motion inside the external concentration field, which allows them to compare concentrations at different positions along their swimming path $\mathbf{r}(t)$.

Noise in sensing and motility imposes tight constraints on cellular chemotaxis strategies. We review three different strategies for dynamic gradient sensing employed by single cells.

Chemotaxis by spatial comparison. The fidelity of spatial gradient sensing across the diameter L of a cell depends strongly on the time $\tau = L/v$ available to integrate noisy local concentration measurements, which in turn depends on the speed v of the cell locomotion[284]. Only slow moving cells, such as the slime mold *Dictyostelium* ($v \approx 1{-}10\,\mu\mathrm{m/min}$), are able to employ spatial comparison for directed motion up a chemical gradient[61] with the efficacy of chemotaxis depending on the signal-to-noise ratio of spatial gradient sensing[294,295].

Biased random walks. Swimming bacteria such as *Escherichia coli* employ a stochastic chemotaxis strategy: they move along biased random walks to steer up chemical gradients, *e.g.* gradients of nutrient concentrations. During so-called 'run' periods, these cells swim along straight paths for a few seconds. These straight 'runs' are interrupted by stochastic reorientation events, termed 'tumbling', during which the bacterium picks a new swimming direction at random[69]. *E. coli* employs a particular form of temporal comparison for gradient-sensing by which the cell computes a smoothed time-derivative of the temporal concentration signal $c(\mathbf{r}(t))$ along its swimming path $\mathbf{r}(t)$. If a decrease of this concentration signal is detected, which is indicative of inadvertently swimming down-gradient, the cell will tumble earlier and more vigorously. This 'run-&-tumble' strategy results in a biased random walk, with net drift towards regions of higher chemoattractant concentration.

Interestingly, noise in chemosensation would render the alternative chemotaxis strategy of spatial comparison too inaccurate for these bacteria[69,284], see also equation (12). In short, *E. coli* is too small and too fast for accurate gradient-sensing by spatial comparison. At the same time, motility fluctuations are similarly substantial for these cells: Sized only a few microns, *E. coli* cells are subject to thermal fluctuations that randomize their swimming direction even during supposedly straight 'runs'. The rotational diffusion time D_{rot}^{-1} of a few seconds limits the available time span for signal integration. Correspondingly, it is observed that 'runs' usually do not last longer than this time span. The information gathered by temporal comparison during a single 'run' is not sufficient to control the steering direction[284], which leads to the genuinely stochastic strategy of bacterial chemotaxis. Thus, sensing and motility fluctuations constrain the possible choice of chemotaxis strategy for bacteria.

Helical chemotaxis. A third navigation strategy exploits chiral self-motion. This strategy is employed *e.g.* by sperm from marine species with external fertilization, which respond to signaling molecules released by the egg[144,296]. These sperm swim along helical paths[91–93], which is a result of the chiral beat

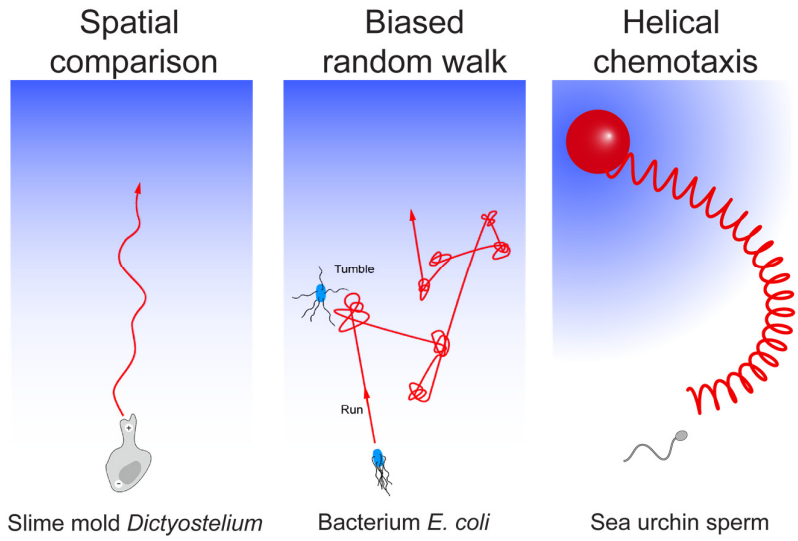

Figure 8: *The three strategies of single cell chemotaxis.* For chemotaxis, motile cells employ very different strategies. *Left*: Cells with crawling motility, such as the slime mold *Dictyostelium,* compares concentration differences across the diameter of the cell, thus representing a case of *spatial comparison.* Subsequently, the cell becomes structurally polar in the direction of the gradient and moves up-gradient. *Middle:* The bacterium *E. coli* employs a chemotaxis strategy of temporal comparison along a *biased random walk*. Short run segments are interrupted by stochastic reorientations events termed 'tumble'. A dynamic regulation of the 'tumbling' frequency according to temporal changes of the concentration signal along their swimming path results in a net drift up the gradient. *Right:* Sperm cells from marine species with external fertilization navigate along helical paths, which represents a stereotypic form of exploratory motion. Although *helical chemotaxis* represents a case of gradient-sensing by temporal comparison as in the case of bacterial chemotaxis, sperm steering responses are deterministic and point in the direction of the gradient, in contrast to the stochastic tumbling events of bacteria. The different chemotaxis strategies of these three cells suggest an adaptation to different noise levels of sensing and motility. Blue: concentration gradient of a signaling molecule, red: cell trajectory. Modified from ref.[8] with permission.

of their flagellum[93]. Helical swimming enables these cells to detect the direction of a chemoattractant gradient perpendicular to the helix axis: when the cell swims along a helix (whose axis is initially not aligned with the gradient), the cell will periodically move up and down the gradient, see figure 9. Thus, the cell perceives a chemoattractant stimulus that oscillates with the frequency of helical swimming. This frequency is about 2 Hz for marine sperm[119]. Thereby, information about the spatial gradient becomes encoded in a temporal oscillation of the chemoattractant signal. This chemoattractant signal is transduced by a chemotactic signaling cascade[297], which generically will elicit an oscillatory flagellar steering response[140]. As a result, the curvature and torsion of the sperm swimming path oscillate with the helix frequency. While a constant value of curvature and torsion characterizes a perfect helix, oscillations of curvature or torsion result in bending helices[140]. As a consequence, the helix axis, which

represents the direction of net motion, aligns with the gradient direction. Correct steering requires that the latency time of chemotactic signaling, which induces a phase-shift between stimulus oscillations and curvature oscillations, adopts an optimal value[140].

Sperm cells swim too fast (v=100 μm/s) in order to employ spatial comparison with sufficient accuracy along the length of their flagellum ($L = 50\,\mu\mathrm{m}$)[8]. Like bacteria, sperm must rely on temporal comparison, *i.e.* sperm detect how the local concentration changes in time while they actively move in a concentration gradient[298]. However, being ten-fold larger than bacteria, sperm cells are 1000-times less affected by thermal rotational diffusion[8]. Thus, sperm cells from marine invertebrates can stably swim along helical paths. Their helical swimming represents a stereotypic form of exploratory movement, which enables these cells to gather information about the direction of concentration gradient. This information is encoded in the relative phase of temporal oscillations of the concentration stimulus. Unlike bacteria that employ a fundamentally stochastic chemotaxis strategy of run-&-tumble, sperm use directed steering responses[8,140]. Generally, helical chemotaxis is expected to be more efficient than a biased random walk. This is because helical chemotaxis enables the cell to align its direction of net motion parallel to the direction of the gradient. Additionally, measuring concentration gradients while moving along helical paths provides an effective mean to integrate out molecular shot noise of chemosensation[141,142].

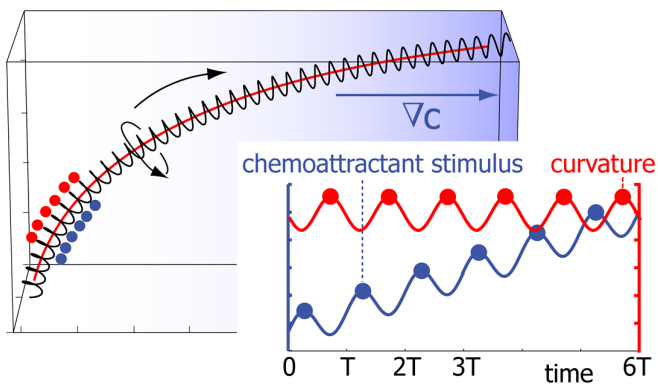

Figure 9: *The principle of helical chemotaxis.* We describe a navigation strategy of helical chemotaxis, which is employed *e.g.* by sperm from marine species with external fertilization that swim along helical paths[8,93,140]. In the presence of chemoattractant gradient, helical swimming paths bend in the direction of the gradient, which aligns the helix axis with the gradient direction. This chemotaxis strategy relies on a simple geometric principle: While swimming along a helix, the cell periodically moves up and down the gradient. The cell thus perceives an oscillatory chemoattractant stimulus that oscillates with the period T of helical swimming. The cell responds to this oscillatory chemical signal with oscillations of its path curvature. As a result, the helix bends to align its axis with the gradient.

Adaptation to spatio-temporal stability of concentration gradients. Cells must navigate in fluctuating environments. For example, chemical gradients established by diffusion in aqueous environments will be not be perfectly linear, but become distorted by turbulent flows[299,300]. As a second example, concentrations gradients of nutrients such as organic debris in the ocean continuously change due to the dynamics of its production and uptake by other organisms[301,302]. In a theoretical description of bacterial chemotaxis, optimal strategies of chemotactic signaling such as time-scales of signal integration or sensory adaptation were found to depend on sensing noise[303], and thus on the characteristics of concentration gradients. Celani and Vergassola formalized a risk-averse *maximin-*

strategy for bacterial chemotaxis, which is adapted to random, short-lived concentration gradients[304]. If concentrations change on a typical time-scale, memory can improve the performance of cellular gradient-sensing. Concepts from control engineering (such as Kalman filters) represent strategies for the robust estimation of concentration gradients[305]. Finally, the availability of extensive memory and computation resources facilitates advanced strategies of gradient search. One example of such an advanced strategy is infotaxis.

For the theoretically proposed mechanism of infotaxis, a hypothetical 'search agent' exploits its full sensation history to compute a detailed likelihood map of the location of a single point source[306]. Put differently, the search agent relies on a cognitive model of environmental variability. The search agent then choses its next movement step such as to maximize the expected reduction in Shannon entropy of this likelihood map. This theoretical mechanism represents a viable solution to the general trade-off choice between *exploration* (*i.e.* active movement geared at gathering additional information about the environment) and *exploitation* (*i.e.* directed movement towards the current estimate of the most-likely target position). Infotaxis was shown to perform even for dilute concentration gradients that are distorted by strongly turbulent flows. For single cells with minimal information processing capabilities, however, navigation strategies that require extensive memory and information processing capabilities such as infotaxis may not be available. Cells have to make optimal use of available resources for sensing, information processing, and memory for spatial navigation[307].

Concluding remark. In this introduction, we highlighted the nonlinear physics of cell motility and self-organized pattern formation in biological systems. In particular, we emphasized how non-equilibrium fluctuations and external perturbations affect cellular function. In the selected publications of chapter 2 and 3, these two central themes, nonlinear dynamics and fluctuations, are studied for specific biological systems. The systems under study range from flagellar swimming, steering, and synchronization to cytoskeletal pattern formation and self-scaling morphogen gradients. We combine analytically tractable theoretical descriptions and computational approaches. Thereby, we provide insight into physical mechanisms of biological function. Further, we enable a quantitative comparison of theory and experiment. Ultimately, we seek to use theoretical physics to contribute to the understanding of fundamental principles that render biological dynamics robust in the presence of strong fluctuations and perturbations.

Bibliography

1. Gray, J. *Ciliary Movements*. (Cambridge Univ. Press, 1928).
2. Brokaw, C. J. Flagellar movement: a sliding filament model. *Science* **178,** 455–462 (1972).
3. Alberts, B. *et al. Molecular Biology of the Cell*. (Garland Science, 2002).
4. Taylor, G. I. Analysis of the swimming of microscopic organisms. *Proc. Roy. Soc. Lond. A* **209,** 447–461 (1951).
5. Geyer, V. F., Jülicher, F., Howard, J. & Friedrich, B. M. Cell-body rocking is a dominant mechanism for flagellar synchronization in a swimming alga. *Proc. Natl. Acad. Sci. U. S. A.* **110,** 18058–18063 (2013).
6. Brumley, D. R., Wan, K. Y., Polin, M. & Goldstein, R. E. Flagellar synchronization through direct hydrodynamic interactions. *eLife* **3,** (2014).
7. Witman, G. B. *Chlamydomonas* phototaxis. *Trends Cell Biol* **3,** 403–408 (1993).
8. Alvarez, L., Friedrich, B. M., Gompper, G. & Kaupp, U. B. The computational sperm cell. *Trends Cell Biol.* **24,** 198–207 (2014).
9. Crenshaw, H. C. A new look at locomotion in microorganisms: Rotating and translating. *Americ. Zool.* **36,** 608–618 (1996).
10. Friedrich, B. M., Fischer-Friedrich, E., Gov, N. & Safran, S. Sarcomeric pattern formation by actin cluster coalescence. *PLoS Comp Biol* **8,** e1002544 (2012).
11. Werner, S. *et al.* Scaling and regeneration of self-organized patterns. *Phys. Rev. Lett.* **114,** 5 (2015).
12. Bray, D. *Cell Movements*. (Garland, 2002).
13. Ben-Isaac, E. *et al.* Effective temperature of red-blood-cell membrane fluctuations. *Phys. Rev. Lett.* **106,** 238103 (2011).
14. Ma, R., Klindt, G. S., Riedel-Kruse, I. H., Jülicher, F. & Friedrich, B. M. Active phase and amplitude fluctuations of flagellar beating. *Phys. Rev. Lett.* **113,** 048101 (2014).
15. Laughlin, S. B. The role of sensory adaptation in the retina. *J. Exp. Biol.* **146,** 39–62 (1989).
16. Smirnakis, S. M., Berry, M. J., Warland, D. K., Bialek, W. & Meister, M. Adaptation of retinal processing to image contrast and spatial scale. *Nature* **386,** 69–73 (1997).
17. Barkai, N. & Leibler, S. Robustness in simple biochemical networks. *Nature* **387,** 913–917 (1997).
18. Kondo, S. & Miura, T. Reaction-diffusion model as a framework for understanding biological pattern formation. *Science* **329,** 1616–1620 (2010).
19. Karsenti, E. Self-organization in cell biology: A Brief History. *Nat. Rev. Mol. Cell Biol.* **9,** 255–262 (2008).
20. Nicolis, G. & Prigogine, I. *Self-Organization in Nonequilibrium Systems*. (Wiley & Sons, 1977).
21. Chrzanowska-Wodnicka, M. & Burridge, K. Rho-stimulated contractility drives the formation of stress fibers and focal adhesions. *J. Cell Biol.* **133,** 1403–1415 (1996).
22. April, E. W. Liquid-crystalline characteristics of the thick filament lattice of striated muscle. *Nature* **257,** 139–141 (1975).
23. Anderson, P. More is different: Broken symmetry and the nature of hierarchial structure of science. *Science* **177,** 393–396 (1972).
24. Nelson, P. *Biological Physics*. (Freeman, 2004).
25. Hodgkin, A. L. & Huxley, A. F. A quantitative description of membrane current and its application to conduction and excitation in nerve. *J. Physiol.* **117,** 500–544 (1952).
26. Süel, G. M., Garcia-Ojalvo, J., Liberman, L. M. & Elowitz, M. B. An excitable gene regulatory circuit induces transient cellular differentiation. *Nature* **440,** 545–50 (2006).
27. Kobayashi, T. J. Implementation of dynamic Bayesian decision making by intracellular kinetics. *Phys. Rev. Lett.* **104,** 228104 (2010).
28. Kruse, K. & Jülicher, F. Oscillations in cell biology. *Curr. Opin. Cell Biol.* **17,** 20–26 (2005).
29. Perkins, T. J. & Swain, P. S. Strategies for cellular decision-making. *Mol. Sys. Biol.* **5,** 326 (2009).
30. Balazsi, G., Van Oudenaarden, A. & Collins, J. J. Cellular decision making and biological noise: From microbes to mammals. *Cell* **144,** 910–925 (2011).
31. Ozbudak, E. M., Thattai, M., Lim, H. N., Shraiman, B. I. & Van Oudenaarden, A. Multistability in the lactose utilization network of *Escherichia coli*. *Nature* **427,** 737–740 (2004).
32. Howard, J. Mechanical signaling in networks of motor and cytoskeletal proteins. *Ann. Rev. Biophys.* **38,** 217–234 (2009).
33. Winfree, A. T. *The geometry of biological time: Interdisciplinary applied mathematics*. *Springer* **24,** (2001).
34. Martin, P., Bozovic, D., Choe, Y. & Hudspeth, A. J. Spontaneous oscillation by hair bundles of the bullfrog's sacculus. *J. Neurosci.* **23,** 4533–48 (2003).

35. Nadrowski, B., Martin, P. & Jülicher, F. Active hair-bundle motility harnesses noise to operate near an optimum of mechanosensitivity. *Proc. Natl. Acad. Sci. U.S.A.* **101,** 12195–200 (2004).
36. Crenshaw, H. C. Negative phototaxis in *Chlamydomonas* is via helical klinotaxis - A new paradigm for phototaxis. *Mol. Biol. Cell.* **7,** 48a (1996).
37. Yoshimura, K. & Kamiya, R. The sensitivity of *Chlamydomonas* photoreceptor is optimized for the frequency of cell body rotation. *Plant Cell Physiol.* **42,** 665–72 (2001).
38. Brokaw, C. J. Thinking about flagellar oscillation. *Cell Motil. Cytoskel.* **66,** 425–436 (2008).
39. Riedel-Kruse, I. H., Hilfinger, A., Howard, J. & Jülicher, F. How molecular motors shape the flagellar beat. *HFSP J.* **1,** 192–208 (2007).
40. Turing, A. M. The chemical basis of morphogenesis. *Phil. Trans. R. Soc. Lond. B* **237,** 37–72 (1952).
41. Gierer, A. & Meinhardt, H. A theory of biological pattern formation. *Kybernetik* **12,** 30–39 (1972).
42. Yoshinaga, N., Joanny, J.-F., Prost, J. & Marcq, P. Polarity patterns of stress fibers. *Phys. Rev. Lett.* **105,** 238103 (2010).
43. Bois, J. S., Jülicher, F. & Grill, S. W. Pattern formation in active fluids. *Phys. Rev. Lett.* **106,** 028103(4) (2011).
44. Engler, A. J. *et al.* Myotubes differentiate optimally on substrates with tissue-like stiffness: pathological implications for soft or stiff microenvironments. *J. Cell Biol.* **166,** 877–87 (2004).
45. Yeung, T. *et al.* Effects of substrate stiffness on cell morphology, cytoskeletal structure, and adhesion. *Cell Motil. Cytoskeleton* **60,** 24–34 (2005).
46. Friedrich, B. M. & Safran, S. A. Nematic order by elastic interactions and cellular rigidity sensing. *Europhys. Lett.* **93,** 28007 (2011).
47. Friedrich, B. M., Buxboim, A., Discher, D. E. & Safran, S. A. Striated acto-myosin fibers can reorganize and register in response to elastic interactions with the matrix. *Biophys. J.* **100,** 2706–2715 (2011).
48. Friedrich, B. M. & Safran, S. How cells feel their substrate: spontaneous symmetry breaking of active surface stresses. *Softmatter* **8,** 3223–3230 (2012).
49. McDonagh, M. J. & Davies, C. T. Adaptive response of mammalian skeletal muscle to exercise with high loads. *Eur. J. Appl. Physiol. Occup. Physiol.* **52,** 139–155 (1984).
50. Turner, C. H. Three rules for bone adapation to mechanical stimuli. *Bone* **23,** 399–407 (1998).
51. Pfeifer, R., Lungarella, M. & Iida, F. Self-organization, embodiment, and biologically inspired robotics. *Science* **318,** 1088–1093 (2007).
52. Alon, U., Surette, M. G., Barkai, N. & Leibler, S. Robustness in chemical networks. *Nature* **397,** 168–171 (1999).
53. Kitano, H. Towards a theory of biological robustness. *Mol. Syst. Biol.* **3,** 137 (2007).
54. Germain, R. N. The art of the probable: system control in the adaptive immune system. *Science* **293,** 240–245 (2001).
55. Murase, M. *The Dynamics of Cellular Motility*. *John Wiley & Sons* **50,** (1992).
56. Berg, H. & Anderson, R. Bacteria swim by rotating their flagellar filaments. *Nature* **245,** 380 – 382 (1973).
57. Shaevitz, J. W., Lee, J. Y. & Fletcher, D. A. Spiroplasma swim by a processive change in body helicity. *Cell* **122,** 941–945 (2005).
58. Gray, J. The movement of sea-urchin spermatozoa. *J. exp. Biol.* **32,** 775–801 (1955).
59. Pollard, T. D. & Borisy, G. G. Cellular motility driven by assembly and disassembly of actin filaments. *Cell* **112,** 453–465 (2003).
60. Rafelski, S. M. & Theriot, J. A. Crawling toward a unified model cell motility : Spatial and temporal regulation of actin dynamics. *Annu. Rev. Biochem.* **73,** 209–39 (2004).
61. Devreotes, P. N. & Zigmond, S. H. Chemotaxis in eukaryotic cells: a focus on leukocytes and *Dictyostelium*. *Annu. Rev. Cell Biol.* **4,** 649–686 (1988).
62. Rappel, W.-J., Thomas, P. J., Levine, H. & Loomis, W. F. Establishing direction during chemotaxis in eukaryotic cells. *Biophys. J.* **83,** 1361–7 (2002).
63. Howard, J. *Mechanics of Motor Proteins and the Cytoskeleton*. (Sinauer, 2001).
64. Fritzsche, M., Lewalle, A., Duke, T., Kruse, K. & Charras, G. Analysis of turnover dynamics of the submembranous actin cortex. *Mol. Biol. Cell* **24,** 757–67 (2013).
65. Footer, M. J., Kerssemakers, J. W. J., Theriot, J. A. & Dogterom, M. Direct measurement of force generation by actin filament polymerization using an optical trap. *Proc. Natl. Acad. Sci. U.S.A.* **104,** 2181–2186 (2007).
66. Nicastro, D. *et al.* The molecular architecture of axonemes revealed by cryoelectron tomography. *Science* **313,** 944–8 (2006).
67. Shih, Y.-L. & Rothfield, L. The bacterial cytoskeleton. *Microbiol. Mol. Biol. Rev.* **70,** 729–754 (2006).

68. Bugyi, B. & Carlier, M.-F. Control of actin filament treadmilling in cell motility. *Annu. Rev. Biophys.* **39,** 449–470 (2010).
69. Berg, H. C. *E. coli in Motion*. (Springer, 2004).
70. Hunt, A. J., Gittes, F. & Howard, J. The force exerted by a single kinesin molecule against a viscous load. *Biophys. J.* **67,** 766–781 (1994).
71. Yasuda, R., Noji, H., Ishiwata, S., Yoshida, M. & Kinosita Jr., K. F_1-ATPase is a highly efficient molecular motor that rotates with discrete 120 steps. *Cell* **93,** 1117–1124 (1998).
72. Itoh, H., Takahashi, A., Adachi, K. & Noji, H. Mechanically driven ATP synthesis by F_1-ATPase. *Nature* **427,** 465–468 (2004).
73. Sowa, Y. & Berry, R. M. Bacterial flagellar motor. *Quart. Rev. Biophys.* **41,** 103–132 (2008).
74. Chen, X. & Berg, H. C. Torque-speed relationship of the flagellar rotary motor of *Escherichia coli*. *Biophys. J.* **78,** 1036–1041 (2000).
75. Calladine, C. R. Design requirements for the construction of bacterial flagella. *J. Theor. Biol.* **57,** 469–489 (1976).
76. Srigiriraju, S. V. & Powers, T. R. Continuum model for polymorphism of bacterial flagella. *Phys. Rev. Lett.* **94,** 248101 (2005).
77. Friedrich, B. M. A mesoscopic model for helical bacterial flagella. *J. Math. Biol.* **53,** 162–178 (2006).
78. Vogel, R. & Stark, H. Motor-driven bacterial flagella and buckling instabilities. *Eur. Phys. J. E* **35,** 12015 (2012).
79. Reichert, M. & Stark, H. Synchronization of rotating helices by hydrodynamic interactions. *Eur. Phys. J. E* **17,** 493–500 (2005).
80. Reigh, S. Y., Winkler, R. G. & Gompper, G. Synchronization and bundling of anchored bacterial flagella. *Soft Matter* **8,** 4363 (2012).
81. Berg, H. C. & Brown, D. A. Chemotaxis in *Escherichia coli* analysed by three-dimensional tracking. *Nature* **239,** 500–504 (1972).
82. Vogel, G. Betting on cilia. *Nature* **310,** 216–218 (2005).
83. Marshall, W. F. & Nonaka, S. Cilia: tuning in to the cell's antenna. *Curr. Biol.* **16,** R604–14 (2006).
84. Gibbons, I. R. & Rowe, A. J. Dynein: A protein with adenosine triphosphatase activity from cilia. *Science* **183,** 139–141 (1965).
85. Machin, K. E. Wave propagation along flagella. *J. exp. Biol.* **35,** 796–806 (1958).
86. Afzelius, B. A., R. Dallai, S. L. & Bellon, P. L. Flagellar structure in normal human spermatozoa and in spermatozoa that lack dynein arms. *Tissue Cell* **27,** 241–247 (1995).
87. Carvalho-Santos, Z., Azimzadeh, J., Pereira-Leal, J. B. & Bettencourt-Dias, M. Tracing the origins of centrioles, cilia, and flagella. *J. Cell Biol.* **194,** 165–175 (2011).
88. Summers, K. E. & Gibbons, I. R. Adenosine Triphosphate-Induced Sliding of Tubules in Trypsin-Treated Flagella of Sea-Urchin Sperm. *Proc. Natl. Acad. Sci.* **68,** 3092–3096 (1971).
89. Brokaw, C. J. Direct measurements of sliding between outer doublet microtubules in swimming sperm flagella. *Science* **243,** 1593–6 (1989).
90. Bui, K. H., Sakakibara, H., Movassagh, T., Oiwa, K. & Ishikawa, T. Asymmetry of inner dynein arms and inter-doublet links in *Chlamydomonas* flagella. *J. Cell Biol.* **186,** 437–46 (2009).
91. Crenshaw, H. C., Ciampaglio, C. N. & McHenry, M. Analysis of the three-dimensional trajectories of organisms: Estimates of velocity, curvature and torsion from positional information. *J. exp. Biol.* **203,** 961–982 (2000).
92. Corkidi, G., Taboada, B., Wood, C. D., Guerrero, A. & Darszon, A. Tracking sperm in three-dimensions. *Biochem. Biophys. Res. Comm.* **373,** 125–129 (2008).
93. Jikeli, J. F. *et al.* Sperm navigation along helical paths in 3D chemoattractant landscapes. *Nat. Comm.* **6,** 7985 (2015).
94. Rüffer, U. & Nultsch, W. Flagellar photoresponses of *Chlamydomonas* cells held on micropipettes: II. Change in flagellar beat frequency. *Cell Mot. Cytoskel.* **15,** 162–167 (1991).
95. Jülicher, F. & Prost, J. Spontaneous oscillations of collective molecular motors. *Phys. Rev. Lett.* **78,** 4510–4513 (1997).
96. Brokaw, C. J. Effects of viscosity and ATP concentration on the movement of reactivated sea-urchin sperm flagella. *J. exp. Biol.* **62,** 701–19 (1975).
97. Alper, J., Geyer, V., Mukundan, V. & Howard, J. Reconstitution of flagellar sliding. *Methods Enzymol.* **524,** 343–369 (2013).
98. Geyer, V. F., Sartori, P., Friedrich, B. M., Jülicher, F. & Howard, J. Independent control of the static and dynamic components of the Chlamydomonas flagellar beat. *Curr. Biol.* **26,** 1098–1103 (2016).
99. Brokaw, C. J. Bend propagation by a sliding filament model for flagella. *J. exp. Biol.* **55,** 289–304 (1971).

100. Camalet, S. & Jülicher, F. Self-organized beating and swimming of internally driven filaments. *Phys. Rev. Lett.* **82,** 1590–1593 (1999).
101. Camalet, S. & Jülicher, F. Generic aspects of axonemal beating. *New J. Phys.* **2,** 1–23 (2000).
102. Lindemann, C. B. A 'geometric clutch' hypothesis to explain oscillations of the axoneme of cilia and flagella. *J. Theor. Biol.* **168,** 175–189 (1994).
103. Bayly, P. V. & Wilson, K. S. Analysis of unstable modes distinguishes mathematical models of flagellar motion. *J. R. Soc. Interface* **12,** 20150124–20150124 (2015).
104. Sartori, P., Geyer, V., Scholich, A., Jülicher, F. & Howard, J. Dynamic curvature regulation accounts for the symmetric and asymmetric beats of *Chlamydomonas* flagella. 1–25 (2015).
105. Rüffer, U. & Nultsch, W. High-speed cinematographic analysis of the movement of *Chlamydomonas*. *Cell Mot.* **5,** 251–263 (1985).
106. Broadhead, R. *et al.* Flagellar motility is required for the viability of the bloodstream trypanosome. *Nature* **440,** 224–227 (2006).
107. Krüger, T. & Engstler, M. Flagellar motility in eukaryotic human parasites. *Semin. Cell Dev. Biol.* **46,** 113–127 (2015).
108. Purcell, E. M. Life at low Reynolds numbers. *Am. J. Phys.* **45,** 3–11 (1977).
109. Lauga, E. & Powers, T. R. The hydrodynamics of swimming microorganisms. *Rep. Prog. Phys.* **72,** 096601 (2009).
110. Elgeti, J., Winkler, R. G. & Gompper, G. Physics of microswimmers - single particle motion and collective behavior: a review. *Rep. Prog. Phys.* **78,** 056601 (2015).
111. Sleigh, M. A. *Cilia and Flagella*. (Academic Press, 1974).
112. Vilfan, A. & Jülicher, F. Hydrodynamic flow patterns and synchronization of beating cilia. *Phys. Rev. Lett.* **96,** 58102 (2006).
113. Golestanian, R. & Ajdari, A. Analytic results for the three-sphere swimmer at low Reynolds number. *Phys. Rev. E* **77,** 036308 (2008).
114. Dreyfus, R., Baudry, J. & Stone, H. A. Purcell's rotator: mechanical rotation at low Reynolds number. *Eur. Phys. J. B* **47,** 161–164 (2005).
115. Polotzek, K. & Friedrich, B. M. A three-sphere swimmer for flagellar synchronization. *New J. Phys.* **15,** 045005 (2013).
116. Klindt, G. S. & Friedrich, B. M. Flagellar swimmers oscillate between pusher- and puller-type swimming. *Phys. Rev. E* **92,** 063019 (2015).
117. Liu, Y. J. *Fast Multipole Boundary Element Method: Theory and Applications in Engineering*. (Cambridge Univ. Press, 2009).
118. Brokaw, C. J. Effects of increased viscosity on the movements of some invertebrate spermatozoa. *J. exp. Biol.* **45,** 113–139 (1966).
119. Friedrich, B. M., Riedel-Kruse, I. H., Howard, J. & Jülicher, F. High-precision tracking of sperm swimming fine structure provides strong test of resistive force theory. *J. exp. Biol.* **213,** 1226–1234 (2010).
120. Shapere, A. & Wilczek, F. Self-propulsion at low Reynolds number. *Phys. Rev. Lett.* **58,** 2051–2054 (1987).
121. Werner, S., Rink, J. C., Riedel-Kruse, I. H. & Friedrich, B. M. Shape mode analysis exposes movement patterns in biology: Flagella and flatworms as case studies. *PLoS One* **9,** e113083 (2014).
122. Elfring, G. & Lauga, E. Hydrodynamic phase locking of swimming microorganisms. *Phys. Rev. Lett.* **103,** 088101 (2009).
123. Singla, V. & Reiter, J. F. The primary cilium as the cell's antenna: signaling at a sensory organelle. *Science* **313,** 629–33 (2006).
124. Brennen, C. & Winet, H. Fluid mechanics of propulsion by cilia and flagella. *Annu. Rev. Fluid Mech.* **9,** 339–398 (1977).
125. Sanderson, M. J. & Sleigh, M. A. Ciliary activity of cultured rabbit tracheal epithelium: beat pattern and metachrony. *J. Cell Sci.* **47,** 331–47 (1981).
126. Worthington, W. C. & Cathcart, R. S. Ependymal cilia: Distribution and activity in the adult human brain. *Science* **139,** 221–222 (1963).
127. Cartwright, J. H. E., Piro, O. & Tuval, I. Fluid-dynamical basis of the embryonic development of left-right asymmetry in vertebrates. *Proc. Natl. Acad. Sci. U.S.A.* **101,** 7234–9 (2004).
128. Freund, J. B., Goetz, J. G., Hill, K. L. & Vermot, J. Fluid flows and forces in development: functions, features and biophysical principles. *Development* **139,** 3063–3063 (2012).
129. Boehmer, M. *et al.* Ca^{2+} spikes in the flagellum control chemotactic behavior of sperm. *Eur. Mol. Biol. Organ. J.* **24,** 2741–2752 (2005).
130. Wood, C. D., Nishigaki, T., Furuta, T., Baba, S. A. & Darszon, A. Real-time analysis of the role of Ca^{2+} in flagellar movement and motility in single sea urchin sperm. *J. Cell Biol.* **169,** 725–31 (2005).

131. Hilfinger, A. & Jülicher, F. The chirality of ciliary beats. *Phys. Biol.* **5,** 016003 (2008).
132. Wilson, L. G., Carter, L. M. & Reece, S. E. High-speed holographic microscopy of malaria parasites reveals ambidextrous flagellar waveforms. *Proc Natl Acad Sci U S A* **110,** 18769–18774 (2013).
133. Ishijima, S., Oshio, S. & Mohri, H. Flagellar movement of human spermatozoa. *Gamete Res.* **13,** 185–197 (1986).
134. Su, T. *et al.* Sperm trajectories form chiral ribbons. *Sci. Rep.* **3,** 1664 (2013).
135. Rothschild, L. Non-random distribution of bull spermatozoa in a drop of sperm suspension. *Nature* **198,** 1221–1222 (1963).
136. Elgeti, J., Kaupp, U. B. & Gompper, G. Hydrodynamics of sperm cells near surfaces. *Biophys. J.* **99,** 1018–26 (2010).
137. Elgeti, J. & Gompper, G. Self-propelled rods near surfaces. *Europhys. Lett.* **85,** 38002 (2009).
138. Smith, D. J., Gaffney, E. A., Blake, J. R. & Kirkman-Brown, J. C. Human sperm accumulation near surfaces: a simulation study. *J. Fluid Mech.* **621,** 289–320 (2009).
139. Crenshaw, H. C. Orientation by helical motion - III. Microorganisms can orient to stiumuli by changing the direction of their rotational velocity. *Bull. Math. Biol.* **55,** 231–255 (1993).
140. Friedrich, B. M. & Jülicher, F. Chemotaxis of sperm cells. *Proc. Natl. Acad. Sci. U. S. A.* **104,** 13256–13261 (2007).
141. Friedrich, B. M. & Jülicher, F. The stochastic dance of circling sperm cells: Sperm chemotaxis in the plane. *New J. Phys.* **10,** 123025(19) (2008).
142. Friedrich, B. M. & Jülicher, F. Steering chiral swimmers along noisy helical paths. *Phys. Rev. Lett.* **103,** 68102 (2009).
143. Eisenbach, M. & Giojalas, L. C. Sperm guidance in mammals - an unpaved road to the egg. *Nat. Rev. Mol. Cell Biol.* **7,** 276–285 (2006).
144. Kaupp, U. B., Hildebrand, E. & Weyand, I. Sperm Chemotaxis in Marine Invertebrates — Molecules and Mechanisms. *J. Cell. Physiol.* **208,** 487–494 (2006).
145. Zacks, D. N. & Spudich, J. L. Gain setting in *Chlamydomonas reinhardtii*: mechanism of phototaxis and the role of the photophobic response. *Cell Motil. Cytoskeleton* **29,** 225–30 (1994).
146. Nonaka, S., Shiratori, H., Saijoh, Y. & Hamada, H. Determination of left-right patterning of the mouse embryo by artificial nodal flow. *Nature* **418,** 96–99 (2002).
147. Winet, H., Bernstein, G. S. & Head, J. Observations on the response of human spermatozoa to gravity, boundaries and fluid shear. *J. Reprod. Fert.* **70,** 511–523 (1984).
148. Miki, K. & Clapham, D. E. Rheotaxis guides mammalian sperm. *Curr. Biol.* **23,** 443–52 (2013).
149. Kantsler, V., Dunkel, J., Blayney, M. & Goldstein, R. E. Rheotaxis facilitates upstream navigation of mammalian sperm cells. *eLife* **3,** e02403 (2014).
150. Heddergott, N. *et al.* Trypanosome motion represents an adaptation to the crowded environment of the vertebrate bloodstream. *PLoS Pathog.* **8,** e1003023 (2012).
151. Wan, K. Y. & Goldstein, R. E. Rhythmicity, recurrence and recovery of flagellar beating. *Phys. Rev. Lett.* **113,** 238103 (2014).
152. Qin, B., Gopinath, A., Yang, J., Gollub, J. P. & Arratia, P. E. Flagellar kinematics and swimming of algal cells in viscoelastic fluids. *Sci. Rep.* **5,** 9190 (2015).
153. Chen, D. T. N., Heymann, M., Fraden, S., Nicastro, D. & Dogic, Z. ATP consumption of eukaryotic flagella measured at a single-cell level. *Biophys. J.* **109,** 2562–2573 (2015).
154. Woolley, D. M., Crockett, R. F., Groom, W. D. I. & Revell, S. G. A study of synchronisation between the flagella of bull spermatozoa, with related observations. *J. exp. Biol.* **212,** 2215–23 (2009).
155. Okuno, M. & Hiramoto, Y. Mechanical stimulation of starfish sperm flagella. *J. exp. Biol.* **65,** 401–13 (1976).
156. Quaranta, G., Aubin-Tam, M. E. & Tam, D. Hydrodynamics versus intracellular coupling in the synchronization of eukaryotic flagella. *Phys. Rev. Lett.* **115,** 238101 (2015).
157. Osterman, N. & Vilfan, A. Finding the ciliary beating pattern with optimal efficiency. *Proc. Natl. Acad. Sci. U.S.A.* **108,** 15727–32 (2011).
158. Elgeti, J. & Gompper, G. Emergence of metachronal waves in cilia arrays. *Proc. Natl. Acad. Sci. U.S.A.* **110,** 4470–5 (2013).
159. Rüffer, U. & Nultsch, W. Flagellar coordination in *Chlamydomonas* cells held on micropipettes. *Cell Motil. Cytoskel.* **41,** 297–307 (1998).
160. Goldstein, R. E., Polin, M. & Tuval, I. Noise and synchronization in pairs of beating eukaryotic flagella. *Phys. Rev. Lett.* **103,** 168103 (2009).
161. Goldstein, R. E., Polin, M. & Tuval, I. Emergence of synchronized beating during the regrowth of eukaryotic flagella. *Phys. Rev. Lett.* **107,** 148103 (2011).
162. Tam, D. & Hosoi, A. E. Optimal feeding and swimming gaits of biflagellated organisms. *Proc. Natl. Acad. Sci. U.S.A.* **108,** 1001–6 (2011).

163. Riedel, I. H., Kruse, K. & Howard, J. A self-organized vortex array of hydrodynamically entrained sperm cells. *Science* **309,** 300–303 (2005).
164. Shiba, K. *et al.* Sperm-activating peptide induces asymmetric flagellar bending in sea urchin sperm. *Zoolog. Sci.* **22,** 293–9 (2005).
165. Josef, K., Saranak, J. & Foster, K. W. Ciliary behaviour of a negatively phototactic *Chlamydomonas reinhardtii*. *Cell Mot. Cytoskel.* **61,** 97–111 (2005).
166. Fujiu, K., Nakayama, Y., Iida, H., Sokabe, M. & Yoshimura, K. Mechanoreception in motile flagella of *Chlamydomonas*. *Nat. Cell Biol.* **13,** 630–632 (2011).
167. Suarez, S. S. Control of hyperactivation in sperm. *Hum. Reprod. Update* **14,** 647–657 (2008).
168. Brokaw, C. J. Calcium-induced asymmetrical beating of triton-demembranated sea urchin sperm flagella. *J. Cell Biol.* **82,** 401–411 (1979).
169. Alvarez, L. *et al.* The rate of change in Ca^{2+} concentration controls sperm chemotaxis. *J Cell Biol* **196,** (2012).
170. Sakato, M. & King, S. M. Calcium regulates ATP-sensitive microtubule binding by *Chlamydomonas* outer arm dynein. *J. Biol. Chem.* **278,** 43571–43579 (2003).
171. DiPetrillo, C. G. & Smith, E. F. Pcdp1 is a central apparatus protein that binds Ca^{2+}-calmodulin and regulates ciliary motility. *J. Cell Biol.* **189,** 601–612 (2010).
172. Mizuno, K. *et al.* Calaxin drives sperm chemotaxis by Ca^{2+}-mediated direct modulation of a dynein motor. *Proc. Natl. Acad. Sci. U. S. A.* **109,** 20497–502 (2012).
173. Turner, R. M. Moving to the beat: A review of mammalian sperm motility regulation. *Reprod. Fertil. Dev.* **18,** 25–38 (2006).
174. Merz, A. J., So, M. & Sheetz, M. P. Pilus retraction powers bacterial twitching motility. *Nature* **407,** 98–102 (2000).
175. Skerker, J. M. & Berg, H. C. Direct observation of extension and retraction of type IV pili. *Proc. Natl. Acad. Sci. U. S. A.* **98,** 6901–6904 (2001).
176. Maier, B. & Wong, G. C. L. How bacteria use type IV pili machinery on surfaces. *Trends Microbiol.* **23,** 775–788 (2015).
177. Zaburdaev, V. *et al.* Uncovering the mechanism of trapping and cell orientation during *Neisseria gonorrhoeae* twitching motility. *Biophys. J.* **107,** 1523–1531 (2014).
178. Friedl, P., Borgmann, S. & Bröcker, E. B. Amoeboid leukocyte crawling through extracellular matrix: lessons from the *Dictyostelium* paradigm of cell movement. *J. Leukoc. Biol.* **70,** 491–509 (2001).
179. Thompson, D. W. *On Growth and Form*. (Cambridge Univ. Press, 1942).
180. Berg, H. C. The rotary motor of bacterial flagella. *Ann. Rev. Biochem.* **72,** 19–54 (2003).
181. Macnab, R. M. How bacteria assemble flagella. *Annu. Rev. Microbiol.* **57,** 77–100 (2003).
182. Rosenbaum, J. L. & Witman, G. B. Intraflagellar transport. *Nat. Rev. Mol. Cell Biol.* **3,** 813–825 (2002).
183. Stepanek, L. & Pigino, G. Microtubule doublets are double-track railways for intraflagellar transport trains. *Science* **352,** 721–724 (2016).
184. Nédélec, F. J., Surrey, T., Maggs, a C. & Leibler, S. Self-organization of microtubules and motors. *Nature* **389,** 305–8 (1997).
185. Schaller, V., Weber, C., Semmrich, C., Frey, E. & Bausch, A. R. Polar patterns of driven filaments. *Nature* **467,** 73–77 (2010).
186. Schaller, V., Weber, C. a, Hammerich, B., Frey, E. & Bausch, A. R. Frozen steady states in active systems. *Proc. Natl. Acad. Sci. U. S. A.* **108,** 19183–8 (2011).
187. Sanchez, T., Welch, D., Nicastro, D. & Dogic, Z. Cilia-Like Beating of Active Microtubule Bundles. *Science* **333,** 456 –459 (2011).
188. Dunkel, J. *et al.* Fluid dynamics of bacterial turbulence. *Phys. Rev. Lett.* **110,** 228102 (2013).
189. Sokolov, A. & Aranson, I. S. Physical properties of collective motion in suspensions of bacteria. *Phys. Rev. Lett.* **109,** 248109 (2012).
190. Vicsek, T., Czirok, A., Ben-Jacob, E., Cohen, I. & Shochet, O. Novel type of phase transition in a system of self propelled particles. *Phys. Rev. Lett.* **75,** 1226–1229 (1995).
191. Toner, J. & Tu, Y. H. Long-range order in a 2-dimensional dynamical XY model: How birds fly together. *Phys. Rev. Lett.* **75,** 4326–4329 (1995).
192. Chaté, H., Ginelli, F., Gregoire, G., Peruani, F. & Raynaud, F. Modeling collective motion: Variations on the Vicsek model. *Eur. Phys. J. B* **64,** 451–456 (2008).
193. Marchetti, M. C. *et al.* Hydrodynamics of soft active matter. *Rev. Mod. Phys.* **85,** 1143–1189 (2013).
194. Loose, M. *et al.* Spatial regulators for bacterial cell division self-organize into surface waves in vitro. *Science* **320,** 789–792 (2008).
195. Sheth, R. *et al.* Hox genes regulate digit patterning by controlling the wavelength of a Turing-type mechanism. *Science* **338,** 1476–1480 (2012).

196. Yamaguchi, M., Yoshimoto, E. & Kondo, S. Pattern regulation in the stripe of zebrafish suggests an underlying dynamic and autonomous mechanism. *Proc. Natl. Acad. Sci. U. S. A.* **104,** 4790–4793 (2007).
197. Watanabe, M. & Kondo, S. Is pigment patterning in fish skin determined by the Turing mechanism? *Trends Genet.* **31,** 88–96 (2015).
198. Winfree, A. T. The prehistory of the Belousov-Zhabotinsky oscillator. *J. Chem. Educ.* **61,** 661 (1984).
199. Backouche, F., Haviv, L., Groswasser, D. & Bernheim-Groswasser, A. Active gels: dynamics of patterning and self-organization. *Phys. Biol.* **3,** 264–273 (2006).
200. Soares e Silva, M. *et al.* Active multistage coarsening of actin networks driven by myosin motors. *Proc. Natl. Acad. Sci. U.S.A.* **108,** 9408–13 (2011).
201. Köhler, S., Schaller, V. & Bausch, A. R. Structure formation in active networks. *Nat. Mater.* **10,** 462–468 (2011).
202. Smith, D. *et al.* Molecular motor-induced instabilities and cross linkers determine biopolymer organization. *Biophys. J.* **93,** 4445–4452 (2007).
203. Gorfinkiel, N. & Blanchard, G. B. Dynamics of actomyosin contractile activity during epithelial morphogenesis. *Curr. Opin. Cell Biol.* **23,** 531–539 (2011).
204. Pullarkat, P. a., Fernández, P. a. & Ott, A. Rheological properties of the eukaryotic cell cytoskeleton. *Phys. Rep.* **449,** 29–53 (2007).
205. Kruse, K. & Jülicher, F. Actively contracting bundles of polar filaments. *Phys. Rev. Lett.* **85,** 1778–81 (2000).
206. Lenz, M., Thoresen, T., Gardel, M. L. & Dinner, A. R. Contractile units in disordered actomyosin bundles arise from F-actin buckling. *Phys. Rev. Lett.* **108,** 238107 (2012).
207. Kruse, K., Zumdieck, A. & Jülicher, F. Continuum theory of contractile fibres. *Eur. Phys. Lett.* **64,** 716–722 (2003).
208. Martin, P. & Lewis, J. Actin cables and epidermal movement in embryonic wound healing. *Nature* **360,** 179–183 (1992).
209. Peterson, L. J. *et al.* Simultaneous stretching and contraction of stress fibers in vivo. *Mol. Biol. Cell* **15,** 3497–3508 (2004).
210. Roland, J., Berro, J., Michelot, A., Blanchoin, L. & Martiel, J.-L. Stochastic severing of actin filaments by actin depolymerizing factor/cofilin controls the emergence of a steady dynamical regime. *Biophys. J.* **94,** 2082–94 (2008).
211. Gregorio, C. C., Granzier, H., Sorimachi, H. & Labeit, S. Muscle assembly: A titanic achievement? *Curr. Opin. Cell Biol.* **11,** 18–25 (1999).
212. Ingber, D. Tensegrity: The architectural basis of cellular mechanotransduction. *Ann. Rev. Phys.* **59,** 575–599 (1997).
213. Hyman, A. a & Karsenti, E. Morphogenetic properties of microtubules and mitotic spindle assembly. *Cell* **84,** 401–410 (1996).
214. Solari, C. A., Ganguly, S., Kessler, J. O., Michod, R. E. & Goldstein, R. E. Multicellularity and the functional interdependence of motility and molecular transport. *Proc. Natl. Acad. Sci. U.S.A.* **103,** 1353–1358 (2006).
215. Svitinka, T., Verkhovsky, A. B. & Borisy, G. G. Improved procedures for electron microscopic visualization of the cytoskeleton of cultured cells. *J Struct Biol* **115,** 290–303 (1995).
216. Paulsen, G. *et al.* Subcellular movement and expression of HSP27, B-crystallin, and HSP70 after two bouts of eccentric exercise in humans. *J Appl Physiol* **107,** 570–582 (2009).
217. Iwamoto, H., Niskikawa, Y., Wakayama, J. & Fujisawa, T. Direct X-ray observations of a single hexagonal myofilament lattice in native myofibrils of striated muscle. *Biophys. J.* **83,** 1074–1081 (2002).
218. Rhee, D., Sanger, J. M. & Sanger, J. W. The premyofibril: evidence for its role in myofibrillogenesis. *Cell Motil. Cytoskeleton* **28,** 1–24 (1994).
219. Sanger, J. W. *et al.* How to build a myofibril. *J. Muscle Res. Cell Mot.* **26,** 343–54 (2005).
220. Borisov, A. B., Martynova, M. G. & Russell, M. W. Early incorporation of obscurin into nascent sarcomeres: implication for myofibril assembly during cardiac myogenesis. *Histochem. Cell Biol.* **129,** 463–78 (2008).
221. Weitkunat, M., Kaya-Copur, A., Grill, S. W. & Schnorrer, F. Tension and force-resistant attachment are essential for myofibrillogenesis in drosophila flight muscle. *Curr. Biol.* **24,** 705–716 (2014).
222. Zemel, A. & Mogilner, A. Motor-induced sliding of microtubule and actin bundles. *Phys. Chem. Chem. Phys.* **11,** 4821–4833 (2009).
223. Wolpert, L. & Tickle, C. *Principles of Development*. (Oxford Univ. Press, 2011).
224. Niehrs, C. On growth and form: a Cartesian coordinate system of Wnt and BMP signaling specifies bilaterian body axes. *Development* **137,** 845–857 (2010).

225. Spencer, F. A., Hoffmann, F. M. & Gelbart, W. M. Decapentaplegic: A gene complex affecting morphogenesis in *Drosophila melanogaster*. *Cell* **28,** 451–461 (1982).
226. Wolpert, L. Positional information and the spatial pattern of cellular differentiation. *J. Theor. Biol.* **25,** 1–47 (1969).
227. Martinez Arias, A. Wnts as morphogens? The view from the wing of *Drosophila*. *Nat. Rev. Mol. Cell Biol.* **4,** 321–325 (2003).
228. Kruse, K., Pantazis, P., Bollenbach, T., Jülicher, F. & González-Gaitán, M. Dpp gradient formation by dynamin-dependent endocytosis: Receptor trafficking and the diffusion model. *Development* **131,** 4843–56 (2004).
229. Wartlick, O. *et al.* Dynamics of Dpp signaling and proliferation control. *Science* **331,** 1154–1159 (2011).
230. Ben-Zvi, D., Pyrowolakis, G., Barkai, N. & Shilo, B. Z. Expansion-repression mechanism for scaling the Dpp activation gradient in *Drosophila* wing imaginal discs. *Curr. Biol.* **21,** 1391–1396 (2011).
231. Hamaratoglu, F., de Lachapelle, A. M., Pyrowolakis, G., Bergmann, S. & Affolter, M. Dpp signaling activity requires pentagone to scale with tissue size in the growing *Drosophila* wing imaginal disc. *PLoS Biol* **9,** (2011).
232. Othmer, H. G. H. G. & Pate, E. E. Scale-invariance in reaction-diffusion models of spatial pattern formation. *Proc. Natl. Acad. Sci. U.S.A.* **77,** 4180–4184 (1980).
233. Ben-Zvi, D. & Barkai, N. Scaling of morphogen gradients by an expansion-repression integral feedback control. *Proc. Natl. Acad. Sci. U.S.A.* **107,** 6924–9 (2010).
234. Wartlick, O., Mumcu, P., Jülicher, F. & Gonzalez-Gaitan, M. Understanding morphogenetic growth control - lessons from flies. *Nat. Rev. Mol. Cell Biol.* **12,** 594–604 (2011).
235. Newmark, P. A. & Sánchez Alvarado, A. Not your father's planarian: A classic model enters the era of functional genomics. *Nat. Rev. Genet.* **3,** 210–9 (2002).
236. Gurley, K. A., Rink, J. C. & Alvarado, A. S. beta-catenin defines head versus tail identity during Planarian regeneration and homeostasis. *Science* **319,** 323–327 (2008).
237. Frey, E. & Kroy, K. Brownian motion: a paradigm of soft matter and biological physics. *Ann. Phys.* **14,** 20–50 (2005).
238. Van Kampen, N. G. *Stochastic Processes in Physics and Chemistry*. (North Holland, 1992).
239. Guptasarma, P. Does replication-induced transcription regulate synthesis of the myriad low copy number proteins of *Escherichia coli*? *Bioessays* **17,** 987–997 (1995).
240. Elowitz, M. B., Levine, A. J., Siggia, E. D. & Swain, P. S. Stochastic gene expression in a single cell. **297,** 1183–1187 (2002).
241. Kussell, E. & Leibler, S. Phenotypic diversity, population growth, and information in fluctuating environments. *Science* **309,** 2075–8 (2005).
242. Carter, N. J. & Cross, R. a. Mechanics of the kinesin step. *Nature* **435,** 308–12 (2005).
243. Dubuis, J. O., Tkacik, G., Wieschaus, E. F., Gregor, T. & Bialek, W. Positional information, in bits. *Proc. Natl. Acad. Sci. U.S.A.* **110,** 16301–16308 (2013).
244. Bialek, W. Physical limits to sensation and perception. *Ann Rev. Biophys. Biochem. Chem.* **16,** 455–78 (1987).
245. Fuortes, M. G. & S., Y. Probability of occurrence of discrete potential waves in the eye of Limulus. *J. Gen. Physiol.* **47,** 443–63 (1964).
246. Baylor, B. Y. D. a, Lamb, T. D. & Yau, K. Responses of retinal rods to single photons. *J. Physiol.* **288,** 613–634 (1979).
247. Nelson, P. C. Old and new results about single-photon sensitivity in human vision. *Phys. Biol.* **13,** 025001 (2016).
248. Menini, A., Picco, C. & Firestein, S. Quantal-like current fluctuations induced by odorants in olfactory receptor cells. *Nature* **373,** 435–437 (1995).
249. Strünker, T., Alvarez, L. & Kaupp, U. B. At the physical limit - chemosensation in sperm. *Curr. Opin. Neurobiol.* **34,** 110–116 (2015).
250. Bialek, W. & Setayeshgar, S. Physical limits to biochemical signaling. *Proc. Natl. Acad. Sci. U.S.A.* **102,** 10040–10045 (2005).
251. Govern, C. C. & Ten Wolde, P. R. Energy dissipation and noise correlations in biochemical sensing. *Phys. Rev. Lett.* **113,** 258102 (2014).
252. Finer, J. T., Simmons, R. M. & Spudich, J. A. Single myosin molecule mechanics: piconewton forces and nanometre steps. *Nature* **367,** 566 – 568 (1994).
253. Kubo, R. The fluctuation-dissipation theorem. *Rep. Prog. Phys.* **29,** 255 (1966).
254. Betz, T., Lenz, M., Joanny, J.-F. & Sykes, C. ATP-dependent mechanics of red blood cells. *Proc. Natl. Acad. Sci. U.S.A.* **106,** 15320–5 (2009).

255. Mizuno, D., Tardin, C., Schmidt, C. F. & Mackintosh, F. C. Nonequilibrium mechanics of active cytoskeletal networks. *Science* **315,** 370–373 (2007).
256. Brangwynne, C. P., Koenderink, G. H., MacKintosh, F. C. & Weitz, D. a. Nonequilibrium microtubule fluctuations in a model cytoskeleton. *Phys. Rev. Lett.* **100,** 118104 (2008).
257. Otten, M. *et al.* Local motion analysis reveals impact of the dynamic cytoskeleton on intracellular subdiffusion. *Biophys. J.* **102,** 758–67 (2012).
258. Martin, P., Hudspeth, A. J. & Jülicher, F. Comparison of a hair bundle's spontaneous oscillations with its response to mechanical stimulation reveals the underlying active process. *Proc. Natl. Acad. Sci. U.S.A.* **98,** 14380–14385 (2001).
259. Polin, M., Tuval, I., Drescher, K., Gollub, J. P. & Goldstein, R. E. *Chlamydomonas* swims with two 'gears' in a eukaryotic version of run-and-tumble. *Science* **325,** 487–490 (2009).
260. Drescher, K., Dunkel, J., Cisneros, L. H., Ganguly, S. & Goldstein, R. E. Fluid dynamics and noise in bacterial cell–cell and cell–surface scattering. *Proc. Natl. Acad. Sci. U.S.A.* **108,** 10940(6) (2011).
261. Endow, S. A. & Higuchi, H. A mutant of the motor protein kinesin that moves in both directions on microtubules. *Nature* **406,** 913–6 (2000).
262. Badoual, M., Jülicher, F. & Prost, J. Bidirectional cooperative motion of molecular motors. *Proc. Natl. Acad. Sci. U. S. A.* **99,** 6696–701 (2002).
263. Plaçais, P.-Y., Balland, M., Guérin, T., Joanny, J.-F. & Martin, P. Spontaneous oscillations of a minimal actomyosin system under elastic loading. *Phys. Rev. Lett.* **103,** 158102 (2009).
264. Pikovsky, A. *et al. Synchronization: A Universal Concept in Nonlinear Sciences*. *Cambridge Nonlinear Science Series 12* (Cambridge Univ. Press, 2003).
265. Adler, R. Locking phenomena in oscillators. *Proc. IRE* **34,** 351–357 (1946).
266. Stratonovich, R. L. *Topics in the Theory of Random Noise*. (Gordon & Breach, 1963).
267. Pourquié, O. The segmentation clock: converting embryonic time into spatial pattern. *Science* **301,** 328–330 (2003).
268. Strogatz, S. H., Abrams, D. M., McRobie, A., Eckhardt, B. & Ott, E. Theoretical mechanics: crowd synchrony on the Millennium Bridge. *Nature* **438,** 43–44 (2005).
269. Hanggi, P., Talkner, P. & Borkovec, M. Reaction-rate theory - 50 years after Kramers. *Rev. Mod. Phys.* **62,** 251–341 (1990).
270. Ringo, D. L. Flagellar motion and the fine structure of the flagellar apparatus in *Chlamydomonas*. *Cell* **33,** 543–571 (1967).
271. Leptos, K. C. *et al.* Antiphase synchronization in a flagellar-dominance mutant of Chlamydomonas. *Phys. Rev. Lett.* **111,** 158101 (2013).
272. Wan, K. Y., Leptos, K. C. & Goldstein, R. E. Lag, lock, sync, slip : The many 'phases' of coupled flagella. *J Roy Soc Interface* **11,** 20131160 (2014).
273. Friedrich, B. M. Hydrodynamic synchronization of flagellar oscillators. *EPJ Spec. Top. 'Microswimmers'* (editorial recommendation for acceptance) 16 pages (2016).
274. Kotar, J., Leoni, M., Bassetti, B., Lagomarsino, M. C. & Cicuta, P. Hydrodynamic synchronization of colloidal oscillators. *Proc. Natl. Acad. Sci. U.S.A.* **107,** 7669–73 (2010).
275. Bruot, N., Damet, L., Kotar, J., Cicuta, P. & Lagomarsino, M. Noise and synchronization of a single active colloid. *Phys. Rev. Lett.* **107,** 094101 (2011).
276. Bruot, N., Kotar, J., de Lillo, F., Cosentino Lagomarsino, M. & Cicuta, P. Driving potential and noise level determine the synchronization state of hydrodynamically coupled oscillators. *Phys. Rev. Lett.* **109,** 164103 (2012).
277. Di Leonardo, R. *et al.* Hydrodynamic synchronization of light driven microrotors. *Phys. Rev. Lett.* **109,** 034104 (2012).
278. Lhermerout, R., Bruot, N., Cicuta, G. M., Kotar, J. & Cicuta, P. Collective synchronization states in arrays of driven colloidal oscillators. *New J. Phys.* **14,** 105023 (2012).
279. Niedermayer, T., Eckhardt, B. & Lenz, P. Synchronization, phase locking, and metachronal wave formation in ciliary chains. *Chaos* **18,** 037128 (2008).
280. Uchida, N. & Golestanian, R. Generic conditions for hydrodynamic synchronization. *Phys. Rev. Lett.* **106,** 058104 (2011).
281. Golestanian, R., Yeomans, J. M. & Uchida, N. Hydrodynamic synchronization at low Reynolds number. *Soft Matter* **7,** 3074 (2011).
282. Theers, M. & Winkler, R. G. Synchronization of rigid microrotors by time-dependent hydrodynamic interactions. *Phys. Rev. E* **88,** 023012 (2013).
283. Friedrich, B. M. & Jülicher, F. Flagellar synchronization independent of hydrodynamic interactions. *Phys. Rev. Lett.* **109,** 138102 (2012).
284. Berg, H. C. & Purcell, E. M. Physics of chemoreception. *Biophys. J.* **20,** 193–219 (1977).
285. Berg, H. C. *Random Walks in Biology*. (Princeton Univ. Press, 1993).

286. Taylor, G. I. Diffusion by continous movements. *Proc. Roy. Soc. A* **20,** 196–212 (1920).
287. Friedrich, B. M. Search along persistent random walks. *Phys. Biol.* **5,** 026007(6) (2008).
288. Dusenbery, D. B. Minimum size limit for useful locomotion by free-swimming microbes. *Proc. Natl. Acad. Sci. U.S.A.* **94,** 10949–10954 (1997).
289. Tu, Y., Shimizu, T. S. & Berg, H. C. Modeling the chemotactic response of Escherichia coli to time-varying stimuli. *Proc. Natl. Acad. Sci. U. S. A.* **105,** 14855–60 (2008).
290. Kollmann, M., Løvdok, L., Bartholomé, K., Timmer, J. & Sourjik, V. Design principles of a bacterial signalling network. *Nature* **438,** 504–507 (2005).
291. Crenshaw, H. C. Helical orientation - A novel mechanism for the orientation of microorganisms. *Lect. Notes Biophys.* **89,** 361–386 (1990).
292. Levine, H., Kessler, D. A. & Rappel, W. Directional sensing in eukaryotic chemotaxis: A balanced inactivation model. *Proc. Natl. Acad. Sci. U.S.A.* **103,** 9761–9766 (2006).
293. Segall, J. E., Block, S. M. & Berg, H. C. Temporal comparisons in bacterial chemotaxis. *Proc. Natl. Acad. Sci. U.S.A.* **83,** 8987–8991 (1986).
294. Song, L. *et al.* Dictyostelium discoideum chemotaxis: threshold for directed motion. *Eur. J. Cell Biol.* **85,** 981–9 (2006).
295. Amselem, G., Theves, M., Bae, A., Beta, C. & Bodenschatz, E. Control parameter description of eukaryotic chemotaxis. *Phys. Rev. Lett.* **109,** 108103 (2012).
296. Miller, R. L. Sperm chemo-orientation in the metazoa. *Biol. Fertil.* **2,** 275–337 (1985).
297. Kaupp, U. B. *et al.* The signal flow and motor response controling chemotaxis of sea urchin sperm. *Nat. Cell Biol.* **5,** 109–117 (2003).
298. Kashikar, N. D. *et al.* Temporal sampling, resetting, and adaptation orchestrate gradient sensing in sperm. *J. Cell Biol.* **198,** 1075–91 (2012).
299. Riffell, J. A. & Krug, P. J. The ecological and evolutionary consequences of sperm chemoattraction. *Proc. Natl. Acad. Sci. U.S.A.* **101,** 4501–4506 (2004).
300. Stocker, R. Marine microbes see a sea of gradients. *Science* **338,** 628–633 (2012).
301. Kiørboe, T. & Jackson, G. A. Marine snow, organic solute plumes, and optimal chemosensory behavior of bacteria. *Limnol. Oceanogr.* **46,** 1309–1318 (2001).
302. Taylor, J. R. & Stocker, R. Trade-Offs of Chemotactic Foraging in Turbulent Water. *Science* **338,** 675–679 (2012).
303. Andrews, B. W., Yi, T.-M. & Iglesias, P. A. Optimal noise filtering in the chemotactic response of Escherichia coli. *PLoS Comp. Biol.* **2,** e154 (2006).
304. Celani, A. & Vergassola, M. Bacterial strategies for chemotaxis response. *Proc. Natl. Acad. Sci. U.S.A.* **107,** 1391–1396 (2010).
305. Aquino, G., Tweedy, L., Heinrich, D. & Endres, R. G. Memory improves precision of cell sensing in fluctuating environments. *Sci. Rep.* **4,** 5688 (2014).
306. Vergassola, M., Villermaux, E. & Shraiman, B. I. 'Infotaxis' as a strategy for searching without gradients. *Nature* **445,** 406–9 (2007).
307. Govern, C. C. & Wolde, P. R. Ten. Optimal resource allocation in cellular sensing systems. *Proc. Natl. Acad. Sci.* **111,** 17486–17491 (2014).

2 Selected publications: Cell motility and motility control

2.1 "Flagellar synchronization independent of hydrodynamic interactions"

Abstract. Inspired by the coordinated beating of the flagellar pair of the green algae *Chlamydomonas*, we study theoretically a simple, mirror-symmetric swimmer, which propels itself at low Reynolds number by a revolving motion of a pair of spheres. We show that perfect synchronization between these two driven spheres can occur due to the motion of the swimmer and local hydrodynamic friction forces. Hydrodynamic interactions, though crucial for net propulsion, contribute little to synchronization for this free-moving swimmer.

B. M. Friedrich, F. Jülicher: Flagellar synchronization independent of hydrodynamic interactions. *Phys. Rev. Lett.* **109**(13), 138102, 2012

DOI: https://doi.org/10.1103/PhysRevLett.109.138102

http://journals.aps.org/prl/abstract/10.1103/PhysRevLett.109.138102

2.2 "Cell body rocking is a dominant mechanism for flagellar synchronization in a swimming green alga"

Abstract. The unicellular green algae *Chlamydomonas* swims with two flagella, which can synchronize their beat. Synchronized beating is required to swim both fast and straight. A long-standing hypothesis proposes that synchronization of flagella results from hydrodynamic coupling, but the details are not understood. Here, we present realistic hydrodynamic computations and high-speed tracking experiments of swimming cells that show how a perturbation from the synchronized state causes rotational motion of the cell body. This rotation feeds back on the flagellar dynamics via hydrodynamic friction forces and rapidly restores the synchronized state in our theory. We calculate that this 'cell body rocking' provides the dominant contribution to synchronization in swimming cells, whereas direct hydrodynamic interactions between the flagella contribute negligibly. We experimentally confirmed the coupling between flagellar beating and cell body rocking predicted by our theory. We propose that the interplay of flagellar beating and hydrodynamic forces governs swimming and synchronization in *Chlamydomonas*.

V. F. Geyer, F. Jülicher, J. Howard, B. M. Friedrich: Cell body rocking is a dominant mechanism for flagellar synchronization in a swimming alga. *Proc. Natl. Acad. Sci. U.S.A.* **110**(45), 18058(6), 2013

DOI: 10.1073/pnas.1300895110

http://www.pnas.org/content/110/45/18058.abstract.html?etoc

2.3 “Active phase and amplitude fluctuations of the flagellar beat”

Abstract. The eukaryotic flagellum beats periodically, driven by the oscillatory dynamics of molecular motors, to propel cells and pump fluids. Small, but perceivable fluctuations in the beat of individual flagella have physiological implications for synchronization in collections of flagella as well as for hydrodynamic interactions between flagellated swimmers. Here, we characterize phase and amplitude fluctuations of flagellar bending waves using shape mode analysis and limit-cycle reconstruction. We report a quality factor of flagellar oscillations, $Q = 38.0 \pm 16.7$ (mean$\pm$s.e.). Our analysis shows that flagellar fluctuations are dominantly of active origin. Using a minimal model of collective motor oscillations, we demonstrate how the stochastic dynamics of individual motors can give rise to active small-number fluctuations in motor-cytoskeleton systems.

R. Ma, G. S. Klindt, I.-H. Riedel-Kruse, F. Jülicher, B. M. Friedrich: Active phase and amplitude fluctuations of flagellar beating. *Phys. Rev. Lett.* **113**(4), 048101, 2014

DOI: https://doi.org/10.1103/PhysRevLett.113.048101

https://journals.aps.org/prl/abstract/10.1103/PhysRevLett.113.048101

2.4 “Sperm navigation in 3D chemoattractant landscapes”

Abstract. Sperm require a sense of direction to locate the egg for fertilization. They follow gradients of chemical and physical cues provided by the egg or the oviduct. However, the principles underlying three-dimensional (3D) navigation in chemical landscapes are unknown. Here using holographic microscopy and optochemical techniques, we track sea urchin sperm navigating in 3D chemoattractant gradients. Sperm sense gradients on two timescales, which produces two different steering responses. A periodic component, resulting from the helical swimming, gradually aligns the helix towards the gradient. When incremental path corrections fail and sperm get off course, a sharp turning manoeuvre puts sperm back on track. Turning results from an ‘off’ Ca2+ response signifying a chemoattractant stimulation decrease and, thereby, a drop in cyclic GMP concentration and membrane voltage. These findings highlight the computational sophistication by which sperm sample gradients for deterministic klinotaxis. We provide a conceptual and technical framework for studying microswimmers in 3D chemical landscapes.

J. F. Jikeli*, L. Alvarez*, B. M. Friedrich*, L.G. Wilson*, R. Pascal, R. Colin, M. Pichlo, A. Rennhack, C. Brenker, U. B. Kaupp: Sperm navigation in 3D chemoattractant landscapes. *Nature Communications* **6**, 7985, 2015

* = these authors contributed equally

DOI: 10.1038/ncomms8985

http://www.nature.com/ncomms/2015/150817/ncomms8985/full/ncomms8985.html

3 Selected publications: Self-organized pattern formation in cells and tissues

3.1 "Sarcomeric pattern formation by actin cluster coalescence"

Abstract. Contractile function of striated muscle cells depends crucially on the almost crystalline order of actin and myosin filaments in myofibrils, but the physical mechanisms that lead to myofibril assembly remains ill-defined. Passive diffusive sorting of actin filaments into sarcomeric order is kinetically impossible, suggesting a pivotal role of active processes in sarcomeric pattern formation. Using a one-dimensional computational model of an initially unstriated actin bundle, we show that actin filament treadmilling in the presence of processive plus-end crosslinking provides a simple and robust mechanism for the polarity sorting of actin filaments as well as for the correct localization of myosin filaments. We propose that the coalescence of crosslinked actin clusters could be key for sarcomeric pattern formation. In our simulations, sarcomere spacing is set by filament length prompting tight length control already at early stages of pattern formation. The proposed mechanism could be generic and apply both to premyofibrils and nascent myofibrils in developing muscle cells as well as possibly to striated stress-fibers in non-muscle cells.

B. M. Friedrich, E. Fischer-Friedrich, N. S. Gov, S. A. Safran: Sarcomeric pattern formation by actin cluster coalescence. *PLoS Comp. Biol.* **8**(6), e1002544, 2012

DOI: https://doi.org/10.1371/journal.pcbi.1002544

http://journals.plos.org/ploscompbiol/article?id=10.1371/journal.pcbi.1002544

3.2 “Scaling and regeneration of self-organized patterns”

Abstract. Biological patterns generated during development and regeneration often scale with organism size. Some organisms e.g. flatworms can regenerate a re-scaled body plan from tissue fragments of varying sizes. Inspired by these examples, we introduce a generalization of Turing patterns that is self-organized and self-scaling. A feedback loop involving diffusing expander molecules regulates the reaction rates of a Turing system, thereby adjusting pattern length scales proportional to system size. Our model captures essential features of body plan regeneration in flatworms as observed in experiments.

S. Werner, T. Stückemann, M. Beirán Amigo, J. C. Rink, F. Jülicher, B. M. Friedrich: Scaling and regeneration of self-organized patterns. *Phys. Rev. Lett.* **114**(13), 138101, 2015

DOI: 10.1103/PhysRevLett.114.138101

http://journals.aps.org/prl/abstract/10.1103/PhysRevLett.114.138101

4 Contribution of the author in collaborative publications

The author is principal author of all publications presented in this thesis. He conceived the original idea for the projects in all-but-one cases. The only exception is publication 2.4: "Sperm navigation …", which represent a combination of experiment and theory on sperm chemotaxis, where the experimental part was initiated first. The theoretical part of this publication has been solely contributed by the author. Below, we list the specific contributions of the author for all publications presented in this thesis.

2.1: "Flagellar synchronization independent of hydrodynamic interactions"

- **contribution of author:** original conception of project, development of theoretical description, all analytic calculations, all stochastic simulations, manuscript preparation including all figures

2.2: "Cell body rocking is a dominant mechanism for flagellar synchronization in a swimming alga"

- **contribution of author:** original conception of project, management of theory-experiment collaboration, development of theoretical description, all analytic calculations, all hydrodynamic computations, development of image analysis software, data analysis, manuscript preparation including all figures

2.3: "Active phase and amplitude fluctuations of the flagellar beat"

- **contribution of author:** original conception of project, development of data analysis method for limit cycle reconstruction, data analysis, development of theoretical description, development of analytical theory together with Rui Ma, manuscript preparation including all figures

2.4: "Sperm navigation in 3D chemical landscapes"

- **contribution of author:** development of theoretical description, hydrodynamic computations of chiral flagellar swimming, algorithm development for data analysis (track smoothing, helix fitting, chemoattractant diffusion, time series analysis), comparison of theory and experiment, writing of theoretical part of manuscript, contribution to introduction and discussion, prepared figure panels (Fig. 1c, Fig. 2, Fig. 3c, Fig. 4c, Fig. 4f, Fig. 6, Fig. S3b Fig. S3f, Fig. S4)

3.1: "Sarcomeric pattern formation by actin cluster coalescence"

- **contribution of author:** original conception of project, development of theoretical description, all stochastic simulations, all analytic calculations, manuscript preparation including all figures

3.2: "Scaling and regeneration of self-organized patterns"

- **contribution of author:** original conception of project, development of initial theoretical description, close supervision of PhD student Steffen Werner who formulated the final description, coordination of the project, manuscript preparation and conception of all figures

5 Eidesstattliche Versicherung

Hiermit versichere ich an Eides statt, dass ich die vorliegende Arbeit ohne unzulässige Hilfe Dritter und ohne Benutzung anderer als der angegebenen Hilfsmittel angefertigt habe. Die aus fremden Quellen direkt oder indirekt übernommenen Gedanken sind als solche kenntlich gemacht.

Die der Habilitationsschrift zugrunde liegenden Publikationen wurden in Zusammenarbeit mit den genannten Autoren angefertigt. Dabei ging jeweils die initiale Idee auf mich zurück. Die Projekte wurden durch mich koordiniert und die Publikationen von mir geschrieben. Die einzige Ausnahme bildet Publikation 2.4 zur Spermien-Chemotaxis, welche Experiment und Theorie kombiniert. Hier beschränkt sich mein Beitrag auf den Theorieteil, d.h. die Entwicklung der theoretischen Beschreibung, alle numerischen Simulationen, sowie die quantitative Auswertung der experimentellen Daten. Eine detaillierte Auflistung meines Beitrags zu den Publikationen findet sich auf Seite 63 dieser Habilitationsschrift.

Diese Arbeit wurde bisher weder im Inland noch im Ausland in gleicher oder ähnlicher Form einer anderen Prüfungsbehörde vorgelegt. Ich habe bisher kein Habilitationsgesuch an anderen Hochschulen eingereicht. Ein Führungszeugnis gemäß § 30 Abs. 5 Bundeszentralregistergesetz wurde bei der zuständigen Meldebehörde beantragt und wird an die Fakultät übersendet.

Dresden, den 23.05.2016

Benjamin M. Friedrich

6 Appendix: Reprints of publications

Publication 2.1: "Flagellar synchronization independent of hydrodynamic interactions"
Published in:
Phys. Rev. Lett. **109**(13), p. 138102, 2012;
5 pages, 4 figures.

Publication 2.2: "Cell body rocking is a dominant mechanism for flagellar synchronization in a swimming green alga"
Published in:
Proc. Natl. Acad. Sci. U.S.A. **110**(45), 18058(6). 2013;
6 pages, 5 figures, 12 pages of supporting material.

Publication 2.3: "Active phase and amplitude fluctuations of the flagellar beat"
Published in:
Phys. Rev. Lett. **113**(4), 048101, 2014;
5 pages, 3 figures, 5 pages of supporting material.

Publication 2.4: "Sperm navigation in 3D chemoattractant landscapes"
Published in:
Nature Communications **6**, 7985, 2015;
10 pages, 6 figures, 14 pages of supporting material.

Publication 3.1: "Sarcomeric pattern formation by actin cluster coalescence"
Published in:
PLoS Comp. Biol. **8**(6), e1002544, 2012;
10 pages, 6 figures, 11 pages of supporting material.

Publication 3.2: "Scaling and regeneration of self-organized patterns"
Published in:
Phys. Rev. Lett. **114**(13), 138101, 2015;
5 pages, 3 figures.

Flagellar Synchronization Independent of Hydrodynamic Interactions

Benjamin M. Friedrich* and Frank Jülicher

Max Planck Institute for the Physics of Complex Systems, Nöthnitzer Straße 38, 01187 Dresden, Germany

(Received 7 June 2012; published 24 September 2012)

Inspired by the coordinated beating of the flagellar pair of the green algae *Chlamydomonas*, we study theoretically a simple, mirror-symmetric swimmer, which propels itself at low Reynolds number by a revolving motion of a pair of spheres. We show that perfect synchronization between these two driven spheres can occur due to the motion of the swimmer and local hydrodynamic friction forces. Hydrodynamic interactions, though crucial for net propulsion, contribute little to synchronization for this free-moving swimmer.

DOI: 10.1103/PhysRevLett.109.138102 PACS numbers: 87.16.Qp, 05.45.Xt, 47.63.−b

Eukaryotic flagella are whiplike cell appendages that can bend actively, propel microorganisms at low Reynolds numbers, and pump fluids, e.g., mucus in our airways [1]. Their active bending waves are generated by a highly conserved cytoskeletal core with cylindrically arranged microtubules intercalated by molecular motors [2] that convert chemical energy into work and heat. Mechanical interactions are thought to underlie the coordinated beating of several flagella as observed in pairs of sperm cells [3] or in ciliary arrays, where hundreds of short flagella beat in synchrony as metachronal waves [4]. Recently, the biflagellate green alga *Chlamydomonas* has emerged as an experimental model system for flagellar synchronization [5–7]. A *Chlamydomonas* cell swims forward by the approximately planar and mirror-symmetric bending waves of its two flagella, thus resembling a breast swimmer [8]; see Fig. 1(a). The synchronous beating of the two flagella is important for swimming along a straight path [9]. Free swimming cells often exhibit synchronized flagellar beating [8,9], raising the question of the underlying synchronization mechanism. For flagella attached to a solid substrate, long-range hydrodynamic interactions can induce flagellar synchronization [10–16]. Synchronization of the flagella of a moving swimmer, however, shows different features: Here, we show that flagellar synchronization can occur as a result of local hydrodynamic friction forces, even in the absence of hydrodynamic interactions.

A model swimmer for biflagellar synchronization.— Inspired by *Chlamydomonas* swimming, we propose a model swimmer of maximal simplicity that retains its basic symmetries. The swimmer consists of three spheres of equal radius a and respective positions $\mathbf{r}_j = (x_j, y_j, 0)$ attached to a planar and mirror-symmetric scaffold; see Fig. 1(b). The swimmer is immersed in a viscous fluid of viscosity η and the swimmer's scaffold is frictionless. The sphere located at $\mathbf{r}_3$ mimics a cell body and defines a material frame of the swimmer with orthonormal vectors $\mathbf{e}_1 = (\cos\alpha_3, \sin\alpha_3, 0)$, $\mathbf{e}_3 = (0, 0, 1)$, and $\mathbf{e}_2 = \mathbf{e}_3 \times \mathbf{e}_1$, where the angular variable α_3 characterizes rotations of the swimmer (around the z axis) with respect to the (x, y, z) laboratory frame; see Fig. 1(b).

The first and the second sphere move along circular orbits of radius R, $\mathbf{r}_i = \mathbf{s}_i + R(-\sin\varphi_i \mathbf{e}_1 + \cos\varphi_i \mathbf{e}_2)$, $i = 1, 2$, being connected by frictionless lever arms to joints located at the corners $\mathbf{s}_i = \mathbf{r}_3 + l[(-1)^i \mathbf{e}_1 + \mathbf{e}_2]$ of an isosceles triangle; see Fig. 1(b). Thus, l sets the size of the swimmer. The orbits are parametrized by respective phase angles φ_i, $i = 1, 2$ such that $\lfloor(\varphi_i(t) - \varphi_i(0))/(2\pi)\rfloor$ denotes the number of full rotations of the ith sphere since time $t = 0$ with respect to the material frame of the swimmer. Similarly, $\lfloor(\alpha_i(t) - \alpha_i(0))/(2\pi)\rfloor$ with $\alpha_i = \alpha_3 + \varphi_i$ denotes the number of rotations with respect to the laboratory frame. Below, the dynamics of the phase angles φ_i is given in terms of active driving torques; the cases $\dot{\varphi}_i < 0$ and $\dot{\varphi}_i > 0$ correspond to either a clockwise or counterclockwise revolution of the driven spheres (viewed along $-\mathbf{e}_3$), respectively. The revolving motion of these driven spheres provides a simplified representation of the periodic bending waves of the two slender flagella of *Chlamydomonas* [10,11], for which each point on a flagellum follows a

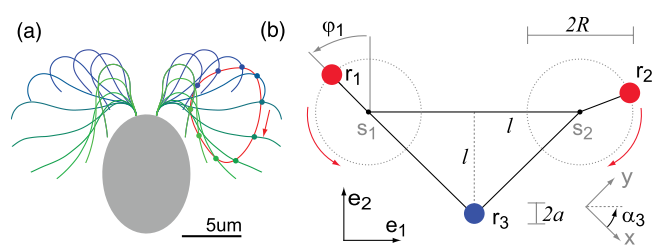

FIG. 1 (color online). (a) Simplified flagellar beat of *Chlamydomonas* showing flagellar shapes at equidistant times representing a full beat cycle ($T \approx 15$ ms), adapted from [34]. The flagellar bending waves are approximately planar and mirror-symmetric. Each point on a flagellum moves on a periodic orbit with respect to a material frame of the cell body. (b) The idealized model swimmer consists of three equal spheres connected by a frictionless scaffold. The first and second sphere (located at $\mathbf{r}_1$ and $\mathbf{r}_2$) can move along a circular trajectory as indicated, being driven by internally generated active torques. (The arrows correspond to the case $\omega_0 > 0$).

periodic orbit in a material frame of the cell body; see Fig. 1(a).

We neglect inertial effects, which implies that fluid flow is governed by the Stokes equation of zero Reynolds number hydrodynamics [1,17]. We consider the hydrodynamic friction force $\mathbf{F}_j$ and torque $\mathbf{T}_j$ (defined with respect to $\mathbf{r}_3$) exerted by the jth sphere on the viscous fluid during motion of the swimmer; $\mathbf{T}'_j = \mathbf{T}_j - \mathbf{F}_j \times (\mathbf{r}_j - \mathbf{r}_3)$ denote torques with respect to $\mathbf{r}_j$. For free swimming, force and torque balance holds, $\mathbf{F}_{\rm ext} = 0$ and $\mathbf{T}_{\rm ext} = 0$ with $\mathbf{F}_{\rm ext} = \mathbf{F}_1 + \mathbf{F}_2 + \mathbf{F}_3$, $\mathbf{T}_{\rm ext} = \mathbf{T}_1 + \mathbf{T}_2 + \mathbf{T}_3$. The linearity of the Stokes equation implies a linear relationship between the generalized velocity vector for planar motion of the three spheres, $\dot{\mathbf{q}}_0$ with $\mathbf{q}_0 = (x_1, y_1, \alpha_1, \ldots, x_3, y_3, \alpha_3)^T$, and the nonzero hydrodynamic friction force and torque components [17],

$$(F_{1x}, F_{1y}, T'_{1z}, \ldots, F_{3x}, F_{3y}, T'_{3z})^T = \Gamma_0 \dot{\mathbf{q}}_0. \tag{1}$$

The symmetric 9×9 hydrodynamic friction matrix Γ_0 can be computed to arbitrary precision in $a/|\mathbf{r}_j - \mathbf{r}_k|$ [18]; in the limit of large separation between the spheres, the friction matrix would be diagonal, $\Gamma_{0,ij} = \gamma_j \delta_{ij}$, with $\gamma_j = \gamma_{\rm rot}$ for $j = 3, 6, 9$ and $\gamma_j = \gamma$ otherwise. Here, $\gamma = 6\pi\eta a$ and $\gamma_{\rm rot} = 8\pi\eta a^3$ denote the translational and rotational friction coefficients of a single sphere of radius a, respectively. In general, the flow field induced by the motion of one sphere will exert forces on the other spheres, thus giving rise to nonzero, off-diagonal components of Γ_0, which characterize hydrodynamic interactions between the spheres. Below, we use the Rotne-Prager-Yamakawa approximation for $\Gamma_0 = \Gamma_0(q_0)$, which generalizes the Oseen tensor and applies to both translational and rotational motion [18].

The swimmer is characterized by 5 degrees of freedom, represented by a vector of generalized coordinates, $\mathbf{q} = (x_3, y_3, \alpha_3, \varphi_1, \varphi_2)$, if its internal constraints are taken into account. In the following, we use the framework of Lagrangian mechanics of dissipative systems [19] to describe the dynamics of our swimmer. First, $\dot{\mathbf{q}}_0 = L\dot{\mathbf{q}}$, with a 9×5 transformation matrix $L_{ij} = \partial q_{0i}/\partial q_j$. The rate $\mathcal{R}_h = \dot{\mathbf{q}}_0{}^T \Gamma_0 \dot{\mathbf{q}}_0$ of hydrodynamic energy dissipation during swimming can be equivalently written as $\mathcal{R}_h = \dot{\mathbf{q}}^T \Gamma_h \dot{\mathbf{q}}$ with the 5×5 friction matrix $\Gamma_h = L^T \Gamma_0 L$. The energy for active swimming is provided by a fuel reservoir, which we take for simplicity as infinite with internal energy $U = -m_1\varphi_1 - m_2\varphi_2$. Here, m_1 and m_2 denote active driving torques that are assumed to be independent of the present phase φ_i (but see [16]). The potential U defines generalized potential forces $Q_j = -\partial U/\partial q_j$, $j = 1, \ldots, 5$. Further, we introduce the Rayleigh dissipation function $\mathcal{R} = \mathcal{R}_h + \mathcal{R}_\kappa$ that sets the rate at which the energy reservoir is depleted, $-\dot{U} = \mathcal{R}$. Here, $\mathcal{R}_\kappa = \kappa(\dot{\varphi}_1^2 + \dot{\varphi}_2^2)$ denotes a rate of internal dissipation associated with the actuation of the two driven spheres. For notational convenience, $\mathcal{R}_\kappa = \dot{\mathbf{q}}^T \Gamma_\kappa \dot{\mathbf{q}}$ with $\Gamma_{\kappa,ij} = 0$ except $\Gamma_{\kappa,44} = \Gamma_{\kappa,55} = \kappa$. The generalized friction forces $P_i = (1/2)\partial\mathcal{R}/\partial\dot{q}_i$ are linear in $\dot{\mathbf{q}}$, $P_i = \Gamma_{ij}\dot{q}_j$ with $\Gamma = \Gamma_h + \Gamma_\kappa$. Neglecting inertial forces and assuming that no external forces act on the swimmer, we find a balance of generalized potential forces and generalized friction forces $Q_j = P_j$, $j = 1, \ldots, 5$. For example, the equation for $j = 4$, corresponding to $q_4 = \varphi_1$, represents a torque balance between a hydrodynamic friction torque, $(1/2)\partial\mathcal{R}_h/\partial\dot{\varphi}_1 = \mathbf{F}_1 \cdot (\partial\mathbf{r}_1/\partial\varphi_1) + T'_{1z}$, and a net motor torque $m_1 - \kappa\dot{\varphi}_1$ provided by active driving. This motor torque obeys a linear torque-velocity relation with stall torque m_1, similar to the net driving force used in [10]. An analogous statement holds for the second sphere. We finally obtain an equation of motion of the swimmer [20],

$$\dot{\mathbf{q}} = \Gamma^{-1}(0, 0, 0, m_1, m_2)^T. \tag{2}$$

We first discuss the case of exactly opposite driving torques $m_1 = -m_2$, which results in a counterrotation of sphere 1 and sphere 2 [Fig. 1(b)], similar to the mirror-symmetric beat patterns of the two flagella of *Chlamydomonas* [Fig. 1(a)]. The angular frequency $\omega_0 = m_1/\kappa$ sets an (inverse) time scale of motion. If $\omega_0 > 0$, the revolution of the first sphere is counterclockwise and clockwise for the second. The two cases $\omega_0 > 0$ and $\omega_0 < 0$ are mapped onto each other by time reversal.

Net propulsion due to hydrodynamic interactions.—For $m_1 = -m_2$, there exists an orbit with perfect in-phase dynamics characterized by $\delta = 0$, where $\delta = \varphi_1 + \varphi_2$. Below, we show that this orbit is stable for $\omega_0 < 0$, but unstable for $\omega_0 > 0$. If initially $\alpha_3(t = 0) = 0$, the swimmer will move parallel to the y axis in an oscillatory manner: In the limit of small spheres and small circular orbits, $a \ll l$, $R \ll l$, we find to leading order $\dot{y} = (2/3)R\omega_0 \sin\varphi_1 + \mathcal{O}(\varepsilon^2)$ with $\dot{\varphi}_1 = \omega_0 + \mathcal{O}(\varepsilon^3)$. Here, we introduced the small expansion parameter $\varepsilon = a/l$ and assume R/a to be of order unity. In this limit, internal dissipation dominates over hydrodynamic dissipation, $\kappa \gg \gamma R^2 + \gamma_{\rm rot}$. Net propulsion is a higher-order effect [21,22] and the time-averaged velocity reads

$$\langle\dot{y}\rangle = -a\omega_0\Theta(a/l)^2 + \mathcal{O}(\varepsilon^4), \tag{3}$$

with $\Theta = [(2\sqrt{2} - 1)(R/a)^2 - 4(1 + \sqrt{2})]/24$. Note that the swimmer can move either forward or backward depending on the value of R/a and the sign of ω_0. For asynchronous beating with $\delta = \varphi_1 + \varphi_2 \neq 0$, α_3 oscillates and the swimmer wiggles along a curved path.

If hydrodynamic interactions were absent, i.e. $\Gamma_{0,ij} = \gamma_j\delta_{ij}$, the center of reaction $\mathbf{r}_c = \sum_j \mathbf{r}_j/3$ of the swimmer could not move since $3\gamma\dot{\mathbf{r}}_c = \mathbf{F}_{\rm ext} = 0$, and net propulsion would be zero. This is a well-known feature of hydrodynamics at zero Reynolds number. Partial screening of hydrodynamic interactions can occur, e.g., for swimming close to a planar substrate.

A system of coupled phase oscillators.—The phase velocities $\dot{\varphi}_1$ and $\dot{\varphi}_2$ cannot depend on the momentary

values of x_3, y_3, α_3, as the phase variables are invariant under a change of laboratory frame, but the position and orientation variables are not. Indeed, one can eliminate the latter from Eq. (2) and obtain a dynamical system for φ_1 and φ_2 in the form of two coupled phase oscillators,

$$\kappa\dot{\varphi}_i = m_i + \varepsilon^3 h_{i1}(\varphi_1, \varphi_2)m_1 + \varepsilon^3 h_{i2}(\varphi_1, \varphi_2)m_2, \quad i = 1, 2. \tag{4}$$

Here the coupling functions h_{ij} depend only on $[\varphi_i] = \varphi_i \bmod 2\pi$ and can be computed from the friction matrix Γ. Importantly, the h_{ij} implicitly account for the motion of the swimmer and imposing constraints on the motion would change these functions.

Synchronization of counterrotating spheres.—For opposite driving torques, $m_1 = -m_2 = \omega_0\kappa$, we find two limit cycles of the phase dynamics characterized by $\delta = 0$ and $\delta = \pi + \mathcal{O}(\varepsilon^3)$, respectively, where $\delta = \varphi_1 + \varphi_2$. The first limit cycle corresponds to perfect in-phase dynamics as considered in the paragraph on net propulsion and is a global attractor for $\omega_0 < 0$, but unstable for $\omega_0 > 0$; see Fig. 3(b). Limit cycles of the (φ_1, φ_2) phase dynamics correspond to fixed points of a Poincaré return map $\delta_n \to \delta_{n+1} = \delta_n + \Lambda(\delta_n)$ that tracks $\delta_n = \delta(t_n)$ at discrete times t_n that mark the completion of n full revolutions of the first sphere, $\varphi_1(t_n) = 2\pi n \mathrm{sgn}(\omega_0)$. The solid curve in Fig. 2(a) shows a numerical solution for $\Lambda(\delta)$ as a function of initial phase sum $\delta = \delta_0$. By symmetry, $\Lambda(0) = 0$, which corresponds to the limit cycle of in-phase synchronization with $\delta = 0$. This limit cycle will be stable if

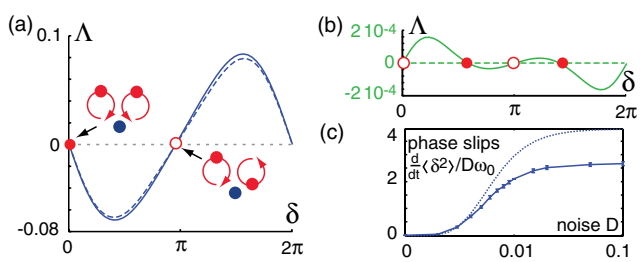

FIG. 2 (color online). (a) Phase synchronization behavior of our model swimmer (here for $m_1 = -m_2 < 0$) can be read off from a Poincaré return map $\Lambda = \delta(T) - \delta(0)$ that tracks the change of the phase sum $\delta = \varphi_1 + \varphi_2$ after a full revolution of the first sphere as function of initial $\delta = \delta(t = 0)$. Fixed points $\Lambda = 0$ correspond to limit cycles of the (φ_1, φ_2)-phase dynamics; see Fig. 3(b1). For the dashed and solid curve, hydrodynamic interactions were neglected or accounted for, respectively. (b) Constraining translation and rotation of the swimmer by clamping the third sphere changes its synchronization behavior completely. (c) In the presence of fluctuations, the phase dynamics of the free swimmer exhibits stochastic phase slips that occur at a frequency $(2\pi)^{-2}d\langle\delta^2\rangle/dt$; shown is $d\langle\delta^2\rangle/dt$ normalized by $D\omega_0$ (solid curve), as well as the analytical result [25] $d\langle\delta^2\rangle/dt \approx 4D\omega_0 I_0^{-2}[\lambda/(4\pi D)]$ for the approximate dynamics given by Eq. (6), (dotted curve). Parameters: $a/l = 0.1$, $R/a = 5$, $\kappa = \eta l^3$.

$\lambda = -d\Lambda/d\delta_{|\delta=0}$ is positive. In the limit of small spheres and small circular orbits, $\Lambda(\delta) = -\lambda \sin\delta + \mathcal{O}(\varepsilon^6)$ with

$$\lambda = -\mathrm{sgn}(\omega_0)3\pi\gamma R^4/(16\kappa l^2) + \mathcal{O}(\varepsilon^6). \tag{5}$$

Thus, in-phase synchronization with $\delta = 0$ is stable for $\omega_0 < 0$ and perturbations decay as $\lim_{n\to\infty}\delta_{n+1}/\delta_n = 1 - \lambda$.

Remarkably, if hydrodynamic interactions are neglected, $\Lambda(\delta)$ does not change significantly; see Fig. 2(a) (dashed curve). In fact, hydrodynamic interactions contribute to $\Lambda(\delta)$ only to higher order as $\mathcal{O}(\varepsilon^6)$. This implies that hydrodynamic interactions have only a marginal effect for the phase synchronization of our model swimmer. Rather, local hydrodynamic friction forces that arise from the motion of the swimmer dominate synchronization: If one driven sphere is ahead of the other, this asynchronous beating results in a rotation of the whole swimmer, accompanied by hydrodynamic friction forces acting on the spheres.

In the presence of constraining forces that prevent the swimmer from translating and rotating, the coupling functions h_{ij} in Eq. (4) change, resulting in weak synchronization toward novel limit cycles; see Fig. 2(b). In this case, synchronization is due to hydrodynamic interactions only.

For a microscopic oscillator such as a beating flagellum powered by molecular motors, noise is prevalent and may counteract synchronization. As a simple model for motor fluctuations, we now consider fluctuating driving torques, $m_1 = k\omega_0 + \xi_1$ and $m_2 = -k\omega_0(1 + \upsilon) + \xi_2$, $\langle\xi_i\rangle = 0$, together with a detuning of driving torques, υ. We assume a noise correlation time short compared to $T = 2\pi/|\omega_0|$, and model ξ_i as Gaussian white noise with $\langle\xi_i(t)\xi_j(t')\rangle = 2D\omega_0\kappa^2\delta_{ij}\delta(t - t')$, where D denotes a dimensionless noise strength. Equation (4) thus becomes a stochastic equation with multiplicative noise (for which Stratonovich interpretation is to be used). For weak noise with $D \ll 1$, the behavior of $\delta = \varphi_1 + \varphi_2$, averaged over cycles of the fast variable $\varphi_1 \approx \omega_0 t$, is to a good approximation [23] given by the prototypical Adler equation [24–26],

$$d\delta/dt \approx \upsilon\omega_0 - (\lambda/T)\sin\delta + \xi, \tag{6}$$

where ξ denotes Gaussian white noise with $\langle\xi(t)\xi(t')\rangle = 4D\omega_0\delta(t - t')$. Equation (6) describes a Brownian particle with position δ that diffuses in a tilted washboard potential. For υ, $D \ll |\lambda|$, δ fluctuates within one potential well (corresponding to transient synchronization), with occasional phase slips from one well to the next. For $\upsilon = 0$, the frequency $(2\pi)^{-2}d\langle\delta^2\rangle/dt$ of these phase slips scales with noise strength D for $D \gg |\lambda|$, but is suppressed for $D \ll |\lambda|$ [25]; see Fig. 2(c). In the case of torque detuning, $\upsilon \neq 0$, phase locking can occur as discussed next.

In the general case of arbitrary driving torques m_1 and m_2 (and no noise), phase locking between φ_1 and φ_2 can occur, i.e. $n_2\varphi_1 - n_1\varphi_2$ remains bounded for some choice of integers n_1, n_2. Figure 3(a) shows parameter regions

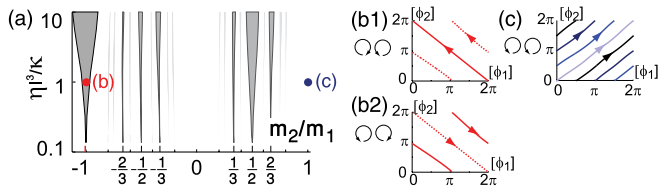

FIG. 3 (color online). (a) Depending on the ratio of the active driving torques m_1 and m_2, phase locking of the phase variables φ_1 and φ_2 describing our model swimmer can occur giving rise to a distinct pattern of Arnold tongues. (b) As specific example, a limit cycle with $\delta = \varphi_1 + \varphi_2 = 0$ is globally attractive for opposite torques with $m_1 = -m_2 < 0$ (b1), but repulsive for $m_1 = -m_2 > 0$ (b2). (c) For equal torques $m_1 = m_2$, the (φ_1, φ_2) phase space is foliated by neutrally stable orbits. Parameters: $a/l = 0.1$, $R/a = 5$, $\kappa = \eta l^3$.

(called Arnold tongues [26]) for which phase locking occurs.

The case of corotating spheres with $m_1 = m_2$ is special in the sense that the dynamics becomes reversible: The mirror operation $(\varphi_1, \varphi_2) \rightarrow (-\varphi_2, -\varphi_1)$ maps each orbit onto itself, but reverses the time arrow. The (φ_1, φ_2) phase space is foliated by neutrally stable orbits; see Fig. 3(c). Hence, for identical driving torques, no specific phase difference is selected. In the presence of a small mismatch υ in driving torque, $m_2 = m_1(1 + \upsilon)$ with $|\upsilon| \ll 1$, we find $\Lambda(\delta) = 2\pi\upsilon + \mathcal{O}(\upsilon\varepsilon^3) \bmod 2\pi$, which rules out the possibility of 2π-periodic orbits for $\upsilon \neq 0$ and therefore synchronization cannot occur in this case.

Generally, symmetries dictate synchronization behavior [27]. For two interacting oscillators, time reversal changes an attractor of their phase dynamics such as a synchronized state into a repeller. If the time-reversed system is equivalent to a mirror image of itself, stable synchronization can therefore not occur [27]. This is exemplified by our swimmer with corotating spheres ($m_1 = m_2$); see Fig. 3(c). Our swimmer with counterrotating spheres ($m_1 = -m_2$) is, after a time reversal, not equivalent to its mirror image. Correspondingly, there exist limit cycles with synchronized dynamics in this case, and their stability reverses under time reversal; see Fig. 3(b). Note that in the absence of the third sphere, time reversal would be equivalent to a reflection at the plane that contains both rotation axes and synchronization would be lost for our model swimmer with its rigid scaffold. Previous research demonstrated that elasticity of the rotating objects introduces additional degrees of freedom that can break symmetries and thus stabilize synchronization [11,12]. However, reversibility may also be broken without evoking elasticity as in the case of our three-sphere swimmer.

A realistic flagellar beat.—The conceptual framework of our model swimmer can be extended in a straightforward manner to any mirror-symmetric microswimmer whose swimming stroke is characterized by two phase angles φ_1 and φ_2. As an example, consider the idealized flagellar beat in Fig. 1(a): During a beat cycle, the centerline $\mathbf{r}_i$ of

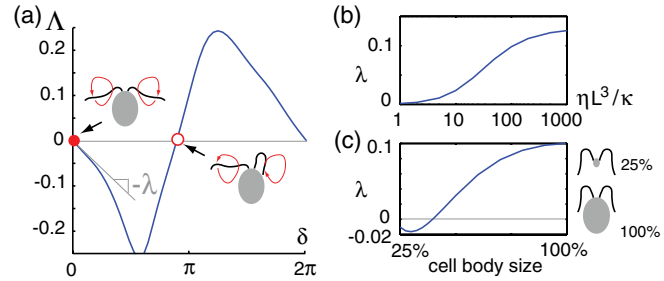

FIG. 4 (color online). Flagellar synchronization of *Chlamydomonas* computed for the beat pattern from Fig. 1(a) using Eq. (7) and resistive force theory. (a) The Poincaré return map $\Lambda(\delta)$ [defined analogous to that of Fig. 2(a)] shows that in-phase flagellar beating with $\delta = 0$ is stable with respect to perturbations. (b),(c) The synchronization parameter $\lambda = -d\Lambda/d\delta_{|\delta=0}$ depends on the ratio of hydrodynamic dissipation and internal dissipation (b) as well as on the size of the cell body (c). Parameters (unless indicated otherwise): flagellar length, $L = 12\ \mu$m; semiaxes of spheroidal cell body 3.7 μm, 5 μm [34]; resistive force coefficients, $\zeta_\parallel = 2\pi\eta/[\ln(2L/r) - 3/2]$, $\zeta_\perp = 4\pi\eta/[\ln(2L/r) - 3/2]$ [29] with flagellar radius $r = 0.1\ \mu$m [2], $\eta L^3/\kappa = 100$.

each of the two flagella can be expressed as a function of arclength s, $0 \leq s \leq L$, and phase angles φ_i, $i = 1, 2$, with $\dot{\varphi}_1 > 0$ and $\dot{\varphi}_2 < 0$ that characterize the phase of the beat cycle: With respect to a material frame $(\mathbf{r}_3; \mathbf{e}_1, \mathbf{e}_2, \mathbf{e}_3)$ of the cell body, $\mathbf{r}_i(s, \varphi_i) = \mathbf{r}_3 + c_{i1}(s, \varphi_i)\mathbf{e}_1 + c_{i2}(s, \varphi_i)\mathbf{e}_2$, $i = 1, 2$. By mirror symmetry of the two flagella, $c_{1j}(s, \varphi) = (-1)^j c_{2j}(s, -\varphi)$. We make the simplifying assumption that hydrodynamic forces do not alter the sequence of flagellar shapes (i.e. the shape functions c_{ij}), but only affect the phase speeds $\dot{\varphi}_i$.

The force balance equations for the dynamics of the three-sphere swimmer generalize to the case of a realistic flagellar beat; the torque balance corresponding to φ_i now reads [28]

$$\int_0^L ds \mathbf{f}_i(s) \cdot \partial \mathbf{r}_i(s)/\partial \varphi_i = m_i - \kappa \dot{\varphi}_i, \qquad i = 1, 2. \tag{7}$$

To compute the density $\mathbf{f}_i(s)$ of hydrodynamic friction forces along the flagellar length as a function of φ_i and $\dot{\varphi}_i$, we employ simple resistive force theory [29–32], while the cell body is approximated by a drag center equivalent to a spheroid.

Resistive force theory accounts for short-range hydrodynamic effects along a single flagellum by assuming effective anisotropic friction coefficients. This is crucial for net propulsion. However, hydrodynamic interactions between the two flagella, or with the cell body are not accounted for. Despite these approximations, we compute realistic, saltatory forward swimming for in-phase flagellar beating with a net swimming speed of 0.66 μm/cycle. As a main result, perfect flagellar synchronization with $\delta = 0$ is stable; see Fig. 4(a). Of note, the synchronization parameter λ has different sign in the case of the realistic

flagellar beat and that of the simple three-sphere swimmer with $m_1 = -m_2 > 0$; this can be related to geometric factors such as cell body size; see Fig. 4(c).

Discussion.—Using a minimal model, we have demonstrated that synchronization can occur between the two flagella of a free-moving swimmer due to the motion of the swimmer itself, independent of hydrodynamic interactions between the flagella. Importantly, the synchronization behavior changes fundamentally if the swimmer is restrained from translating and rotating. Local hydrodynamic friction forces couple the flagellar oscillators via movements of the swimmer, even in the absence of hydrodynamic interactions. Coupling of oscillators by swimmer movements can be strongly influenced by externally imposed constraints, which typically exist in experiments. For our model swimmer, synchronization of the flagellar phases attenuates if the swimmer is restrained from translating and rotating. In *Chlamydomonas*, perfect in-phase synchronization of its two flagella was reported also for cells held in a micropipette [5–7], and even for isolated flagellar pairs detached from the cell body [33]. Hydrodynamic interactions between the two flagella and flexibility of the flagellar beat, as proposed by others [10,11], may contribute to synchronization. We anticipate that synchronization depends sensitively on elastic properties of the flagellar base.

We thank J. Baumgart, E. Fischer-Friedrich, V. Geyer, J. Howard, R. Ketzmerick, L. Morelli, and A. Vilfan for stimulating discussions.

Note added in proof.—After submission of this Letter, we learned from R. Bennett and R. Golestanian that they have independently developed a similar three-sphere model for *Chlamydomonas* [35].

*ben@pks.mpg.de

[1] E. Lauga and T. R. Powers, Rep. Prog. Phys. **72**, 096601 (2009).
[2] B. Alberts, D. Bray, J. Lewis, M. Raff, K. Roberts, and J. D. Watson, *Molecular Biology of the Cell* (Garland Science, New York, 2002), 4th ed.
[3] D. M. Woolley, R. F. Crockett, W. D. I. Groom, and S. G. Revell, J. Exp. Biol. **212**, 2215 (2009).
[4] M. J. Sanderson and M. A. Sleigh, J. Cell Sci. **47**, 331 (1981).
[5] U. Rüffer and W. Nultsch, Cell Motil. Cytoskeleton **41**, 297 (1998).
[6] R. E. Goldstein, M. Polin, and I. Tuval, Phys. Rev. Lett. **103**, 168103 (2009).
[7] R. E. Goldstein, M. Polin, and I. Tuval, Phys. Rev. Lett. **107**, 1 (2011).
[8] U. Rüffer and W. Nultsch, Cell Motil. **5**, 251 (1985).
[9] M. Polin, I. Tuval, K. Drescher, J. P. Gollub, and R. E. Goldstein, Science **325**, 487 (2009).
[10] A. Vilfan and F. Jülicher, Phys. Rev. Lett. **96**, 058102 (2006).
[11] T. Niedermayer, B. Eckhardt, and P. Lenz, Chaos **18**, 037128 (2008).
[12] M. Reichert and H. Stark, Eur. Phys. J. E **17**, 493 (2005).
[13] S. Gueron and K. Levit-Gurevich, Proc. Natl. Acad. Sci. U.S.A. **96**, 12240 (1999).
[14] M. Kim and T. R. Powers, Phys. Rev. E **69**, 061910 (2004).
[15] J. Kotar, M. Leoni, B. Bassetti, M. C. Lagomarsino, and P. Cicuta, Proc. Natl. Acad. Sci. U.S.A. **107**, 7669 (2010).
[16] N. Uchida and R. Golestanian, Phys. Rev. Lett. **106**, 058104 (2011).
[17] J. Happel and H. Brenner, *Low Reynolds Number Hydrodynamics* (Kluwer, Boston, 1965).
[18] J. Dhont, *An Introduction to Dynamics of Colloids* (Elsevier, New York, 1996).
[19] H. Goldstein, C. Poole, and J. Safko, *Classical Mechanics* (Addison-Wesley, Reading, MA, 2002), 3rd ed.
[20] Γ is always positive definite, while Γ_h can become singular for special configurations $\mathbf{q}$.
[21] A. Shapere and F. Wilczek, Phys. Rev. Lett. **58**, 2051 (1987).
[22] A. Najafi and R. Golestanian, Phys. Rev. E **69**, 062901 (2004).
[23] Specifically, if $\bar{\delta}$ is defined as the solution to Eq. (6) with $\bar{\delta}(0) = \delta(0)$, then after one cycle, $\bar{\delta}$ will have the same statistics as δ to leading order, $\langle \bar{\delta}^n(T) \rangle = \langle \delta^n(T) \rangle + \mathcal{O}(\varepsilon^3 v, \varepsilon^3 D, \varepsilon^6)$.
[24] R. Adler, Proc. IRE **34**, 351 (1946).
[25] R. L. Stratonovich, *Topics in the Theory of Random Noise* (Gordon and Breach, New York, 1963).
[26] A. Pikovsky, M. Rosenblum, and J. Kurths, *Synchronization* (Cambridge University Press, Cambridge, England, 2001).
[27] G. Elfring and E. Lauga, Phys. Rev. Lett. **103**, 1 (2009).
[28] We neglect local torques corresponding to rotations of infinitesimal flagellar segments around their center.
[29] J. Gray and G. T. Hancock, J. Exp. Biol. **32**, 802 (1955).
[30] B. M. Friedrich, I. H. Riedel-Kruse, J. Howard, and F. Jülicher, J. Exp. Biol. **213**, 1226 (2010).
[31] P. V. Bayly, B. L. Lewis, E. C. Ranz, R. J. Okamoto, R. B. Pless, and S. K. Dutcher, Biophys. J. **100**, 2716 (2011).
[32] M. S. Jones, L. Le Baron, and T. J. Pedley, J. Fluid Mech. **281**, 137 (1994).
[33] J. S. Hyams and G. G. Borisy, Science **189**, 891 (1975).
[34] C. J. Brokaw and D. J. Luck, Cell Motil. **3**, 131 (1983).
[35] R. Bennett and R. Golestanian (private communication).

Cell-body rocking is a dominant mechanism for flagellar synchronization in a swimming alga

Veikko F. Geyer[a], Frank Jülicher[b], Jonathon Howard[a], and Benjamin M. Friedrich[b,1]

[a]Max Planck Institute of Molecular Cell Biology and Genetics, 01307 Dresden, Germany; and [b]Max Planck Institute for the Physics of Complex Systems, 01187 Dresden, Germany

Edited by Charles S. Peskin, New York University, Manhattan, NY, and approved September 23, 2013 (received for review February 21, 2013)

The unicellular green alga *Chlamydomonas* swims with two flagella that can synchronize their beat. Synchronized beating is required to swim both fast and straight. A long-standing hypothesis proposes that synchronization of flagella results from hydrodynamic coupling, but the details are not understood. Here, we present realistic hydrodynamic computations and high-speed tracking experiments of swimming cells that show how a perturbation from the synchronized state causes rotational motion of the cell body. This rotation feeds back on the flagellar dynamics via hydrodynamic friction forces and rapidly restores the synchronized state in our theory. We calculate that this "cell-body rocking" provides the dominant contribution to synchronization in swimming cells, whereas direct hydrodynamic interactions between the flagella contribute negligibly. We experimentally confirmed the two-way coupling between flagellar beating and cell-body rocking predicted by our theory.

flagellar force–velocity relation | low-Reynolds-number hydrodynamics

Eukaryotic cilia and flagella are long, slender cell appendages that can bend rhythmically and thus present a prime example of a biological oscillator (1). The flagellar beat is driven by the collective action of dynein molecular motors, which are distributed along the length of the flagellum. The beat of flagella, with typical frequencies ranging from 20–60 Hz, pumps fluids, for example, mucus in mammalian airways (2), and propels unicellular microswimmers such as *Paramecia*, spermatozoa, and algae (3). The coordinated beating of collections of flagella is important for efficient fluid transport (2, 4, 5) and fast swimming (6). This coordinated beating represents a striking example for the synchronization of oscillators, prompting the question of how flagella couple their beat. Identifying the specific mechanism of synchronization can be difficult because synchronization may occur even for weak coupling (7). Further, the effect of the coupling is difficult to detect once the synchronized state has been reached.

Hydrodynamic forces were suggested to play a significant role for flagellar synchronization already in 1951 by Taylor (8). Since then, direct hydrodynamic interactions between flagella were studied theoretically as a possible mechanism for flagellar synchronization (9–12). Another synchronization mechanism that is independent of hydrodynamic interactions was recently described in the context of a minimal model swimmer (13–15). This mechanism crucially relies on the interplay of swimming motion and flagellar beating.

Here, we address the hydrodynamic coupling between the two flagella in a model organism for flagellar coordination (16–19), the unicellular green alga *Chlamydomonas reinhardtii*. *Chlamydomonas* propels its ellipsoidal cell body, which has typical diameter of 10 μm, using a pair of flagella, whose lengths are about 10 μm (16). The two flagella beat approximately in a common plane, which is collinear with the long axis of the cell body. In that plane, the two beat patterns are nearly mirror-symmetric with respect to this long axis. The beating of the two flagella of *Chlamydomonas* can synchronize, that is, adopt a common beat frequency and a fixed phase relationship (16–19). In-phase synchronization of the two flagella is required for swimming along a straight path (19). The specific mechanism leading to flagellar synchrony is unclear.

Here, we use a combination of realistic hydrodynamic computations and high-speed tracking experiments to reveal the nature of the hydrodynamic coupling between the two flagella of free-swimming *Chlamydomonas* cells. Previous hydrodynamic computations for *Chlamydomonas* used either resistive force theory (20, 21), which does not account for hydrodynamic interactions between the two flagella, or computationally intensive finite element methods (22). We employ an alternative approach and represent the geometry of a *Chlamydomonas* cell by spherical shape primitives, which provides a computationally convenient method that fully accounts for hydrodynamic interactions between different parts of the cell. Our theory characterizes flagellar swimming and synchronization by a minimal set of effective degrees of freedom. The corresponding equation of motion follows naturally from the framework of Lagrangian mechanics, which was used previously to describe synchronization in a minimal model swimmer (13, 15). These equations of motion embody the key assumption that the flagellar beat speeds up or slows down according to the hydrodynamic friction forces acting on the flagellum, that is, if there is more friction and therefore higher hydrodynamic load, then the beat will slow down. This assumption is supported by previous experiments that showed that the flagellar beat frequency decreases when the viscosity of the surrounding fluid is increased (23, 24). The simple force–velocity relationship for the flagellar beat employed by us coarse-grains the behavior of thousands of dynein molecular motors that collectively drive the beat. Similar force–velocity properties have been described for individual molecular motors (25) and reflect a typical behavior of active force generating systems.

Our theory predicts that any perturbation of synchronized beating results in a significant yawing motion of the cell, reminiscent of rocking of the cell body. This rotational motion imparts different hydrodynamic forces on the two flagella, causing one of them to beat faster and the other to slow down. This interplay

Significance

The eukaryotic flagellum is a best-seller of nature: These slender cell appendages propel sperm and many other microswimmers, including disease-causing protists. In mammalian airways or the oviduct, collections of flagella beat in synchrony to pump fluids efficiently. Flagellar synchronization was proposed to rely on mechanical feedback by hydrodynamic forces, but the details are not well understood. Here, we used theory and experiment to elucidate a mechanism of synchronization in the model organism *Chlamydomonas*, a green algal cell that swims with two flagella like a breaststroke swimmer. Our analysis shows how synchronization arises by a coupling of swimming and flagellar beating and characterizes an exemplary force–velocity relationship of the flagellar beat.

Author contributions: B.M.F. designed research; V.F.G. and B.M.F. performed research; B.M.F. contributed new reagents/analytic tools; V.F.G. and B.M.F. analyzed data; and V.F.G., F.J., J.H., and B.M.F. wrote the paper.

The authors declare no conflict of interest.

This article is a PNAS Direct Submission.

[1]To whom correspondence should be addressed. E-mail: benjamin.friedrich@pks.mpg.de.

This article contains supporting information online at www.pnas.org/lookup/suppl/doi:10.1073/pnas.1300895110/-/DCSupplemental.

between flagellar beating and cell-body rocking rapidly restores flagellar synchrony after a perturbation. Using the framework provided by our theory, we analyze high-speed tracking experiments of swimming cells, confirming the proposed two-way coupling between flagellar beating and cell-body rocking.

Previous experiments restrained *Chlamydomonas* cells from swimming, holding their cell body in a micropipette (17–19). Remarkably, flagellar synchronization was observed also for these constrained cells. This observation seems to argue against a synchronization mechanism that relies on swimming motion. However, the rate of synchronization observed in these experiments was faster by an order of magnitude than the rate we predict for synchronization by direct hydrodynamic interactions between the two flagella in the absence of any motion. In contrast, we show that rotational motion with a small amplitude of a few degrees only, which may result from either a residual rotational compliance of the clamped cell or an elastic anchorage of the flagellar pair, provides a possible mechanism for rapid synchronization, which is analogous to synchronization by cell-body rocking in free-swimming cells.

Results and Discussion

High-Precision Tracking of Confined *Chlamydomonas* Cells. To study the interplay of flagellar beating and swimming motion, we recorded single wild-type *C. reinhardtii* cells swimming in a shallow observation chamber using high-speed phase-contrast microscopy (1,000 frames per second). The chamber heights were only slightly larger than the cell diameter so that the cells did not roll around their long body axis, but only translated and rotated in the focal plane. This confinement of cell motion to two space dimensions and the fact that the approximately planar flagellar beat was parallel to the plane of observation greatly facilitated data acquisition and analysis. From high-speed recordings we obtained the projected position and orientation of the cell body as well as the shape of the two flagella (Fig. 1*A* and Fig. S1).

In the reference frame of the cell body, each flagellum undergoes periodic shape changes. To formalize this observation, we defined a flagellar phase variable by binning flagellar shapes according to shape similarity (Fig.1*B* and Fig. S2). A time series of flagellar shapes is represented by a point cloud in an abstract shape space. This point cloud comprises an effectively one-dimensional shape cycle, which reflects the periodicity of the flagellar beat. Each shape point can be projected on the centerline of the point cloud. We define a phase variable φ running from 0 to 2π that parameterizes this limit cycle by requiring that the phase speed $\dot{\varphi}$ be constant for synchronized beating. Approximately, we determine this parameterization from the condition that the averaged phase speed is independent of the location along the limit cycle. This defines a unique flagellar phase for each tracked flagellar shape. The width of the point cloud shown in Fig. 1*B* is a measure for the variability of the flagellar beat during subsequent beat cycles. We find that the variations of flagellar shapes for the same value of the phase variable are much smaller than the shape changes during one beat cycle. For our analysis, we therefore neglect these variations of the flagellar beat. In this way, we characterize a swimming *Chlamydomonas* cell by 5 degrees of freedom: its position (x,y) in the plane, the orientation angle α of its cell body, and the two flagellar phase variables φ_L and φ_R for the left and right flagellum, respectively. Our theoretical description will employ the same 5 degrees of freedom and use flagellar shapes tracked from experiment for the hydrodynamic computations.

Hydrodynamic Forces and Interactions. For a swimming *Chlamydomonas* cell, inertial forces are negligible [as characterized by a low Reynolds number of $\mathrm{Re} \sim 10^{-3}$ (22)], which implies that the hydrodynamic friction forces exerted by the cell depend only on its instantaneous motion (26). To conveniently compute hydrodynamic friction forces and hydrodynamic interactions, we represented the geometry of a *Chlamydomonas* cell by 300 spherical shape primitives (Fig. 2*A*). The spheres constituting the cell body

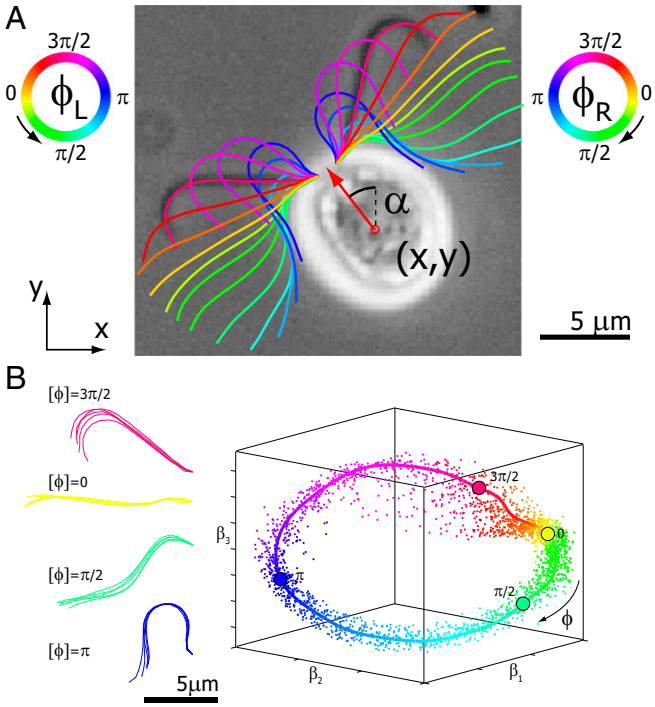

Fig. 1. Five degrees of freedom for *Chlamydomonas*. (*A*) In our experiments, conducted in shallow observation chambers, *Chlamydomonas* cells swim in a plane. At each time, the position and orientation of the cell body is characterized by its center position (x,y) and the angle α of its long axis with respect to the laboratory frame. The beating of each flagellum is characterized by a single periodic phase variable, φ_L and φ_R for the left and right flagellum, respectively. The flagellar shapes shown in different colors were tracked from high-speed recordings and correspond to a time-difference of 2 ms. This beat pattern was used for all computations. (*B*) Binning of tracked flagellar shapes according to shape similarity defines a flagellar phase angle as shown on the left. More precisely, we employed a nonlinear dimensionality reduction technique as specified in *Supporting Information* to represent each tracked planar flagellar shape as a point in an abstract shape space. This representation reveals the periodicity of the flagellar beat and supports our description of the flagellar beat as a fixed sequence of flagellar shapes parameterized by a single phase variable φ.

are treated as a rigid cluster. For simplicity, we consider free-swimming cells and do not include wall effects in our hydrodynamic computations. Flagellar beating and swimming corresponds to a simultaneous motion of all 300 spheres of our cell model. The dependence of the corresponding hydrodynamic friction forces and torques on the velocities of the individual spheres is characterized by a grand hydrodynamic friction matrix G. We computed this friction matrix G using a Cartesian multipole expansion technique (27); *Materials and Methods* gives details. Fig. 2 *C* and *D* shows a submatrix that relates force and velocity components parallel to the long axis of the cell. The entries of the color matrix depict the force exerted by any of the flagellar spheres or by the cell-body cluster (row index), if a single flagellar sphere or the cell-body cluster is moved (column index). The indexing of flagellar spheres is indicated by cartoon drawings of the cell next to the color matrix. The diagonal entries of this friction matrix are positive and account for the usual Stokes friction of a single "flagellar sphere" (or of the cell body). Off-diagonal entries are negative and represent hydrodynamic interactions. We find considerable hydrodynamic interactions between spheres of the same flagellum, as well as between each flagellum and the cell body. However, interactions between the two flagella are comparably weak.

Theoretical Description of Flagellar Beating and Swimming. We now present dynamical equations for the minimal set of 5 degrees of freedom shown in Fig. 1*A* to describe flagellar beating, swimming,

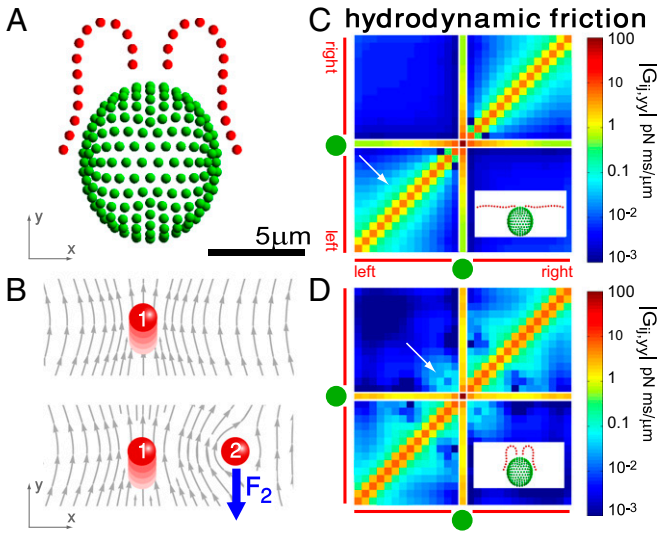

Fig. 2. Hydrodynamic interactions between the two flagella are weak. (*A*) Model *Chlamydomonas* cell represented by an ensemble of 300 spheres used to compute hydrodynamic friction forces at low Reynolds numbers. In our calculations, the model cell was assumed to be far from any surfaces. (*B*) Illustration of hydrodynamic interactions between spheres. A single sphere (labeled 1) moving with velocity $v_{1y} > 0$ along the *y* axis will drag fluid alongside and thus exert a total hydrodynamic friction force $F_{1y} = G_{11,yy} v_{1y} > 0$ on the fluid. If a second sphere (labeled 2) is held fixed close to the first one, it will locally slow down this fluid flow. The force F_2 required to hold the second sphere equals the force exerted by this sphere on the fluid; its *y* component $F_{2y} = G_{21,yy} v_{1y} < 0$ defines a friction coefficient $G_{21,yy}$ that characterizes hydrodynamic interactions between the two spheres. (*C*) Hydrodynamic interactions between different parts of the model cell. Analogous to *B*, one defines a matrix $G_{ij,yy}$ of hydrodynamic friction coefficients for the ensemble of $2 \cdot 14$ flagellar spheres and the rigid sphere cluster constituting the cell body that together represent a *Chlamydomonas* cell (*Inset*). Each column of the color-coded matrix shows the magnitude of hydrodynamic friction exerted by a flagellar sphere (or the cell body), if a single sphere or the cell body is moved parallel to the long cell body axis. Off-diagonal entries characterize hydrodynamic interactions, which are particularly pronounced along a single flagellum (white arrow), or between one flagellum and the cell body (central column). Hydrodynamic interactions between the two flagella are very weak and partly screened by the cell body. (*D*) Same as in *C*, but for a recovery stroke configuration. There are weak hydrodynamic interactions between the proximal segments of the two flagella (white arrow). All friction coefficients shown scale with the viscosity of the fluid, which was taken as the viscosity of water at 20 °C, $\eta = 1$ pN ms/μm^2.

and later flagellar synchronization in *Chlamydomonas*. These equations of motion follow naturally from the framework of Lagrangian mechanics of dissipative systems, which defines generalized forces conjugate to effective degrees of freedom.

Motivated by our experiments, we describe the progression through subsequent beat cycles of each of the two flagella by respective phase angles φ_L and φ_R (Fig. 1*A*). The angular frequency ω_j of flagellar beating is given by the time-averaged phase speed $\langle \dot{\varphi}_j \rangle$, so we can think of the phase speed as the instantaneous beat frequency. We are interested in variations of the phase speed that can restore a synchronized state after a perturbation. We introduce the key assumption that changes in hydrodynamic friction during the flagellar beat cycle can increase or decrease the phase speed of each flagellum. Specifically, we assume that for both the left and right flagellum, $j = L, R$, the respective flagellar phase speed $\dot{\varphi}_j$ is determined by a balance of an active driving force Q_j that coarse-grains the active processes within the flagellum and a generalized hydrodynamic friction force P_j, which depends on $\dot{\varphi}_j$. Note that in addition to hydrodynamic friction, dissipative processes within the flagella may contribute to the friction forces P_L and P_R. We do not consider such internal friction in our description because it does not change our results qualitatively. The hydrodynamic friction forces P_j have to be computed self-consistently for a swimming cell.

We restrict our analysis to planar motion in the "*xy*" plane and thus consider the position (x, y) and the orientation α of the cell body with respect to a fixed laboratory frame (Fig. 1*A*).

Any change of the degrees of freedom x, y, α, φ_L, or φ_R results in the dissipation of energy into the fluid at some rate $\mathcal{R}$. This dissipation rate $\mathcal{R}$ characterizes the mechanical power output of the cell and plays the role of a Rayleigh dissipation function known in Lagrangian mechanics; it can be written as $\mathcal{R} = \dot{x}P_x + \dot{y}P_y + \dot{\alpha}P_\alpha + \dot{\varphi}_L P_L + \dot{\varphi}_R P_R$, which defines the generalized friction forces P_j conjugate to the different degrees of freedom. The forces P_L, P_R, and P_α are conjugate to an angle and have physical unit, piconewtons times micrometer. We compute the generalized friction forces using the grand hydrodynamic friction matrix G introduced above. In brief, the superposition principle of low-Reynolds-number hydrodynamics relevant for *Chlamydomonas* swimming (26) implies that the generalized friction forces relate linearly to the generalized velocities, $P_j = \Gamma_{jx}\dot{x} + \Gamma_{jy}\dot{y} + \Gamma_{j\alpha}\dot{\alpha} + \Gamma_{jL}\dot{\varphi}_L + \Gamma_{jR}\dot{\varphi}_R$. This defines the generalized hydrodynamic friction coefficients Γ_{ji}, which are suitable linear combinations of the entries of the grand hydrodynamic friction matrix G (*Materials and Methods* and Figs. S3 and S4).

The friction force P_x conjugate to the x coordinate of the cell position represents just the x component of the total force exerted by the cell on the fluid, and an analogous statement applies for P_y ; P_α is the total torque associated with rotations around an axis normal to the plane of swimming. If the swimmer is free from external forces and torques, we have $P_x = P_y = 0$ and $P_\alpha = 0$. Together with the proposed balance of flagellar friction and driving forces, $P_L = Q_L$ and $P_R = Q_R$, we have a total of five force balance equations, which allow us to solve for the time derivatives of the 5 degrees of freedom. We obtain an equation of motion that combines swimming and flagellar phase dynamics

$$(\dot{x}, \dot{y}, \dot{\alpha}, \dot{\varphi}_L, \dot{\varphi}_R)^T = \Gamma^{-1}(0, 0, 0, Q_L, Q_R)^T. \quad [1]$$

The phase dependence of the active driving forces $Q_j(\varphi_j)$ is uniquely specified by the condition that the phase speeds should be constant, $\dot{\varphi}_j = \omega_0$, for synchronized flagellar beating with zero flagellar phase difference $\delta = 0$, where $\delta = \varphi_L - \varphi_R$.

In essence, this generic description implies that the phase speed of one flagellum is determined by hydrodynamic friction forces, which in turn depend on the swimming motion of the cell. Because the swimming motion is determined by the beating of both flagella, Eq. **1** effectively defines a feedback loop that couples the two flagellar oscillators.

Theory and Experiment of *Chlamydomonas* Swimming. Using the equation of motion (Eq. **1**), we can compute the swimming motion of our model cell. For mirror-symmetric flagellar beating with zero flagellar phase difference $\delta = 0$, the model cell follows a straight path with an instantaneous velocity that is positive during the effective stroke but becomes negative during a short period of the recovery stroke (Fig. 3*A*, *Left*). *Chlamydomonas* swims two steps forward, one step back. This saltatory motion is also observed experimentally by us (Fig. 3*A*, *Right*) and others (16, 28, 29). In our computation, the instantaneous swimming velocity reaches values up to 200 μm/s, which agrees with experimental measurements for free-swimming cells (29), but overestimates the observed translational swimming speeds in shallow chambers, in which wall effects are expected to reduce the speed of translational motion (compare left and right panels in Fig. 3*A*). If the two flagella are beating out of phase, the cell will not swim straight anymore, but the cell body yaws (Fig. 3*B*). Cell-body yawing is observed experimentally (Fig. 3*B*, *Right*), with measured yawing rates that agree well with our computations (Fig. 3*B*, *Left*). The proximity of boundary walls is known to reduce translational motion but to affect rotational motion to a much lesser extent for a given distance from the wall (21). This is indeed observed in our experiments with cells swimming in shallow chambers: Whereas the observed translational speed is smaller than predicted (Fig. 3*A* and Fig. S5), the observed yawing rates are very similar to the

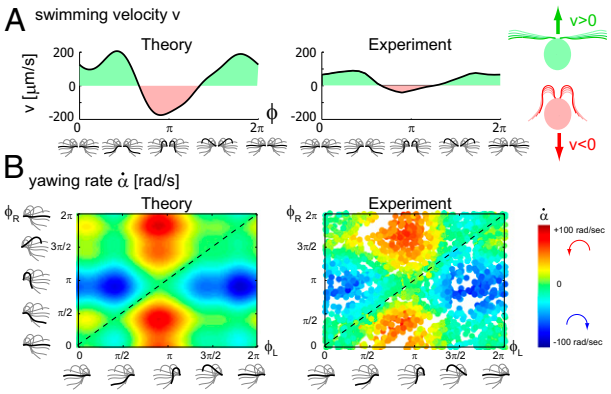

Fig. 3. (*A*) For synchronized flagellar beating, we compute saltatory forward swimming with positive instantaneous velocity during effective stroke beating, and a backward motion during the recovery stroke (*Left*); this behavior is summarized by cartoon drawings (*Extreme Right*). A typical experimental velocity profile of a *Chlamydomonas* cell in a shallow observation chamber measured during a cycle of synchronized beating is shown for comparison in the middle panel. (*B*) Flagellar asynchrony causes cell-body yawing, both in theory and experiment. Shown is the instantaneous rotation rate $\dot{\alpha}$ of the cell body in color code as a function of the respective phase of the two flagella. For in-phase synchronized flagellar beating (dashed line), the cell body does not rotate (green). For out-of-phase flagellar beating, however, we find significant cell-body rocking (blue, clockwise; red, counter-clockwise).

predicted ones (Fig. 3*B*). The good agreement between theory and experiment for the yawing rate supports our hydrodynamic computation as well as our description of flagellar beating using a single phase variable. In the next section, we show that rotational motion is crucial for flagellar synchronization, whereas translational motion is less important.

Theory of Flagellar Synchronization by Cell-Body Yawing. We now demonstrate how yawing of the cell body leads to flagellar synchronization. We first examine the flagellar phase dynamics after a perturbation of in-phase flagellar synchrony. Fig. 4*A* shows numerical results for a free-swimming cell obtained from solving the equation of motion (Eq. **1**). The initial flagellar asynchrony causes a yawing motion of the model cell, which is characterized by periodic changes of the cell's orientation angle $\alpha(t)$. The phase difference δ between the left and right flagellum decays approximately exponentially as $\delta(t) \sim \exp(-\lambda t/T)$ with a rate constant λ (measured in beat periods $T = 2\pi/\omega_0$) that will serve as a measure of the strength of synchronization.

To mimic experiments in which external forces constrain cell motion, we now consider the idealized case of a cell that cannot translate, while cell-body yawing is constrained by an elastic restoring force $Q_\alpha = -k\alpha$. Again, the two flagella synchronize in-phase, provided some residual cell-body yawing is allowed (Fig. 4*B*). In the absence of an elastic restoring force ($k = 0$), when the model cell cannot translate, but can still freely rotate, its yawing motion and synchronization behavior is very similar to the case of a free-swimming cell that can rotate and translate. For a fully clamped cell body, however, the synchronization strength is strongly attenuated and is solely due to the direct hydrodynamic interactions between the two flagella. In this case of synchronization by hydrodynamic interactions, the time constant for synchronization is decreased approximately 20-fold compared to the case of free swimming. These numerical observations point to a crucial role of cell-body yawing for flagellar synchronization. The underlying mechanism of synchronization can be explained as follows. For in-phase synchronization, the flagellar beat is mirror-symmetric and the cell swims along a straight path. If, however, the left flagellum has a small head-start during the effective stroke, this causes a counter-clockwise rotation of the cell (Fig. 3*B*). This cell-body yawing increases (decreases) the hydrodynamic friction encountered by the left (right) flagellum, causing the left flagellum to beat slower and the right one to beat faster. As a result, flagellar synchrony is restored.

Next, we present a formalized version of this argument using a reduced equation of motion. We thus arrive at a simple theory for biflagellar synchronization, which will later allow for quantitative comparison with experiments. As in Fig. 4*B*, we assume that the cell is constrained such that it cannot translate ($\dot{x} = \dot{y} = 0$). The cell can still yaw, possibly being subject to an elastic restoring force $Q_\alpha = -k\alpha$. This leaves only 3 degrees of freedom: φ_L, φ_R, and α. Neglecting direct hydrodynamic interactions between the flagella, we can reduce the equations of motion for a clamped cell (Eq. **1** with constraint $\dot{x} = \dot{y} = 0$) to a set of three coupled equations for the three remaining degrees of freedom:

$$\dot{\varphi}_L = \omega_L - \mu(\varphi_L)\dot{\alpha}, \quad [2]$$

$$\dot{\varphi}_R = \omega_R + \mu(\varphi_R)\dot{\alpha}, \quad [3]$$

$$k\alpha + \rho(\varphi_L, \varphi_R)\dot{\alpha} = -\nu(\varphi_L)\dot{\varphi}_L + \nu(\varphi_R)\dot{\varphi}_R. \quad [4]$$

The coupling function μ in Eq. **2** characterizes the effect of cell-body yawing on the flagellar beat as detailed below, and ν describes how asynchronous flagellar beating results in yawing; ρ is the hydrodynamic friction coefficient for yawing of the whole cell. The coupling functions μ, ν, and ρ can be computed using our

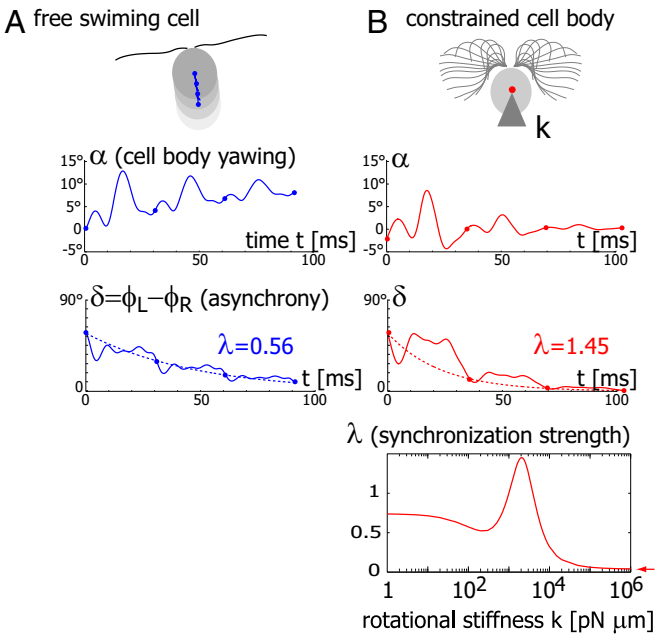

Fig. 4. Flagellar synchronization by cell-body yawing. (*A*) For a free-swimming cell (*Top*), the equation of motion (Eq. **1**) predicts a yawing motion of the cell body characterized by $\alpha(t)$ if the two flagella are initially out of synchrony (*Middle*). The flagellar phase difference δ is found to decrease with time (*Bottom*, solid line), approximately following an exponential decay $\sim \exp(-\lambda t/T)$ (dotted line), where T is the period of the flagellar beat and λ defines a dimensionless synchronization strength. Thus, in-phase synchronized beating is stable with respect to perturbations. Dots mark the completion of a full beat cycle of the left flagellum. (*B*) To mimic experiments where external forces constrain cell motion, we simulated the idealized case of a cell that cannot translate, while cell-body yawing is constricted by an elastic restoring torque $Q_\alpha = -k\alpha$ that acts at the cell body center (*Top*). Again, the two flagella synchronize (*Middle*) with a synchronization strength λ that can become even larger than in the case of a free swimming as shown here for $k = 2 \cdot 10^3$ pN μm, which is close to the rotational stiffness for which the synchronization strength λ is maximal (*Bottom*). For very large clamping stiffness k, the cell body cannot move and the synchronization strength λ attenuates to a basal value $\lambda \approx 0.03$, which arises solely from direct hydrodynamic interactions between the two flagella (arrow). Parameters: $2\pi/\omega_0 = 30$ ms.

hydrodynamic model.* Their dependence on the flagellar phase is shown in Fig. 5 (*Left*). The physical significance of Eqs. **2–4** can be explained as follows. Eq. **2** implies that during the effective stroke of the left flagellum ($\varphi \sim 0°$), a counter-clockwise rotation of the whole cell slows down the flagellar beat, whereas a clockwise rotation speeds it up (Fig. 5*B*, $\mu > 0$). Eq. **3** implies the converse for the right flagellum. During the recovery stroke ($\varphi \sim 180°$), the effect is opposite and a counter-clockwise rotation of the cell would speed up the beat of the left flagellum ($\mu < 0$). Eq. **4** states that flagellar beating causes the cell body to yaw: If the right flagellum were absent, the model cell would rotate clockwise ($\dot{\alpha} < 0$) during the effective stroke of the left flagellum (Fig. 5*A*, $\nu > 0$), and counter-clockwise during its recovery stroke ($\nu < 0$). This swimming behavior is observed for uniflagellar mutants (21). For synchronized beating of the two flagella, the right-hand side of Eq. **4** cancels to zero and the model cell swims straight. For asynchronous flagellar beating with a finite phase difference $\delta = \varphi_L - \varphi_R$, the phase dependence of the coupling function $\nu(\varphi)$ results in an imbalance of the torques generated by the left and right flagellum, respectively, which is balanced by a rotation of the whole cell.

We study the dynamical system given by Eqs. **2–4** after a small perturbation of the synchronized state at $t = 0$ with initial flagellar phase difference $0 < \delta(0) \ll 1$. For simplicity, we assume equal intrinsic beat frequencies, $\omega_L = \omega_R = \omega_0$. The synchronization strength λ is given by $\lambda = -\int_0^T dt\, \dot{\delta}/\delta$. In the limit of a small elastic constraint, we find (*Supporting Information*)

$$\lambda = -\oint_0^{2\pi} d\varphi \frac{2\mu(\varphi)\nu'(\varphi)}{\rho(\varphi,\varphi) - 2\mu(\varphi)\nu(\varphi)} \quad \text{for } k \ll \rho\omega_0, \qquad [5]$$

where a prime denotes differentiation with respect to φ. Using the coupling functions μ, ν, and ρ computed above, we obtain $\lambda > 0$, which implies stable in-phase synchronization (Fig. 4). In the case of a stiff elastic constraint, we obtain a different result for λ:

$$\lambda = -\oint_0^{2\pi} d\varphi \frac{\mu(\varphi)\nu''(\varphi)}{k/\omega_0} \quad \text{for } k \gg \rho\omega_0. \qquad [6]$$

Synchronization in the absence of an elastic restoring force as characterized by Eq. **5**, and synchronization involving a strong elastic coupling as characterized by Eq. **6** shows interesting differences, which relate to the fact that in the first case the flagellar phase dynamics depends only on the yawing rate $\dot{\alpha}$, but not on α itself. The difference between these two synchronization mechanisms is best illustrated in a special case, in which both the ratio $\sigma = \mu/\nu$ and ρ are constant. A constant σ correspond to an active flagellar driving force that does not depend on the flagellar phase, whereas for constant ρ the angular friction for yawing would not depend on the flagellar configuration. In the limit of a stiff elastic constraint, $k \gg \rho\omega_0$, we readily find $\lambda = -\sigma\omega_0 \oint \nu\nu''/k = \sigma\omega_0 \oint (\nu')^2/k > 0$, which indicates stable in-phase synchronization. In the limit of a weak elastic constraint, $k \ll \rho\omega_0$, however, the integral on the right-hand side of Eq. **5** evaluates to zero, which implies that synchronization does not occur. Hence, synchronization in the absence of an elastic restoring force requires that either μ/ν or ρ depend on the flagellar phase.

For our realistic *Chlamydomonas* model, μ and ν differ (Fig. 5*A*), and also ρ is not constant (Fig. S3). This allows for rapid synchronization also in the absence of elastic forces. Previous work on synchronization in minimal systems showed that elastic restoring forces can facilitate synchronization (11, 30). Here, we have shown that elastic forces can increase the synchronization strength (Fig. 4), but they are not required for flagellar synchronization in swimming *Chlamydomonas* cells, even if hydrodynamic interactions are neglected.

Our discussion of flagellar synchronization can be extended to the case, where the intrinsic beat frequencies of the two flagella do not match. If the frequency mismatch $|\omega_L - \omega_R|$ is small compared to the inverse time scale of synchronization λ/T, a general result implies that the two flagellar oscillators will still synchronize (7). For a frequency mismatch that is too large, the two flagella display phase drift with a phase difference that increases monotonously (18).

Experiments Show Coupling of Beating and Yawing. We reconstructed the coupling functions $\mu(\varphi)$ and $\nu(\varphi)$ between beating and yawing from experimental data using the theoretical framework developed in the previous section. In brief, (*i*) we extracted the instantaneous yawing rate $\dot{\alpha}$ and flagellar phase speeds $\dot{\varphi}_L$ and $\dot{\varphi}_R$ from high-speed videos of swimming *Chlamydomonas* cells, (*ii*) we represented the coupling functions by a truncated Fourier series, and (*iii*) we obtained the unknown Fourier coefficients by linear regression using Eqs. **2–4**. The high temporal resolution of our imaging enabled us to accurately determine phase speeds as time derivatives of flagellar phase angle data. Fig. 5*B* displays averaged coupling functions obtained by fitting for a typical *Chlamydomonas* cell; fits for five more cells are shown in Figs. S6 and S7. We find a significant coupling between flagellar phase speeds and yawing rates, which are in good qualitative agreement with the theoretical predictions.

For the experimental conditions used, we commonly observed cells that displayed a large frequency mismatch between the two flagella. In the cells selected for analysis, this frequency mismatch exceeded 30%. This large frequency mismatch caused flagellar phase drift, which resulted in pronounced cell-body yawing and enabled us to accurately measure the coupling of yawing and flagellar beating. Experiments were done using either white-light illumination, which gave maximal image quality, or red-light illumination, which reduces a possible phototactic stimulation of the cells.

The observed modulation of flagellar phase speed according to the rate of yawing is consistent with a force–velocity dependence of flagellar beating, for which the speed of the beat decreases if the hydrodynamic load increases. We propose that a similar load characteristic of the flagellar beat holds also in cases of small frequency mismatch, where it allows for flagellar synchronization.

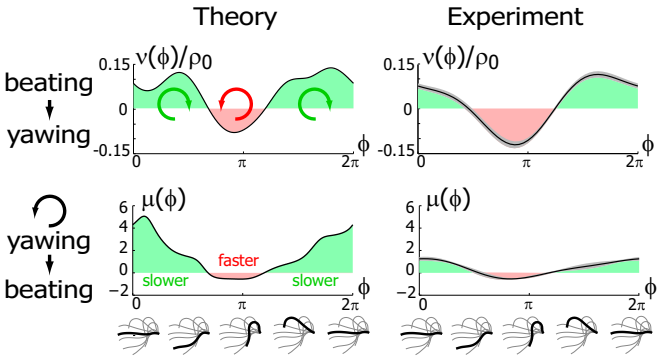

Fig. 5. Flagellar beating and cell-body yawing are coupled in a bidirectional way. (*Upper Left*) In our theory, the beat of the left flagellum generates a torque, which, in the absence of the right flagellum, has to be counterbalanced by a yawing motion of cell body (Eq. **4**). This effect is quantified by the coupling function $\nu(\varphi)$ shown, normalized here by $\rho_0 = \langle\rho\rangle$: The effective stroke ($\varphi_L \sim 0°$) of the left flagellum causes the cell to yaw clockwise. (*Lower Left*) Conversely, yawing of the cell changes the hydrodynamic friction force that opposes the flagellar beat, which, in our theory, speeds up or slows down the beat (Eq. **2**). This effect is quantified by the coupling function $\mu(\varphi)$ shown: a counter-clockwise yawing during the effective stroke of the left flagellum slows down its beat. The coupling of beating and yawing allows for flagellar synchronization in a free-swimming cell. (*Right*) By fitting Eqs. **2** and **4** to experimental time-series data, we can recover the coupling functions $\mu(\varphi)$ and $\nu(\varphi)/\rho_0$ (1 cell, $n = 5$ time series of 0.5-s duration; gray regions denote mean ± SE).

*Specifically, $\mu(\varphi) = \Gamma_{L\alpha}(\varphi,\varphi)/\Gamma_{LL}(\varphi,\varphi)$, $\nu(\varphi) = \Gamma_{\alpha L}(\varphi,\varphi)$, $\rho(\varphi_L,\varphi_R) = \Gamma_{\alpha\alpha}(\varphi_L,\varphi_R)$. For simplicity, the active flagellar driving forces were approximated as $Q_L = \omega_L\Gamma_{LL}$ and $Q_R = \omega_R\Gamma_{RR}$ for constrained translational motion.

Conclusion and Outlook

We have presented a theory on the hydrodynamic coupling underlying flagellar synchronization in swimming *Chlamydomonas* cells. We have shown that direct hydrodynamic interactions between the two flagella as considered in refs. 9–11 give only a minor contribution to the computed synchronization strength and are unlikely to account for the rapid synchronization observed in experiments (16–19). In contrast, rotational motion of the swimmer caused by asynchronous beating imparts different hydrodynamic friction forces on the two flagella, which rapidly brings them back in tune: *Chlamydomonas* rocks to get into synchrony.

Using high-speed tracking experiments, we could confirm the two-way coupling between flagellar beating and cell-body yawing predicted by our theory. The striking reproducibility of our fits for the corresponding coupling functions and their favorable comparison to our theory is highly suggestive of a regulation of flagellar phase speed by hydrodynamic friction forces that depend on rotational motion. Thus, coupling of flagellar beating and cell-body yawing provides a strong candidate for the mechanism that underlies flagellar synchronization of swimming *Chlamydomonas* cells. A similar mechanism may account for synchronization in isolated flagellar pairs (31) (Fig. S8).

To explain a previously observed synchronization for cells held in a micropipette (17–19), we propose a finite clamping compliance that still allows for residual cell-body yawing with an amplitude of a few degrees, which is sufficient for rapid synchronization. Alternatively, a compliant basal anchorage of the flagellar pair or bending deformations of the elastic cell body would allow for flagellar synchronization by a completely analogous mechanism. In fact, the simple theory for biflagellar synchronization by rotational motion presented here (Eqs. **2–4**) applies analogously to a pivoting motion of an elastically anchored flagellar pair (Figs. S9 and S10). From the observed value $\lambda = 0.3$ for the synchronization strength in clamped cells (19), we estimate a rotational stiffness of $k \sim 10^4$ pN μm for either of these two cases.

Finally, the coupling of two phase oscillators by a third degree of freedom, in this case rotational motion, could allow for synchronization also in other contexts. For example, one may consider that synchronization in ciliar arrays (2) is mediated by an elastic coupling through the matrix with elastic deformations playing the role of the third degree of freedom.

Materials and Methods

Hydrodynamic Computation of Swimming *Chlamydomonas*. We represent a *Chlamydomonas* cell by an ensemble of 300 spheres of radius $a = 0.25$ μm (Fig. 2*A*) and use a freely available hydrodynamic library based on a Cartesian multipole expansion technique (27) to compute the grand hydrodynamic friction matrix G (26) for this ensemble of spheres. We assume a rigid cell body, and hence that the spheres constituting the cell body move as a rigid unit, which results in $n = 2 \cdot 14 + 1$ independently moving objects. The matrix G has dimensions $6n \times 6n$ and relates the components of the translational and rotational velocities, v_i and Ω_i, of each of the n objects to the hydrodynamic friction forces and torques, F_j and T_j, exerted by the j-th object on the fluid, $(F_{1x}, F_{1y}, F_{1z}, T_{1x}, T_{1y}, T_{1z}, F_{2x}, F_{2y}, \ldots, T_{ny}, T_{nz}) = \mathrm{G}\dot{\mathrm{q}}_0$ with $\dot{\mathrm{q}}_0 = (v_{1x}, v_{1y}, v_{1z}, \Omega_{1x}, \Omega_{1y}, \Omega_{1z}, v_{2x}, v_{2y}, \ldots, \Omega_{ny}, \Omega_{nz})$. Fig. 2 *C* and *D* shows a submatrix of G that relates force and velocity components parallel to the long axis of the cell body. The reduced friction matrix Γ for a set of m effective degrees of freedom q is computed from G as $\Gamma = \mathrm{L}^T \mathrm{G} \mathrm{L}$ with $6n \times m$ transformation matrix $L_{ij} = \partial \dot{q}_{0,i} / \partial \dot{q}_j$, where $\mathrm{q} = (x, y, \alpha, \varphi_L, \varphi_R)$ (13). Initial tests confirmed that the friction matrix of only the cell body gave practically the same result as the analytic solution for the enveloping spheroid; similarly, the computed friction matrix of only a single flagellum matched the prediction of resistive force theory (26).

Imaging *Chlamydomonas* Swimming in a Shallow Observation Chamber. For cell culture, *C. reinhardtii* cells (CC-125 wild-type mt+ 137c, R. P. Levine via N. W. Gillham, 1968) were grown in 300 mL TAP+P buffer (32) (with 4× phosphate) at 24 °C for 2 d under conditions of constant illumination (two 75-W fluorescent bulbs) and constant air bubbling to a final density of 10^6 cells/mL.

For high-speed video microscopy, an assay chamber was made of precleaned glass and sealed using Valap, a 1:1:1 mixture of lanolin, paraffin, and petroleum jelly, heated to 70 °C. The surface of that chamber was blocked using casein solution (solution of casein from bovine milk, 2 mg/mL, for 10 min) prior to the experiment. Single, noninteracting cells were visualized using phase-contrast microscopy set up on a Zeiss Axiovert 100 TV Microscope using a 63× Plan-Apochromat NA1.4 PH3 oil lens in combination with an 1.6× tube lens and an oil phase-contrast condenser N.A. 1.4. The sample was illuminated using a 100-W tungsten lamp. For red-light imaging, an e-beam-driven luminescent light pipe (Lumencor) with spectral range of 640–657 nm and power of 75 mW was used. The sample temperature was kept constant at 24° C using an objective heater (Chromaphor). For image acquisition, an EoSens Cmos high-speed camera was used. Videos were acquired at a rate of 1,000 frames per second with exposure times of 1 ms (white light) and 0.6 ms (red light). Finally, cell positions and flagellar shapes were tracked using custom-build Matlab software (*Supporting Information* gives details).

1. Alberts B, et al. (2002) *Molecular Biology of the Cell* (Garland Science, New York), 4th Ed.
2. Sanderson MJ, Sleigh MA (1981) Ciliary activity of cultured rabbit tracheal epithelium: beat pattern and metachrony. *J Cell Sci* 47:331–347.
3. Gray J (1928) *Ciliary Movements* (Cambridge Univ Press, Cambridge, UK).
4. Osterman N, Vilfan A (2011) Finding the ciliary beating pattern with optimal efficiency. *Proc Natl Acad Sci USA* 108(38):15727–15732.
5. Elgeti J, Gompper G (2013) Emergence of metachronal waves in cilia arrays. *Proc Natl Acad Sci USA* 110(12):4470–4475.
6. Brennen C, Winet H (1977) Fluid mechanics of propulsion by cilia and flagella. *Annu Rev Fluid Mech* 9:339–398.
7. Pikovsky A, Rosenblum M, Kurths J (2001) *Synchronization* (Cambridge Univ Press, Cambridge, UK).
8. Taylor GI (1951) Analysis of the swimming of microscopic organisms. *Proc R Soc Lond A Math Phys Sci* 209(1099):447–461.
9. Gueron S, Levit-Gurevich K (1999) Energetic considerations of ciliary beating and the advantage of metachronal coordination. *Proc Natl Acad Sci USA* 96(22):12240–12245.
10. Vilfan A, Jülicher F (2006) Hydrodynamic flow patterns and synchronization of beating cilia. *Phys Rev Lett* 96(5):058102.
11. Niedermayer T, Eckhardt B, Lenz P (2008) Synchronization, phase locking, and metachronal wave formation in ciliary chains. *Chaos* 18(3):037128.
12. Golestanian R, Yeomans JM, Uchida N (2011) Hydrodynamic synchronization at low Reynolds number. *Soft Matter* 7:3074.
13. Friedrich BM, Jülicher F (2012) Flagellar synchronization independent of hydrodynamic interactions. *Phys Rev Lett* 109(13):138102.
14. Bennett RR, Golestanian R (2013) Emergent run-and-tumble behavior in a simple model of Chlamydomonas with intrinsic noise. *Phys Rev Lett* 110(14):148102.
15. Polotzek K, Friedrich BM (2013) A three-sphere swimmer for flagellar synchronization. *New J Phys* 15(4):045005.
16. Rüffer U, Nultsch W (1985) High-speed cinematographic analysis of the movement of Chlamydomonas. *Cell Motil* 5(3):251–263.
17. Rüffer U, Nultsch W (1998) Flagellar coordination in Chlamydomonas cells held on micropipettes. *Cell Motil Cytoskeleton* 41(4):297–307.
18. Polin M, Tuval I, Drescher K, Gollub JP, Goldstein RE (2009) Chlamydomonas swims with two "gears" in a eukaryotic version of run-and-tumble locomotion. *Science* 325(5939):487–490.
19. Goldstein RE, Polin M, Tuval I (2009) Noise and synchronization in pairs of beating eukaryotic flagella. *Phys Rev Lett* 103(16):168103.
20. Tam D, Hosoi AE (2011) Optimal feeding and swimming gaits of biflagellated organisms. *Proc Natl Acad Sci USA* 108(3):1001–1006.
21. Bayly PV, et al. (2011) Propulsive forces on the flagellum during locomotion of Chlamydomonas reinhardtii. *Biophys J* 100(11):2716–2725.
22. O'Malley S, Bees MA (2012) The orientation of swimming biflagellates in shear flows. *Bull Math Biol* 74(1):232–255.
23. Brokaw CJ (1975) Effects of viscosity and ATP concentration on the movement of reactivated sea-urchin sperm flagella. *J Exp Biol* 62(3):701–719.
24. Garcia M, Berti S, Peyla P, Rafaï S (2011) Random walk of a swimmer in a low-Reynolds-number medium. *Phys Rev E Stat Nonlin Soft Matter Phys* 83(3 Pt 2):035301.
25. Hunt AJ, Gittes F, Howard J (1994) The force exerted by a single kinesin molecule against a viscous load. *Biophys J* 67(2):766–781.
26. Happel J, Brenner H (1965) *Low Reynolds Number Hydrodynamics* (Kluwer, Boston).
27. Hinsen K (1995) HYDR0LIB : A library for the evaluation of hydrodynamic interactions in colloidal suspensions. *Comput Phys Commun* 88(2-3):327–340.
28. Racey TJ, Hallett R, Nickel B (1981) A quasi-elastic light scattering and cinematographic investigation of motile Chlamydomonas reinhardtii. *Biophys J* 35(3):557–571.
29. Guasto JS, Johnson KA, Gollub JP (2010) Oscillatory flows induced by microorganisms swimming in two dimensions. *Phys Rev Lett* 105(16):168102.
30. Reichert M, Stark H (2005) Synchronization of rotating helices by hydrodynamic interactions. *Eur Phys J E Soft Matter* 17(4):493–500.
31. Hyams JS, Borisy GG (1975) Flagellar coordination in Chlamydomonas reinhardtii: isolation and reactivation of the flagellar apparatus. *Science* 189(4206):891–893.
32. Gorman DS, Levine RP (1965) Cytochrome f and plastocyanin: their sequence in the photosynthetic electron transport chain of Chlamydomonas reinhardi. *Proc Natl Acad Sci USA* 54(6):1665–1669.

Supporting Information

Geyer et al. 10.1073/pnas.1300895110

A. Image Analysis

High-speed movies were analyzed using custom-made Matlab software (MathWorks Inc); our image analysis pipeline is illustrated in Fig. S1. In a first step, estimates for position and orientation of the cell body in a movie frame were obtained by a cross-correlation analysis using rotated template images. In a second step, these position and orientation estimates were refined by tracking the bright phase halo surrounding the cell. The first and second area moments of the cell rim provide accurate estimates for the center of the cell body and its long orientation axis. While the tracking precision of the first step amounts to <500 nm for the position and a few degrees for the orientation, these values are reduced to <50 nm and <0.5° after the second step, respectively. Special care was taken to reduce any potential bias of the flagellar phase on the cell-body tracking; for example, the cell rim close to the flagellar bases was obtained by interpolation instead of direct tracking. The flagellar base is visible as a continuous, parabola-shaped curve that connects the proximal ends of the two flagella; tracking of this flagellar base was done by a combination of line scans and local fitting of a Gaussian line model (step 3). Flagella were tracked by advancing along their length using exploratory line-scans in a successive manner (step 4). Flagellar tracking can be refined by local fitting of a Gaussian line model. A movie consisting of 1,000 frames can be analyzed in an automated manner within 10 h on a standard personal computer. Movies from red-light illumination conditions were of lower quality and required manual correction of the automated tracking results for each frame.

B. Flagellar Shape Analysis

We employ a nonlinear dimension reduction technique to represent tracked flagellar shapes as points in a low-dimensional abstract shape space. In a first step, smoothed tracked flagellar shapes corresponding to one cycle of synchronized flagellar beating (shown in Fig. 1*A*) were used to define the basis of the shape space. Flagellar shapes can be conveniently represented with respect to the material frame of the cell using a tangent angle representation (1, 2). In terms of this tangent angle $\theta(s)$, the $x(s)$ and $y(s)$ coordinates of the flagellar midline as functions of arclength s along the flagellum can be expressed as

$$x(s) = x(0) + \int_0^s d\xi \, \cos[\alpha + \theta(\xi)] \quad \text{and}$$
$$y(s) = y(0) + \int_0^s d\xi \, \sin[\alpha + \theta(\xi)]. \qquad \textbf{[S1]}$$

Here, α is the orientation angle of the long axis of the cell body (Fig. 1*A*), which implies that $\theta(\xi)$ characterizes flagellar shapes with respect to a material frame of the cell body. By averaging the tangent angle profiles $\theta(s,t)$ over a full beat cycle, we define a time-averaged flagellar shape characterized by a tangent angle $\overline{\theta}(s)$. To characterize variations from this mean flagellar shape, we employed a kernel principal component analysis (PCA) (3). The kernel used to compute the Gram matrix D for the kernel PCA must account for the 2π periodicity of the tangent angle data and was taken as $D_{ij} = \int_0^L ds \, \cos[\theta(s,t_i) - \theta(s,t_j)]$. The first three shape eigenmodes account for 97% of the spectrum of D and are shown in Fig. S2*A*. The relative contributions to the spectrum read 67% (first mode), 18% (second mode), and 12% (third mode). Whereas the first mode $\theta_1(s)$ (blue) describes nearly uniform bending of the flagellum, the second mode $\theta_2(s)$ (green) and the third mode $\theta_3(s)$ (red) together comprise the components of a traveling bending wave.

Next, any flagellar shape can be projected onto the shape space spanned by these three shape modes: Given a flagellar midline with coordinates $x(s)$ and $y(s)$, we seek the optimal approximating shape with coordinates $\hat{x}(s)$, $\hat{y}(s)$ whose tangent angle $\hat{\theta}(s)$ is a linear combination of the fundamental shape modes:

$$\hat{\theta}(s) = \overline{\theta}(s) + \beta_1\theta_1(s) + \beta_2\theta_2(s) + \beta_3\theta_3(s). \qquad \textbf{[S2]}$$

The coefficients β_1, β_2, and β_3 are obtained by a non-linear fit that minimizes the squared Euclidean distance $\int_0^{L'} ds |x(s) - \hat{x}(s)|^2 + |y(s) - \hat{y}(s)|^2$. This procedure is robust and works even if flagellar shapes could only be tracked partially with tracked length L' shorter than the total flagellar length L. Note that for nonsmoothed flagellar shapes the tangent angle representations can be noisy and are thus less suitable for fitting as compared to x, y coordinates.

A time sequence of tracked flagellar shapes thus results in a point cloud in the shape space parameterized by the shape mode coefficients β_1, β_2, and β_3. We fitted a closed curve to the torus-like point cloud (Fig. S2*B*, solid line). This closed curve represents a limit cycle of periodic flagellar beating. Each tracked flagellar shape can be assigned the "closest" point on this limit cycle (i.e., the point for which the corresponding flagellar shape has minimal Euclidean distance). By choosing a phase angle parameterization for the limit cycle, the phase angle of each flagellar shape is determined modulo 2π. A time-series of flagellar shapes thus yields a time-series of the flagellar phase angle $\varphi(t)$. The phase angle parameterization of the limit cycle had been chosen such that the flagellar phase angle φ and its time derivative are not correlated. Finally, the zero point $\varphi = 0$ was chosen such that the corresponding flagellar shape was nearly straight and perpendicular to the long cell axis.

C. Computation of Hydrodynamic Friction Forces

For our hydrodynamic computations, we represented a *Chlamydomonas* cell by an ensemble of $N = 300$ equally sized spheres of radius $a = 0.25$ μm. The cell body was chosen spheroidal and is represented by 272 spheres that are arranged in a symmetric fashion to retain mirror symmetries. Each flagellum is represented by a chain of 14 spheres that are aligned along a flagellar midline with equidistant spacing. The shapes of the flagellar midlines depend on respective phase angles φ_L and φ_R for the left and right flagellum. These flagellar shapes were taken from experiment for one full period of synchronized beating and are shown in Fig. 1*A*. We assume that the 272 spheres constituting the cell body move as a rigid sphere cluster. Each of the flagellar spheres represents a cluster with just one sphere, which results in a total of $n = 2 \cdot 14 + 1 = 29$ sphere clusters. We then computed the $6n \times 6n$ grand hydrodynamic friction matrix G for this ensemble of n spheres clusters using a freely available hydrodynamic library based on a Cartesian multipole expansion technique (4). Recall that the grand hydrodynamic friction matrix G relates the forces and torques exerted by the $6n$ sphere clusters to their translational and rotational velocities (5):

$$\mathrm{P}_0 = \mathrm{G} \cdot \dot{\mathrm{q}}_0. \qquad \textbf{[S3]}$$

Here, $\dot{\mathrm{q}}_0$ denotes a $6n$ vector that combines the translational and rotational velocity components of the n sphere clusters,

$$\dot{\mathrm{q}}_0 = \left(v_{1x}, v_{1y}, v_{1z}, \omega_{1x}, \omega_{1y}, \omega_{1z}, \ldots, \omega_{nz}\right), \quad \textbf{[S4]}$$

whereas the $6n$ vector P_0 combines the components of the resultant hydrodynamic friction forces and torques,

$$\mathrm{P}_0 = \left(F_{1x}, F_{1y}, F_{1z}, T'_{1x}, T'_{1y}, T'_{1z}, \ldots, T'_{nz}\right). \quad \textbf{[S5]}$$

(Primed torques represent torques with respect to the center of the respective sphere cluster.) Fig. 2*C* in the main text shows a submatrix of the grand friction matrix, which was defined as $G_{ij,yy} = G_{6i-4,6j-4}$, $i,j = 1,\ldots,n$. In this figure, it was assumed that the long cell body axis is aligned with the y axis of the laboratory frame (i.e., $\alpha = 0$), which implies that the submatrix relates motion in the direction of the long cell axis and the hydrodynamic force components projected on this axis.

For our hydrodynamic computations, the multipole expansion order was chosen as three. An estimate for the accuracy of our computation could be obtained by increasing the expansion order parameter, which changed the computed friction coefficients by less than 1%. Initial tests confirmed that the friction matrix of only the cell body gave practically the same result as the analytic solution for the enveloping spheroid (6); similarly, the computed friction matrix of only a single flagellum matched the prediction of resistive-force theory (7) assuming a flagellar radius equal to the sphere radius. Note that the precise value of the flagellar radius is expected to affect hydrodynamic friction coefficients only as a logarithmic correction (8).

Below, we consider an extension of the theoretical description given in the main text that additionally considers the possibility of an elastically anchored flagellar base, which allows for pivoting of the flagellar basal apparatus (Fig. S9). In this case, the flagellar midlines were rotated by an angle ψ.

A set of 2,400 precomputed configurations was then used to construct a spline-based lookup table of the (reduced) hydrodynamic friction matrix as a function of the degrees of freedom φ_L, φ_R, and ψ. The interpolation error was confirmed to be on the order of 1% or less. This lookup table was then used for the numerical integration of the (stiff) equations of motion, Eqs. **1** and **S17**.

D. Generalized Hydrodynamic Friction Forces

We employ the framework of Lagrangian mechanics of dissipative systems (9) to define generalized hydrodynamic friction forces and derive an equation of motion for the effective degrees of freedom in our theoretical description of *Chlamydomonas* swimming and synchronization. The $6n$ degrees of freedom q_0 for the n sphere clusters used in our hydrodynamic computations are enslaved by the five effective degrees of freedom in our coarse-grained theory (Fig. 1). Below, one more degree of freedom, ψ, is introduced to characterize pivoting of an elastically anchored flagellar basal apparatus. We thus have

$$\mathrm{q}_0 = \mathrm{q}_0(\mathrm{q}), \quad \textbf{[S6]}$$

where we introduced the six-component vector $\mathrm{q} = (x, y, \alpha, \varphi_L, \varphi_R, \psi)$ that comprises the six effective degrees of freedom. The reduced 6×6 hydrodynamic friction matrix Γ for these six effective degrees of freedom can be computed from the grand hydrodynamic friction matrix G as

$$\Gamma = \mathrm{L}^T \cdot \mathrm{G} \cdot \mathrm{L} \quad \textbf{[S7]}$$

with a $6n\times 6$ transformation matrix L given by refs. 10 and 11:

$$L_{ij} = \partial \dot{q}_{0,i} / \partial \dot{q}_j. \quad \textbf{[S8]}$$

The rate of hydrodynamic dissipation can now be equivalently written as a quadratic function of either $\dot{\mathrm{q}}_0$ or $\dot{\mathrm{q}}$:

$$\mathcal{R} = \dot{\mathrm{q}}_0^T \cdot \mathrm{G} \cdot \dot{\mathrm{q}}_0 = \dot{\mathrm{q}}^T \cdot \Gamma \cdot \dot{\mathrm{q}}. \quad \textbf{[S9]}$$

The generalized hydrodynamic friction coefficients Γ_{ij} are depicted in Fig. S3. In this context, generalized hydrodynamic friction forces can be defined as

$$P_j = \Gamma_{jx}\dot{x} + \Gamma_{jy}\dot{y} + \Gamma_{j\alpha}\dot{\alpha} + \Gamma_{jL}\dot{\varphi}_L + \Gamma_{jR}\dot{\varphi}_R + \Gamma_{j\psi}\dot{\psi}, \quad j = x, y, \alpha, L, R, \psi. \quad \textbf{[S10]}$$

Interestingly, the generalized hydrodynamic friction force conjugated to one degree of freedom depends also on the rates of the change of the other degrees of freedom, which implies a coupling between the various degrees of freedom. This fact is illustrated by Fig. S4. Fig. S4*A* depicts the translational velocities of the flagellar spheres caused by pure yawing of the cell body with rate $\dot{\alpha}$. This motion is characterized by a $6n$ vector of velocity components, $\dot{\mathrm{q}}_0^{(\alpha)} = \mathrm{L}\cdot(0,0,\dot{\alpha},0,0,0)^T$. Similarly, the beating of the left flagellum induces hydrodynamic friction forces as shown in Fig. S4*B*. The resultant force (and torque) components are combined in the $6n$ vector $\mathrm{P}_0^{(L)} = \mathrm{G}\cdot\mathrm{L}\cdot(0,0,0,\dot{\varphi}_L,0,0)^T$. Fig. S4 indicates that the scalar product $\dot{\mathrm{q}}_0^{(\alpha)} \cdot \mathrm{P}_0^{(L)} = \dot{\alpha}\Gamma_{\alpha L}\dot{\varphi}_L$ does not vanish, which implies a nonzero friction coefficient $\Gamma_{\alpha L}$ and thus a coupling between cell-body yawing and flagellar beating.

In our theoretical description, the phase dynamics of the left flagellum, say, is governed by a balance of the generalized hydrodynamic friction force P_L and an active driving force Q_L, similarly $Q_R = P_L$ for the right flagellum. In the case of free swimming, force and torque balance imply $P_x = P_y = 0$ and $P_\alpha = 0$. Together with an equation for P_ψ, these equation allow to self-consistently solve for the rate of change $\dot{\mathrm{q}}$ of the 6 degrees of freedom. If one degree of freedom were constrained, $q_j = 0$, the corresponding force equation becomes void, since a constraining force Q_j equal to P_j then balances the generalized hydrodynamic friction force P_j associated with this degree of freedom.

In general, the active driving forces Q_L and Q_R will depend on the flagellar phase. This phase dependence is fully determined by the requirement that the flagellar phase speeds should be constant, $\dot{\varphi}_j = \omega_0$, in the case of synchronized flagellar beating with $\delta = 0$. Here, ω_0 denotes the angular frequency of synchronized flagellar beating. Explicitly, we find

$$Q_L(\varphi_L) = \omega_0\Big[\Gamma_{LL}(\varphi_L,\varphi_L) + \Gamma_{LR}(\varphi_L,\varphi_L) - 2\Gamma_{Ly}^2(\varphi_L,\varphi_L)/\Gamma_{yy}(\varphi_L,\varphi_L)\Big]. \quad \textbf{[S11]}$$

An analogous expression holds for $Q_R(\varphi_R)$. Note that the generalized active driving forces are conjugate to an angle, and therefore have the physical unit piconewtons times micrometer. These phase-dependent active driving forces can be written as potential forces $Q_j = -\partial U/\partial\varphi_j$, $j = L, R$, where the potential U reads

$$U = -\int_{-\infty}^{\varphi_L} d\varphi_L Q_L(\varphi_L) - \int_{-\infty}^{\varphi_R} d\varphi_R Q_R(\varphi_R). \quad \textbf{[S12]}$$

The potential U continuously decreases with time, indicating the depletion of an internal energy store and the dissipation of energy into the fluid during flagellar swimming. The rate of hydrody-

namic dissipation equals the rate at which potential energy is dissipated:

$$\mathcal{R} = -\dot{U} = Q_L\dot{\varphi}_L + Q_R\dot{\varphi}_R. \quad \textbf{[S13]}$$

E. Analytic Expression for the Flagellar Synchronization Strength

We present details on the derivation of Eqs. **5** and **6** for the synchronization strength λ in the case of the reduced equations of motion, Eqs. **2–4**. We assume equal intrinsic beat frequencies, $\omega_L = \omega_R = \omega_0$, and a small initial phase difference, $0 < \delta(0) \ll 1$. To leading order in δ, we find relations that link the rotation rate $\dot{\alpha}$ and the rate $\dot{\delta}$ at which the phase difference changes,

$$k\alpha + \rho(\varphi,\varphi)\dot{\alpha} = -d[\nu(\varphi)\delta]/dt \quad \textbf{[S14]}$$

$$\dot{\delta} = -2\mu(\varphi)\dot{\alpha}. \quad \textbf{[S15]}$$

Here $\varphi \approx \omega_0 t$ denotes the mean flagellar phase. The first equation describes how flagellar asynchrony causes a yawing motion of the cell body, and the second equation describes how this yawing motion then changes the flagellar phase difference. In the absence of any elastic constraint for yawing, $k = 0$, we can solve for $\dot{\delta}$:

$$(\rho - 2\mu\nu)\dot{\delta} = 2\mu\nu'\omega_0\delta. \quad \textbf{[S16]}$$

Now, Eq. **5** follows from Eq. **S16** using $\lambda = -\int_0^T dt\, \dot{\delta}/\delta$ and a variable transformation $\varphi(t) = \omega_0 t + \mathcal{O}(\delta)$.

In the case of a very stiff elastic constraint with $k \gg \rho\omega_0$, we make use of the fact that variations of the phase difference δ during one beat cycle will be small compared to its mean value $\delta_0 = \langle\delta\rangle$. As a consequence, Eq. **S14** can be approximated as $k\alpha = -\nu'\omega_0\delta_0$. Using this approximation and Eq. **S15**, Eq. **6** follows.

F. Comparison of Experiment and Theory

We can compare instantaneous swimming velocities predicted by our hydrodynamic computation with experimental measurements and find favorable agreement (Fig. 3 and Fig. S5). Note that wall effects present in our experiments, but not accounted for by our hydrodynamic computations, are expected to reduce translational velocities (but less so rotational velocities) (12). The hydrodynamic computations are based on a fixed flagellar beat pattern parameterized by a flagellar phase angle, which was obtained experimentally for one beat cycle with synchronized beating (Fig. 1*A*). The good agreement between theoretical predictions and experimental measurements for the instantaneous swimming velocities further validate our reductionist description of the flagellar shape dynamics by just a single phase variable for each flagellum. Next, we tested the applicability of the reduced equations of motion, Eqs. **2–4**, in the experimental situation. For this aim, we reconstructed the coupling functions $\mu(\varphi)$, $\nu(\varphi)$ and $\rho(\varphi)$ from experimental time series data for $\dot{\alpha}$, $\dot{\varphi}_L$, and $\dot{\varphi}_R$. The coupling functions were represented by truncated Fourier series and the unknown Fourier coefficients determined by a linear regression of Eqs. **2**, **3**, or **4**, respectively (Fig. S6). Repeating this fitting procedure for data from six different cells gave consistent results (Fig. S7). Moreover, the phase dependence of the fitted coupling functions agrees qualitatively with our theoretical predictions. Note that our simple theory does not involve any adjustable parameters.

G. An Elastically Anchored Flagellar Basal Apparatus

In the main text, we had assumed for simplicity that the flagellar base is rigidly anchored to the cell body. Whereas the proximal segments of the two flagella are tightly mechanically coupled with each other by so-called striated fibers to form the flagellar basal apparatus, the flagellar basal apparatus itself is only connected to an array of 16 long microtubules spanning the cell (13). We now consider the possibility that this anchorage allows for some pivoting of the flagellar basal apparatus as a whole by an angle ψ (Fig. S9*A*). In addition to the 5 degrees of freedom of *Chlamydomonas* beating and swimming considered in the main text (Fig. 1), we now include this pivot angle ψ as a 6th degree of freedom. The rate of hydrodynamic dissipation is now given by $\mathcal{R} = \dot{x}P_x + \dot{y}P_y + \dot{\alpha}P_\alpha + \dot{\varphi}_L P_L + \dot{\varphi}_R P_R + \dot{\psi}P_\psi$, with P_ψ being the generalized hydrodynamic friction force conjugate to the pivot angle ψ. Assuming Hookean behavior for the elastic basal anchorage with rotational pivoting stiffness $\bar{k}$, we readily arrive at an equation of motion that reads in the case of free swimming:

$$(\dot{x}, \dot{y}, \dot{\alpha}, \dot{\varphi}_L, \dot{\varphi}_R, \dot{\psi})^T = \Gamma^{-1}\left(0, 0, 0, Q_L, Q_R, -\bar{k}\psi\right)^T. \quad \textbf{[S17]}$$

Fig. S9*B* shows flagellar synchronization for a free-swimming cell with elastically anchored flagellar base: Although some basal pivoting occurs as a result of flagellar asynchrony, the swimming and synchronization behavior is very similar to the case of a rigidly anchored flagellar base, as shown in Fig. 4*A*. For a cell that can neither translate nor yaw, however, the situation is different (Fig. S9*C*). We find strong flagellar synchronization provided the elastic stiffness $\bar{k}$ is not too large. Flagellar synchronization by basal pivoting is thus effective also for a fully clamped cell. In contrast, for a rigidly anchored flagellar base, the synchronization strength λ would be relatively weak in this case, being due only to direct hydrodynamic interactions between the two flagella.

Flagellar synchronization by basal pivoting is conceptually very similar to synchronization by cell-body yawing as discussed in the main text. In the case of a fully clamped cell, we can approximate the synchronization dynamics by virtually the same generic equation of motion as Eqs. **2–4**, when we substitute ψ for α:

$$\dot{\varphi}_L = \omega_0 - \bar{\mu}(\varphi_L)\dot{\psi}, \quad \textbf{[S18]}$$

$$\dot{\varphi}_R = \omega_0 + \bar{\mu}(\varphi_R)\dot{\psi}, \quad \textbf{[S19]}$$

$$\bar{k}\psi + \bar{\rho}(\varphi_L, \varphi_R)\dot{\psi} = -\bar{\nu}(\varphi_L)\dot{\varphi}_L + \bar{\nu}(\varphi_R)\dot{\varphi}_R. \quad \textbf{[S20]}$$

Here, the coupling functions $\bar{\mu}$, $\bar{\nu}$, and $\bar{\rho}$ play a similar role as the previously defined μ, ν , and ρ for Eqs. **2–4** and show a qualitatively similar dependence on the flagellar phase (Fig. S10). To derive Eqs. **S18–S20**, we neglected direct hydrodynamic interactions between the two flagella and approximated the active driving forces by $Q_L(\varphi) = \omega_0\Gamma_{LL}(\varphi,\varphi)_{|\psi=0}$ and $Q_R(\varphi) = \omega_0\Gamma_{RR}(\varphi,\varphi)_{|\psi=0}$. The coupling functions are defined as $\bar{\mu}(\varphi) = -\Gamma_{L\psi}(\varphi,\varphi)/\Gamma_{LL}(\varphi,\varphi)_{|\psi=0}$, $\bar{\nu}(\varphi) = -\Gamma_{\psi L}(\varphi,\varphi)_{|\psi=0}$, and $\bar{\rho}(\varphi,\varphi) = \Gamma_{\psi\psi}(\varphi_L,\varphi_R)_{|\psi=0}$. This choice retains the key nonlinearities of the full equation of motion (Fig. S3). Eq. **S18** states that pivoting of the flagellar basal apparatus with $\dot{\psi} > 0$ slows down the effective stroke of the left flagellum (and speeds up the right flagellum). For synchronized flagellar beating, there will be no pivoting of the flagellar base. For asynchronous beating, however, the flagellar base will be rotated out of its symmetric rest position by an angle ψ if the stiffness $\bar{k}$ is not too large. Any pivoting motion of the flagellar base during the beat cycle changes the hydrodynamic friction forces that oppose the flagellar beat, which in turn can either slow down or speed up the respective flagellar beat cycles, and thus restore flagellar synchrony.

To gain further analytical insight, we study the response of the dynamical system in Eqs. **S18–S20** after a small perturbation $0 < \delta(0) \ll 1$. To leading order in $\delta = \varphi_L - \varphi_R$, we find (with $\varphi \approx \omega_0 t$)

$$\bar{k}\psi + \rho(\varphi,\varphi)\dot{\psi} = -d[\bar{\nu}(\varphi)\delta]/dt, \quad \textbf{[S21]}$$

$$\dot{\delta} = -2\bar{\mu}(\varphi)\dot{\psi}. \quad \textbf{[S22]}$$

In the biologically relevant case of a relatively stiff basal anchorage of the flagellar basal apparatus with $\bar{k} \gg \rho\omega_0$, we find for the synchronization strength a result analogous to Eq. **6**:

$$\bar{\lambda} = -\oint_0^{2\pi} d\varphi \; \frac{\bar{\mu}(\varphi)\bar{\nu}''(\varphi)}{\bar{k}/\omega_0}. \qquad \textbf{[S23]}$$

1. Riedel-Kruse IH, Hilfinger A, Howard J, Jülicher F (2007) How molecular motors shape the flagellar beat. *HFSP J* 1(3):192–208.
2. Friedrich BM, Riedel-Kruse IH, Howard J, Jülicher F (2010) High-precision tracking of sperm swimming fine structure provides strong test of resistive force theory. *J Exp Biol* 213(Pt 8):1226–1234.
3. Scholkopf B, Smola AJ, Bernhard S (2002) *Learning with Kernels: Support Vector Machines, Regularization, Optimization, and Beyond* (*Adaptive Computation and Machine Learning*) (MIT, Cambridge, MA).
4. Hinsen K (1995) HYDR0LIB : A library for the evaluation of hydrodynamic interactions in colloidal suspensions. *Comput Phys Commun* 88:327–340.
5. Happel J, Brenner H (1965) *Low Reynolds Number Hydrodynamics* (Kluwer, Boston).
6. Perrin F (1934) Mouvement Brownien d'un ellipsoide (I). Dispersion diélectrique pour des molécules ellipsoidales. *J Phys Radium* 7:497–511.
7. Gray J, Hancock GT (1955) The propulsion of sea-urchin spermatozoa. *J Exp Biol* 32:802–814.
8. Brennen C, Winet H (1977) Fluid mechanics of propulsion by cilia and flagella. *Annu Rev Fluid Mech* 9:339–398.
9. Goldstein H, Poole C, Safko J (2002) *Classical Mechanics* (Addison-Wesley, Reading, MA), 3rd Ed.
10. Friedrich BM, Jülicher F (2012) Flagellar synchronization independent of hydrodynamic interactions. *Phys Rev Lett* 109(13):138102.
11. Polotzek K, Friedrich BM (2013) A three-sphere swimmer for flagellar synchronization. *New J Phys* 15:045005.
12. Bayly PV, et al. (2011) Propulsive forces on the flagellum during locomotion of Chlamydomonas reinhardtii. *Biophys J* 100(11):2716–2725.
13. Ringo DL (1967) Flagellar motion and fine structure of the flagellar apparatus in Chlamydomonas. *J Cell Biol* 33(3):543–571.

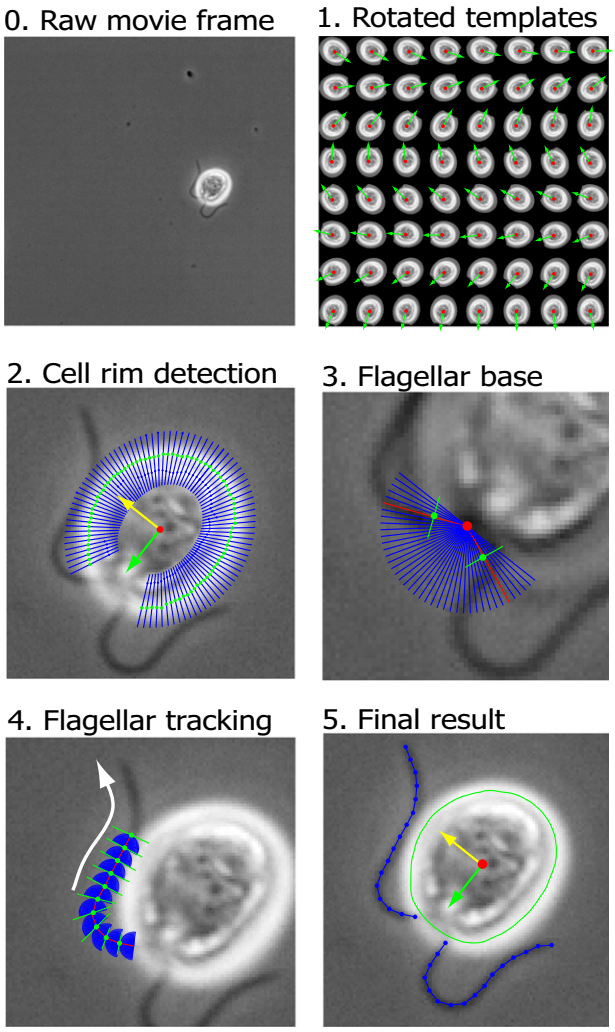

Fig. S1. Image analysis pipeline used to automatically track planar cell position and orientation as well as flagellar shapes in high-speed movies of swimming *Chlamydomonas* cells. (*0*) A typical movie frame. (*1*) Rotated template images used for a cross-correlation analysis to estimate cell position and orientation in a movie frame. (*2*) The cell body outline was tracked by detecting intensity maxima (green) of line scans along rays (shown in blue), which emanate from the putative cell-body center. From the cell-body outline, we obtain refined estimates for cell position and orientation. (*3*) The position of the flagellar base was then determined using a fan of line scans (along the blue lines), followed by a line scan (green) in a direction perpendicular to the maximal intensity direction (red). (*4*) Finally, flagellar shapes were tracked in a successive manner using combinations of line scans similar to those in step 3. (*5*) The final result of our tracking software provides for each frame: cell body position (red dot) and orientation (green arrow), cell body rim (green), as well as center lines of the two flagella (blue).

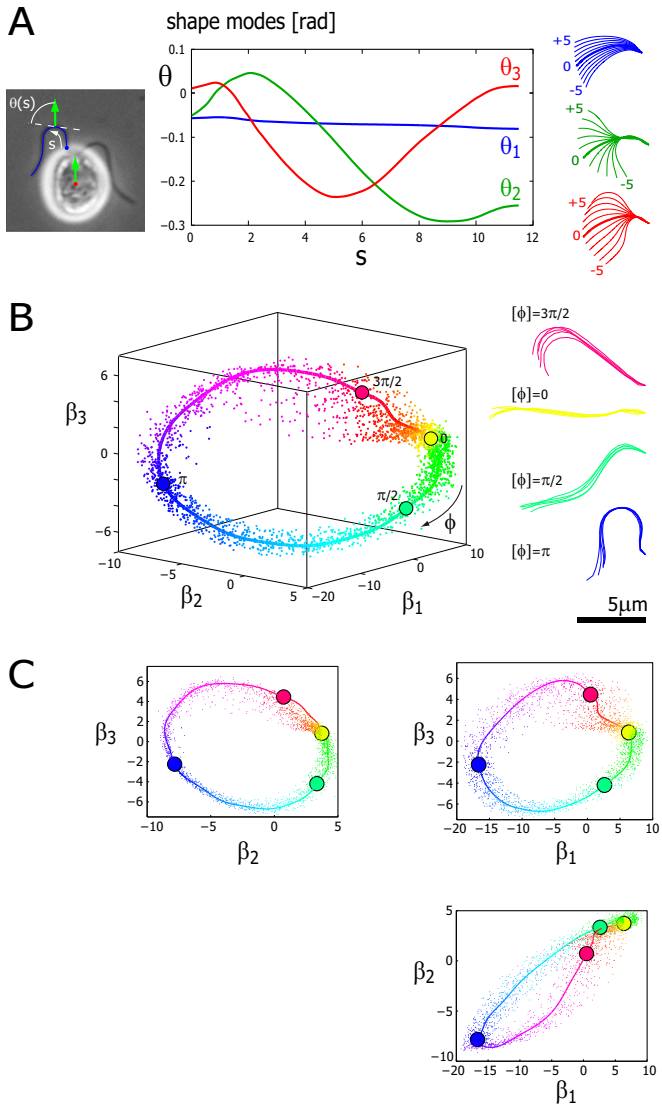

Fig. S2. We represent a single flagellar shape by $n=3$ shape coefficients as a point in an abstract shape space that is spanned by three principal shape modes. (*A*) The principal shape modes were determined by employing a kernel PCA to the tangent angle representation $\theta(s)$ of smoothed flagellar shapes that were tracked from the left flagellum of cell no. 2 during one beat cycle of synchronized flagellar beating. From the PCA, we obtained three dominant shape modes with respective tangent angle representations $\theta_1(s)$, $\theta_2(s)$, and $\theta_3(s)$ as shown. Together, these principal shape modes account for 97% of the variance of this tangent angle dataset. For sake of illustration, exemplary flagellar shapes corresponding to the superposition of the mean flagellar shape and just one shape mode with tangent angle $\overline{\theta}(s)+\beta_i\theta_i(s)$, $i=1,2,3$ are shown to the right $(-5\leq\beta_i\leq 5)$. (*B*) Each tracked flagellar shape from one flagellum can be represented by a single point in an abstract shape space that is spanned by the three principal shape modes. More specifically, the coordinates $(\beta_1,\beta_2,\beta_3)$ of this point are obtained by approximating the tracked flagellar shape by a superposition of a previously computed mean flagellar shape and the three principal shape modes (Eq. **S2**). The set of flagellar shapes from an entire experimental movie thus corresponds to a point cloud. This point cloud scatters around a closed curve (solid line), which reflects the periodic nature of the flagellar beat. This closed curve has been obtained by a simple fit to the point cloud of flagellar shapes and can be considered as a limit cycle of flagellar beating. Deviations from this limit cycle measure the variability of the flagellar beat. We can use this representation to define a distinct flagellar phase angle φ (modulo 2π) for each tracked flagellar shape as indicated by the color code by mapping each flagellar shape onto the limit cycle. A time series of flagellar shapes thus yields a time series of the flagellar phase angle $\varphi(t)$. As an illustration of this assignment, superpositions of flagellar shapes are shown to the right, each of which corresponds to flagellar shapes that were assigned the same flagellar phase modulo 2π. (*C*) Two-dimensional projections corresponding to the three-dimensional shape space representation in *B*.

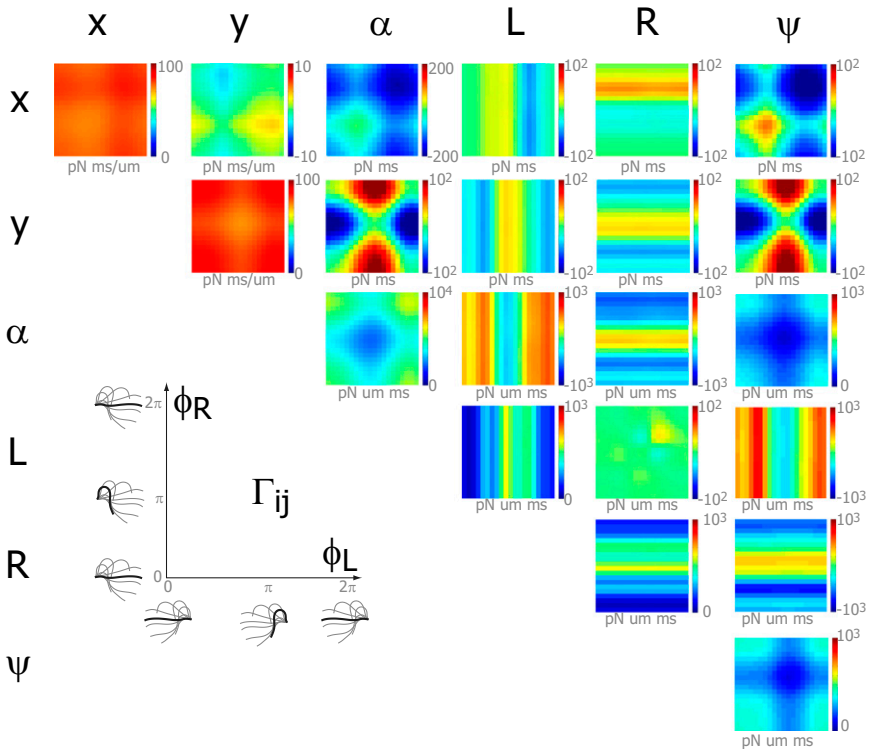

Fig. S3. Generalized hydrodynamic friction matrix Γ_{ij} associated with the effective degrees of freedom x, y, α, φ_L, φ_R, and ψ. This generalized friction matrix determines the generalized hydrodynamic friction forces P_i conjugate to the degrees of freedom $\mathrm{q}=(x,y,\alpha,\varphi_L,\varphi_R,\psi)$ as $P_i=\Gamma_{ij}\dot{q}_j$, and is computed as a projection of the grand hydrodynamic friction matrix (Eq. **S7**). Each friction coefficient Γ_{ij} is a periodic function of the two phase angles φ_L and φ_R, $\Gamma_{i,j}=\Gamma_{i,j}(\varphi_L,\varphi_R)$ and is represented as a color plot with axes as indicated. Here, α is set to zero; different values of α would correspond to a simple rotation of the matrix shown. By Onsager symmetry, $\Gamma_{ij}=\Gamma_{ji}$. Several features are noteworthy. The coefficient Γ_{LR} characterizes hydrodynamic interactions between the two flagella and is found to be small compared to, for example, Γ_{LL}. The other coefficients $\Gamma_{Lj}=\Gamma_{jL}$, which set the friction force P_L conjugate to φ_L, depend strongly on φ_L, but almost not on φ_R. This is yet another manifestation of the fact that direct hydrodynamic interactions between the two flagella are comparably weak. Analogous statements hold for the coefficients Γ_{Rj}. A counter-clockwise rotation of the cell, $\dot{\alpha}>0$, will increase the friction force P_L during the effective stroke of the left flagellum $(\Gamma_{L\alpha}>0)$ but decrease the corresponding respective friction force P_R for the right flagellum during its effective stroke $(\Gamma_{R\alpha}<0)$. Mirror symmetry of the swimmer amounts to invariance of the friction matrix under the substitution $(x,y,\alpha,\varphi_L,\varphi_R)\rightarrow(-x,y,-\alpha,\varphi_R,\varphi_L)$, which implies a number of symmetry relations, for example, $\rho=\Gamma_{\alpha\alpha}$ must be symmetric in φ_L and φ_R. Finally, this rotational friction coefficient $\rho=\Gamma_{\alpha\alpha}$ depends on the flagellar phases in a more pronounced way than the translational friction coefficients Γ_{xx} and Γ_{yy}. This is in line with the general fact that rotational friction coefficients depend more strongly (as $\sim l^3$) on the effective linear dimension l of an object than translational friction coefficients $(\sim l)$. The coefficients $\Gamma_{j\alpha}$ and $\Gamma_{j\psi}$ associated with yawing of the whole cell and pivoting of the flagellar apparatus, respectively, show a similar dependence on the flagellar phases.

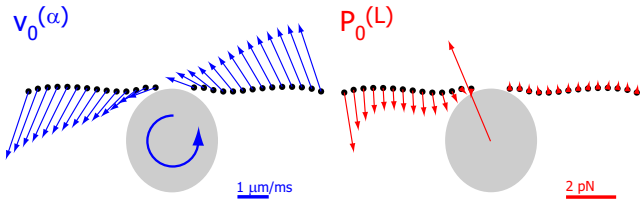

Fig. S4. Coupling of cell-body yawing and flagellar beating. (*Left*) Translational velocities of the flagellar spheres used in our hydrodynamic computation associated with a pure yawing motion of the cell body with rate $\dot{\alpha}$. (*Right*) Hydrodynamic friction forces exerted by the flagellar spheres (as well as by the cell body), if the left flagellum advances along its beat cycle with rate $\dot{\varphi}_L$. The generalized hydrodynamic friction coefficient $\Gamma_{\alpha L}$ that couples cell-body yawing and beating of the left flagellum can be computed as a scalar product between the velocity profile resulting from yawing and the force profile resulting from flagellar beating and is found to be non-zero. Parameters: $\dot{\varphi}_L=\omega_0$, $\dot{\alpha}=0.2\omega_0$, and $2\pi/\omega_0=30$ ms.

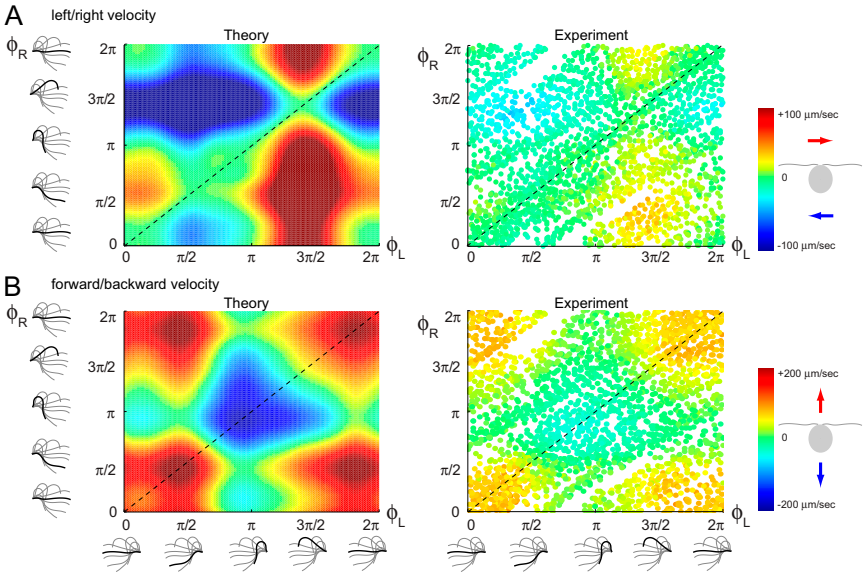

Fig. S5. (*A*) Instantaneous swimming velocity in the direction perpendicular to the long cell axis as a function of the flagellar phase angles φ_L and φ_R. For synchronized flagellar beating (dashed line), this velocity vanishes in our theory for symmetry reasons (green). If the two flagella are out of synchrony, however, significant sideward motion of the cell is observed, both in theory and experiment. Note that wall effects present in the experiments, but not considered in the computations, reduce translational velocities. (*B*) Instantaneous swimming velocity in the direction of the long cell axis, again as a function of the flagellar phase angles.

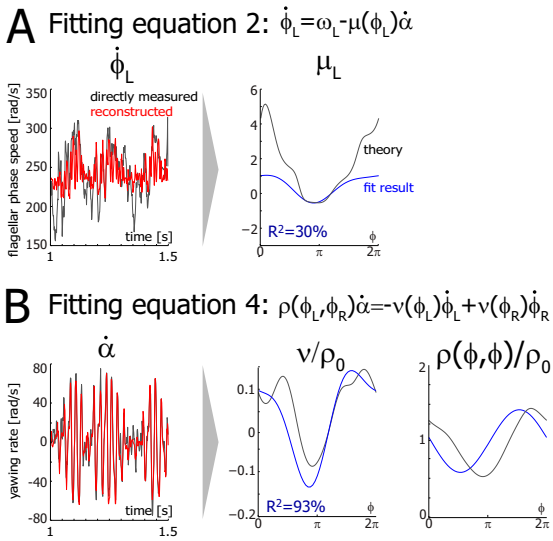

Fig. S6. The reduced equations of motion, Eqs. **2**–**4**, were fitted to experimental time-series data for the yawing rate $\dot{\alpha}$ of the cell, as well as the flagellar phase speeds $\dot{\varphi}_L$ and $\dot{\varphi}_R$. This provided experimental estimates for the phase-dependent coupling functions μ, ν, and ρ. Specifically, we represented each coupling function as a truncated Fourier series and determined the unknown Fourier coefficients by a linear regression using Eqs. **2**–**4**. (*A*) Linear regression of Eq. **2**. Shown to the left in black is the instantaneous flagellar phase speed of the left flagellum $\dot{\varphi}_L$ (smoothed with a span of 15 ms). Shown in red is a reconstructed phase speed $\omega_L-\mu_L(\varphi_L)\dot{\alpha}$ that depends on the instantaneous cell-body yawing rate $\dot{\alpha}$, as well as the intrinsic flagellar frequency ω_L and phase-dependent coupling function μ_L for the left flagellum, which were obtained by the fit. The coefficient of determination was $R^2=30\%$. The estimate for μ_L obtained from this fit is shown to the right (blue), together with a theoretical prediction (black) (see also Fig. 5*A*). (*B*) Linear regression of Eq. **4**. Shown to the left is the measured instantaneous yawing rate $\dot{\alpha}$ of the cell body (black) and a yawing rate reconstructed from the flagellar phase dynamics, $[-\nu(\varphi_L)\dot{\varphi}_L+\nu(\varphi_R)\dot{\varphi}_R]/\rho(\varphi_L,\varphi_R)$ (red). The coefficient of determination was $R^2=93\%$. From this fit, we obtain an experimental estimate for the coupling functions $\nu(\varphi)$ and $\rho(\varphi_L,\varphi_R)$ (blue); theoretical predictions are shown in black.

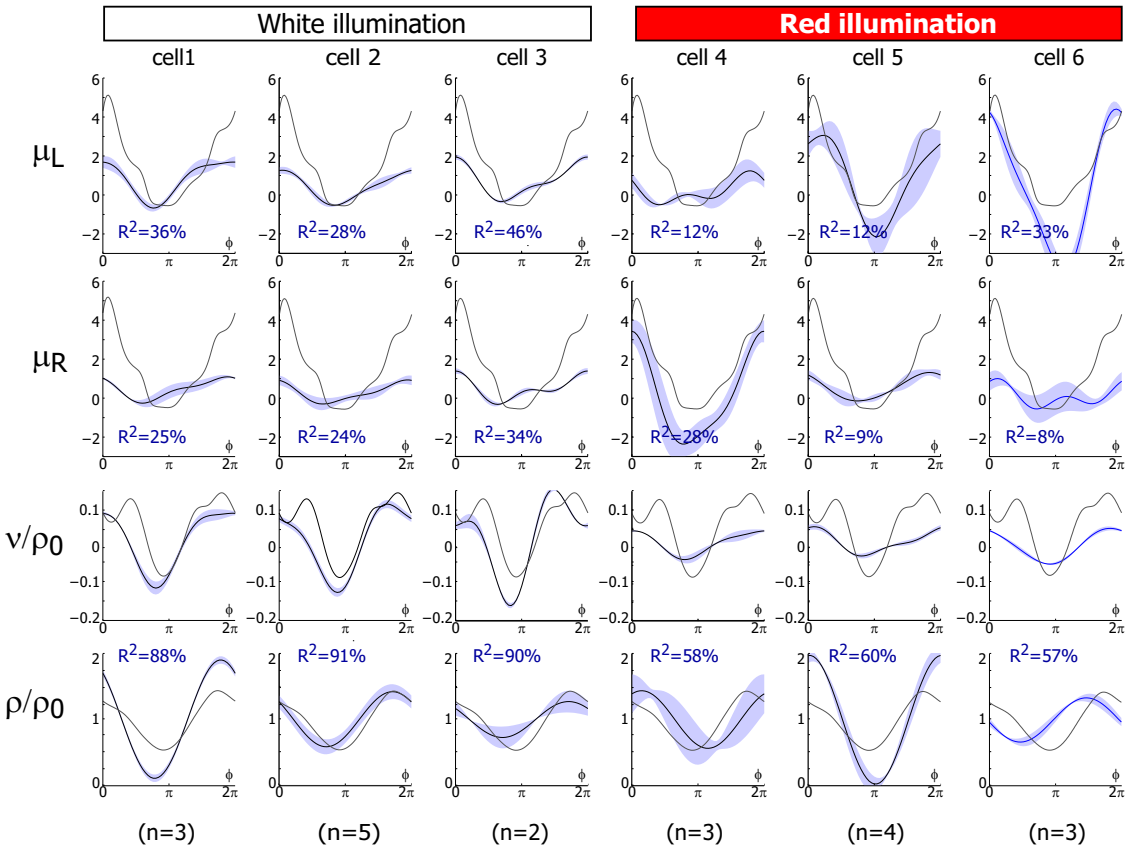

Fig. S7. Experimental fits for the coupling functions μ, ν, and ρ introduced in Eqs. **2–4** (blue curves, shaded regions indicate mean $\pm$ SE) and theoretical predictions (black). The coupling functions μ, ν, and ρ relate flagellar beating and cell-body yawing. Fitting results are shown for six different cells illuminated by either white or red light as indicated. For each cell, we employed n fits using n nonoverlapping time series of duration 0.4–0.5 s with n as indicated. The blue curves represent the average of the fitted coupling functions for the n fits; the averaged coefficient of determination R^2 is stated.

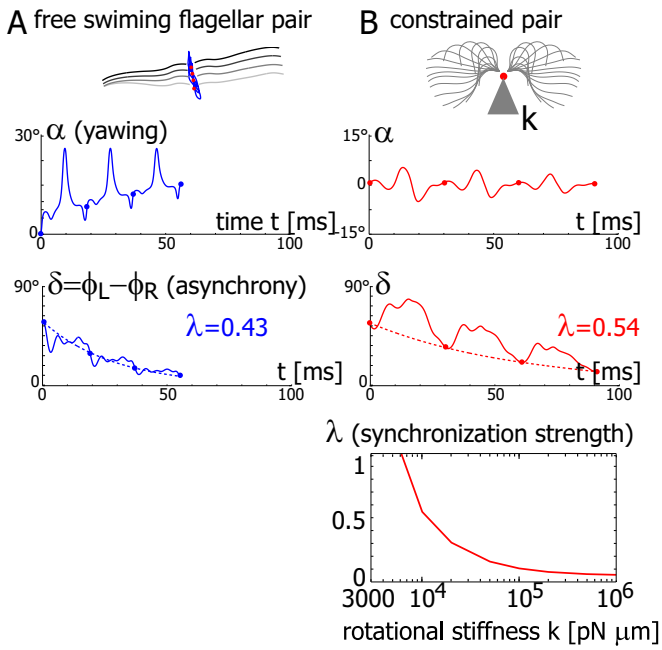

Fig. S8. Theory of flagellar synchronization for an isolated flagellar pair. Inspired by experiments by Hyams and Borisy (1) reporting synchronization in isolated flagellar pairs, we computed the swimming and synchronization behavior of a flagellar pair with cell body removed. For the computations, we used flagellar shapes and flagellar driving forces $Q_j(\varphi)$, $j=L,R$, determined from an intact cell (Fig. 1) (*A*) For a free-swimming flagellar pair, we observe a characteristic yawing motion of the flagellar pair characterized by $\alpha(t)$, if the two flagella are initially out of synchrony. The flagellar phase difference δ is found to decrease with time (solid line), approximately following an exponential decay (dotted line). This implies that the in-phase synchronized state is stable with respect to perturbations. Each completion of a full beat cycle of the left flagellum is marked by a dot. (*B*) To mimic experiments in which external forces constrain the motion of the flagellar pair, we simulated the idealized case of a pair that cannot translate, while yawing of the pair is constricted by an elastic restoring torque $Q_\alpha = -k\alpha$ that acts at the basal apparatus (red dot). As in the case of a free-swimming pair, the flagellar phase difference δ decays with time, indicating stable synchronization. In the case of a constrained cell, the synchronization strength λ strongly depends on the clamping stiffness k. Parameters: $2\pi/\omega_0 = 30$ ms, $k = 10^4$ pN μm/rad. To enhance numerical stability, we added a small constant $\kappa = 10$ pN μm ms to the flagellar friction coefficients, $\Gamma_{jj}(\varphi_L,\varphi_R)$, $j=L,R$, which corresponds to internal dissipation (2).

1. Hyams JS, Borisy GG (1975) Flagellar coordination in *Chlamydomonas reinhardtii*: isolation and reactivation of the flagellar apparatus. *Science* 189(4206):891–893.
2. Friedrich BM, Jülicher F (2012) Flagellar synchronization independent of hydrodynamic interactions. *Phys Rev Lett* 109(13):138102.

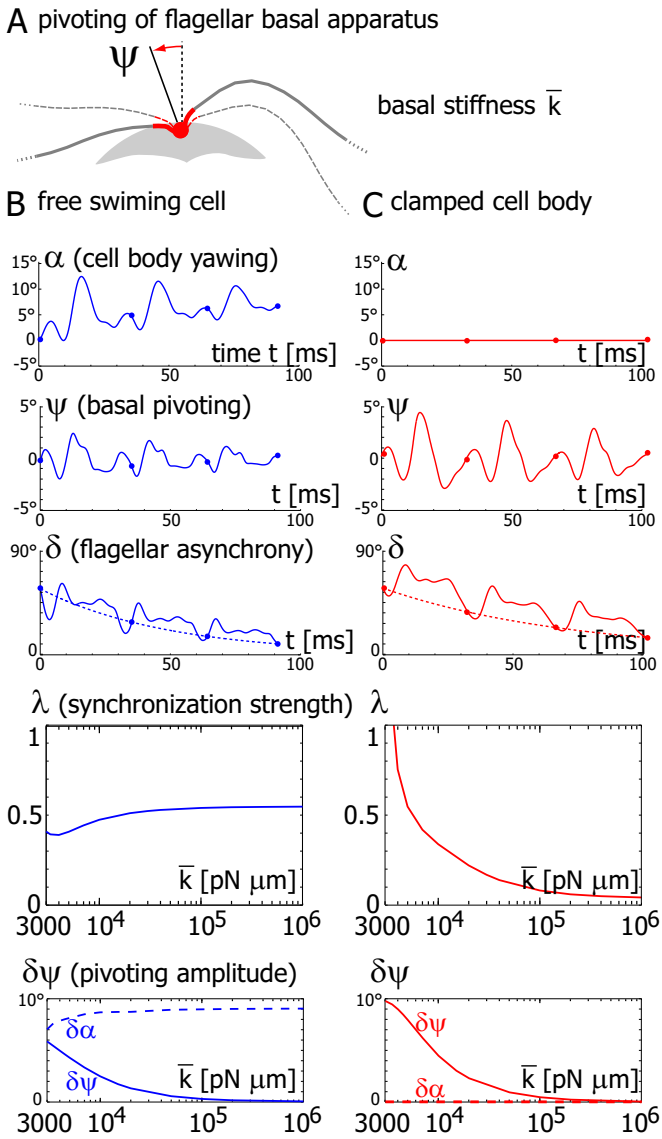

Fig. S9. Theory of flagellar synchronization by basal pivoting. (*A*) We consider the possibility of an elastically anchored flagellar basal apparatus (red), which allows for pivoting of the basal apparatus (solid lines) by an angle ψ from its symmetric reference configuration (dashed lines). (*B*) For a free-swimming cell, the equation of motion, Eq. **S17**, predicts both a yawing motion of the cell characterized by $\alpha(t)$ and a pivoting motion of the flagellar base characterized by $\psi(t)$, if the two flagella are initially out of synchrony. The flagellar phase difference δ is found to decrease with time (solid line), approximately following an exponential decay (dotted line). This implies that the in-phase synchronized state is stable with respect to perturbations. Each completion of a full beat cycle of the left flagellum is marked by a dot. The synchronization behavior in the case of an elastically anchored flagellar basal apparatus is nearly identical to the case of a stiff anchorage, as shown in the main text in Fig. 4. The lowest panel shows typical amplitudes of basal pivoting ($\delta\psi$, solid line) and cell-body yawing ($\delta\alpha$, dashed line) as a function of basal stiffness $\bar{k}$. Amplitudes were determined as half the range of variation during one beat cycle for an initial phase difference of $\delta(0)=\pi/2$. (*C*) For a clamped cell that can neither translate nor rotate, the flagellar apparatus can still pivot and will do so if the two flagella are initially out of phase. As in the case of a free-swimming cell, the flagellar phase difference δ decays with time, indicating stable synchronization. In the case of a clamped cell, the synchronization strength λ strongly depends on the stiffness $\bar{k}$ of the elastic anchorage of the basal flagellar apparatus, which sets the amplitude of basal pivoting. Parameters: $2\pi/\omega_0=30$ ms, $\bar{k}=10^4$ pN μm/rad.

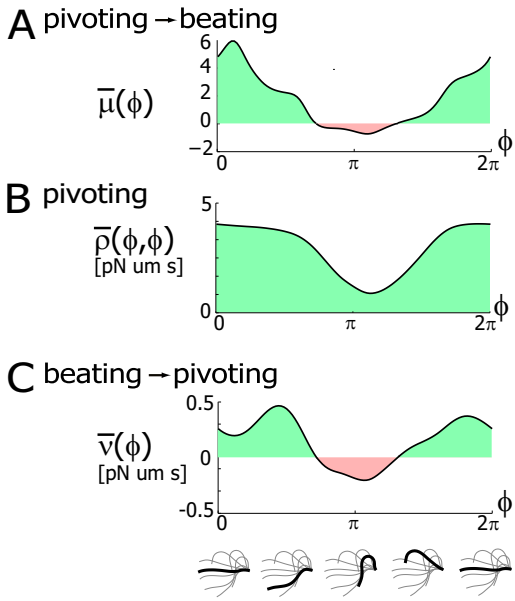

Fig. S10. Theoretical coupling functions for the case of a pivoting flagellar base. (*A*) A pivoting motion of the flagellar base changes the hydrodynamic friction force associated with flagellar beating and thereby speeds up or slows down the flagellar beat cycle in our theory. This effect is quantified by a coupling function $\bar{\mu}$ (Eq. **S18**). (*B*) Hydrodynamic friction associated with pivoting of the flagellar base (and the attached flagella) is characterized by a friction coefficient $\bar{\rho}$ (Eq. **S20**). This friction coefficient is maximal when the two flagella extend maximally from the cell body during their effective stroke. (*C*) The beat of the left flagellum causes pivoting of the flagellar base. This effect is quantified by a coupling function $\bar{\nu}$ (Eq. **S20**).

Active Phase and Amplitude Fluctuations of Flagellar Beating

Rui Ma,[1,2] Gary S. Klindt,[1] Ingmar H. Riedel-Kruse,[3] Frank Jülicher,[1] and Benjamin M. Friedrich[1,*]
[1]Max Planck Institute for the Physics of Complex Systems, 01187 Dresden, Germany
[2]Institute for Advanced Study, Tsinghua University, 100084 Beijing, China
[3]Department of Bioengineering, Stanford University, Stanford, California 94305, USA
(Received 27 January 2014; published 21 July 2014)

The eukaryotic flagellum beats periodically, driven by the oscillatory dynamics of molecular motors, to propel cells and pump fluids. Small but perceivable fluctuations in the beat of individual flagella have physiological implications for synchronization in collections of flagella as well as for hydrodynamic interactions between flagellated swimmers. Here, we characterize phase and amplitude fluctuations of flagellar bending waves using shape mode analysis and limit-cycle reconstruction. We report a quality factor of flagellar oscillations $Q = 38.0 \pm 16.7$ (mean $\pm$ s.e.). Our analysis shows that flagellar fluctuations are dominantly of active origin. Using a minimal model of collective motor oscillations, we demonstrate how the stochastic dynamics of individual motors can give rise to active small-number fluctuations in motor-cytoskeleton systems.

DOI: 10.1103/PhysRevLett.113.048101 PACS numbers: 87.16.Qp, 05.40.Ca, 47.63.Gd, 87.18.Tt

Systems far from equilibrium such as living matter display active, nonthermal fluctuations as well as directed motion and oscillations, which are important for biological function. As a prominent example, molecular motors coupled to cytoskeletal filaments convert chemical energy into work and heat to generate motion at the cellular scale. Motor-filament systems can drive mechanical oscillations including spontaneous hair bundles oscillations in the ear [1], mitotic spindle oscillations during cell division [2], sarcomere oscillations in insect flight muscle [3], and the regular bending waves of cilia and flagella, which propel cells in a liquid including sperm and green algae [4], as well as clear mucus in mammalian airways [5]. Cilia and flagella are slender cell appendages of 10–100 μm length, ubiquitously found in nonbacterial cells, which comprise a conversed cylindrical scaffold of microtubules interspersed by dynein molecular motors.

The collective dynamics of the motors working against a viscoelastic load drives flagellar oscillations via a dynamic instability [6]. Force generation by individual motors relies on the stochastic progression through a mechanicochemical cycle [7]. The stochastic nature of force generation should manifest itself in oscillations that display a characteristic level of noise, representative of active fluctuations. Intriguingly, previous work reported Fourier peaks of finite width in power spectra of flagellar oscillations [8] and phase slips in pairs of synchronized flagella [9–11], which allowed an indirect assessment of flagellar noise. A direct measurement of flagellar fluctuations is pending, let alone a mechanistic understanding. Flagellar fluctuations impart on biological function: Phase fluctuations of flagellar beating should counteract synchronization in collections of flagella, which is important for fast swimming [12] and efficient fluid pumping [13]. Amplitude fluctuations will result in noisy swimming paths of flagellated swimmers and impart on hydrodynamic interactions between swimmers [14].

Here, we report direct measurements of phase and amplitude fluctuations of the flagellar beat and discuss the microscopic origin of active flagellar fluctuations using a minimal model. We further illustrate the impact of flagellar fluctuations on swimming and synchronization. Our analysis contributes to a recent interest in driven, out-of-equilibrium systems and their fluctuation fingerprint [15–18] by characterizing noisy limit-cycle dynamics in an ubiquitous motility system, the flagellum.

Flagellar shape analysis.—We characterize flagellar beat patterns as the superposition of principal shape modes. This dimensionality reduction is key to our fluctuation analysis. We analyze planar beat patterns of bull sperm swimming close to a boundary surface [19], filmed at 250 frames/s (corresponding to about 8 frames per beat cycle). The flagellar centerline $\mathbf{r}(s,t)$, tracked as function of arclength position s and time t, can be expressed with respect to a material frame of the sperm head in terms of a tangent angle $\psi(s,t)$

$$\mathbf{r}(s,t) = \mathbf{r}_h(t) - \int_0^s ds'[\cos\psi(s',t)\mathbf{e}_1 + \sin\psi(s',t)\mathbf{e}_2]. \tag{1}$$

Here, $\mathbf{r}_h(t)$ denotes the sperm head center, and $\mathbf{e}_1$ and $\mathbf{e}_2$ are orthonormal vectors with $\mathbf{e}_1$ pointing along the long head axis; see Fig. 1(a). A space-time plot of $\psi(s,t)$ reveals the periodicity of the flagellar beat; see Fig. 1(b). This high-dimensional data set can be projected on a low-dimensional "shape space" using shape mode analysis based on principal component analysis [20]. The time-averaged tangent angle $\psi_0(s) = \sum_{i=1}^n \psi(s,t_i)/n$ characterizes the mean

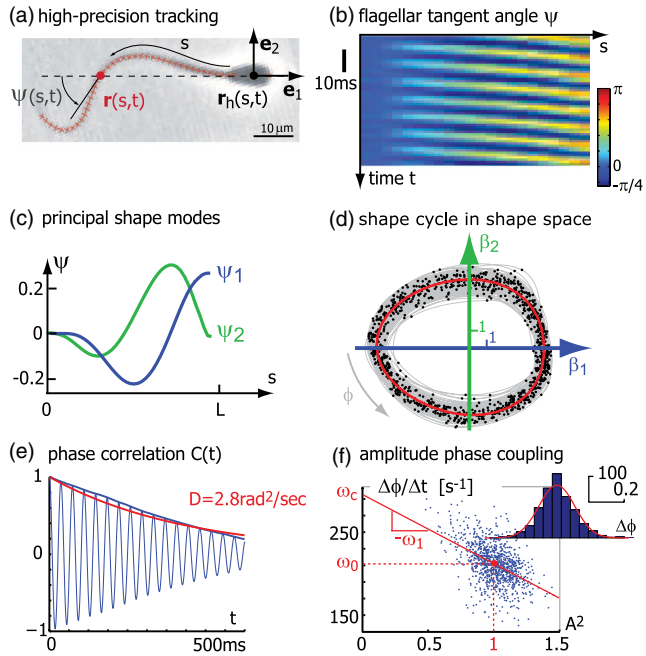

FIG. 1 (color online). The flagellar beat of sperm cells displays active fluctuations. (a) Tracked flagellar shapes are conveniently characterized by a tangent angle $\psi(s,t)$. (b) The kymograph of this tangent angle reveals the periodicity of the flagellar beat. (c) Using principal component analysis, we identify two principal shape modes $\psi_1(s)$, $\psi_2(s)$, whose superpositions account for 95% of the variability of the tangent angle data. (d) By projecting the tangent angle data on the shape space spanned by $\psi_1(s)$ and $\psi_2(s)$, each flagellar shape is assigned a pair of shape coefficients (β_1, β_2); see Eq. (2). This representation allows us to define a limit cycle of perfect periodic beating (red). By projection onto this limit cycle, we define a phase φ for each flagellar shape. (e) The flagellar phase-diffusion coefficient D is determined by fitting an exponential decay (red) to the phase correlation function ($|C(t)|$: thick blue, $\mathrm{Re}\, C(t)$: thin blue). (f) Phase speed $\Delta\varphi_i/\Delta t$ and squared amplitude $A(t_i)$ are negatively correlated. Inset: phase increments are approximately normally distributed.

shape of the beating flagellum ($n = 1024$ frames in each movie). We further define a two-point correlation matrix $M(s,s') = \sum_i [\psi(s,t_i) - \psi_0(s)][\psi(s',t_i) - \psi_0(s')]$, where s, s' range over m equidistant arclength positions along the flagellum. The eigenvectors $\psi_j(s)$ of the symmetric $m \times m$-matrix M, sorted by decreasing magnitude of the corresponding eigenvalues, characterize principal shape modes of the flagellar beat. The first two shape modes account for $95 \pm 1\%$ of the variance of the tangent angle data (all measurements are mean±s.e., $n = 7$ cells). We project the full data set on a two-dimensional shape space spanned by these two shape modes

$$\psi(s,t) \approx \psi_0(s) + \beta_1(t)\psi_1(s) + \beta_2(t)\psi_2(s) \qquad (2)$$

with shape coefficients β_1, β_2 obtained by least-square fit; see Figs. 1(c), 1(d). Flagellar beating implies periodic shape changes of the flagellum and, thus, noisy oscillations of the shape coefficients with mean frequency $\omega_0 = 2\pi/T$, where $T = 32.4 \pm 1.9$ ms. Individually, $\beta_1(t)\psi_1(s)$ and $\beta_2(t)\psi_2(s)$ describe standing waves; their combination results in a traveling wave propagating from the base to the tip of the flagellum, thereby facilitating net propulsion.

Limit-cycle reconstruction.—The point cloud representing subsequent flagellar shapes in Fig. 1(d) forms a closed loop. This allows us to define a limit cycle of noisy flagellar oscillations (red) by fitting a closed curve $(\bar{\beta}_1(\varphi), \bar{\beta}_2(\varphi))$, parametrized by a phase φ. The phase parametrization of the limit cycle is defined such that the mean of the phase speed is independent of φ [21]. Thus, φ slightly differs from the polar angle in the (β_1, β_2) plane. Next, we assign a unique flagellar phase to each tracked flagellar shape by projecting the corresponding point in the (β_1, β_2) plane radially onto the limit cycle. The shape trajectory $(\beta_1(t), \beta_2(t))$ avoids the singular origin; thus, the instantaneous phase speed $\dot{\varphi}$ is well defined.

Phase fluctuations.—The phase speed $\dot{\varphi}$ has a mean equal to the frequency ω_0 of the beat but can fluctuate around this mean. Phase speed fluctuations cause a decay of the phase-correlation function $C(t) = \langle \exp i[\varphi(t_0 + t) - \varphi(t_0)] \rangle$; see Fig. 1(e). This decay is insensitive to measurement noise that is uncorrelated from frame to frame. The frame-to-frame phase increments $\Delta\varphi_i = \varphi(t_{i+1}) - \varphi(t_i)$ are approximately normally distributed [Fig. 1(f), inset]. Furthermore, the correlation time of phase speed fluctuations is on the order of our temporal resolution 4 ms or below and, thus, short compared to the time scale of phase decoherence. We can, thus, interpret the observed phase decoherence using an idealized model of δ-correlated phase speed fluctuations,

$$\dot{\varphi} = \omega_0 + \zeta, \qquad (3)$$

where ζ is Gaussian white noise with $\langle \zeta(t)\zeta(t') \rangle = 2D\delta(t - t')$ and D denotes a phase-diffusion coefficient. In this idealization, $|C(t)| = \exp(-D|t|)$. By fitting an exponential to measured $|C(t)|$, we obtain the phase-diffusion coefficient of sperm flagellar beating $D = 3.2 \pm 1.9\ \mathrm{s}^{-1}$; see Fig. 1(e). An alternative measure for the phase stability of oscillations is the quality factor, $Q = \omega_0/(2D) = 38.0 \pm 16.7$, where ω_0/Q indicates the width at half-maximum of the principal peak in the power spectral density of $\exp[i\varphi(t)]$.

The observed phase fluctuations of the flagellar beat are dominantly of active origin and surpass passive, thermal fluctuations by orders of magnitude (as suggested by earlier, indirect measurements [10]): For a simple estimate, we consider a flagellar beat that is constrained to move along the shape limit cycle with φ as the only degree of freedom. The friction force P_φ conjugate to φ comprises hydrodynamic friction $\gamma\dot{\varphi}$ and dissipation within the flagellum. We estimate $\gamma \approx 3\ \mathrm{pN}\,\mu\mathrm{m\,s}$ [22,23]. We, thus,

obtain an upper bound $k_B T/\gamma \approx 0.0015\ \mathrm{s}^{-1}$ for the contribution of thermal fluctuations to phase diffusion D, which is a thousandfold smaller than the value measured.

Amplitude fluctuations.—We define an instantaneous amplitude of the flagellar beat $A(t) = |\beta_1(t) + i\beta_2(t)|/\rho_0(\varphi(t))$, normalized by $\rho_0(\varphi) = |\bar{\beta}_1(\varphi) + i\bar{\beta}_2(\varphi)|$. Thus, the complex oscillator variable $Z(t) = A(t)e^{i\varphi(t)}$ maps the shape limit cycle onto the unit circle. In our data, the amplitude $A(t)$ is approximately normally distributed with $\sigma_A^2 = \langle A(t)^2\rangle - 1 = 0.0070 \pm 0.0023$ [24]. The autocorrelation function of amplitude fluctuations decays with time constant $\tau_A = 5.9 \pm 1.8$ ms. Interestingly, we find that phase speed correlates with amplitude squared; the slope $-\omega_1$ of a linear regression gives $\omega_1/\omega_0 = 0.38 \pm 0.10$; see Fig. 1(f). Thus, the beating flagellum is represented as a nonisochronous oscillator (with approximate isochrones $\varphi - 2\tau_A\omega_1 \ln A = \mathrm{const}$ [25]). Nonisochrony of nonlinear oscillators has been related to synchronization [26,27].

Noisy normal form.—Previous theoretical work described the onset of flagellar oscillations as a supercritical Hopf bifurcation [28] with normal form ($\mu > 0$) [29]

$$\dot{Z} = i(\omega_c - \omega_1|Z|^2)Z + \mu(\Lambda - |Z|^2)Z + \Xi. \qquad (4)$$

In the absence of noise $\Xi = 0$ as considered originally [28], the complex oscillator variable $Z(t) = A(t)e^{i\varphi(t)}$ exhibits spontaneous oscillations with amplitude $A = \Lambda^{1/2}$ and frequency $\omega_0 = \omega_c - \omega_1\Lambda$ for effective motor activity $\Lambda > 0$. In this case, we may assume $\Lambda = 1$ after a parameter transformation.

To study the role of fluctuations, we add a multiplicative noise term $\Xi = Z(\zeta_A + i\zeta_\varphi)$ with uncorrelated Gaussian white noise variables satisfying $\langle\zeta_j(t)\zeta_k(t')\rangle = 2D_j\delta_{jk}\delta(t-t')$, $j,k \in \{A,\varphi\}$ and use Stratonovich interpretation. This choice represents the simplest phase-invariant noise term with tunable phase and amplitude noise strengths D_φ and D_A [30]. For weak noise D_A, $D_\varphi \ll \mu\Lambda$, amplitude fluctuations satisfy $\langle A(t_0)A(t_0+t)\rangle - 1 \approx \sigma_A^2 \exp(-|t|/\tau_A)$ with correlation time $\tau_A = (2\mu\Lambda)^{-1}$ and variance $\sigma_A^2 = D_A\tau_A\Lambda$. Phase fluctuations are colored with effective phase-diffusion coefficient $D = D_\varphi + (\omega_1/\mu)^2 D_A$. Our measurements of active flagellar fluctuations, thus, allow the full parametrization of Eq. (4) (with $\Lambda = 1$). Note that in the special case $D_A = D_\varphi \ll \mu\Lambda$ our choice of multiplicative noise gives the same long-term behavior as additive noise.

Flagellar fluctuations imply nondeterministic swimming.—Using measured noise strengths, we simulated realistic beat patterns and corresponding stochastic swimming paths; see Fig. 3(a). Specifically, we (i) use Eq. (4) to simulate $Z(t) = A(t)e^{i\varphi(t)}$, (ii) construct shape coefficients $\beta_1(t) + i\beta_2(t) = A(t)\rho_0(\varphi(t))$ and tangent angles $\psi(s,t)$ by Eq. (2), and (iii) compute the path $\mathbf{r}_h(t)$ using resistive force theory [22] as described in Ref. [23]. We find that the center $\mathbf{R}(t)$ of sperm swimming circles diffuses with diffusion coefficient $D_R = 3.3\ \mu\mathrm{m}^2/\mathrm{s}$, which is on the same order of magnitude, albeit smaller, than a value $D_R = 9 \pm 2\ \mu\mathrm{m}^2/\mathrm{s}$ measured for sea urchin sperm [8]. Our analysis includes amplitude and phase fluctuations but neglects additional shape fluctuations; thus, our value is a lower bound.

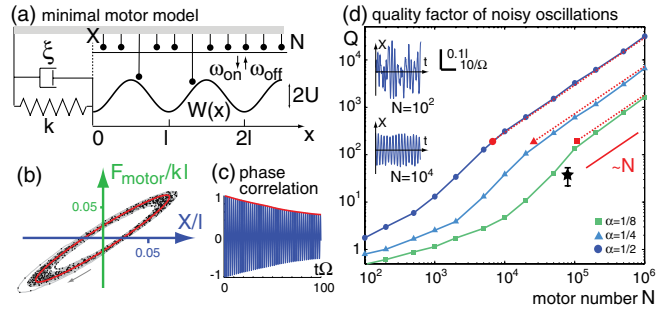

FIG. 2 (color online). A minimal model of coupled motors predicts noisy oscillations. (a) An ensemble of N motors, grafted at a rigid backbone (gray), can bind and unbind to a filament with transition rates ω_{on} and ω_{off}. Bound motors interact with the filament through an interaction potential $W(x)$. Filament and backbone are coupled viscoelastically. (b) The motor model exhibits spontaneous, noisy oscillations, here visualized by filament position X and total motor force. The deterministic limit cycle is shown in red. (c) The phase correlation function $C(t)$ (real part shown in blue) decays exponentially $|C(t)| \approx \exp(-Dt)$, defining the phase-diffusion coefficient D. (d) The quality factor $Q = \omega_0/(2D)$ scales with N for large N, consistent with our analytic approximation (dashed red, Eq. (5)). The star indicates the experimentally measured Q. For all simulations, we chose parameters close to the Hopf bifurcation ($\xi_a/\xi = 1.2\pi^2$, $\nu = 10$, $\alpha = \eta = 0.5$, $N = 10^4$, unless indicated otherwise; errors smaller than symbol size).

Although phase and amplitude fluctuations are correlated, we can ask separately for their respective effect on swimming. Phase fluctuations cause fluctuations in swimming speed but do not change the shape of the path. This is because the Stokes equation governing self-propulsion at low Reynolds numbers [31] is invariant under (stochastic) reparametrizations of time.

To gain qualitative insight into the microscopic origin of noisy oscillations and the dependence of phase diffusion on microscopic parameters, we now discuss a minimal motor model and show how it can be mapped onto Eq. (4).

A minimal model for noisy motor oscillations.—We exemplify how a finite collection of motors drives spontaneous oscillations with characteristic small-number fluctuations using the classical two-state model [6,32] in its most simple form: A collection of N motors, rigidly attached to an inextensible backbone interacts with a filament through an effective potential $W(x) = U[1 - \cos(2\pi x/l)]$; see Fig. 2(a). Here, x is the coordinate of the motor along the filament, and l is the periodicity of the filament. Individual motors

can bind to and unbind from the filament with rates $\omega_{\rm on}(x) = \Omega[\eta - \alpha\cos(2\pi x/l)]$ and $\omega_{\rm off} = \Omega - \omega_{\rm on}$. Here, η denotes the mean fraction of attached motors ("duty ratio"). Importantly, the binding rates are spatially inhomogeneous, characterized by α, and break detailed balance. If the filament is now coupled to the backbone by a viscoelastic element with viscosity ξ and elastic stiffness k, we obtain a force-balance equation for the position $X(t)$ of the filament $kX + \xi\dot{X} = F_{\rm m}$ with $F_{\rm m} = -\sum_i \partial_X W(x_i - X)$, where the sum extends over all bound motors and $x_i = il/N$ is a simple choice for the positions of the motors along the backbone.

To properly define a thermodynamic limit for large N, we rescale stiffness and viscosity as $k = k_0 N$ and $\xi = \xi_0 N$. In the limit $N \to \infty$, the system can exhibit spontaneous oscillations by a supercritical Hopf bifurcation, when the normalized motor activity $\xi_a/\xi = 2\pi^2\alpha U/(\Omega l^2 \xi_0)$ exceeds the threshold $1 + \nu$, where $\nu = k/(\xi\Omega)$ [32]. For a finite motor number, we numerically observe noisy oscillations; see Fig. 2.

In the following, we analytically compute the quality factor Q in the limit of large (yet finite) motor number N, assuming that we are close to the Hopf bifurcation with $\varepsilon = \xi_a/\xi - 1 - \nu$ positive and small. Following Refs. [32,33], we first approximated the stochastic binding and unbinding dynamics of individual motors by a diffusion approximation, thus arriving at a Fokker-Planck equation for the probability distribution of filament position and density $\rho(x)$ of bound motors (see Supplemental Material [34] for details). Because of the simple choice of potential $W(x)$, the dynamics of the first Fourier mode of $\rho(x)$ decouples from that of the higher modes, resulting in a three-dimensional stochastic system [33]. A nonlinear coordinate transformation maps this system onto Hopf normal form Eq. (4), with oscillator variable Z satisfying $\mathrm{Re}\, Z = X/l + \mathcal{O}(\varepsilon^{3/2})$ and phase-dependent noise term $\Xi = i\zeta$, where $\langle\zeta(t)\zeta(t')\rangle = 4D\Lambda\delta(t - t')$. The quality factor $Q = \omega_0/(2D)$ is found to scale with N

$$Q \approx \frac{\omega_0}{2\Omega}\frac{N\Lambda}{\eta(1-\eta)}\left(\frac{2\pi\alpha}{\sqrt{\nu} + 1/\sqrt{\nu}}\right)^2. \qquad (5)$$

Furthermore, $\Lambda \approx \varepsilon(1 + 4\nu)/[3\pi^2\nu(1 + 2\nu)]$, $\mu \approx \Omega\varepsilon/(2\Lambda)$, $\omega_0 \approx \Omega\sqrt{\nu}[1 + \varepsilon/(2 + 4\nu)]$. Interestingly, the motor duty ratio η controls oscillation quality, although η affects neither amplitude nor frequency (for $N \to \infty$). To understand this, note that the number of bound motors fluctuates with mean ηN and variance $\eta(1 - \eta)N$. This number characterizes a spatially homogeneous "background" of bound motors, which does not contribute directly to the oscillations but sets the amplitude of motor density fluctuations responsible for phase diffusion. Oscillations become also more regular for increasing amplitude. Equation (5) and simulations of the full model agree well close to the Hopf bifurcation; see Fig. 2. This minimal motor model recapitulates the experimental observation of phase diffusion in a minimal setting and illustrates how noisy oscillations can arise from small-number fluctuations.

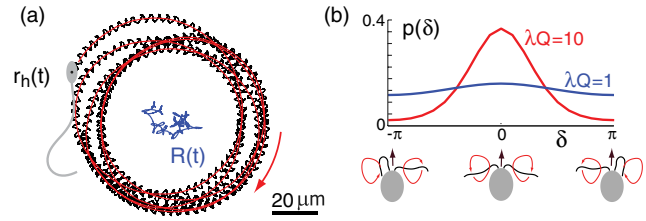

FIG. 3 (color online). Flagellar fluctuations imply nondeterministic swimming and counteract synchronization. (a) We simulated stochastic sperm swimming paths $r_h(t)$ (black), using measured flagellar fluctuation strengths. Fluctuations imply that the blue center $R(t)$ of red sperm swimming circles diffuses, with apparent diffusion coefficient $D_R = 3.30 \pm 0.01\ \mu\mathrm{m}^2/\mathrm{s}$. **B**. Pairs of flagella can synchronize, e.g., in the green alga *Chlamydomonas*. In a simple description of flagellar synchronization, the phase difference δ between its two flagella peaks around zero for realistic noise strength ($\lambda Q = 10$) but is almost uniformly distributed for tenfold stronger noise ($\lambda Q = 1$), indicating lack of synchronization.

Flagellar synchronization.—Phase fluctuations cause phase slips in pairs of synchronized flagella, e.g., in the green algae *Chlamydomonas* [10].*Chlamydomonas* swims with two flagella, which can synchronize their beat. Analysis of phase slips allowed a previous, indirect estimate of flagellar phase fluctuations, corresponding to $Q \approx 25$ for the quality factor of individual flagella [10]. A latter study indicated a length dependence of Q, with corresponding Q ranging from ≈70–120 for length increasing from 6 to 12 μm [35]. Interestingly, flagellar synchronization in *Chlamydomonas* seems to operate just below a tolerable level of noise: Consider the approximate dynamics of the phase difference δ between two identical, coupled oscillators $\dot{\delta} = -\lambda/T \sin\delta + \zeta$, where ζ is Gaussian white noise with $\langle\zeta(t)\zeta(t')\rangle = 4D\delta(t - t')$ [10,36]. Using the estimate $\lambda \approx 0.3$ for the synchronization strength [10], we find $\lambda Q \approx 10$, which yields robust synchronization. A tenfold higher noise level, however, implies failure of synchronization; see Fig. 3(b).

Conclusion.—The beating flagellum is a noisy oscillator, driven by $N \approx 8 \times 10^4$ dynein motor domains [37]. Here, we precisely measured its phase and amplitude fluctuations, using a novel method of limit-cycle reconstruction [20]. We obtain a quality factor $Q = 38 \pm 16.7$ of flagellar oscillations. Values estimated in other cytoskeletal oscillators are $Q = 2.2 \pm 1.0$ ($N \approx 2500$) for spontaneous hair bundle oscillations [38] and $Q = 1.4 \pm 1.1$ ($N = 10$–100) for an *in vitro* acto-myosin system [16]. We find that the strength of flagellar phase fluctuations is several orders of magnitudes above the level corresponding to thermal noise, highlighting the active origin of flagellar fluctuations.

We compute the quality factor Q in a minimal model of motor-filament oscillations and find that Q is proportional to the number of motors. A simple numerical example [39] yields noisy oscillations with amplitude, frequency, and quality factor $Al \approx 68$ nm, $\omega_0 \approx 228\ \mathrm{s}^{-1}$, $Q \approx 33$, which roughly match measured values ($Al \approx 100$ nm, $\omega_0 \approx 200\ \mathrm{s}^{-1}$ [19], $Q \approx 38$). Our analytic approximation Eq. (5) is not applicable for these large-amplitude oscillations. Note that the model does not fully capture flagellar oscillations quantitatively because it strongly simplifies flagellar geometry and motor dynamics.

We show that phase and amplitude fluctuations affect sperm swimming differently: Whereas amplitude fluctuations cause an effective diffusion of sperm swimming circles, phase fluctuations imply speed fluctuations but do not change the shape of the path. Additionally, phase fluctuations introduce phase slips in collections of synchronized flagella [10].

We thank J. Baumgart, V. F. Geyer, J. Howard, P. Romanczuk, P. Sartori, and T. Schwalger for stimulating discussions. Experimental data were recorded previously by I. H. Riedel-Kruse in the laboratory of J. Howard. We gratefully acknowledge support within the DFG priority program SPP 1726 "Microswimmers" (FR 3429/1-1).

*benjamin.friedrich@pks.mpg.de

[1] P. Martin, D. Bozovic, Y. Choe, and A. J. Hudspeth, J. Neurosci. **23**, 4533 (2003).
[2] S. W. Grill, K. Kruse, and F. Jülicher, Phys. Rev. Lett. **94**, 108104 (2005).
[3] B. Jewell and J. Ruegg, Proc. R. Soc. B **164**, 428 (1966).
[4] J. Gray, *Ciliary Movements* (Cambridge University Press, Cambridge, England, 1928).
[5] M. J. Sanderson and M. A. Sleigh, J. Cell Sci. **47**, 331 (1981).
[6] F. Jülicher and J. Prost, Phys. Rev. Lett. **78**, 4510 (1997).
[7] J. Howard, *Mechanics of Motor Proteins and the Cytoskeleton* (Sinauer, Sunderland, MA, 2001).
[8] I. H. Riedel, K. Kruse, and J. Howard, Science **309**, 300 (2005).
[9] M. Polin, I. Tuval, K. Drescher, J. P. Gollub, and R. E. Goldstein, Science **325**, 487 (2009).
[10] R. E. Goldstein, M. Polin, and I. Tuval, Phys. Rev. Lett. **103**, 168103 (2009).
[11] K. Y. Wan, K. C. Leptos, and R. E. Goldstein, J. R. Soc. Interface **11**, 20131160 (2014).
[12] C. Brennen and H. Winet, Annu. Rev. Fluid Mech. **9**, 339 (1977).
[13] N. Osterman and A. Vilfan, Proc. Natl. Acad. Sci. U.S.A. **108**, 15727 (2011).
[14] K. Drescher, J. Dunkel, L. H. Cisneros, S. Ganguly, and R. E. Goldstein, Proc. Natl. Acad. Sci. U.S.A. **108**, 10940 (2011).
[15] T. Betz, M. Lenz, J.-F. Joanny, and C. Sykes, Proc. Natl. Acad. Sci. U.S.A. **106**, 15320 (2009).
[16] P.-Y. Plaçais, M. Balland, T. Guérin, J.-F. Joanny, and P. Martin, Phys. Rev. Lett. **103**, 158102 (2009).
[17] E. Ben-Isaac, Y. Park, G. Popescu, F. L. H. Brown, N. S. Gov, and Y. Shokef, Phys. Rev. Lett. **106**, 238103 (2011).
[18] M. Otten, A. Nandi, D. Arcizet, M. Gorelashvili, B. Lindner, and D. Heinrich, Biophys. J. **102**, 758 (2012).
[19] I. H. Riedel-Kruse, A. Hilfinger, J. Howard, and F. Jülicher, HFSP J. **1**, 192 (2007).
[20] V. F. Geyer, F. Jülicher, J. Howard, and B. M. Friedrich, Proc. Natl. Acad. Sci. U.S.A. **110**, 18058 (2013).
[21] B. Kralemann, L. Cimponeriu, M. Rosenblum, A. Pikovsky, and R. Mrowka, Phys. Rev. E **77**, 066205 (2008).
[22] J. Gray and G. T. Hancock, J. Exp. Biol. **32**, 802 (1955).
[23] B. M. Friedrich, I. H. Riedel-Kruse, J. Howard, and F. Jülicher, J. Exp. Biol. **213**, 1226 (2010).
[24] The contribution from measurement noise is small. As a test, we added random perturbations to $\mathbf{r}(s,t)$, using known accuracies of tracking [19]. Phases and amplitudes for perturbed and unperturbed data were strongly correlated; results for σ_A did not significantly change.
[25] A. Pikovsky, M. Rosenblum, and J. Kurths, *Synchronization* (Cambridge University Press, Cambridge, England, 2001).
[26] T. Niedermayer, B. Eckhardt, and P. Lenz, Chaos **18**, 037128 (2008).
[27] M. Leoni and T. B. Liverpool, Phys. Rev. E **85**, 040901 (2012).
[28] S. Camalet and F. Jülicher, New J. Phys. **2** (2000).
[29] J. Crawford, Rev. Mod. Phys. **63**, 991 (1991).
[30] R. Graham, Phys. Rev. A **25**, 3234 (1982).
[31] E. Lauga and T. R. Powers, Rep. Prog. Phys. **72**, 096601 (2009).
[32] T. Guérin, J. Prost, and J.-F. Joanny, Eur. Phys. J. E **34** (2011).
[33] T. Guérin, J. Prost, and J.-F. Joanny, Phys. Rev. E **84**, 041901 (2011).
[34] See Supplemental Material at http://link.aps.org/supplemental/10.1103/PhysRevLett.113.048101 for additional details on the derivation of Eq. (5).
[35] R. E. Goldstein, M. Polin, and I. Tuval, Phys. Rev. Lett. **107**, 148103 (2011).
[36] R. L. Stratonovich, *Topics in the Theory of Random Noise* (Gordon and Breach, New York, 1963).
[37] D. Nicastro, C. Schwartz, J. Pierson, R. Gaudette, M. E. Porter, and J. R. McIntosh, Science **313**, 944 (2006).
[38] J. Barral, K. Dierkes, B. Lindner, F. Jülicher, and P. Martin, Proc. Natl. Acad. Sci. U.S.A. **107**, 8079 (2010).
[39] $N = 8\times10^4$, $l = 8$ nm, $k \approx 2$ nN/μm [7], $\xi \approx 40$ pN s/μm, $\Omega = 10^4\ \mathrm{s}^{-1}$, $\xi_a/\xi = 2$, $\alpha = \eta = 0.5$.

Supplemental Material:
Active phase and amplitude fluctuations of flagellar beating

Rui Ma,[1,2] Gary S. Klindt,[1] Ingmar H. Riedel-Kruse,[3] Frank Jülicher,[1] and Benjamin M. Friedrich[1]

[1]*Max Planck Institute for the Physics of Complex Systems, Dresden, Germany*
[2]*Institute for Advanced Study, Tsinghua University, Beijing, China*
[3]*Department of Bioengineering, Stanford University, Stanford, CA, USA*

(Dated: June 30, 2014)

Here, we present details on the determination of the quality factor of noisy motor-filament oscillations for the minimal motor model discussed in the main text. We first derive a Langevin equation [see Eq. (S16)] for the stochastic motor dynamics using methods presented in [31, 32]. We then show how this Langevin equation can be transformed into a stochastic Hopf normal form using a center manifold technique, see Eq. (S23). From this, we obtain an approximation for the quality factor, see Eq. (S33).

In the minimal motor model [6, 31], a collection of N motors is rigidly connected to a common backbone at equally spaced positions $x_i = il/N$, see Fig. 1 (Fig. 2A in the main text). These motors interact with a filament of periodicity l: Individual motors can bind and unbind from the filament with position-dependent transition rates

$$\omega_{\rm on}(x) = \Omega[\eta - \alpha\cos(2\pi x/l)], \tag{S1}$$

$$\omega_{\rm off}(x) = \Omega - \omega_{\rm on}. \tag{S2}$$

Here, Ω denotes a characteristic transition rate, η the duty ratio of motors, and x a coordinate along the filament, while α characterizes spatial variation of the transition rates. Note that $\omega_{\rm on}(x) + \omega_{\rm off}(x) = \Omega$. This so-called uniform rate assumption greatly simplifies the analytical treatment of the model [31]. Motors bound to the filament are subject to an interaction potential

$$W(x) = U[1 - \cos(2\pi x/l)]. \tag{S3}$$

The filament is connected to the motor backbone via an elastic spring of stiffness $k = Nk_0$ and a dashpot with drag coefficient $\xi = N\xi_0$ operating in parallel, see Fig. 1. The dynamics of the filament is now given by

$$kX + \xi\dot{X} = -\sum_i \partial_X W(x_i - X). \tag{S4}$$

To properly define a thermodynamic limit for large N, we will rescale stiffness and viscosity as $k = k_0 N$ and $\xi = \xi_0 N$.

FOKKER-PLANCK EQUATION OF MOTOR-FILAMENT DYNAMICS

We now derive a continuum description for the dynamics of the discrete set of motors. In order to define a probability density $\rho_0(z)$ of bound motors, we divide the interval $[0, l]$ into m bins of width $\Delta = l/m$ and respective bin centers $z_i = i\Delta - \Delta/2$, and set $\rho_0(z_i) = (1/\Delta)n_i/N$, where n_i denotes the number of bound motors within the i-th bin.

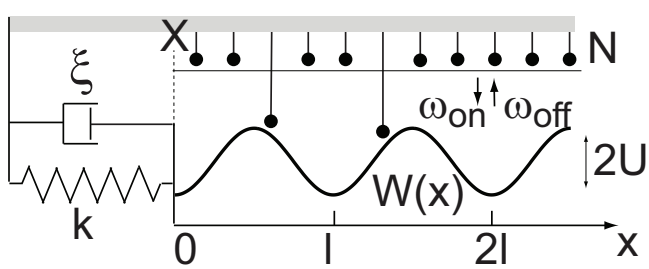

FIG. 1: An ensemble of N motors, grafted at a rigid backbone (gray), can bind and unbind to a filament with transition rates $\omega_{\rm on}$ and $\omega_{\rm off}$. Bound motors interact with the filament through an interaction potential $W(x)$. Filament and backbone are coupled visco-elastically through a spring and dashpot operating in parallel.

Following [32], we can formulate a master equation that governs the evolution of the joint probability distribution $P(X, n_1, \ldots, n_m)$ for the filament position X and the bin counts n_i

$$\begin{aligned}\frac{\partial P}{\partial t} =& -\frac{\partial}{\partial X}\left[\left(\sum_{i=1}^{m}\frac{W'(z_i - X)}{\xi_0}\frac{n_i}{N} - \frac{k_0}{\xi_0}X\right)P\right] \\ &+ \sum_{i=1}^{m}\omega_{\text{off}}(z_i - X)(\mathbf{E}_i^+ - 1)\, n_i P \\ &+ \sum_{i=1}^{m}\omega_{\text{on}}(z_i - X)(\mathbf{E}_i^- - 1)\left(\frac{N}{m} - n_i\right)P.\end{aligned} \tag{S5}$$

Here, $\mathbf{E}_i^{\pm}$ denote step operators, whose action on any function $f(n_i)$ obeys $\mathbf{E}_i^{\pm} f(n_i) = f(n_i \pm 1)$. Using bin center positions as approximate motor positions introduces a relative coarse-graining error $\mathcal{O}(1/m^2)$. To obtain a Fokker-Planck equation for $\rho_0(z)$, we replace $P(X, \{n_i\})$ by $P(X, \rho_0)$, expand Eq. (S5) using the operator expansion

$$\mathbf{E}_i^{\pm} = 1 \pm \frac{\partial}{\partial n_i} + \frac{1}{2}\frac{\partial^2}{\partial n_i^2} \pm \cdots \tag{S6}$$

and neglect all derivatives higher than the second order, which implies a truncation error of order $\mathcal{O}(1/N^2)$, as well as a coarse-graining error of relative order $\mathcal{O}(1/m^2)$. For further simplification, we change the reference frame from the common motor backbone to the co-moving frame of the filament, and use henceforth the density $\rho(x)$ of bound motors with respect to the filament coordinate, $\rho(x) = \rho_0(z - X)$ (where $\rho(x)$ shall be extended outside the interval $[-X, l - X]$ by periodic continuation for mathematical convenience). This finally leads to a functional Fokker-Planck equation for the distribution function $P(X, \rho)$ (see also [32])

$$\begin{aligned}\frac{\partial P}{\partial t} &= -\frac{\partial}{\partial X}vP + \int_0^l dx\, \frac{\delta}{\delta\rho(x)}AP \\ &+ \frac{1}{2N}\int_0^l dx \int_0^l dy\, \delta(x-y)\frac{\delta^2}{\delta\rho(x)\delta\rho(y)}CP.\end{aligned} \tag{S7}$$

The drift terms read

$$v = \int_0^l dx\, \frac{W'(x)}{\xi_0}\rho(x) - \frac{k_0}{\xi_0}X, \tag{S8}$$

$$A = \omega_{\text{off}}(x)\rho(x) - \omega_{\text{on}}(x)[1/l - \rho(x)] - v\partial_x\rho(x), \tag{S9}$$

while the diffusion term reads

$$C = \omega_{\text{off}}(x)\rho(x) + \omega_{\text{on}}(x)[1/l - \rho(x)]. \tag{S10}$$

Choosing a bin size $m \sim \sqrt{N}$ that increases with the number of motors, we find that both drift terms and diffusion terms in Eq. (S7) are each accurate to leading order in $1/N$.

Spatial Fourier Expansion

We expand $\rho(x)$ into a spatial Fourier series

$$\rho(x) = \frac{\eta}{l}a_0 + \frac{\alpha}{l}\sum_{n=1}^{\infty} a_n \cos\left(2\pi n\frac{x}{l}\right) + b_n \sin\left(2\pi n\frac{x}{l}\right), \tag{S11}$$

and rewrite the functional Fokker-Planck equation (S7) in terms of the Fourier coefficients [32]

$$\begin{aligned}\frac{\partial}{\partial t}P(\{a_n, b_n\}, X, t) =& -\frac{\partial}{\partial X}(vP) - \sum_n\left(\frac{\partial}{\partial a_n}A_n P + \frac{\partial}{\partial b_n}B_n P\right) \\ &+ \sum_{m,n}\frac{\partial^2 D_{mn}^{aa}P}{\partial a_m \partial a_n} + 2\frac{\partial^2 D_{mn}^{ab}P}{\partial a_m \partial b_n} + \frac{\partial^2 D_{mn}^{bb}P}{\partial b_m \partial b_n}.\end{aligned} \tag{S12}$$

The drift terms A_n, B_n characterize the deterministic mean-field dynamics of the system, and read

$$A_n = \frac{2}{\alpha}\int_0^l A(x)\cos(2\pi nx/l)dx, \quad B_n = \frac{2}{\alpha}\int_0^l A(x)\sin(2\pi nx/l)dx \tag{S13}$$

for $n \geq 1$, while $A_0 = (1/\eta)\int_0^l A(x)dx$ and $B_0 = 0$. The elements of the diffusion matrix characterize the noise effect due to a finite number of motors, and read

$$\begin{aligned} D^{aa}_{mn} &= \frac{2}{N\alpha^2}\int_0^l C(x)\cos(2\pi mx/l)\cos(2\pi nx/l)dx, \\ D^{ab}_{mn} &= \frac{2}{N\alpha^2}\int_0^l C(x)\cos(2\pi mx/l)\sin(2\pi nx/l)dx, \\ D^{bb}_{mn} &= \frac{2}{N\alpha^2}\int_0^l C(x)\sin(2\pi mx/l)\sin(2\pi nx/l)dx. \end{aligned} \tag{S14}$$

In general, the noise strengths are state-dependent. For small oscillation amplitudes and in the limit of weak noise, we can approximate them by their respective values evaluated at the fixed point of the deterministic dynamics, characterized by $a_0 = 1$, $a_1 = -1$, $b_1 = 0$. Specifically, we find

$$\begin{aligned} D_a = D^{aa}_{11} &= \frac{\Omega}{2N}\left[\frac{2\eta}{\alpha^2}(1 + a_0(1-2\eta)) + 3a_1\right] \approx \frac{\Omega}{2N}\left[\frac{4\eta(1-\eta)}{\alpha^2} - 3\right], \\ D_b = D^{bb}_{11} &= \frac{\Omega}{2N}\left[\frac{2\eta}{\alpha^2}(1 + a_0(1-2\eta)) + a_1\right] \approx \frac{\Omega}{2N}\left[\frac{4\eta(1-\eta)}{\alpha^2} - 1\right], \\ D^{ab}_{11} &= \frac{\Omega}{2N}b_1 \approx 0. \end{aligned} \tag{S15}$$

Remarkably, the dynamics of the principlal Fourier modes $a = a_1$, $b = b_1$, and filament position X decouples from the other modes [32] with corresponding Langevin dynamics

$$\begin{aligned} \dot{a} &= -\Omega(a + 1 - \gamma b^2 + \beta bX/l) + \zeta_a(t), \\ \dot{b} &= -\Omega(b + \gamma ba - \beta aX/l) + \zeta_b(t), \\ \dot{X} &= \frac{\Omega l}{2\pi}(\gamma b - \beta X/l), \end{aligned} \tag{S16}$$

where $\zeta_i(t)$ denote Gaussian white noise terms satisfying $\langle \zeta_i(t)\zeta_j(t)\rangle = 2D_i\,\delta_{ij}\delta(t-t')$ for $i, j = a, b$, and $\beta/(2\pi) = \nu = k_0/(\xi_0\Omega)$, $\gamma = \xi_a/\xi_0 = 2\pi^2\alpha U/(\Omega l^2\xi_0)$.

We now show how Eq. (S16) can be transformed into Hopf normal form. We first treat the noise-free case, $D_a = D_b = 0$. We first do a linear transformation of the coordinate tuple (a, b, X) to a new set of coordinates, comprising a real variable y and a complex variable Y,

$$\begin{pmatrix} a+1 \\ 2b \\ 2X/l \end{pmatrix} = \begin{pmatrix} 1 & 0 & 0 \\ 0 & \chi & \chi^* \\ 0 & 1 & 1 \end{pmatrix}\begin{pmatrix} y \\ Y^* \\ Y \end{pmatrix}, \tag{S17}$$

where $\chi = \pi(-\epsilon + 2\nu + 2i\sqrt{\nu})/(\sqrt{\nu} + i)^2$, $\epsilon = \gamma - 1 - \nu$. Conversely, $Y = i(b - \chi X/l)/\mathrm{Im}\chi$ with $\mathrm{Im}\chi = -2\pi/(\sqrt{\nu} + 1/\sqrt{\nu}) + \mathcal{O}(\epsilon)$. In the new coordinate set, the linearized dynamics at the fixed point $(y, Y) = (0, 0)$ is diagonal

$$\frac{d}{dt}\begin{pmatrix} y \\ Y \end{pmatrix} = \begin{pmatrix} -\Omega & 0 \\ 0 & \Omega(\epsilon/2 + i\sqrt{\nu}) \end{pmatrix}\begin{pmatrix} y \\ Y \end{pmatrix} \tag{S18}$$

One can show that y relaxes to an invariant manifold $y = y(Y, Y^*)$ that is tangential to the plane $y = 0$ at $(y, Y) = (0, 0)$. For this so-called center manifold [28], we make a quadratic ansatz

$$y = h_1 Y^2 + h_1^* Y^{*2} + h_2 YY^* + \mathcal{O}(|Y|^3) \tag{S19}$$

with complex coefficients h_i that can be determined self-consistently from the full nonlinear dynamics. The dynamics of Y on the manifold defined by (S19) comprises a linear term, as well as cubic terms as leading order nonlinearity

$$\frac{dY}{dt} = \Omega\left(\frac{\epsilon}{2} + i\sqrt{\nu}\right)Y - g_0 Y^3 - g_1 Y^2 Y^* - g_2 YY^{*2} - g_3 Y^{*3} + \mathcal{O}(|Y|^4), \tag{S20}$$

where g_i are complex numbers. Using nonlinear coordinate transformations of the form $Y = Z + \theta Z^p Z^{*(3-p)}$, all cubic nonlinearities can eliminated, with the exception of $Z^2 Z^*$. Thus, we have brought the dynamics of Z into Hopf normal form

$$\frac{dZ}{dt} = \mu(\Lambda - |Z|^2)Z + i(\omega_c - \omega_1|Z|^2)Z + \mathcal{O}(|Z|^4), \tag{S21}$$

with parameters

$$\mu = \frac{3\pi^2\Omega\nu(1+2\nu)}{2(1+4\nu)}, \quad \Lambda = \frac{\Omega\epsilon}{2\mu} = \frac{1}{\pi^2}\frac{\epsilon(1+4\nu)}{3\nu(1+2\nu)}, \quad \omega_c = \Omega\sqrt{\nu}, \quad \omega_1 = -\frac{\mu\sqrt{\nu}}{1+2\nu}. \tag{S22}$$

For $\epsilon > 0$, in the absence of noise, the complex oscillator variable $Z = A \exp i\varphi$ oscillates with amplitude $A = |Z| = \sqrt{\Lambda}$ and frequency $\omega_0 = \omega_c - \omega_1\Lambda$.

In the case of weak noise, we can apply the same series of coordinate transformations used above to the Langevin equation (S16), while neglecting noise-induced drift terms of order $\mathcal{O}(1/N)$

$$\frac{dZ}{dt} = \mu(\Lambda - |Z|^2)Z + i(\omega_c - \omega_1|Z|^2)Z + i\zeta(t), \tag{S23}$$

where $\zeta(t)$ denotes Gaussian white noise with $\langle\zeta(t)\zeta(t')\rangle = 4D_0\Lambda\delta(t-t')$ and noise strength

$$4D_0\Lambda = 2D_b\left(\frac{\sqrt{\nu}+1/\sqrt{\nu}}{2\pi}\right)^2 + \mathcal{O}(\epsilon). \tag{S24}$$

We now compute the variance of amplitude fluctuations and the phase diffusion coefficient. We consider the limit of weakly perturbed oscillations, $\sigma_A^2 \ll \Lambda$. Using Stratonovich calculus, we derive from Eq. (S23) equations for the instantaneous amplitude A and phase ϕ

$$\dot{A} = \mu(\Lambda - A^2)A + \sin\phi\,\zeta(t), \tag{S25}$$

$$\dot{\phi} = \omega_c - \omega_1 A^2 + \frac{\cos\phi}{A}\zeta(t). \tag{S26}$$

We approximate the phase-dependent noise strengths by their phase-averaged expectation values, which will reproduce, to leading order in the noise-strength, the same dynamics on time-scales longer than the oscillation period. We also linearize the stochastic dynamics Eq. (S25) for small amplitude fluctuation δA, neglecting terms of order $\mathcal{O}(\delta A^2)$,

$$\frac{d}{dt}\delta A \approx -2\mu\Lambda\delta A + \frac{1}{\sqrt{2}}\zeta(t), \tag{S27}$$

$$\dot{\phi} \approx \omega_c - \omega_1\Lambda - 2\omega_1\sqrt{\Lambda}\,\delta A + \frac{1}{\sqrt{2\Lambda}}\zeta(t). \tag{S28}$$

The first equation describes an Ornstein-Uhlenbeck process with correlation time $\tau_A = (2\mu\Lambda)^{-1}$ and variance

$$\sigma_A^2 = D_0\Lambda\tau_A = D_0/(2\mu). \tag{S29}$$

For the phase-diffusion coefficient, we find

$$D = \lim_{t\to\infty}\frac{1}{2t}\left(\langle[\varphi(t)-\varphi(0)]^2\rangle - \langle[\varphi(t)-\varphi(0)]\rangle^2\right) \tag{S30}$$

$$= \lim_{t\to\infty}\frac{1}{2t}\langle\int_0^t\int_0^t dt_1 dt_2\,\dot{\varphi}(t_1)\dot{\varphi}(t_2)\rangle - \omega_0^2 \tag{S31}$$

$$= \left[1 + \left(\frac{\omega_1}{\mu}\right)^2\right]D_0. \tag{S32}$$

We now readily find for the qualify factor

$$Q = \frac{\omega_0}{2D} = \Theta\frac{\omega_0}{2\Omega}\frac{N\Lambda}{\eta(1-\eta)}\left(\frac{2\pi\alpha}{\sqrt{\nu}+1/\sqrt{\nu}}\right)^2 \tag{S33}$$

with prefactor

$$\Theta = \left[1 - \frac{\alpha^2}{4\eta(1-\eta)}\right]\left[1 + \left(\frac{\omega_1}{\mu}\right)^2\right]. \tag{S34}$$

This prefactor can be shown to vary around 1 within close bounds,

$$3/4 \leq \Theta \leq 9/8, \tag{S35}$$

and has therefore been omitted in the approximation presented in the main text. The proof of inequality (S35) involves $0 \leq \alpha \leq \eta$ and $\alpha \leq (1-\eta)$, as well as $|\omega_1/\mu| = \sqrt{\nu}/(1+2\nu) = 2^{-1/2}/[(2\nu)^{-1/2} + (2\nu)^{1/2}) \leq 2^{-3/2}$.

This approximation is only valid for weakly perturbed oscillations with $\sigma_A^2 \ll \Lambda$; the latter condition can be rephrased as $N \gg 1/\epsilon^2$. We remark that amplitude fluctuations remain finite, even at the Hopf bifurcation, and can be shown to scale as $\sigma_A^2 \sim N^{-1/2}$ for $\epsilon = 0$.

[6] F. Jülicher and J. Prost, Phys. Rev. Lett., **78**, 4510 (1997)
[28] J. D. Crawford, Rev. Mod. Phys., **63**, 991 (1991).
[31] T. Gúerin, J. Prost, and J.-F. Joanny, Eur. Phys. J. E, **34**, 60 (2011).
[32] T. Gúerin, J. Prost, and J.-F. Joanny, Phys. Rev. E, **84**, 041901 (2011).

nature COMMUNICATIONS

ARTICLE

Received 13 Mar 2015 | Accepted 2 Jul 2015 | Published 17 Aug 2015

DOI: 10.1038/ncomms8985

OPEN

Sperm navigation along helical paths in 3D chemoattractant landscapes

Jan F. Jikeli[1,*], Luis Alvarez[1,*], Benjamin M. Friedrich[2,*], Laurence G. Wilson[3,*], René Pascal[1], Remy Colin[4], Magdalena Pichlo[1], Andreas Rennhack[1], Christoph Brenker[5] & U. Benjamin Kaupp[1]

Sperm require a sense of direction to locate the egg for fertilization. They follow gradients of chemical and physical cues provided by the egg or the oviduct. However, the principles underlying three-dimensional (3D) navigation in chemical landscapes are unknown. Here using holographic microscopy and optochemical techniques, we track sea urchin sperm navigating in 3D chemoattractant gradients. Sperm sense gradients on two timescales, which produces two different steering responses. A periodic component, resulting from the helical swimming, gradually aligns the helix towards the gradient. When incremental path corrections fail and sperm get off course, a sharp turning manoeuvre puts sperm back on track. Turning results from an 'off' Ca^{2+} response signifying a chemoattractant stimulation decrease and, thereby, a drop in cyclic GMP concentration and membrane voltage. These findings highlight the computational sophistication by which sperm sample gradients for deterministic klinotaxis. We provide a conceptual and technical framework for studying microswimmers in 3D chemical landscapes.

[1] Molecular Sensory Systems, Center of Advanced European Studies and Research (caesar), Ludwig-Erhard-Allee 2, 53175 Bonn, Germany. [2] Biological Physics, Max Planck Institute for the Physics of Complex Systems, Nöthnitzer Straße 38, 01187 Dresden, Germany. [3] Department of Physics, University of York, YO10 5DD Heslington, York, UK. [4] Max Planck Institute for Terrestrial Microbiology, Karl-von-Frisch Straße 16, 35043 Marburg, Germany. [5] Centre of Reproductive Medicine and Andrology, University of Muenster, 48149 Muenster, Germany. * These authors contributed equally to this work. Correspondence and requests for materials should be addressed to L.A. (email: luis.alvarez@caesar.de) or to B.M.F. (email: benjamin.friedrich@pks.mpg.de) or to L.G.W. (email: laurence.wilson@york.ac.uk).

Many motile sperm rely on chemical and physical cues to locate the egg[1–4]. A beating hair-like filament, called the flagellum, serves both as an antenna that gathers sensory cues and as a motor that propels the cell. Receptors on the flagellar surface transduce these sensory cues into cellular signals. Ultimately, these signals modulate the wave-like beating of the flagellum that steers a sperm's swimming path (for review see ref. 5).

Sperm from many species, in particular marine animals, are attracted to the egg by chemical factors—a process called chemotaxis. Previous chemotaxis studies tracked sperm only in two-dimensions (2D); at the glass/water interface of shallow observation chambers, sperm swim on a plane in circles[6–10]. While cruising on circular paths in a chemical gradient, sperm sample the chemoattractant concentration either continuously or intermittently and gradually adjust their swimming path—a mechanism called klinotaxis. The repetitive stimulation entrains a suite of Ca^{2+} bursts that modulate the waveform of the flagellar beat[5,9,11,12]. The ensuing alternate periods of symmetrical and asymmetrical beating give rise to a looping swimming pattern ('drifting circles') up a gradient. However, unrestricted sperm from species such as sea urchin swim on a 3D helical path[13–17]. The conceptual work by Crenshaw[17,18] suggests that in a chemical gradient, sperm orient by helical klinotaxis, that is, by alignment of the helix towards the gradient. In addition, Crenshaw[17,18] shows that such alignment could be theoretically achieved if the components of the cell's rotational velocity are simple functions of the stimulus.

A generic quantitative theory of this chemotactic steering by Friedrich and Jülicher[19] captures the essence of navigation along periodic paths: a cellular signalling system transforms the periodic stimulation $s(t)$ (chemoattractant binding) into a periodic intracellular signal $i(t)$ (Ca^{2+} bursts) that in turn modulates the swimming path curvature $\kappa_p(t)$. The phase lag between $s(t)$ and $\kappa_p(t)$, that is, the latency of the Ca^{2+} signal, is a crucial determinant of the directed drift of circles up or down a 2D chemical gradient. This theory also predicts bending of the swimming helix in 3D. However, these theories have not been experimentally tested in a well-defined 3D chemical gradient; moreover, the mechanisms of 3D klinotaxis cannot be derived from 2D swimming at interfaces, not least because of the hydrodynamic interactions between the flagellum and the surface of the recording chamber[20,21]. In fact, 3D navigation mechanisms remain unknown for any swimming eukaryotic cell, because of the technical challenges to rapidly establish and quantitatively characterize a chemical gradient and to track rapidly moving cells as they traverse a complex chemical 3D landscape.

We chose the sea urchin *Arbacia punctulata* to study the search strategy of sperm in a 3D chemoattractant landscape. *A. punctulata* are broadcast spawners that release their gametes into the ocean, where sperm swim freely. For several reasons, *A. punctulata* sperm provide an unmatched model to address fundamental questions of cell navigation[22]: (1) chemotaxis has been well-established[22,23]; (2) the chemoattractant is known[24], and the signalling pathway has been studied in depth[25–29]; (3) conditions for swimming in an aqueous medium can be readily emulated; finally, (4) *Arbacia* sperm, unlike mammalian sperm, represent a homogenous population, that is, most sperm are chemotactically active.

Here we study freely swimming sperm using digital inline high-speed holographic microscopy[30]. Moreover, 3D landscapes with defined spatio-temporal pattern are created by light using a caged chemoattractant[31]. In addition, we study by reverse optochemical engineering of signalling events, how steering responses are adjusted during navigation in a gradient. Finally, using hydrodynamic simulations and a minimal model of sperm signalling, we provide a theoretical framework accounting for sperm navigation in 3D.

Results

Tracking sperm in 3D. Sperm were illuminated with coherent laser light. Light scattered by sperm interfered with the unscattered background, and this interference was recorded by a camera at 600 holograms per s (h.p.s.). Applying the Rayleigh–Sommerfeld back-propagator[32], we determined numerically from each hologram the 3D coordinates of the sperm head[33] (Supplementary Fig. 1). Far from boundaries, *A. punctulata* sperm swam on a regular helical path with a mean speed $v = 200 \pm 57\,\mu m\,s^{-1}$ (Fig. 1a); mean helix parameters were: radius $r_0 = 8.4 \pm 3.1\,\mu m$, pitch $p_0 = 47.6 \pm 9.1\,\mu m$, helix period $T = 0.38 \pm 0.07\,s$, path curvature $\kappa_p = 0.065 \pm 0.013\,\mu m^{-1}$ and path torsion $\tau_p = 0.067 \pm 0.031\,\mu m^{-1}$ (track duration 1 s; $n = 20$ cells, mean ± s.d.). For comparison, near a glass/water interface, sperm swim on circles of radius $r_0 = 23.5 \pm 0.9\,\mu m$ with swimming speed $v = 160 \pm 29\,\mu m\,s^{-1}$, and circle period $T = 0.9 \pm 0.2\,s$ ($n = 6$). Thus, 2D and 3D kinematic parameters are distinctively different, underscoring the notion that 2D and 3D navigation are fundamentally different[20].

The sperm head wiggles around the average path with a frequency identical to that of the flagellar beat[34]; passive head wiggling counterbalances periodic forces generated by active flagellar bending[35]. For freely swimming sperm, head wiggling indicated a flagellar beat frequency of $43.5 \pm 3.5\,Hz$ (Fig. 1b;

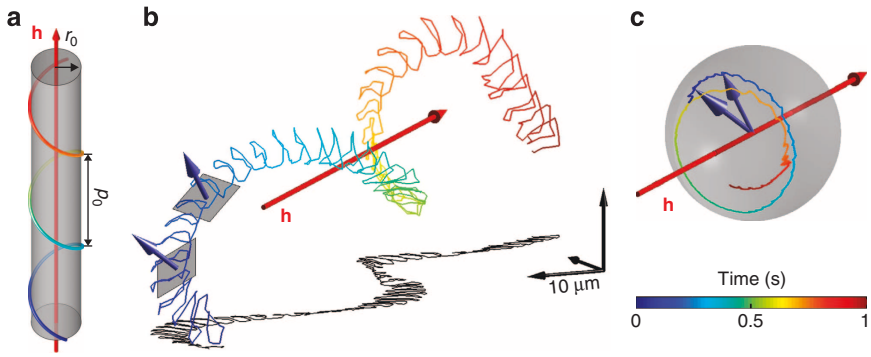

Figure 1 | Sperm navigate along helical paths. (**a**) Diagram showing the averaged swimming path of unstimulated sperm (duration 1 s, see color bar). Radius r_0 and pitch p_0 are drawn to scale. (**b**) Reconstruction of the 3D swimming path far from walls. Head wiggling was used to determine the beating plane orientation. (**c**) The vector normal to the beating plane (blue arrows) precesses around the helical axis (**h**, red arrow) with fixed inclination, describing a circle on the surface of a unit sphere centred around **h**. Vectors are not to scale.

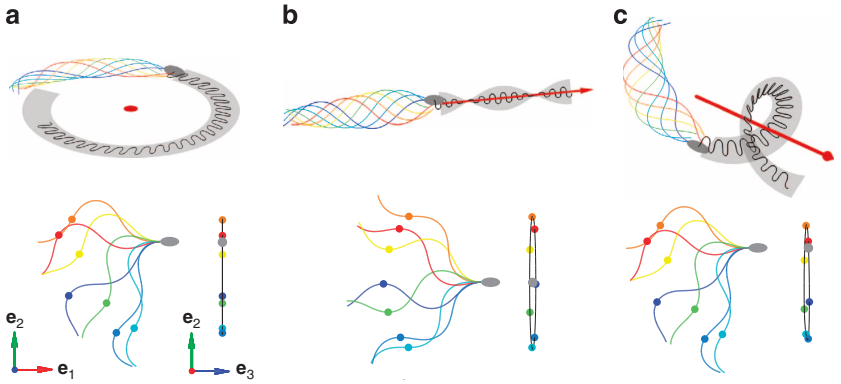

Figure 2 | Simulated swimming paths for three prototypical flagellar waveforms. The top of each panel illustrates the swimming path, while at the bottom is shown a waveform sequence for aligned sperm head (grey) with a coloured reference point on the flagellum (left: top view; right: side view). (**a**) Planar and asymmetrical beating (mean flagellar curvature, $K_0>0$) results in circular paths. (**b**,**c**) A small flagellar twist ($\tau_f>0$) results in non-planar beat patterns and swimming paths. For symmetric beating ($K_0=0$), the resulting swimming path is a twisted ribbon (**b**), whereas for asymmetric beating ($K_0>0$) sperm swim on helices, and the beating plane has a constant inclination with the helix vector **h** (**c**).

$n=20$). Moreover, head wiggling was approximately planar, consistent with an approximately planar beat pattern. While sperm swim along a helix, the head-wiggling plane slowly rotates around the helix axis: the normal vector describes a circle on the unit sphere (Fig. 1c), characterized by a constant inclination to the helix axis (52.0° ± 11.5°; circular mean ± circular s.d., $n=20$).

To gain insight into the mechanisms producing a helical path, we simulated swimming paths resulting from different flagellar waveforms using resistive-force theory[35,36]. The flagellar shape was characterized by a constant flagellar twist τ_f and a flagellar curvature $\kappa_f(l,t)=K_0+B\ \cos(\omega_0 t-\lambda l)$ describing a travelling bending wave with beat amplitude B, wave speed ω_0/λ and mean flagellar curvature K_0 along the arc length l of the flagellum. We calculated the swimming path produced by three different flagellar waveforms: asymmetric/non-twisted ($K_0>0$; $\tau_f=0$), symmetric/twisted ($K_0=0$; $\tau_f>0$) and asymmetric/twisted ($K_0>0$; $\tau_f>0$). Without twist, the beat pattern and swimming path were planar (Fig. 2a), that is, sperm moved on circles of radius $r_p\approx 1.3/K_0$ that is set by the flagellar beat asymmetry. The symmetric/twisted beat produced a non-planar beat pattern, and sperm swam on twisted ribbons (Fig. 2b). A fraction of human sperm adopts this pattern[37]. Finally, an asymmetric/twisted beat produced a helical path, which is observed for some sperm species[13,14], and head wiggling occurred in a plane that slowly rotated around the helix axis (Fig. 2c). Both features are borne out by our experiments (Fig. 1b). This beat pattern could result from a combination of periodic motor activity travelling down the flagellum, which drives planar bending waves and persistent motor activity, which twists the flagellum[38].

3D steering is deterministic. Using a photosensitive caged form of the chemoattractant resact, we sculpted by light well-defined 3D profiles of chemoattractant. The intensity profile of the uncaging ultraviolet light was approximated by a Gaussian beam (Supplementary Fig. 2, Supplementary Movie 1). To mimic an egg that continuously releases resact, ultraviolet illumination was maintained during the measurement. The time-dependent concentration profile $c(\mathbf{x},t)$ was reconstructed numerically from the light profile using the resact diffusion coefficient[39] and the extinction coefficient and quantum yield of caged resact (Fig. 3a, Supplementary Movie 2). From the swimming path $\mathbf{r}(t)$ and the concentration profile $c(\mathbf{x},t)$, we derived the chemoattractant stimulus encountered by sperm $s(t)=c(\mathbf{r}(t),t)$ (Fig. 3b, Supplementary Fig. 3, Supplementary Movies 3,4).

Sperm might employ either a deterministic or stochastic strategy of chemotactic steering. For deterministic steering, correcting path adjustments are directed towards the gradient. Alternatively, during stochastic steering, path adjustments are chosen at random; afterwards, the microswimmer decides whether this choice was favourable and acts accordingly. Bacteria follow a stochastic search strategy; they alternate between episodes of straight swimming ('runs') and stochastic tumbling, which randomizes cell orientation and, thereby, produces a random walk[40]. However, 'runs' up a gradient are longer, producing a biased drift towards the chemoattractant source. To distinguish between deterministic and stochastic search strategies, we analysed the distribution of helical adjustments relative to the local concentration gradient for sperm crossing a chemoattractant field. The bending of the helix axis ($d\mathbf{h}/dt$) is biased towards the perpendicular component $\nabla_\perp c$ of the local gradient, that is, the optimal direction for local alignment with the gradient (Fig. 3c). Thus, steering responses of sperm are deterministic rather than stochastic.

The sensori-motor transfer function. We identified two different steering modes while sperm navigate in a chemoattractant gradient. Steady bending of the helix aligned its axis with the gradient direction, thereby ramping up the mean stimulation level ('on response'); occasionally bending was interrupted by a vigorous steering event that abruptly changed the swimming direction ('off response') (Fig. 3b). Using a Fourier filter, we decomposed the stimulus function $s(t)$ into high and low frequency components. One component represents stimulus oscillations of about 2 Hz, resulting from the helical nature of the path; this 2 Hz component was superimposed on the steady increase or decrease of the mean stimulus level (Fig. 4a,d). Remarkably, oscillations in curvature and torsion of the swimming helix are highly correlated with the stimulus oscillations, suggesting that subtle changes in helix geometry are underlying its smooth alignment with the gradient, that is, the 'on response' (Fig. 4d,e).

We used a simple model of phase-locked oscillations to fit the cross-correlation of stimulus and swimming response: $A\cos(\Omega_0\Delta t+\phi)e^{-D\Delta t}$, where Ω_0 is the helix frequency, ϕ is the phase shift between path curvature or torsion and the stimulus, and D accounts for phase diffusion (Fig. 4f). We find a phase shift between stimulus oscillations and oscillations

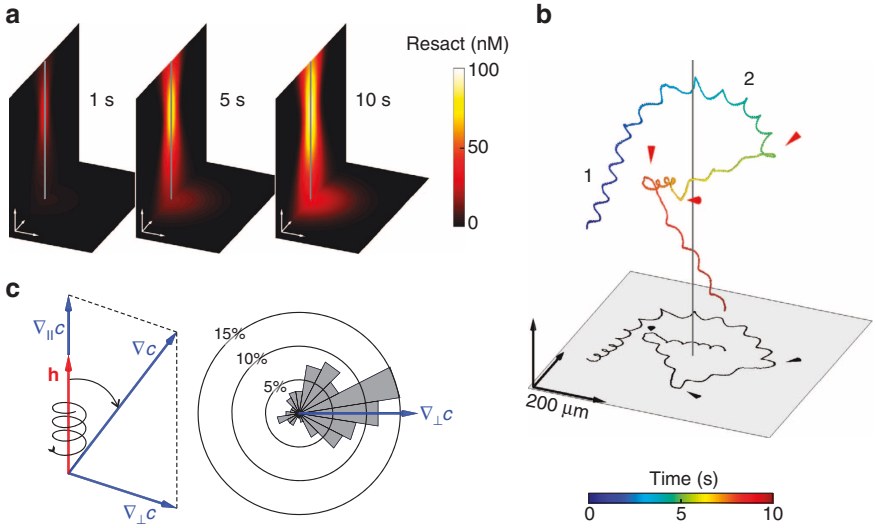

Figure 3 | Tracking sperm in 3D chemoattractant gradients. (**a**) 3D resact gradients were established by photolysis of caged resact with a Gaussian ultraviolet-beam. The calculated free resact concentration is shown as a function of space and time, accounting for continuous photo-release and diffusion. The concentration field is rotationally symmetric about an axis shown by the vertical grey line. (**b**) Sperm chemotaxis in a 3D resact gradient. A grey line indicates the centre of the photolyzing beam. Initially, sperm swim on a perfect helix (1). While approaching the resact field, the helix axis bends smoothly towards the gradient centre (2). When small gradual corrections of the swimming path fail and sperm get off course, a sharp directional turn is initiated (arrowheads). (**c**) Left: the gradient ∇c (blue) can be decomposed into components parallel $\nabla_{\parallel}c$ and perpendicular $\nabla_{\perp}c$ to the helical axis (**h**; red). The helical axis aligns with the gradient when it rotates towards $\nabla_{\perp}c$. Right: the histogram ($n=10$ cells) shows that the direction into which the helix axis changes scatters around $\nabla_{\perp}c$ in a deterministic rather than random manner.

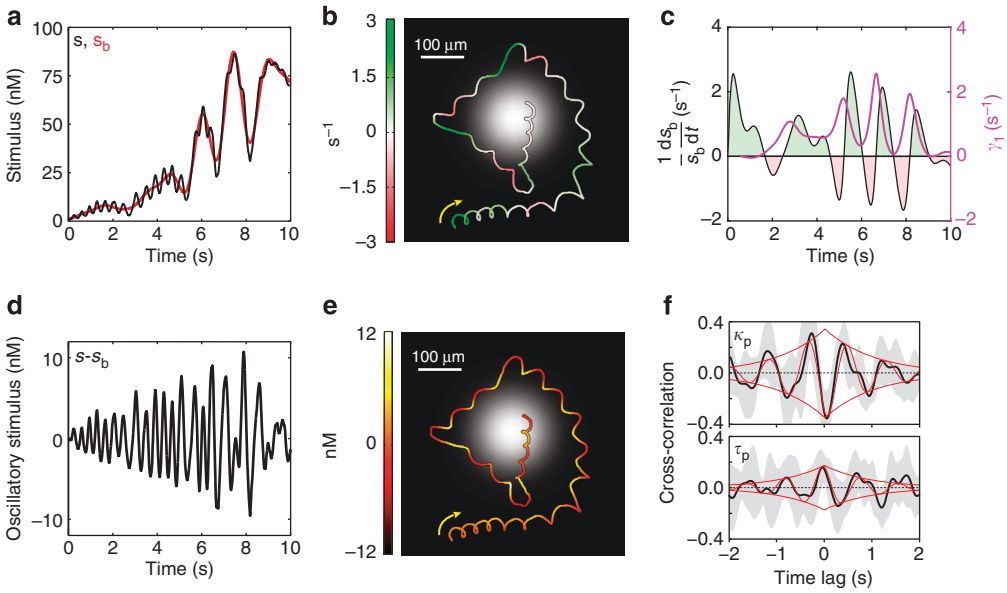

Figure 4 | Chemical stimulus and cellular steering responses are coupled. (**a**) Attractant stimulus encountered by the sperm cell moving along the trajectory shown in Fig. 3b. The stimulus (black) can be decomposed into a slowly changing stimulus baseline (s_b, red) and 2 Hz oscillations superimposed onto the baseline. (**b**) Top view of the swimming path. The light profile of the photolyzing beam at the focal plane is shown in grey shades. The time derivative of the stimulus baseline (ds_b/dt) relative to the stimulus baseline is colour coded along the path. Shortly after down the gradient swimming (red), the cell turns abruptly ('off response'). After each 'off response', the cell swims up the gradient again (green). (**c**) Relative time derivative of s_b (magenta) and alignment rate (γ_1; see Methods) of the helix axis with the concentration gradient (black). Phases of up the gradient and down the gradient swimming are characterized by increases (green) and decreases (red) of s_b. The helix predominantly aligns with the gradient ($\gamma_1>0$). However, sharp steering responses, characterized by high γ_1, are observed whenever s_b decreases. (**d**) High-frequency component of the stimulus (approximately 2 Hz oscillations). (**e**) The oscillatory stimulus at *ca.* 2 Hz (colour coded) results from the periodic component of helical swimming in the gradient. (**f**) Cross-correlations between the high-frequency stimulus and modulations of path curvature (κ_p; top) or torsion (τ_p; bottom) with mean values shown in black and s.d. in grey ($n=10$ cells). Thin red lines show the fitted model of phase-locked oscillations and its exponential amplitude decay.

of curvature and torsion of $\phi_\kappa=205.7°$ (184.8°, 233.2°) and $\phi_\tau=-16.3°$ ($-72.2°$, 43.6°), respectively, where the numbers in parentheses indicate 95% confidence intervals by bootstrap ($n=10$ cells). For optimal alignment, theory predicts[19] a $\phi_\kappa=180°$ and $\phi_\tau=0°$—in fair agreement with our experimental results (see Supplementary Note 1).

Strong steering responses were initiated when the slow stimulus component began to decline, that is, when sperm were about to lose track of the gradient, hence 'off response' (Fig. 4b,c). Nine out of 10 cells displayed such 'off responses', and during a total recording time of 77 s 'off responses' were observed on 31 occasions. Strong 'off responses' provide sperm with the means to evoke an emergency steering manoeuvre when steady helix alignment ('on response') is not sufficient.

In conclusion, sperm survey a chemical landscape on two different timescales simultaneously. While swimming up the gradient (mean stimulation level increases), the rapid periodic stimulus component smoothly and continuously bends the swimming helix towards the gradient. When swimming down the gradient (mean stimulation level decreases), sperm respond with a vigorous, yet almost optimally directed turn. While the smooth helix bending during the 'on response' involves only subtle adjustments of helix parameters, the strong 'off response' affords major transient distortions of helix geometry. After getting back on track, sperm resume regular helical swimming.

The behavioural 'off response' is generated by Ca^{2+}. Sperm host a sophisticated pathway for Ca^{2+} signalling that controls the flagellar beat waveform (Fig. 5a). Briefly, chemoattractant stimulation produces a pulse of cyclic GMP (cGMP), the intracellular messenger[31]. The rise is caused by cGMP synthesis via the chemoreceptor, a guanylyl cyclase[27] and the decay by cGMP hydrolysis via phosphodiesterase (PDE) activity. cGMP opens cyclic nucleotide-gated K^+-selective channels[28] (CNGK) and, thereby hyperpolarizes sperm[25]. During the decline from hyperpolarization, voltage-dependent Ca^{2+} channels (CatSper) open[26]. Ultimately, Ca^{2+} entering the sperm flagellum initiates a change in the flagellar waveform and a steering response[7,9,11,31].

The behavioural 'off response' when swimming down the gradient indicates that not only an increase, but also a decrease of chemoattractant evokes a Ca^{2+} signal. To test this idea, we developed a technique for optochemical control of a cellular response. We imposed a temporal pattern of photo-stimulation on sperm loaded with membrane-permeable caged cGMP[31,39]. The cGMP dynamics inside sperm is controlled via the balance between extrinsic 'synthesis' by photolysis of caged cGMP and intrinsic hydrolysis by PDE. Thereby, we mimicked an increase or decrease of resact. We produced cGMP with 393-nm light and simultaneously followed the changes in Ca^{2+} concentration and membrane potential V_m by a Ca^{2+} indicator dye (Fluo-4) and a voltage probe (di-8-ANEPPS), respectively. As a control, we mimicked a brief puff of chemoattractant by a light pulse that is shorter than the latency of the Ca^{2+} response (<200 ms). The control stimulus, after a short latency, evoked a transient Ca^{2+} signal (Fig. 5b)[31]. Using a longer light pulse, the waveform of the Ca^{2+} signal changed in two respects: the amplitude of the initial Ca^{2+} signal became much smaller and, unexpectedly, a second Ca^{2+} signal was generated precisely when the photolyzing light was switched off. In keeping with our nomenclature, we refer to the first and second Ca^{2+} signal as 'on' and 'off' Ca^{2+} response, respectively.

To elucidate the cellular mechanism underlying the Ca^{2+} 'off response', we probed the cGMP-induced voltage response using the same light protocol. Light stimulation produced a hyperpolarization[25] (Fig. 5b). For both brief and long light pulses, the waveform of the rising phase of the hyperpolarization was identical. However, for long light pulses (that is, with prolonged cGMP 'synthesis'), the decline from the hyperpolarizing peak was slower and incomplete; after the light was switched off (that is, when cGMP production ceased), the recovery from hyperpolarization was rapidly completed. The rapid V_m drop coincided with the onset of the Ca^{2+} 'off response'. The following model readily accounts for these observations[22,26]: Voltage-dependent CatSper channels open during recovery from hyperpolarization. While the photolyzing light is on, cGMP does not return to baseline levels as quickly and completely as compared with a brief light pulse. Consequently, a fraction of CNGK channels are kept open, and sperm stay partially hyperpolarized. When cGMP production by light ceases, cGMP levels rapidly drop due to PDE activity. The rapid return to resting V_m opens additional CatSper channels and, thereby, produces the Ca^{2+} 'off response'. The behavioural 'off response' triggered by this Ca^{2+} signal results in a major correction of the swimming path. Along the new direction of swimming, sperm experience again an ascending chemoattractant concentration in time.

Model of chemotactic steering. Previous theoretical models did not address how the flagellar beat steers a cell in a gradient[15,19].

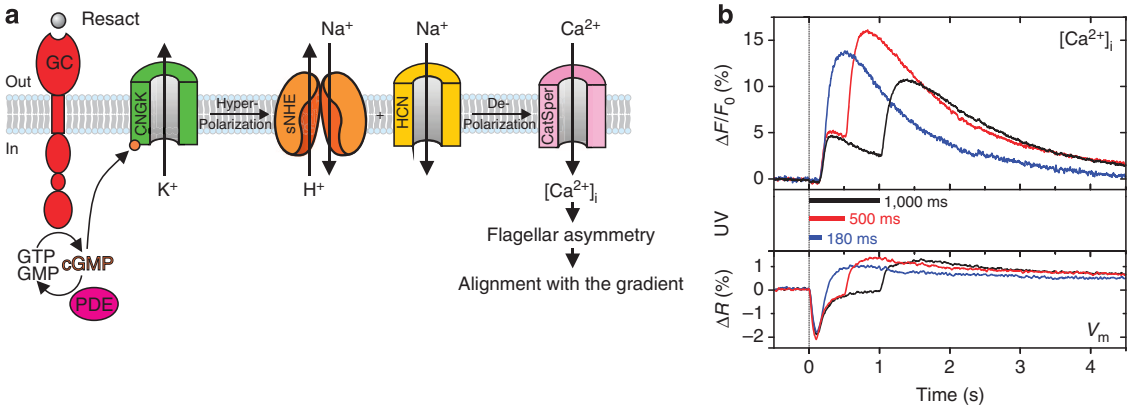

Figure 5 | Signalling events underlying the 'off responses'. (**a**) Signalling pathway underlying chemotaxis of *A. punctulata* sperm. The balance of synthesis by the chemoreceptor guanylyl cyclase (GC) and hydrolysis by PDE determines intracellular cGMP concentration. cGMP levels set the membrane potential of the cell via a cyclic nucleotide-gated K^+-selective channel (CNGK). When sperm hyperpolarize, intracellular alkalization via a Na^+/H^+ exchanger (sNHE) and depolarization via hyperpolarization-activated and cyclic nucleotide-gated (HCN) channels prime the sperm-specific Ca^{2+} channel (CatSper) to open. When cGMP synthesis ceases, the cell quickly depolarizes, more CatSper channels open and a strong steering 'off response' takes place. (**b**) Relative changes in $[Ca^{2+}]_i$ ($\Delta F/F_0$; top) and relative changes in membrane potential V_m detected with a ratiometric dye (ΔR; bottom) of sperm suspensions on release cGMP by light pulses of 180, 500 or 1,000 ms duration. Release of cGMP results in a rapid hyperpolarization and depolarization of sperm followed by a rise in $[Ca^{2+}]_i$ ('on response'). When photolysis ceases, a second Ca^{2+} signal takes place ('off response').

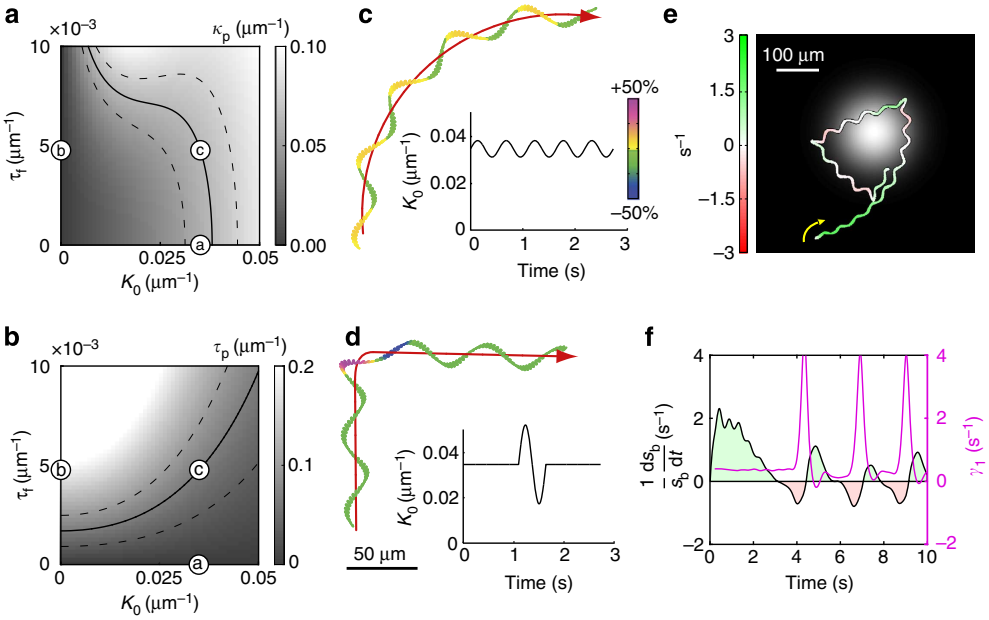

Figure 6 | Theoretical model for sperm steering. (**a**,**b**) Path curvature (κ_p; **a**) and torsion (τ_p; **b**) predicted by theory as a function of the mean flagellar curvature K_0 and flagellar twist τ_f. The range of experimentally measured values is shown as contour lines (solid: mean, dashed: mean ± s.d.). Labelled circles correspond to the beat patterns used in Fig. 2a–c. Only one pair ($K_0 = 0.035\,\mu m^{-1}$, $\tau_f = 4.8 \times 10^{-3}\,\mu m^{-1}$) produces a helical path with the observed mean path curvature and path torsion (encircled c). (**c**) Computed swimming path (left) resulting from modulating K_0 at the frequency of helical swimming. The colour coding and the graph to the right show K_0. Smooth bending of the helical path accounts for gradual 'on responses'. The helical centre line is shown in red. (**d**) A pulse-like change of K_0 accounts for sharp helix turns during 'off responses'. (**e**) Computed path of a cell navigating in a chemoattractant gradient (grey shades), where K_0 is dynamically adjusted by a simple steering feedback (combining a response to fast stimulus oscillations and a dynamic regulation of feedback strength by slow changes of the stimulus baseline, see Supplementary Note 1). (**f**) Relative change in baseline stimulus and alignment rate (γ_1) for the simulated path shown in **e**.

Moreover, they predicted steady adjustment of the swimming path by a constant feedback mechanism. We developed further the theory of chemotactic steering in two respects: a dynamic regulation of flagellar waveform and an adaptive steering feedback. For steering, sperm must alter the waveform of their flagellum. Therefore, we first computed helix parameters for constant waveforms (characterized by mean flagellar curvature K_0 and constant flagellar twist); this allowed the identification of a unique parameter set that reproduces the helix geometry in the absence of stimulation (Fig. 6a,b). Furthermore, 2D experiments suggest that a chemotactic signalling pathway regulates the mean flagellar curvature[9,12]. Therefore, we simulated the 3D swimming path resulting from variations of K_0. A small-amplitude, periodic modulation of K_0 causes steady helix bending (Fig. 6c), whereas a single large-amplitude modulation elicits a sharp turn (Fig. 6d). Helix bending and sharp turn are reminiscent of the 'on' and 'off response', respectively. Second, in an extended model of chemotactic steering, K_0 is dynamically adjusted to the stimulus concentration sampled by the swimming cell (see Supplementary Note 1). For up the gradient swimming, when only small course corrections are needed to align the helix, the signalling feedback strength is small; consequently, the amplitude of K_0 oscillations is small too, resulting in steady alignment ('on responses'). If, however, sperm swim down a gradient, an upregulated feedback strength allows for sharp turns ('off responses'). Simulations using this generic model account for the chemotactic 'on' and 'off' steering responses and show robust chemotaxis towards the summit of a resact concentration profile (Fig. 6e,f).

Discussion

We identify the principal features of sperm navigation in a 3D chemical landscape. Sperm probe the chemoattractant concentration along helical paths and, thereby, a spatial gradient is translated into a temporal stimulus pattern that oscillates with the 2 Hz periodicity of helical movement. Thus, the swimming path organizes the temporal stimulus pattern perceived by sperm, a principle known as information self-structuring[41]. The periodic component is superimposed on a mean stimulus level (baseline) that either increases or decreases slowly when swimming up or down a continuous gradient, respectively. The rapid stimulus oscillations provide a sense of direction, whereas the baseline slope controls the response strength. A positive slope signifying a chemoattractant increase produces weak 'on responses'; a negative slope when losing track evokes strong 'off responses'. This regulation of response strength allows sperm to tune klinotaxis behaviour ranging from subtle helix bending to abrupt emergency turns.

Response regulation can be achieved by dynamic adjustment of feedback strength, which is superior to a previous model with only constant feedback[19]. What might be the cellular signalling mechanisms underlying dynamic feedback strength? The cGMP dynamics, resulting from cGMP degradation by PDE activity and inactivation of the receptor guanylyl cyclase[27], controls the recovery from hyperpolarization and, thereby, the amplitude and timing of Ca^{2+} responses. Based on our macroscopic Ca^{2+} measurements, we propose a model in which slowly increasing stimulation during helix alignment keeps cGMP levels elevated and the recovery from hyperpolarization is, therefore, slower and incomplete; consequently, Ca^{2+} responses turn out small. When stimulation is waning while drifting down the gradient, cGMP hydrolysis outcompetes cGMP synthesis. As a result, CNGK channels close swiftly and V_m rapidly drops to resting values, thus triggering a large 'off' Ca^{2+} signal that drives an 'off response'. We propose that the regulated feedback strength resides in the dynamic balance between cGMP synthesis and hydrolysis.

Future work needs to combine holographic microscopy with fluorescence imaging techniques to monitor the signalling events in single cells during 3D chemotaxis.

While sperm from many marine invertebrates reach the egg by free 3D swimming, sperm from some fish swim on the 2D surface of the large egg during their search for a small fertilization site, known as the micropyle[42]. Moreover, mammalian sperm swim along the narrow oviduct and intermittently interact with the convoluted epithelium that lines the oviduct[43], thus mammalian sperm probably switch between 2D and 3D navigation. How similar are 2D and 3D navigation mechanisms? For sea urchin sperm, the drifting-circle pattern observed during 2D chemotaxis on a surface is equivalent to the helix-bending mode of 3D klinotaxis. Because the 'off response' is inherently rooted in the design of cellular signalling, we expect that the control logic is similar for 2D and 3D scenarios. Thus, why have 'off responses' escaped detection in studies of 2D navigation? For 2D swimming at interfaces, movements are constrained and subject to hydrodynamical interactions with the surface. Consequently, the ballistic component of movement along the helical path is missing because movement across the surface is not possible. The degree of freedom for 3D swimming is manifold larger and thus is the likelihood that sperm eventually will swim away from the chemical source. Therefore, the 'off response' is more important and prominent for 3D than for 2D swimming. Future work needs to address the behavioural 'off response' under 2D conditions, for example, by applying the approach of reversed optochemical engineering at the single cell level.

How common are navigation strategies of sperm across phyla? For mammalian sperm, three different mechanisms of guidance have been proposed: chemotaxis[44,45], thermotaxis[46,47] and rheotaxis[4,48]. Human sperm, when rapidly stimulated with progesterone, a putative chemoattractant, released from caged progesterone[49] undergo hyperactive episodes that change the swimming direction[45]. Similar events are observed in a thermotaxis assay after a temperature shift to lower values[47]. Superficially, these hyperactive episodes observed in human sperm are reminiscent of the 'off responses'. However, unlike 'off responses', they initiate a stochastic rather than deterministic reorientation and are more akin to stochastic tumbling episodes of bacterial chemotaxis.

Klinotaxis is a basic mechanism of navigation displayed by many motile cells and organisms[50], including the nematode *Caenorhabditis elegans*, larva from *Drosophila*, *Platynereis* and zebrafish primordial germ cells, protists and even some bacteria[51–55]. Sensory modalities as diverse as phototaxis, thermosensation, taste, olfaction and electroreception employ klinotaxis. In many animals, neuronal circuits are dedicated to analyse the temporal pattern of sensory stimuli that instruct the klinotactic response. Moreover, neuronal circuits are composed of 'on' and 'off cells' that register the ups and downs of sensory stimuli. Temporal sampling during klinotaxis is either accomplished along a periodic path or by undulatory movements of the body. It is quite remarkable that a signalling pathway can encompass these computational features in a single cell.

On a final note, chemoattractant landscapes around an egg in a natural habitat are not known and are expected to be rather complex. Local chemoattractant concentrations might be rapidly changing and distorted by turbulent fluid flow and drifting of eggs, giving rise to 'plumes' rather than Gaussian-shaped continuous gradients[56]. To emulate these native conditions and to study how sperm, and any other microswimmers, cruise in such complex chemical landscapes is the next frontier of enquiry. The optochemical and microscopy techniques presented here combined with computational models provide the means to generate and quantify complex landscapes and to reveal the search strategy during microswimmer navigation in general.

Methods

Sample preparation. Sperm spawning was evoked by injecting 0.5 ml of 0.5 M KCl into the body cavity of sea urchins from the species *A. punctulata*. Sperm were collected using a Pasteur pipette and stored on ice. Artificial seawater (ASW) contained (in mM) 423 NaCl, 9.27 $CaCl_2$, 9 KCl, 22.94 $MgCl_2$, 25.5 $MgSO_4$, 0.1 EDTA and 10 HEPES. The pH was adjusted to pH 7.8 with NaOH.

Imaging chamber. Dry sperm were diluted 6.6×10^4 fold with ASW supplemented with 0.5% Pluronic F127 (Sigma-Aldrich) and studied in a custom-made observation chamber ($11.5 \times 11.5 \times 1\ mm^3$). The chamber featured two openings for sperm injection. To minimize convective flow, the laboratory and the microscope incubator were set to 18 °C. The temperature of 18 °C was chosen because it roughly corresponds to the average temperature of the northern Atlantic coast during the fertility season of *A. punctulata*[57].

Optical set-up. Freely swimming sperm were tracked using an inverted microscope (IX71; Objective ×20, 0.75 numerical aperture, UPLSAPO; Olympus). Coherent illumination was achieved with a laser light source (LDH-D-C-510, PicoQuant GmbH) and the corresponding controller (Sepia II Multichannel Processor, PicoQuant GmbH). Laser light was coupled into a multimode fibre. A custom-made adapter was used to position the fibre parallel to the optical axis of the objective. The illumination intensity was adjusted to use the dynamical range of the camera (12-bit; PCO Dimax HD). Movies were collected at 600 frames per second; each frame represents a holographic image containing the complete 3D information of the sperm cell.

Caged compounds were photolyzed using a 365-nm LED (M365L2-C; Thorlabs). The ultraviolet light was coupled into a liquid guide (77566; Newport) followed by two Plano-convex lenses (LA 1951-A $f = 25.4$ mm; LA 1509-A $f = 100$ mm; Thorlabs) and coupled to the imaging optical path with a dichroic filter (ff 495-Di03; Semrock). The irradiation power (0.8 mW) was measured with a power meter (detector PowerMax and head model PS19Q; Coherent). The light spectrum was recorded with a spectrometer (51024 DW; Ocean Optics). Photolysis and data acquisition were synchronized using a wave generator (33500B; Agilent).

Reconstruction of the 3D swimming path. The 3D swimming path was reconstructed in several steps. First, we created a 'background' image from the average intensity value of the hologram sequence (usually 24,000 frames). Because moving objects in the hologram sequence are averaged out, the background image contains only the non-scattered light and the fringes resulting from interference of the source with non-moving particles. Dividing each hologram by the background image results in distinct interference patterns of moving sperm[32]. To curb the data volume, single sperm cells were tracked within the plane of the image using a custom-made tracking programme written in Java (Java 1.6 24; ImageJ v.1.47 m). The determined position was used to define a moving region-of-interest (ROI) of typically 300×300 pixels around the sperm cell for each frame; this ROI was used for further analysis.

The Rayleigh–Sommerfeld back-propagation scheme was used to numerically refocus each background-free hologram. Numerical refocusing resulted in a focus stack of computed images. The z-position of the cell corresponded to the point of contrast inversion (Gouy phase anomaly[58]; Supplementary Fig. 1). Contrast inversion was identified by an image-processing filter that highlights axial gradients in the image stack, such as the Sobel filter[33,59,60].

Caged compounds and flash photolysis. N-Fmoc-S-(2-Nitroveratryl)-L-cysteine was obtained as described[61] and used for solid-phase peptide synthesis (Biosyntan GmbH, Berlin, Germany) to obtain caged Cys8-S-DMNB-resact[31]. The extinction coefficient of caged resact (20 μM) in ASW was measured by an absorption spectrophotometer (Varian Carry 5000). To determine the photochemical quantum yield (ϕ_{chem}), a 50 μM solution of the caged peptide in ASW was irradiated with a 365 ± 5 nm ultraviolet-LED providing an power flux of $90\ mW\ cm^{-2}$ (NCSU033A(T), Nichia, Japan). At several time points aliquots were taken and analysed via HPLC ($n = 3$). From the initial slope of linear release (0–15% conversion) and the rate of photon absorption, determined by ferrioxalate actinometry[62], we determined a photochemical quantum yield of $\phi_{chem} = 0.4 \pm 0.1\%$. DEACM-caged cGMP was synthesized as described[63].

Characterization of the 3D gradient. The ultraviolet-light profile was characterized by measuring optical sections along the z-axis. A stack of seven glass cover-slides (150-μm thickness each) was placed at the location of the observation chamber. The ultraviolet profile was measured between slides by adding fluorescein (10 μl; 1 mM) and imaging the fluorescence emission (emission filter ET 510 LP; Chroma) that resulted from excitation of fluorescein using the LED ultraviolet source. Because the geometry of the spatial light profile is fixed with respect to the objective lens, focusing on the individual planes was achieved by moving the

camera to the corresponding conjugate plane. The resulting image was rescaled to compensate for the change in magnification. The scaling factor was measured by imaging a grid (DV2 calibration grid; Photometrics) at each camera position. Individual fluorescence pictures, corresponding to the ultraviolet projection on the different planes, were fitted to a Gaussian function ($R^2 > 0.977$). The change in width along the different optical sections was well-described by a Gaussian beam[64] (Supplementary Fig. 2).

To calculate the resact concentration in time and space, we numerically solved Fick's second law in 3D using the Euler method for both resact and caged resact. Space was discretized on cubes of 5-μm side, and the integration time step chosen was 1.67 ms. The diffusion of resact[39] ($D_{\mathrm{resact}} = 239\,\mu\mathrm{m}^2\,\mathrm{s}^{-1}$) and caged resact were assumed to be identical. The release of resact from its caged analogue (100 nM caged resact) was calculated on each iteration based on the power and spectrum of the ultraviolet source, the extinction coefficient ($\varepsilon = 4{,}100\,\mathrm{M}^{-1}\,\mathrm{cm}^{-1}$) and the photochemical quantum yield of DMNB-caged resact. Programmes were written in MATLAB (Mathworks).

Quantification of the helical swimming path. From the tracked sperm head trajectory, we define an averaged path $\mathbf{r}(t)$ by averaging out wiggling of the sperm head at the frequency of the flagellar beat, using a least-square fit that simultaneously minimizes the average disance of $\mathbf{r}(t)$ to the head trajectory and the third time derivative of track coordinates. The implicit prior on the third spatial derivative ensures smoothness of the averaged path without introducing a bias on the path curvature. We then fitted perfect helices to short $\mathbf{r}(t)$ segments using sliding windows of 0.75 s. This defines a helical path centre line $\mathbf{R}(t)$, and the helix vector $\mathbf{h} = \mathrm{d}\mathbf{R}/\mathrm{d}t/|\mathrm{d}\mathbf{R}/\mathrm{d}t|$.

We define $s(t) = c(\mathbf{r}(t),t)$ as a proxy for the concentration stimulus sampled by the cell in a concentration field $c(\mathbf{x},t)$ and compute the local gradient direction $\nabla c(\mathbf{R},t)$. This gradient can be decomposed into components parallel ($\nabla_{||}c = (\nabla c \cdot \mathbf{h})\mathbf{h}$) and perpendicular ($\nabla_{\perp}c = \nabla c - \nabla_{||}c$) to the helix vector (Fig. 3c). If the helix were perfectly aligned with the gradient direction, $\nabla_{\perp}c$ would be zero.

We characterize helix bending ($\mathrm{d}\mathbf{h}/\mathrm{d}t$) with respect to the local gradient direction ∇c as

$$\frac{\mathrm{d}\mathbf{h}}{\mathrm{d}t} = \gamma_1 \mathbf{g_1} + \gamma_2 \mathbf{g_2}, \tag{1}$$

where $\mathbf{g_1} = \nabla_{\perp}c/|\nabla_{\perp}c|$, $\mathbf{g_2} = \mathbf{h} \times \mathbf{g_1}$ and $\mathbf{h}$ form a local coordinate system that moves along the helix centre line. Thus, aligment occurs when the helix bends towards $\mathbf{g_1}$ ($\gamma_1 > 0$). Any bending in the direction $\mathbf{g_2}$ does not contribute to chemotaxis. For the histogram showing the direction of helix bending relative to the gradient direction (Fig. 3c), we analysed $n = 10$ cells along their full tracks every 0.75 s, corresponding to 152 data points.

To compute path curvature $\kappa_{\mathrm{p}}(t)$ and torsion $\tau_{\mathrm{p}}(t)$ of $\mathbf{r}(t)$, we fitted perfect helices to sliding path segments of duration 0.25 s. To stabilize the nonlinear helix fitting algorithm, we included a prior to the cost function that penalizes strong deviations from the helix parameters obtained for fitting a helix to a longer path segment of 0.75-s duration. The path curvature and path torsion were obtained from the radius and pitch of the fitted helical segments. We define the oscillatory part of $s(t)$, $\kappa_{\mathrm{p}}(t)$ and $\tau_{\mathrm{p}}(t)$ by subtracting a baseline defined by a Fourier filter with cut-off frequency at 1 Hz. To determine the phase-shifts (ϕ_{κ} and ϕ_{τ}) between stimulus and curvature/torsion oscillations, we fitted a model $A\cos(\Omega_0 \Delta t + \phi)\mathrm{e}^{-D\Delta t}$ of phase-locked oscillations to their normalized cross-correlation, where Ω_0 is the helix frequency and D accounts for phase diffusion.

To characterize the fraction of cells displaying 'off responses', we selected those cells for which at least 3,000 frames (equivalent to 5 s) had been successfully tracked using our 3D tracking algorithm. 'Off responses' were attributed to alignment events where the angle between the helical axis and the gradient abruptly changed from values exceeding 90°.

We determined the plane of head wiggling by fitting planes to short segments of the head trajectory of 150-ms duration, using singular-value-decomposition on centred coordinate data.

Numerical simulations of swimming sperm. We numerically reconstructed the swimming path that would result from prototypical flagellar waveforms using resistive-force theory[35,36]. Specifically, we computed the anisotropic hydrodynamic friction forces associated with shape changes of the slender flagellum. This allowed us to self-consistently solve for the instantaneous motion of the cell's material frame under conditions of force balance. Instantaneous translations and rotations were integrated using an explicit Euler scheme and the formalism of rigid body transformations. The time-dependent shape of the flagellum was characterized by the position vector $\mathbf{r_f}(l,t)$ of the flagellar centre line as a function of arc length l along the flagellum and time t, as well as a Cosserat frame consisting of three orthonormal vectors $\mathbf{e}_1(l,t)$, $\mathbf{e}_2(l,t)$ and $\mathbf{e}_3(l,t)$, such that $\mathbf{e}_3$ is tangential to the flagellar centre line $\mathbf{r_f}$, and $\mathbf{e}_1$ and $\mathbf{e}_2$ span a normal cross-section of the flagellum. Bending and twisting of the flagellum are characterized by rotations of the Cosserat frame:

$$\frac{\mathrm{d}\mathbf{r_f}}{\mathrm{d}l} = \mathbf{e}_3,\ \frac{\mathrm{d}\mathbf{e}_3}{\mathrm{d}l} = \kappa_{\mathrm{f}}\mathbf{e}_1,\ \frac{\mathrm{d}\mathbf{e}_1}{\mathrm{d}l} = -\kappa_{\mathrm{f}}\mathbf{e}_3 + \tau_{\mathrm{f}}\mathbf{e}_2,\ \frac{\mathrm{d}\mathbf{e}_2}{\mathrm{d}l} = -\tau_{\mathrm{f}}\mathbf{e}_1, \tag{2}$$

where $\kappa_{\mathrm{f}}(l,t)$ denotes flagellar curvature and τ_{f} denotes flagellar twist. We assume a constant flagellar twist τ_{f} and a flagellar curvature κ_{f} given by a travelling bending wave,

$$\kappa_{\mathrm{f}}(l,t) = K_0 + B\cos(\omega_0 t - \lambda l), \tag{3}$$

where K_0 is mean curvature, B the amplitude, ω_0 the angular frequency and $2\pi/\lambda$ the wavelength of the flagellar bending waves.

We assumed parallel and normal flagellar friction coefficients $\xi_{||} = 0.99\eta$, and $\xi_{\perp} = 1.81\xi_{||}$, respectively, where η denotes the dynamic viscosity of the surrounding liquid[35]. The flagellar length (41 μm), flagellar wavelength ($2\pi/\lambda = 29.6\,\mu\mathrm{m}$) and amplitude of the flagellar curvature wave ($B = 0.160\,\mu\mathrm{m}^{-1}$) were estimated from flagellar tracking of sperm swimming close to a water/glass interface. The beat period ($2\pi/\omega_0 = 23$ ms) was estimated from the frequency of head wiggling for sperm swimming in 3D. Mean flagellar curvature ($K_0 = 0.0351\,\mu\mathrm{m}^{-1}$) and flagellar twist ($\tau_{\mathrm{f}} = 0.00477\,\mu\mathrm{m}^{-1}$) were obtained by a nonlinear fit to reproduce the experimentally measured helix parameters, see Fig. 5a,b. The sperm head was approximated by an ellipsoid with axes 2.5, 1.25 and 1.25 μm, as estimated from electron micrographs. Finally, the proximal end of the flagellum (neck) is assumed collinear with the long axis of the sperm head.

Numerical simulation of sperm chemotaxis. Using our hydrodynamic simulation scheme, we computed sperm swimming paths $\mathbf{r}(t)$ in a concentration landscape $c(\mathbf{x},t)$ of chemoattractant. We assume a dynamic regulation of the shape of the flagellar beat in response to the concentration stimulus $s(t)$ sampled by the cell along its path:

$$s(t) = c(\mathbf{r}(t), t). \tag{4}$$

The time-dependent stimulus $s(t)$ is transduced by a simple adaptation module[19,65,66], where $p(t)$ denotes a dynamic sensitivity, $a(t)$ the signalling output variable and μ a signalling time-scale:

$$\begin{aligned} \mu\frac{\mathrm{d}a}{\mathrm{d}t} &= ps - a \\ \mu\frac{\mathrm{d}p}{\mathrm{d}t} &= p(a-1). \end{aligned} \tag{5}$$

This minimal description embodies key characteristics of the sperm chemotactic signalling system as observed in experiments, namely an adaptation of sensitivity according to the baseline stimulus level[39], as well as relaxation to the rest state ($a = 1$) for any stimulus that does not change in time[9]. Further characteristics of the signalling module (equation (5)) are provided in the Supplementary Information text. The output variable $a(t)$ regulates the mean flagellar curvature K_0 of the flagellar beat according to:

$$K_0 = K_{\mathrm{b}} - \chi(a-1). \tag{6}$$

Here K_{b} denotes the mean flagellar curvature of unstimulated sperm and χ denotes a feedback strength. For simplicity, all other parameters of the flagellar beat are assumed constant. A dynamic regulation of mean flagellar curvature on chemotactic stimulation has been demonstrated in previous 2D experiments[12].

To conceptualize our novel experimental finding of 'off responses', we employ a dynamic feedback strength $\chi(t)$ that can alternate between a low (χ_{on}) and a high value (χ_{off}) for steady swimming up or down the gradient, respectively. We introduce a signalling variable $q(t)$, which tracks changes of the stimulus baseline, and that obeys the following low-pass filter dynamics:

$$\eta\frac{\mathrm{d}q}{\mathrm{d}t} = a - q, \tag{7}$$

where η denotes a relaxation time-scale. In our minimal description, the dynamic feedback strength $\chi(t)$ takes either of the two values, depending on whether $q(t)$ exceeds a threshold θ:

$$\chi = \begin{cases} \chi_{\mathrm{on}} & \text{for } q > \theta \\ \chi_{\mathrm{off}} & \text{for } q < \theta \end{cases}. \tag{8}$$

For the simulations, we employed the concentration landscape $c(\mathbf{x},t)$ corresponding to the experiment shown in Fig. 3b. Parameters: $\mu = 150$ ms, $\eta = 500$ ms, $\theta = 0.95$, $\chi_{\mathrm{on}} = K_{\mathrm{b}}$, $\chi_{\mathrm{off}}/\chi_{\mathrm{on}} = 8$ and $K_{\mathrm{b}} = 0.0351\,\mu\mathrm{m}^{-1}$.

Measurement of changes in $[Ca^{2+}]_i$ and membrane voltage V_m. We measured changes in $[Ca^{2+}]_i$ and V_m using a rapid-mixing device (SFM-400; Bio-logic) in the stopped-flow mode. Changes in $[Ca^{2+}]_i$ and V_m were measured with the Ca^{2+} indicator Fluo-4 AM and the voltage-sensitive indicator di-8-ANEPPS (Molecular Probes), respectively. Dry sperm were suspended 1:6 (vol/vol) in loading buffer containing ASW and the indicator, in the absence (di-8-ANEPPS) or presence (Fluo-4 AM) of 0.5% Pluronic F127 (Molecular Probes). After incubation for at least 45 min with Fluo-4 AM or 5 min for di-8-ANEPPS at 17 °C, the sample was diluted 1:20 with ASW. Sperm were allowed to equilibrate in the new medium for 5 min. In the stopped-flow device, the sperm suspension was rapidly mixed 1:1 (vol/vol) with resact in ASW or ASW alone. Concentrations of resact are given as final concentrations after mixing. Fluorescence was excited by a SpectraX Light Engine (Lumencor). Emission was recorded by photomultiplier modules (H9656-20; Hamamatsu Photonics). The signal was amplified and filtered through

a voltage amplifier (DLPVA-100-B-S; Femto Messtechnik). Data acquisition was performed with a data acquisition pad (PCI-6221; National Instruments) and Bio-Kine software v. 4.49 (Bio-Logic). For Ca^{2+} and V_m recordings, the excitation light was passed through a BrightLine 475/28 nm filter (Semrock) (SpectraX Light Engine). For Ca^{2+} measurements, the emitted light was passed through a BrightLine 536/40-nm filter (Semrock). Ca^{2+} signals represent the average of at least two recordings and are depicted as the per cent change in fluorescence (ΔF) with respect to the mean of the first 5–10 data points before the onset of the signal (F_0). The control (ASW) $\Delta F/F_0$ signal was subtracted from the resact- or cGMP-induced signals. The V_m signals were recorded in dual-emission mode. The filters in front of the two photomultipliers were BrightLine 536/40 nm and BrightLine 628/40 nm (Semrock). The Bio-Logic software was used to record the fluorescence in the ratiometric dual-emission mode. The V_m signals are the ratio of F536/628 or R. The control (ASW) R signal was subtracted from the resact- or cGMP-induced signals. The mean R of the first 5–10 data points before the onset of the changes in fluorescence was set to 0, yielding ΔR. The V_m signals represent the average of at least three recordings and were digitally smoothed with five-point average smoothing. The changes in di-8-ANEPPS fluorescence were calibrated into V_m (mV) by stimulating sperm with 2.5 nM resact concentrations in ASW (9 mM K^+) and ASW of 30 mM and 100 mM extracellular K^+. Plotting the resact-evoked ΔR against $[K^+]_o$ allowed the interpolation of V_{rest} and ΔR/mV as previously described[25]. Calibration of ΔR to mV was performed within each set of experiments. The data obtained from ensemble measurements were analysed using OriginPro 9.0 (OriginLab Corporation).

Data analysis. All data are given as mean ± s.d. unless otherwise stated.

References

1. Kantsler, V., Dunkel, J., Blayney, M. & Goldstein, R. E. Rheotaxis facilitates upstream navigation of mammalian sperm cells. *eLife* **3,** e02403 (2014).
2. Eisenbach, M. & Giojalas, L. C. Sperm guidance in mammals - an unpaved road to the egg. *Nat. Rev. Mol. Cell Biol.* **7,** 276–285 (2006).
3. Publicover, S., Harper, C. V. & Barratt, C. $[Ca^{2+}]_i$ signalling in sperm - making the most of what you've got. *Nat. Cell Biol.* **9,** 235–242 (2007).
4. Miki, K. & Clapham, D. E. Rheotaxis guides mammalian sperm. *Curr. Biol.* **23,** 443–452 (2013).
5. Alvarez, L., Friedrich, B. M., Gompper, G. & Kaupp, U. B. The computational sperm cell. *Trends Cell Biol.* **24,** 198–207 (2014).
6. Cosson, M. P., Carre, D. & Cosson, J. Sperm chemotaxis in siphonophores. II. Calcium-dependent asymmetrical movement of spermatozoa induced by the attractant. *J. Cell Sci.* **68,** 163–181 (1984).
7. Guerrero, A. *et al.* Tuning sperm chemotaxis by calcium burst timing. *Dev. Biol.* **344,** 52–65 (2010).
8. Miyashiro, D. *et al.* Chemotactic response with a constant delay-time mechanism in *Ciona* spermatozoa revealed by a high time resolution analysis of flagellar motility. *Biol. Open* **4,** 109–118 (2015).
9. Böhmer, M. *et al.* Ca^{2+} spikes in the flagellum control chemotactic behavior of sperm. *EMBO J.* **24,** 2741–2752 (2005).
10. Gray, J. The movement of sea-urchin spermatozoa. *J. Exp. Biol.* **32,** 775–800 (1955).
11. Alvarez, L. *et al.* The rate of change in Ca^{2+} concentration controls sperm chemotaxis. *J. Cell Biol.* **196,** 653–663 (2012).
12. Wood, C. D., Nishigaki, T., Furuta, T., Baba, S. A. & Darszon, A. Real-time analysis of the role of Ca^{2+} in flagellar movement and motility in single sea urchin sperm. *J. Cell Biol.* **169,** 725–731 (2005).
13. Crenshaw, H. C. *Lecture Notes in Biomathematics*. (eds Alt, W. & Hofmann, G.) 361–386 (Springer, 1990).
14. Corkidi, G., Taboada, B., Wood, C. D., Guerrero, A. & Darszon, A. Tracking sperm in three-dimensions. *Biochem. Biophys. Res. Commun.* **373,** 125–129 (2008).
15. Crenshaw, H. C. Orientation by helical motion - III. Microorganisms can orient to stimuli by changing the direction of their rotational velocity. *Bull. Math. Biol.* **55,** 231–255 (1993).
16. Crenshaw, H. C. Orientation by helical motion - I. Kinematics of the helical motion of organisms with up to six degrees of freedom. *Bull. Math. Biol.* **55,** 197–212 (1993).
17. Crenshaw, H. C. & Edelstein-Keshet, L. Orientation by helical motion - II. Changing the direction of the axis of motion. *Bull. Math. Biol.* **55,** 213–230 (1993).
18. Crenshaw, H. C. A new look at locomotion in microorganisms: Rotating and translating. *Am. Zool.* **36,** 608–618 (1996).
19. Friedrich, B. M. & Jülicher, F. Chemotaxis of sperm cells. *Proc. Natl Acad. Sci. USA* **104,** 13256–13261 (2007).
20. Guerrero, A. *et al.* Strategies for locating the female gamete: the importance of measuring sperm trajectories in three spatial dimensions. *Mol. Hum. Reprod.* **17,** 511–523 (2011).
21. Elgeti, J., Kaupp, U. B. & Gompper, G. Hydrodynamics of sperm cells near surfaces. *Biophys. J.* **99,** 1018–1026 (2010).
22. Kaupp, U. B. 100 years of sperm chemotaxis. *J. Gen. Physiol.* **140,** 583–586 (2012).
23. Ward, G. E., Brokaw, C. J., Garbers, D. L. & Vacquier, V. D. Chemotaxis of *Arbacia punctulata* spermatozoa to resact, a peptide from the egg jelly layer. *J. Cell Biol.* **101,** 2324–2329 (1985).
24. Shimomura, H., Dangott, L. J. & Garbers, D. L. Covalent coupling of a resact analogue to guanylate cyclase. *J. Biol. Chem.* **261,** 15778–15782 (1986).
25. Strünker, T. *et al.* A K^+-selective cGMP-gated ion channel controls chemosensation of sperm. *Nat. Cell Biol.* **8,** 1149–1154 (2006).
26. Seifert, R. *et al.* The CatSper channel controls chemosensation in sea urchin sperm. *EMBO J.* **34,** 379–392 (2015).
27. Pichlo, M. *et al.* High density and ligand affinity confer ultrasensitive signal detection by a guanylyl cyclase chemoreceptor. *J. Cell Biol.* **206,** 541–557 (2014).
28. Bönigk, W. *et al.* An atypical CNG channel activated by a single cGMP molecule controls sperm chemotaxis. *Sci. Signal* **2,** ra68 (2009).
29. Gauss, R., Seifert, R. & Kaupp, U. B. Molecular identification of a hyperpolarization-activated channel in sea urchin sperm. *Nature* **393,** 583–587 (1998).
30. Garcia-Sucerquia, J. *et al.* Digital in-line holographic microscopy. *Appl. Opt.* **45,** 836–850 (2006).
31. Kaupp, U. B. *et al.* The signal flow and motor response controling chemotaxis of sea urchin sperm. *Nat. Cell Biol.* **5,** 109–117 (2003).
32. Lee, S. H. & Grier, D. G. Holographic microscopy of holographically trapped three-dimensional structures. *Opt. Exp.* **15,** 1505–1512 (2007).
33. Wilson, L. G., Carter, L. M. & Reece, S. E. High-speed holographic microscopy of malaria parasites reveals ambidextrous flagellar waveforms. *Proc. Natl Acad. Sci. USA* **110,** 18769–18774 (2013).
34. Serres, C., Feneux, D., Jouannet, P. & David, G. Influence of the flagellar wave development and propagation on the human-sperm movement in seminal plasma. *Gamete Res.* **9,** 183–195 (1984).
35. Friedrich, B. M., Riedel-Kruse, I. H., Howard, J. & Jülicher, F. High-precision tracking of sperm swimming fine structure provides strong test of resistive force theory. *J. Exp. Biol.* **213,** 1226–1234 (2010).
36. Gray, J. & Hancock, G. J. The propulsion of sea-urchin spermatozoa. *J. Exp. Biol.* **32,** 802–814 (1955).
37. Su, T. W. *et al.* Sperm trajectories form chiral ribbons. *Sci. Rep.* **3,** 1664 (2013).
38. Hilfinger, A. & Jülicher, F. The chirality of ciliary beats. *Phys. Biol.* **5,** 016003 (2008).
39. Kashikar, N. D. *et al.* Temporal sampling, resetting, and adaptation orchestrate gradient sensing in sperm. *J. Cell Biol.* **198,** 1075–1091 (2012).
40. Berg, H. C. & Brown, D. A. Chemotaxis in *Escherichia coli* analysed by three-dimensional tracking. *Nature* **239,** 500–504 (1972).
41. Lungarella, M. & Sporns, O. Mapping information flow in sensorimotor networks. *PLoS Comp. Biol.* **2,** e144 (2006).
42. Yanagimachi, R. *et al.* Sperm attractant in the micropyle region of fish and insect eggs. *Biol. Reprod.* **88,** 47 (2013).
43. Suarez, S. S. Regulation of sperm storage and movement in the mammalian oviduct. *Int. J. Dev. Biol.* **52,** 455–462 (2008).
44. Eisenbach, M. Sperm chemotaxis. *Rev. Reprod.* **4,** 56–66 (1999).
45. Armon, L. & Eisenbach, M. Behavioral mechanism during human sperm chemotaxis: involvement of hyperactivation. *PloS ONE* **6,** e28359 (2011).
46. Bahat, A., Caplan, S. R. & Eisenbach, M. Thermotaxis of human sperm cells in extraordinarily shallow temperature gradients over a wide range. *PloS ONE* **7,** e41915 (2012).
47. Boryshpolets, S., Perez-Cerezales, S. & Eisenbach, M. Behavioral mechanism of human sperm in thermotaxis: a role for hyperactivation. *Hum. Reprod.* **30,** 884–892 (2015).
48. Bretherton, F. Rothschild rheotaxis of spermatozoa. *Proc. R. Soc. Lond. B Biol. Sci.* **153,** 490 (1961).
49. Kilic, F. *et al.* Caged progesterone: a new tool for studying rapid nongenomic actions of progesterone. *J. Am. Chem. Soc.* **131,** 4027–4030 (2009).
50. Fraenkel, G. S. & Gunn, D. L. *The Orientation of Animals: Kinesis, Taxes and Compass Reactions* (Dover Publications, Inc., 1961).
51. Thar, R. & Fenchel, T. True chemotaxis in oxygen gradients of the sulfur-oxidizing bacterium *Thiovulum majus*. *Appl. Environ. Microbiol.* **67,** 3299–3303 (2001).
52. Bussmann, J. & Raz, E. Chemokine-guided cell migration and motility in zebrafish development. *EMBO J.* **34,** 1309–1318 (2015).
53. Riedl, J. & Louis, M. Behavioral neuroscience: crawling is a no-brainer for fruit fly larvae. *Curr. Biol.* **22,** R867–R869 (2012).
54. Faumont, S., Lindsay, T. H. & Lockery, S. R. Neuronal microcircuits for decision making in *C. elegans*. *Curr. Opin. Neurobiol.* **22,** 580–591 (2012).
55. Lockery, S. R. The computational worm: spatial orientation and its neuronal basis in *C. elegans*. *Curr. Opin. Neurobiol.* **21,** 782–790 (2011).
56. Zimmer, R. K. & Riffell, J. A. Sperm chemotaxis, fluid shear, and the evolution of sexual reproduction. *Proc. Natl Acad. Sci. USA* **108,** 13200–13205 (2011).

57. Water Temperature Table of the Northern Atlantic Coast. http://www.nodc.noaa.gov/dsdt/cwtg/natl.html (2015).
58. Born, M. & Wolf, E. *Principles of Optics* 6th edn (Cambridge Univ. Press, 1998).
59. Hall, E. L. *Computer Image Processing and Recognition* (Academic Press, 1979).
60. Wilson, L. & Zhang, R. J. 3D Localization of weak scatterers in digital holographic microscopy using Rayleigh–Sommerfeld back-propagation. *Opt. Exp.* **20,** 16735–16744 (2012).
61. Pedersen, H. *et al.* A method for directed evolution and functional cloning of enzymes. *Proc. Natl Acad. Sci. USA* **95,** 10523–10528 (1998).
62. Hatchard, C. G. & Parker, C. A. A new sensitive chemical actinometer.2. potassium ferrioxalate as a standard chemical actinometer. *Proc. R. Soc. Lond. Ser-A* **235,** 518–536 (1956).
63. Hagen, V. *et al.* Highly efficient and ultrafast phototriggers for cAMP and cGMP by using long-wavelength ultraviolet/Vis-activation. *Angew. Chem. Int. Ed.* **40,** 1046–1048 (2001).
64. Saleh, B. E. A. & Teich, M. C. *Fundamentals of Photonics* 2nd edn (Wiley Interscience, 2007).
65. Barkai, N. & Leibler, S. Robustness in simple biochemical networks. *Nature* **387,** 913–917 (1997).
66. Friedrich, B. M. & Jülicher, F. Steering chiral swimmers along noisy helical paths. *Phys. Rev. Lett.* **103,** 068102 (2009).

Acknowledgements

This work was supported by the German Research Foundation (DFG; SPP micro-swimmers 1726) and the Rowland Institute at Harvard. We thank Drs Seifert and Wachten for discussions and critically reading the manuscript.

Author contributions

J.F.J., L.A. and U.B.K. conceived the project. J.F.J., L.A., L.G.W., R.P. and U.B.K. designed the experiments. J.F.J., L.A., L.G.W., R.P. and C.B. further developed the stopped-flow and the motility set-ups. J.F.J., R.P., M.P. and U.B.K. performed the experiments. J.F.J., L.A., B.M.F., L.G.W. and R.C. developed software to analyse the data. J.F.J, L.A., B.M.F., L.G.W., R.P., R.C. and M.P. analysed the data. B.M.F. developed the mathematical model and performed the simulations. A.R. synthetized and characterized the photochemical properties of caged resact. J.F.J., L.A., B.M.F., L.G.W. and U.B.K. wrote the manuscript. All authors edited the text and and commented on the same.

Additional information

Supplementary Information accompanies this paper at http://www.nature.com/naturecommunications

Competing financial interests: The authors declare no competing financial interests.

Reprints and permission information is available online at http://npg.nature.com/reprintsandpermissions/

How to cite this article: Jikeli, J. F. *et al.* Sperm navigation along helical paths in 3D chemoattractant landscapes. *Nat. Commun.* 6:7985 doi: 10.1038/ncomms8985 (2015).

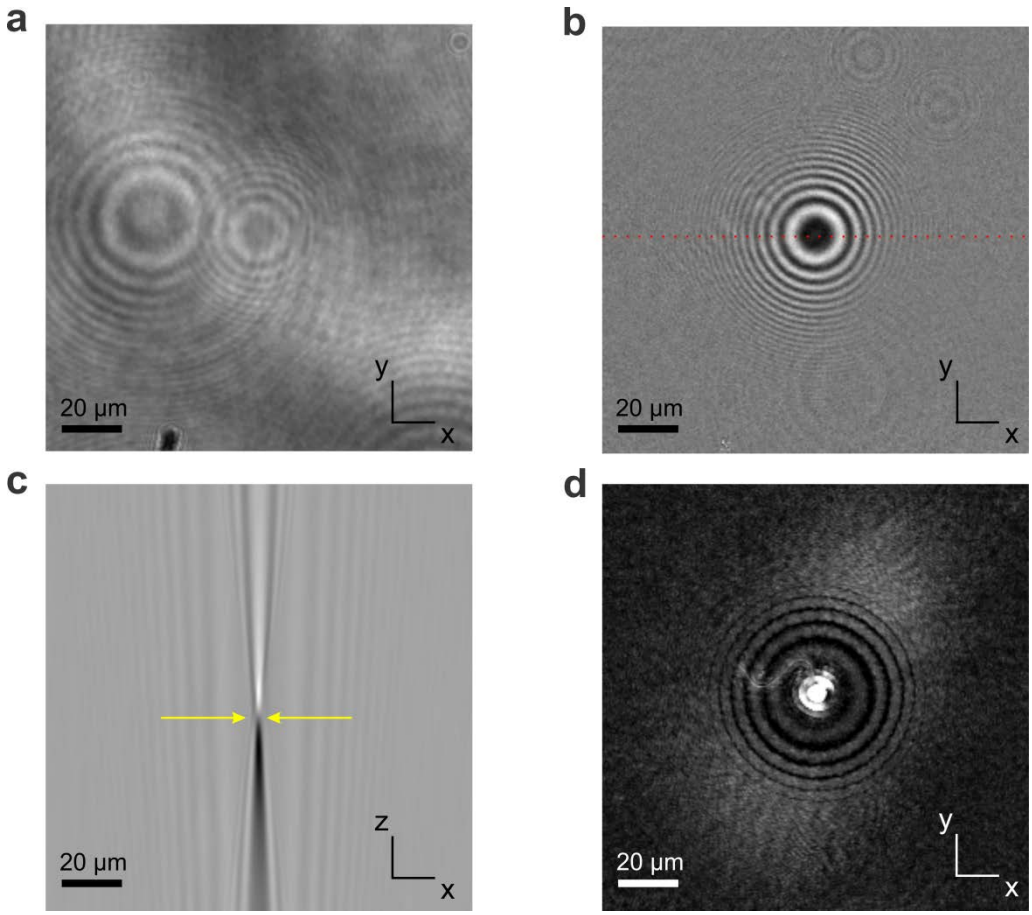

Supplementary Figure 1: Tracking of sperm head from individual holograms. (**a**) A frame of raw holographic data; the sperm head can be seen as the fainter series of concentric diffraction fringes at the centre of the image. (**b**) A frame of background-corrected holographic data (see methods). The centroid of the circular diffraction pattern provides the x-y position of the head. From background-corrected holograms, a refocused image stack was created. (**c**) Section through the refocused stack at a fixed y-position. The position is indicated by the red dashed line in (b). The z-coordinate of the sperm head is derived from the steepest intensity gradient along z (the point of contrast inversion is indicated by yellow arrows). (**d**) A portion of the refocused stack around the cell was extracted and a gradient filter was applied to highlight axial intensity gradients. This gradient stack was projected along the z-direction, retaining the maximum intensity value at each x-y position. A faint image of the flagellum becomes visible.

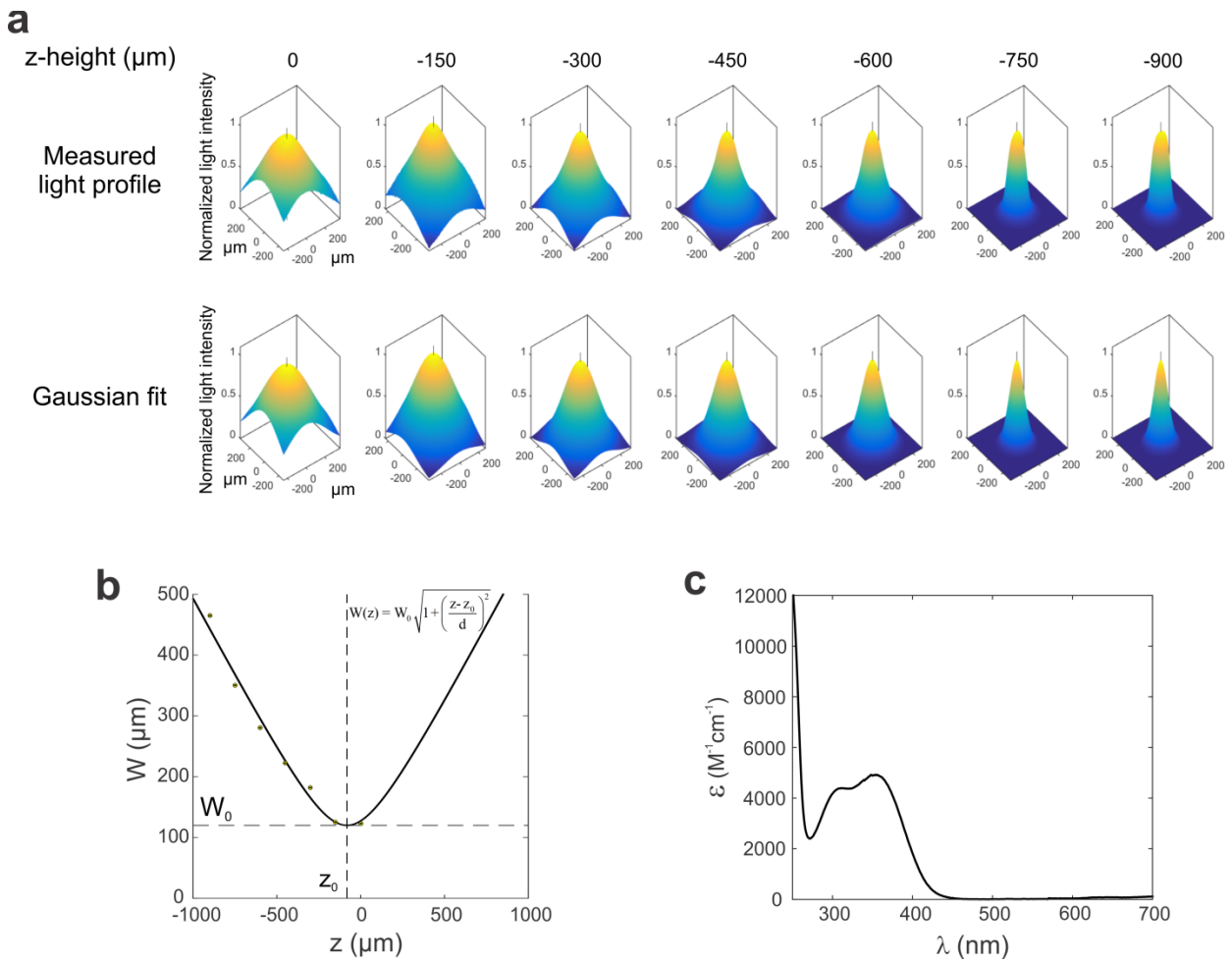

Supplementary Figure 2: Characterization of the chemoattractant release. (**a**) Normalized profile of UV light used for release of resact (top). The UV profile was measured by exciting fluorescein sheets distributed at different *z*-positions along the optical axis of the microscope. The focal plane of the objective corresponds to $z = 0$ µm. Individual sections were fitted to a Gaussian function (bottom). (**b**) Fitted width of the UV light profile at different heights along the optical axis (data in points yellow with black outline; thin black error bars lay within the points). The width of the light at different *z*-positions resembles a Gaussian beam (equation, and corresponding fit shown as a thick black line). (**c**) Molar extinction coefficient of caged resact in ASW.

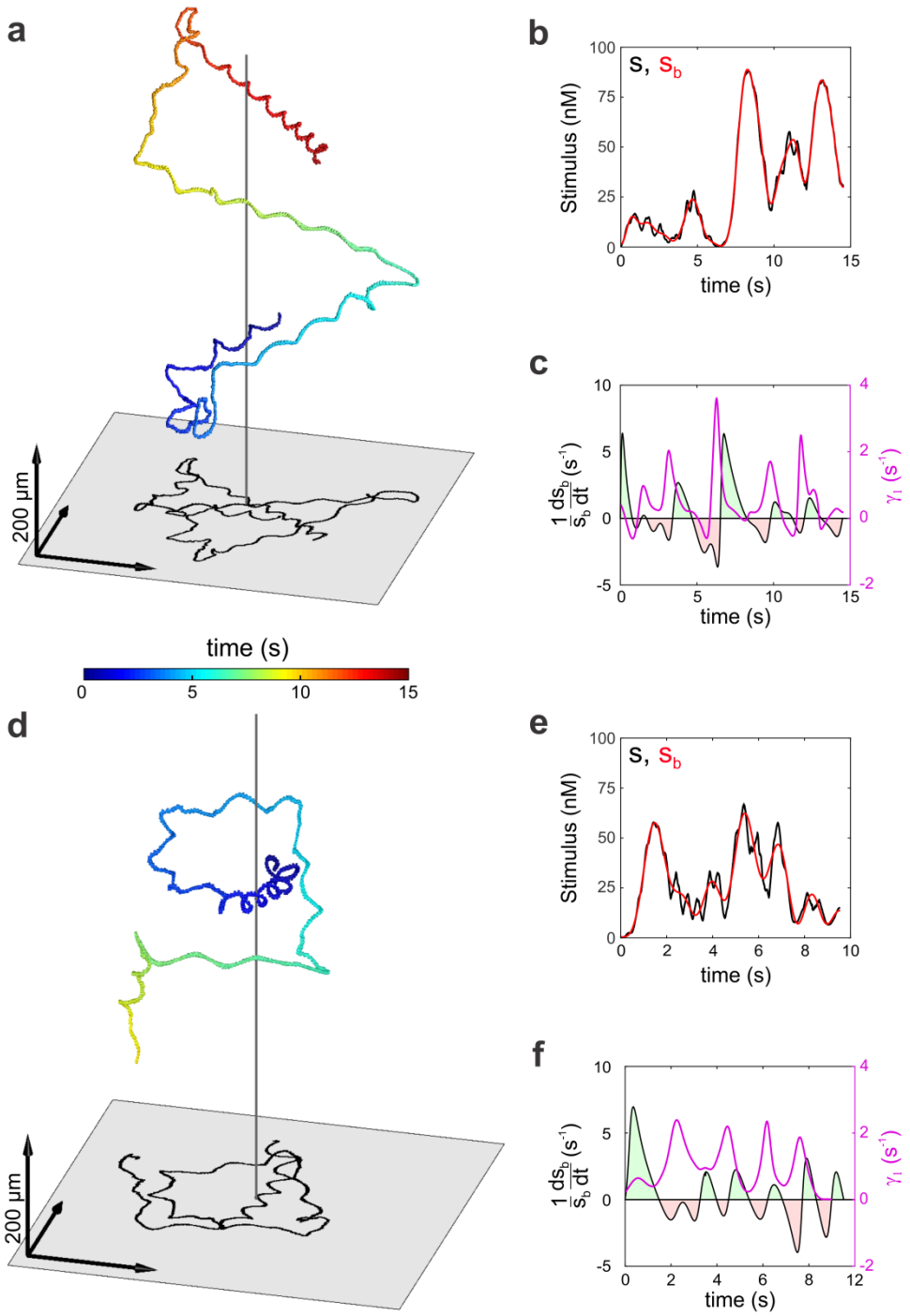

Supplementary Figure 3: Sperm steering in a 3D gradient. (**a, d**) representative swimming paths of sperm in the gradient shown in Figure 3a. (**b**, **e**) Corresponding stimulus encountered by sperm while swimming in the gradient. (**c, f**) Relative changes of the stimulus baseline and alignment of the helical path.

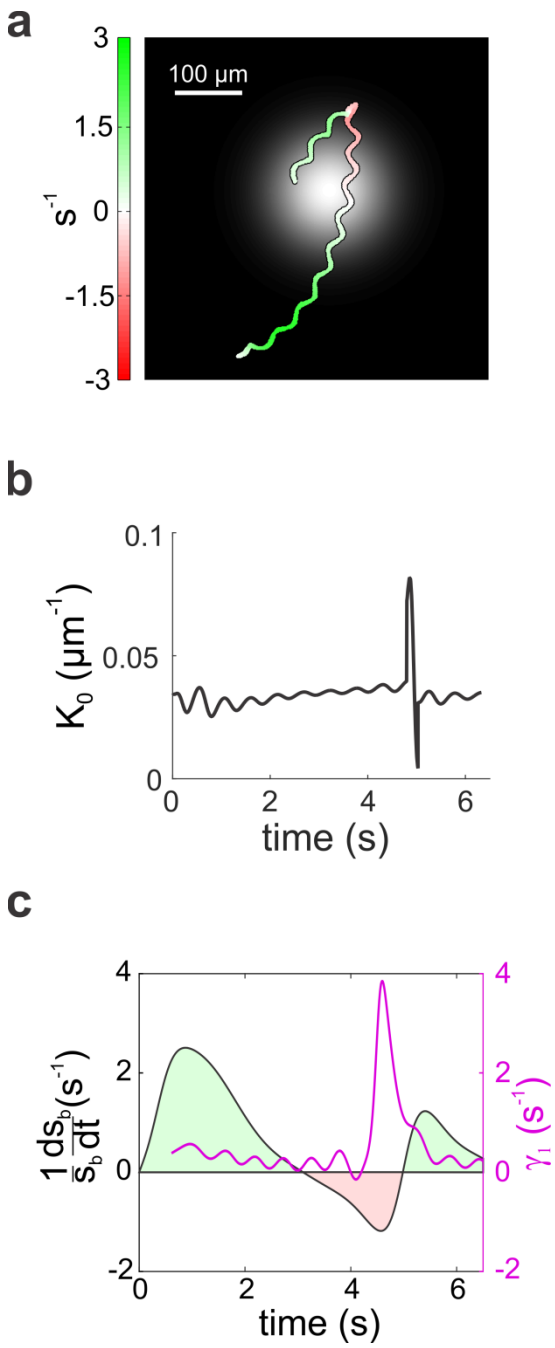

Supplementary Figure 4: Exemplary simulation of sperm chemotaxis when chemoreceptors are located along the flagellum. (**a**) Computed path of a cell navigating in a chemoattractant gradient (grey shades), where K_0 is dynamically adjusted by a simple feedback. The chemoattractant sensors have been assumed to be distributed uniformly along the flagellar surface (see Supplementary Note). Regardless of the chemoreceptor location (head versus flagellum) the navigation behaviour is analogous (see Fig. 6. and Supplementary Note). (**b**) Mean flagellar curvature in time K_0 for the simulated path shown in panel a. During swimming up the gradient, K_0 modulations are small. Swimming down the gradient triggers a large modulation of the mean flagellar curvature and results in a large correction of the swimming direction. (**c**) Relative change in baseline stimulus and alignment rate (γ_1) for the simulated path shown in panel a.

Supplementary Note

Jan F. Jikeli[1]*, Luis Alvarez[1]*, Benjamin M. Friedrich[2]*, Laurence Wilson[3]*, René Pascal[1], Remy Colin[4], Magdalena Pichlo[1], Andreas Rennhack[1], Christoph Brenker[5], and U. Benjamin Kaupp[1]: **Sperm navigation along helical paths in 3D chemoattractant landscapes**

Theoretical description of steering along helical paths

This SI text presents a theoretical analysis of our mathematical model of sperm chemotaxis along helical paths. We first summarize symbols and equations used. Second, we characterize the input-output transfer function of the signaling module for three prototypical stimulus functions $s(t)$. We then review the kinematics of swimming along perfect helical paths, as well as steering along bent helices by oscillating path curvature and path torsion. We specifically address *on* and *off* steering responses. We discuss the role of phase lags – both due to signaling latency as well as due to the dynamics of swimming – between stimulus and motor response.

List of symbols used:

t:	time
$\mathbf{x}$:	space coordinates
$\mathbf{r}(t)$:	averaged swimming path of the sperm cell
$c(\mathbf{x},t)$:	chemoattractant concentration-field
$s(t)$:	concentration stimulus sampled by the cell along its path
$\mathbf{R}(t)$:	centerline of helical swimming path $\mathbf{r}(t)$
$\mathbf{h}(t)$:	unit vector pointing along the helical axis of a helical swimming path $\mathbf{r}(t)$
$\nabla c(t)$:	chemical gradient at $\mathbf{r}(t)$
$\nabla_{\parallel} c(t)$:	component of the gradient parallel to $\mathbf{h}(t)$

$\nabla_{\perp} c(\mathbf{x},t)$:	component of the gradient perpendicular to $\mathbf{h}(t)$
$\mathbf{g}_1(t)$:	unit vector parallel $\nabla_{\perp} c(t)$
$\mathbf{g}_2(t)$:	unit vector perpendicular to $\mathbf{h}(t)$ and $\mathbf{g}_1(t)$
$\gamma_1(t)$:	alignment rate of the helix vector $\mathbf{h}(t)$ towards $\mathbf{g}_1(t)$
$\gamma_2(t)$:	alignment rate of the helix vector $\mathbf{h}(t)$ towards $\mathbf{g}_2(t)$
$p(t)$:	dynamic sensitivity of signaling system
$a(t)$:	signaling output variable
μ:	signaling time-scale
$\chi(t)$:	steering feedback strength
χ_{on}:	steering feedback strength during *on* resonse
χ_{off}:	steering feedback strength during *off* response
$q(t)$:	trigger variable that monitors changes of the stimulus baseline
θ:	trigger threshold for *off* responses
η:	time-scale of stimulus filtering
$v(t)$:	swimming speed
$\kappa_{\text{p}}(t)$:	path curvature of swimming path $\mathbf{r}(t)$
$\tau_{\text{p}}(t)$:	path torsion of swimming path $\mathbf{r}(t)$
$\mathbf{t}(t)$:	tangent vector of the Frenet frame along the swimming path $\mathbf{r}(t)$
$\mathbf{n}(t)$:	normal vector of the Frenet frame along the swimming path $\mathbf{r}(t)$
$\mathbf{b}(t)$:	binormal vector of the Frenet frame along the swimming path $\mathbf{r}(t)$
r_0:	helix radius
p_0, $2\pi h_0$:	helix pitch

Ω_0:	angular frequency of helical swimming
$K_0(t)$:	mean flagellar curvature
K_b:	mean flagellar curvature in the absence of stimulation
l:	arc-length coordinate along the flagellum
$\mathbf{r}_f(l,t)$:	position of the flagellar centerline
$\kappa_f(l,t)$:	flagellar curvature
τ_f:	flagellar twist
ω_0:	angular flagellar beat frequency
$2\pi/\lambda$:	wavelength of flagellar bending wave
$\mathbf{e_1}(l,t)$:	normal vector of the Cosserat frame along the flagellum
$\mathbf{e_2}(l,t)$:	binormal vector of the Cosserat frame along the flagellum
$\mathbf{e_3}(l,t)$:	tangent vector of the Cosserat frame along the flagellum

List of equations:

Helix bending:

$$\dot{\mathbf{h}} = \gamma_1 \mathbf{g_1} + \gamma_2 \mathbf{g_2} \tag{1}$$

(dot denotes time-derivative)

Flagellar wave form dynamics:

$$\frac{\mathrm{d}\mathbf{r}_f}{\mathrm{d}l} = \mathbf{e}_3, \ \frac{\mathrm{d}\mathbf{e}_3}{\mathrm{d}l} = \kappa_f \mathbf{e}_1, \ \frac{\mathrm{d}\mathbf{e}_1}{\mathrm{d}l} = -\kappa_f \mathbf{e}_3 + \tau_f \mathbf{e}_2, \ \frac{\mathrm{d}\mathbf{e}_2}{\mathrm{d}l} = -\tau_f \mathbf{e}_1, \tag{2}$$

$$\kappa_f(l,t) = K_0(t) + B\cos(\omega_0 t - \lambda l) \tag{3}$$

Signalling dynamics:

$$s(t) = c(\mathbf{r}(t), t) \tag{4}$$

$$\mu \dot{a} = ps - a \tag{5.1}$$

$$\mu \dot{p} = p(a-1) \tag{5.2}$$

$$K_0 = K_b - \chi(a-1) \tag{6}$$

$$\eta \frac{\mathrm{d}q}{\mathrm{d}t} = a - q \tag{7}$$

$$\chi = \begin{cases} \chi_{\text{on}} & \text{for } q > \theta \\ \chi_{\text{off}} & \text{for } q < \theta \end{cases} \tag{8}$$

Characterisation of the adapation module

We discuss the input-output characteristic of the adaptation module in equations (5.1) and (5.2) for three prototypical stimuli $s(t)$.

Constant stimulus

For a constant stimulus of the form $s(t) = s_0$, the output $a(t)$ is always constant, $a(t) = 1$.

Oscillatory stimulus

An oscillating stimulus $s(t) = s_0 + s_1 \cos(\Omega t)$ with frequency Ω and (small) amplitude s_1 will elicit oscillations of the output variable around its rest value, $a(t) \approx 1 + \rho_a s_1 \cos(\Omega t + \phi_a)$, with amplitude gain ρ_a and phase-lag ϕ_a. Here,

$$\rho_a e^{i\phi_a} = \frac{1}{s_0} \frac{i\Omega}{1 + i\Omega\mu - \Omega^2\mu^2} \tag{S1}$$

denotes the so-called complex susceptibility of the signaling system. Note that the phase-lag ϕ_a between $s(t)$ and $a(t)$ is independent of the base-level s_0. The oscillation amplitude $\rho_a s_1$ scales as s_1/s_0, and thus, the output variable $a(t)$ displays adaptation because it responds to relative changes of the input stimulus.

Of note, the trigger variable $q(t)$ (see equation 7) oscillates only weakly in this case with an amplitude that is attenuated by a factor $|1+i\Omega\eta|^{-1}$ as compared to $a(t)$.

Exponential stimulus

We consider a stimulus baseline $s(t) = s_0 \exp(\sigma t)$ that changes in time at a rate σ that can be either positive (increasing stimulus) or negative (decreasing stimulus). In this case the output is detuned from its rest-value:

$$a(t) = 1 + \mu\sigma \,. \tag{S2}$$

The amount of detuning is set by a competition between the time-scale of adaptation (μ) and the time-scale on which the stimulus changes ($|\sigma|^{-1}$). Thus, the condition $q > \theta$ on the trigger variable q(t) is equivalent to the rate σ to exceed a threshold:

$$\sigma > \sigma^* = \frac{\theta - 1}{\mu} \,. \tag{S3}$$

The stimuli sampled by swimming cells can be approximated as a superposition of fast oscillations and a slowly changing baseline, and thus represent a superposition of these idealized cases.

A theory of steering along helical paths

The Frenet frame; curvature and torsion

The bending and twisting of a swimming path $\mathbf{r}(t)$ is characterized by its signed curvature $\kappa_\mathrm{p}(t)$ and torsion $\tau_\mathrm{p}(t)$. These quantities describe the dynamics of an orthonormal coordinate system that moves along $\mathbf{r}(t)$, consisting of the tangent vector $\mathbf{t} = \dot{\mathbf{r}}/v$, the normal vector $\mathbf{n} = \dot{\mathbf{t}} \big/ \left|\dot{\mathbf{t}}\right|$, and the binormal vector $\mathbf{b} = \mathbf{t} \times \mathbf{n}$. This so-called Frenet frame rotates along the path according to the Frenet-Serret formulas:

$$\dot{\mathbf{r}} = v\,\mathbf{t},\;\; \dot{\mathbf{t}} = v\,\kappa_\mathrm{p}\,\mathbf{n},\;\; \dot{\mathbf{n}} = -v\,\kappa_\mathrm{p}\,\mathbf{t} + v\,\tau_\mathrm{p}\,\mathbf{b},\;\; \dot{\mathbf{b}} = -v\,\tau_\mathrm{p}\,\mathbf{b} \tag{S4}$$

Note that the signed curvature is only defined up to a global choice of sign. The sign of τ_p distinguishes right-handed helices ($\tau_\mathrm{p} > 0$) and left-handed helices ($\tau_\mathrm{p} < 0$).

Swimming along perfect helices

Flagellar propulsion with an asymmetric, nonplanar beat pattern that is perfectly periodic in time implies an averaged swimming path $\mathbf{r}(t)$ that is a perfect helix with constant curvature κ_p and torsion τ_p. The vector $\mathbf{\Omega}(t) = v[\tau_\mathrm{p}\,\mathbf{t}(t) - \kappa_\mathrm{p}\,\mathbf{b}(t)]$ can be shown to be an invariant of this motion. In fact, $\Omega_0 = |\mathbf{\Omega}|$ is the angular frequency of helical swimming, while the helix vector $\mathbf{h} = \mathbf{\Omega}/\Omega_0$ points along the centerline of the helix. The vector $\mathbf{\Omega}$ characterizes rotations of the Frenet frame, e.g. $\dot{\mathbf{t}} = \mathbf{\Omega}\times\mathbf{t}$. Thus, the tangent vector $\mathbf{t}$ performs a precession motion around the helix vector $\mathbf{h}$ with a constant rotation rate Ω_0. We note the useful formulas $\mathbf{\Omega}\cdot\mathbf{t} = v\,\tau_\mathrm{p}$ and $|\mathbf{\Omega}\times\mathbf{t}| = v|\kappa_\mathrm{p}|$. The radius and pitch of the helix can be computed as $r_0 = \kappa_\mathrm{p}/(\kappa_\mathrm{p}^2 + \tau_\mathrm{p}^2)$ and $2\pi h_0 = 2\pi\tau_\mathrm{p}/(\kappa_\mathrm{p}^2 + \tau_\mathrm{p}^2)$, respectively. Note that planar circular paths (Fig. 2a) and twisted ribbons (Fig. 2b) can be considered as degenerate cases of helical swimming characterized by $\tau_\mathrm{p} = 0$ and $\kappa_\mathrm{p} = 0$, respectively.

Sampling a concentration gradient along helical paths

We now consider the idealized case of a cell moving along a perfect helical path $\mathbf{r}(t)$ inside a linear concentration field $c(\mathbf{x}) = c_0 + \nabla c\cdot\mathbf{x}$. Relative to the helix vector $\mathbf{h}$, the concentration gradient vector ∇c can be decomposed as

$$\nabla c = \nabla_{\|} c + \nabla_{\perp} c \qquad \textbf{(S5)}$$

with (i) a component parallel to the helix vector, $\nabla_{\|} c = (\nabla c\cdot\mathbf{h})\mathbf{h}$, and (ii) a component perpendicular to the helix vector, $\nabla_{\perp} c = \nabla c - \nabla_{\|} c$, see Fig. 3c in the main text. While swimming along a helical path, the cell samples a concentration stimulus $s(t) = c(\mathbf{r}(t))$ from the concentration field that comprises (i) a slow change of the stimulus baseline resulting from a net motion along the direction $\mathbf{h}$ and (ii) a fast oscillation with the frequency Ω_0 of helical swimming. For an appropriate choice of coordinate system, we find

$$s(t) = c_0 + (\nabla_{\|} c\cdot\mathbf{h})h_0\Omega_0 t + |\nabla_{\perp} c|\, r_0 \cos(\Omega_0 t)\,. \qquad \textbf{(S6)}$$

Chemotaxis by phase-locked oscillations of path curvature and torsion

The time-dependent concentration stimulus sampled by a sperm cell along its path serves as input for a signaling system that controls the shape of the flagellar beat, and thus changes curvature $\kappa_p(t)$ and torsion $\tau_p(t)$ of the swimming path. Generally, an oscillatory concentration stimulus as in equation (S6) will elicit phase-locked oscillations of path curvature and torsion. We consider an idealized case of perfect curvature and torsion oscillations with the frequency Ω_0 of helical swimming

$$\kappa_p(t) = \kappa_0 + \kappa_1 \cos(\Omega_0 t + \phi_\kappa), \tag{S7}$$

and analogously, $\tau_p(t) = \tau_0 + \tau_1 \cos(\Omega_0 t + \phi_\tau)$. Here, we explicitly account for a phase-shift ϕ_κ between oscillations of $s(t)$ and $\kappa_p(t)$, which characterizes latency times of chemotactic signal processing. Oscillating curvature and torsion yield bent helices: Using a theory put forward previously[1-3], we can compute the bending rates γ_1 and γ_2 of helical paths defined in the Methods section equation (1)

$$\gamma_1 = \frac{\Omega_0}{2}\left(r_0\tau_1 \cos\phi_\tau - h_0\kappa_1 \cos\phi_\kappa\right) \tag{S8}$$

$$\gamma_2 = \frac{\Omega_0}{2}\left(h_0\kappa_1 \sin\phi_\kappa - r_0\tau_1 \sin\phi_\tau\right) \tag{S9}$$

Thus, a sufficient condition for optimal alignment of the helix axis with respect to the concentration gradient characterized by $\gamma_1 > 0$ and $\gamma_2 = 0$ is given by $\phi_\kappa = \pi$ and $\phi_\tau = 0$, implying that curvature oscillations would be anti-phase to stimulus oscillations, while torsion oscillations would be in-phase. These results pertain also in more realistic cases of slightly nonlinear concentration fields, and concentration stimuli sampled along helical paths that are perturbed by steering feedback, as long as the feedback is weak (characterized by $\chi\rho_a|\nabla c|r_0 \ll 1$).

The "off response"

Whether the helical path is directed up the concentration gradient $(\nabla c \cdot \mathbf{h} > 0)$ or down the concentration gradient $(\nabla c \cdot \mathbf{h} < 0)$ is reflected by a slow increase or decrease of the stimulus baseline, respectively. From Equations (S6) and (7), we find for the trigger variable $q(t)$

$$q \approx 1 + \mu\Omega_0 \frac{\nabla c \cdot \mathbf{h}}{c} h_0 . \qquad \textbf{(S10)}$$

Thus, an *off* response is triggered in our simulations whenever the relative gradient strength in the direction of the helix axis falls below the critical value:

$$\frac{\nabla_{\parallel} c}{c} < \frac{\theta - 1}{\mu\Omega_0 h_0} . \qquad \textbf{(S11)}$$

For the parameters used, we have $(\theta - 1)/(\mu\Omega_0 h_0) = -1.2 \cdot 10^{-3}\,\mu\mathrm{m}^{-1}$ or about -6% over one helix pitch $2\pi h_0 \approx 50\,\mu\mathrm{m}$. During an *off* response, the helix axis rotates rapidly as a result of large-amplitude oscillations of path curvature and torsion. While the geometric principle is fully analogous to the case of *on* responses, equations (S8) and (S9) will only hold in an approximate sense and the directional precision of these vigorous steering responses might be reduced as compared to the case of *on* responses.

Phase-lags in simulations

In our simulations, path curvature $\kappa_{\mathrm{p}}(t)$ and torsion $\tau_p(t)$ are regulated only indirectly by dynamically adjusting the mean flagellar curvature K_0, see equation (6). For the parameters chosen, we observe an additional phase-lag ϕ_{K_0} between oscillations of K_0 and κ_{p}, where $\phi_{K_0} \approx \pi/3$. This phase-lag depends on the oscillation frequency Ω and vanishes if we impose adiabatically slow oscillations of mean flagellar curvature. The effective phase-lag ϕ_κ that governs the bending rate in equation (S8) is the sum of (i) the phase-lag ϕ_{a} due to signaling latency and (ii) the phase-lag ϕ_{K_0} arising from the dynamic regulation of the beat pattern,

$$\phi_\kappa = \phi_a + \phi_{K_0} . \tag{S12}$$

For the parameters chosen, we find $\phi_a \approx 2\pi/3$ according to equation (S1). Thus, $\phi_\kappa \approx \pi$. Similarly, $\phi_\tau \approx 0$. From equation (S8) and (S9), we find $\gamma_1 > 0$ and $\gamma_2 \approx 0$, corresponding to positive chemotaxis with the helix axis bending in the direction of the concentration gradient.

Location of stimulus receptor

The minimal theory presented above assumed for simplicity that stimulus concentration $s(t)$ is measured at the position $\mathbf{r}(t)$ of the sperm head, see equation (4). However, chemoattractant molecules bind to surface receptors distributed along the flagellar length [4]. We can account for this by defining a flagellar stimulus $s_w(t)$ that represents a weighted average of the local stimulus concentration along the flagellum

$$s_w(t) = \int_0^L c(\mathbf{r}_\mathbf{f}(l,t),\mathrm{t})w(l)\,\mathrm{d}l . \tag{S13}$$

Here, $\mathbf{r}_\mathbf{f}(l,t)$ denotes the centerline of the flagellum parametrized by arc-length l and w(l) is a normalized density of receptors as a function of l. For the special case of a δ-distribution located at the head position, we recover the previous definition. We also define the trajectory of the weighted "center of mass" $\mathbf{r}_w(t)$ of the receptor ensemble

$$\mathbf{r}_w(t) = \int_0^L \mathbf{r}_\mathbf{f}(l,t)w(l)\,\mathrm{d}l \tag{S14}$$

as well as the corresponding path curvature $\kappa_w(t)$ of its averaged path. We can use the stimulus $s_w(t)$ instead of the head stimulus $s(t)$ as input for the adaptation module given in equation (5). Simulation results are largely independent of the choice of $w(l)$, provided the delay time of the adaptation module is adjusted accordingly. Generally, there is a phase lag ϕ_f between the flagellar stimulus $s_w(t)$ and the head stimulus $s(t)$ such that, $s_w(t) \approx s(t + \Omega_0^{-1}\phi_f)$. This additional phase lag can be compensated by changing the delay time of the adaptation module to ensure that the effective phase lag $\phi_\kappa = \phi_a - \phi_f + \phi_{K_0}$ between oscillations of head stimulus $s(t)$ and oscillations of head path curvature $\kappa(t)$ still sum up to π. For the case of uniformly distributed receptors along the flagellum ($w(l) = 1/L$), we find e.g. $\phi_f \approx \pi/2$. Choosing η = 60 ms in

simulations, yielded $\phi_a \approx 5\pi/3$ and thus positive chemotaxis with $\phi_\kappa \approx \pi$. Note that equations (S8) and (S9) governing the direction of helix bending generalize to the case of an arbitrary receptor distribution $w(l)$, provided ϕ_κ is replaced by the phase lag between oscillations of flagellar stimulus $s_w(t)$ and oscillations of the weighted flagellar path curvature $\kappa_w(t)$. As anticipated, simulations accounting for a uniform receptor distribution along the flagellum do not qualitatively differ to the minimal model considered in the main text, where the stimulus concentration is measured at the position of the sperm head (see Supplementary Fig. 4).

References

1. Friedrich, B.M. Chemotaxis of Sperm Cells. PhD thesis (Technische Universität Dresden, Germany2008).
2. Friedrich, B.M. & Jülicher, F. Steering chiral swimmers along noisy helical paths. *Phys. Rev. Lett.* **103**, 068102 (2009).
3. Friedrich, B.M. & Jülicher, F. Chemotaxis of sperm cells. *Proc. Natl. Acad. Sci. USA* **104**, 13256-13261 (2007).
4. Bönigk, W. *et al.* An atypical CNG channel activated by a single cGMP molecule controls sperm chemotaxis. *Sci. Signal.* **2**, ra68 (2009).

Sarcomeric Pattern Formation by Actin Cluster Coalescence

Benjamin M. Friedrich[1,2]*, Elisabeth Fischer-Friedrich[2,3], Nir S. Gov[3], Samuel A. Safran[1]

1 Department of Materials and Interfaces, Weizmann Institute of Science, Rehovot, Israel, 2 Max Planck Institute for the Physics of Complex Systems, Dresden, Germany, 3 Department of Chemical Physics, Weizmann Institute of Science, Rehovot, Israel

Abstract

Contractile function of striated muscle cells depends crucially on the almost crystalline order of actin and myosin filaments in myofibrils, but the physical mechanisms that lead to myofibril assembly remains ill-defined. Passive diffusive sorting of actin filaments into sarcomeric order is kinetically impossible, suggesting a pivotal role of active processes in sarcomeric pattern formation. Using a one-dimensional computational model of an initially unstriated actin bundle, we show that actin filament treadmilling in the presence of processive plus-end crosslinking provides a simple and robust mechanism for the polarity sorting of actin filaments as well as for the correct localization of myosin filaments. We propose that the coalescence of crosslinked actin clusters could be key for sarcomeric pattern formation. In our simulations, sarcomere spacing is set by filament length prompting tight length control already at early stages of pattern formation. The proposed mechanism could be generic and apply both to premyofibrils and nascent myofibrils in developing muscle cells as well as possibly to striated stress-fibers in non-muscle cells.

Citation: Friedrich BM, Fischer-Friedrich E, Gov NS, Safran SA (2012) Sarcomeric Pattern Formation by Actin Cluster Coalescence. PLoS Comput Biol 8(6): e1002544. doi:10.1371/journal.pcbi.1002544

Editor: Shoichiro Ono, Emory University, United States of America

Received January 3, 2012; **Accepted** March 26, 2012; **Published** June 7, 2012

Funding: This work was supported by the German Academic Exchange Service (BMF), a Minerva post-doctoral fellowship (EFF), the Israel Science Foundation (SAS), and the historic generosity of the Perlman Family Foundation. The funders had no role in study design, data collection and analysis, decision to publish, or preparation of the manuscript.

Competing Interests: The authors have declared that no competing interests exist.

* E-mail: ben@pks.mpg.de

Introduction

The intriguing striations of muscles were first observed more than a century ago [1]. All skeletal and cardiac muscle cells develop striated acto-myosin bundles of striking regularity termed mature myofibrils, which are characterized by a periodic localization of myosin II filaments alternating with crosslinking regions rich in α-actinin [2]. An analogous, though less regular, arrangement of actin and myosin filaments can be found in adherent, non-muscle cells that express striated stress fibers [3,4]. Some developing muscle cells contain similar striated stress-fiber like acto-myosin bundles termed premyofibrils and nascent myofibrils [5–7] that have been proposed to represent intermediate structures for the formation of mature myofibrils [8]. Figure 1 depicts the periodic structure of mature myofibrils. Periodically spaced crosslinking regions termed Z-bodies or Z-bands delineate 1μm-wide sarcomeric regions that comprise actin filaments of organized polarity and crosslinking myosin filaments in the sarcomere midzone. How are these surprisingly regular structures assembled? Numerous proteins involved in myofibrillogenesis have been identified together with their critical role in several muscle diseases [9]. However, the mechanistic basis for sarcomere self-assembly and the establishment of striated order remains elusive. There is evidence that striated fibers are preceded by unstriated fibers, which lack apparent sarcomeric localization of myosin and crosslinkers. Nascent striations first become visible as agglomerations of the actin crosslinker α-actinin, which then grow and change position to establish a regular, periodic spacing [10]. The formation of these early, unstriated bundles requires the parallel alignment of actin filaments, their mutual crosslinking as well as some means to control bundle thickness. Initial bundle formation depends on actin crosslinking, and possibly Onsager nematic alignment and depletion attractions of entropic origin [11,12], or kinetic effects due to polar actin flow [13]. The thickness of such actin bundles might be kinetically controlled [14]; additionally, geometric frustration effects due to the chirality of actin filaments have been proposed to set bundle thickness [15–17]. Here, we focus on the stage of development in which there is already a pre-formed, unstriated bundle of finite thickness and present a mechanism to explain the subsequent emergence of initial sarcomeric order within this unstriated bundle. In muscle cells, subsequent myofibrillar maturation processes, not modeled here, and fine-tuning of actin filament length, *e.g.* by nebulin [18,19], drive the transition to final crystalline order.

So far, a number of sarcomeric scaffolding proteins such as titin, N-RAP, and WASP have been identified [18–23] and it is highly probable that these scaffolding proteins help to enhance and maintain striated order. However, it is unclear if these scaffolding proteins are able to establish initial striated order in the first place. To do this, these proteins would have to align in a periodic manner on a super-micrometer length-scale by some yet unknown mechanism. Additionally, it is unclear how myosin filaments, which normally walk towards actin plus-ends, become localized near actin minus-ends during myofibril assembly. Here, we ask if physical interactions of actin and myosin filaments, as well as crosslinkers are sufficient to induce initial striated order in filament bundles. Such a mechanism could be generic and could also apply to the formation of striations in acto-myosin stress fibers in

Author Summary

Muscle contraction driving voluntary movements and the beating of the heart relies on the contraction of highly regular bundles of actin and myosin filaments, which share a periodic, sarcomeric pattern. We know little about the mechanisms by which these 'biological crystals' are assembled and it is a general question how order on a scale of 100 micrometers can emerge from the interactions of micrometer-sized building blocks, such as actin and myosin filaments. In our paper, we consider a computational model for a bundle of actin filaments and discuss physical mechanisms by which periodic order emerges spontaneously. Mutual crosslinking of actin filaments results in the formation and coalescence of growing actin clusters. Active elongation and shrinkage dynamics of actin filaments generates polymerization forces and causes local actin flow that can act like a conveyor belt to sort myosin filaments in place.

non-muscle cells. We show that the combination of treadmilling actin filaments and processive, plus-end tracking crosslinkers suffices to account for the self-organization of striated order and the localization of myosin filaments. Some examples of plus-end tracking crosslinkers such as formins and VASP are known in the biological literature [24,25]. We emphasize that the plus-end tracking crosslinking of actin filaments in acto-myosin bundles is probably not due tothe action of a single protein, but rather to the concerted assembly by several, interacting structural proteins such as the plus-end capping protein CapZ, the actin crosslinker α-actinin and the giant scaffolding protein titin [26,27]. Our simple, coarse-grained model replaces this interplay of Z-body proteins by a single "effective" crosslinker that processively grafts actin plus-ends. Note that molecular details may be species-specific: In a recent study by Rui *et al.* [28], the concerted action of the Z-band proteins Zasp, Zipper, kettin, and titin was demonstrated to be pivotal for Z-body formation in Drosophila muscle, while α-actinin seemed to be dispensable. The strongest evidence for our key assumption of an effective plus-end tracking crosslinker has been provided by recent FRAP-experiments in myofibrils. In these experiments, plus-ends of actin filaments remained localized at the crosslinking band, yet these actin filaments showed polymerization dynamics at their plus-ends. This observation is consistent with the picture of a Z-body acting as a processive, plus-end tracking crosslinker that allows the insertion of new actin monomers while holding the actin filament plus-ends linked with each other. Such a crosslinker could undergo rapid binding and unbinding cycles with actin plus-ends. One study identified a pool of very dynamic actin filaments in mature myofibrils [29]. Physically, a processive plus-end tracking crosslinker results in the condensation of actin filaments into clusters or I-Z-I complexes that consist of two adjacent domains of polarity-sorted actin filaments (I-bands) held together by a crosslinking Z-band, see figure 1. In this paper, we present a minimal model whose analysis shows that actin filament treadmilling and crosslinking can account for the initial establishment of striated order.

Survey of previous modeling approaches

Several groups have proposed polarity sorting of actin filaments by myosin activity [30,31]. However, those mechanisms localize myosin filaments close to actin filament plus-ends, which is opposite to the myosin localization observed in striated stress fibers and myofibrils, where myosin resides in the mid region between neighboring crosslinks that attach to the actin plus-ends, see figure 1. In simulations of a generic bundle of polar filaments crosslinked by populations of both plus- and minus-end directed motors, Zemel *et al.* demonstrated sarcomeric ordering with correct polarity sorting if applied to actin bundles [32], see also [33]. However, in the context of actin bundles, there is little evidence for an unconventional, minus-end directed myosin [34].

The concept of a plus-end tracking crosslinker as put forward here has been introduced earlier in the framework of a mean field description [35]. Recently, the group of Joanny proposed a description for the establishment of striated order by stress-induced polarity sorting in terms of a one-dimensional, active gel [36]. However, this mechanism relies on a phenomenological coupling term and as such does not provide insight into the microscopic mechanisms that eventually underlie this coupling.

Model

A bundle of treadmilling actin filaments

To describe the transition from an unstriated actin bundle to a striated one, we consider in our simulations a single, long bundle that consists of N_a parallel actin filaments aligned with the long axis of the fiber (chosen to be the x-axis). In biological cells, striated fibers have an extension in the transverse direction of only a few hundred nanometers. In our computational model, we therefore ignore the transverse position of the individual actin filaments and assume that each filament can interact with any other provided their projections on the fiber axis overlap. This assumption corresponds to a mean-field treatment of the transverse degrees of freedom.

For simplicity, filaments are assumed to be rigid and incompressible with respective lengths $L_j, j=1,\ldots,N_a$. For figures 2, 3, 4, filament lengths are monodisperse with $L_j = L_0$ for all j; whereas for figure 4 filament length are chosen from a log-normal

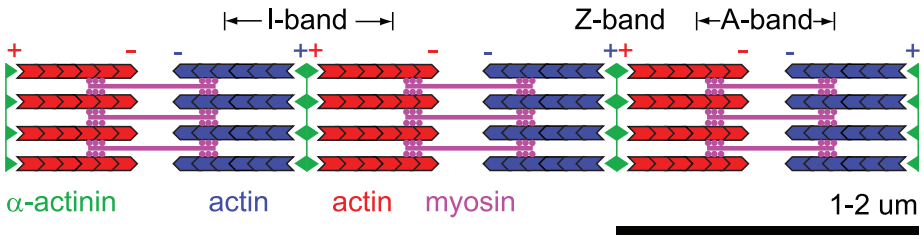

Figure 1. Schematic depiction of sarcomeric organization in myofibrils. Actin filaments (blue and red) are grafted at their plus-ends in an α-actinin rich crosslinking band, termed the Z-band (green). The repetitive units spanning from one Z-band to the next are referred to as sarcomeres and measure $1-2\mu m$ in length. The myosin band (magenta) is traditionally called A-band, while the myosin-free part of the actin band is called I-band. Numerous auxiliary proteins ensure structural integrity and tune elastic properties.
doi:10.1371/journal.pcbi.1002544.g001

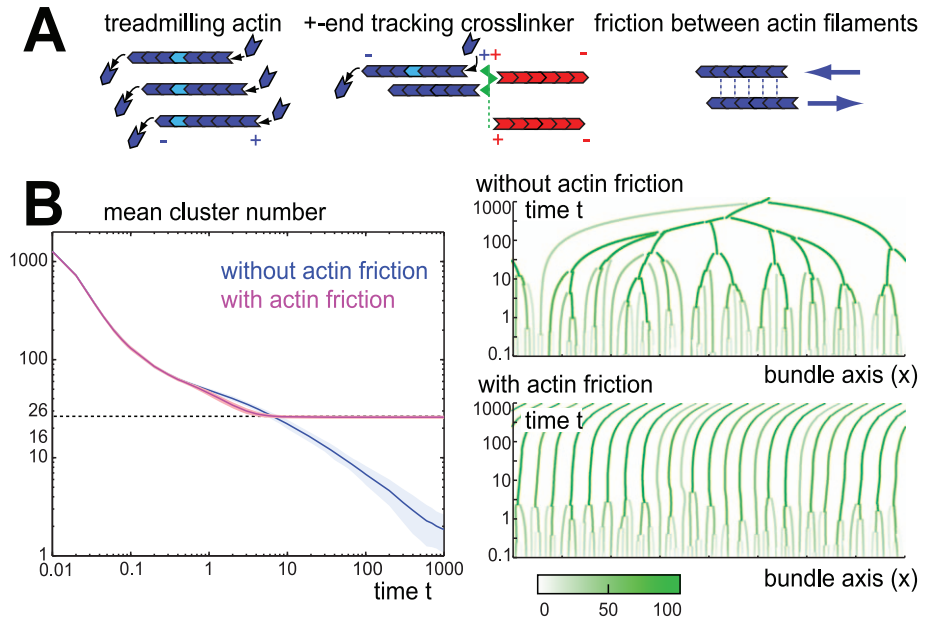

Figure 2. Actin cluster formation and coalescence. A. Our computational model of sarcomeric pattern formation considers a one-dimensional bundle of parallel actin filaments, which undergo treadmilling, *i.e.* filaments polymerize at their plus-ends and depolymerize at their minus-ends resulting in a net motion of the plus-end with respect to the individual monomers. Plus-end tracking crosslinkers (green) can permanently attach to the plus-ends of actin filaments (blue and red, indicating filament polarity), while still allowing for polymerization at filament plus-ends. **B.** Plus-end tracking crosslinking results in the formation and coalescence of actin clusters as reflected by a reduction in the number of actin clusters (single actin filaments are counted as one cluster). If there is no friction between sliding filaments ($\zeta=0$), all actin clusters eventually coalesce into a small number of very large clusters (blue, mean $\pm$ s.e., $n=100$). Time is measured in units of actin length divided by treadmilling speed, L_0/v_0. In the presence of inter-filament friction ($\zeta=0.1\gamma_a$), however, actin clusters above a critical size effectively repel each other, resulting in a kinetically stabilized configuration with a finite number of actin clusters (magenta). To the right, example kymographs of actin cluster coalescence are shown for the cases without friction and with friction, respectively. A small imbalance in the number of filaments treadmilling either to the right or to the left within the final striated bundle causes a slow motion of the entire bundle as a whole as is reflected by the tilted cluster trajectories. Using static instead of periodic boundary conditions impedes this motion, see SI text S1. The color scheme encodes filament number in actin clusters as shown in the color bar.

doi:10.1371/journal.pcbi.1002544.g002

distribution that satisfies $\langle L_j \rangle = L_0$ and $\langle L_j^2 \rangle - L_0^2 = v^2 L_0^2$, see also the Supporting Information (SI).

Actin filaments are structurally polar and filaments ends are referred to as either the plus-end or the minus end, see figure 2A. We distinguish actin filaments with plus-ends that face either the positive x-direction (orientation $\varepsilon_j = 1$, blue in figures), or the negative x-direction ($\varepsilon_j = -1$, red in figures). Actin filament polymerization is a non-equilibrium process and polymerization and depolymerization rates differ for the plus- and minus-ends, respectively. In a deterministic description of filament polymerization dynamics at steady state, we assume that the individual actin filaments possess a net polymerization speed v_0 at their plus-ends whose absolute magnitude is equal to the net depolymerization speed at their minus ends. (The corresponding polymerization rate is thus v_0/a, where a denotes actin monomer length.) The broken symmetry of the polymerization dynamics results in a velocity difference $\varepsilon_j v_0$ between the current plus-end position x_j of the j-th filament (with a lab-frame velocity $v_j = \dot{x}_j$) and its individual monomers (velocity $v_j^0 = v_j - \varepsilon_j v_0$). This phenomenon is commonly referred to as filament treadmilling [2], see figure 2A. For an actin filament that is subject only to a friction force $f_j = \gamma_a L_j v_j^0$ for motion relative to the cytosol, the plus-end advances with velocity $v_j = \varepsilon_j v_0$, while the monomers are at rest, $v_j^0 = 0$, and the friction force f_j is zero due to force balance. Here, γ_a is an effective friction coefficient that accounts for rapid binding and unbinding interactions with the surrounding actin gel, and, possibly, integrin-mediated interactions with a substrate. This situation changes, if rigid crosslinks between actin filaments constrain their motion.

Processive actin crosslinking

In addition to treadmilling actin filaments, the second key ingredient of our model is a processive, plus-end tracking actin crosslinker that effectively describes the concerted action of several Z-body proteins, see figure 2A. In our simulations, actin filaments become irreversibly crosslinked with a rate $\rho(|x_j - x_k|)$, if their respective plus-end positions x_j and x_k are close. The precise functional form of ρ affects results only slightly and we chose $\rho = \rho_0 \exp(-|x_j - x_k|/\delta)/\delta$ with $\rho_0 = v_0/L_0$ and $\delta = 0.05$ (measured in units of L_0). A case of reversible plus-end crosslinking for which actin filaments can spontaneously dissociate again is considered in the SI text S1. Subsequent crosslinking results in the formation of 'actin filament clusters' that consist of many actin filaments whose respective plus-ends are aligned and which are permanently crosslinked by effective plus-end tracking crosslinkers. Such an actin cluster will move as a whole subject to the sum of forces acting on its constituent actin filaments. These crosslinked actin clusters can grow by fusion. If two actin filaments belonging to two small clusters establish a new crosslink, the new x-coordinate of the merged cluster is taken as the weighted average of the respective x-coordinates of the two clusters. In real nascent striated fibers, the longitudinal alignment of plus-ends of crosslinked filaments supposedly involves a dynamic reorganization of

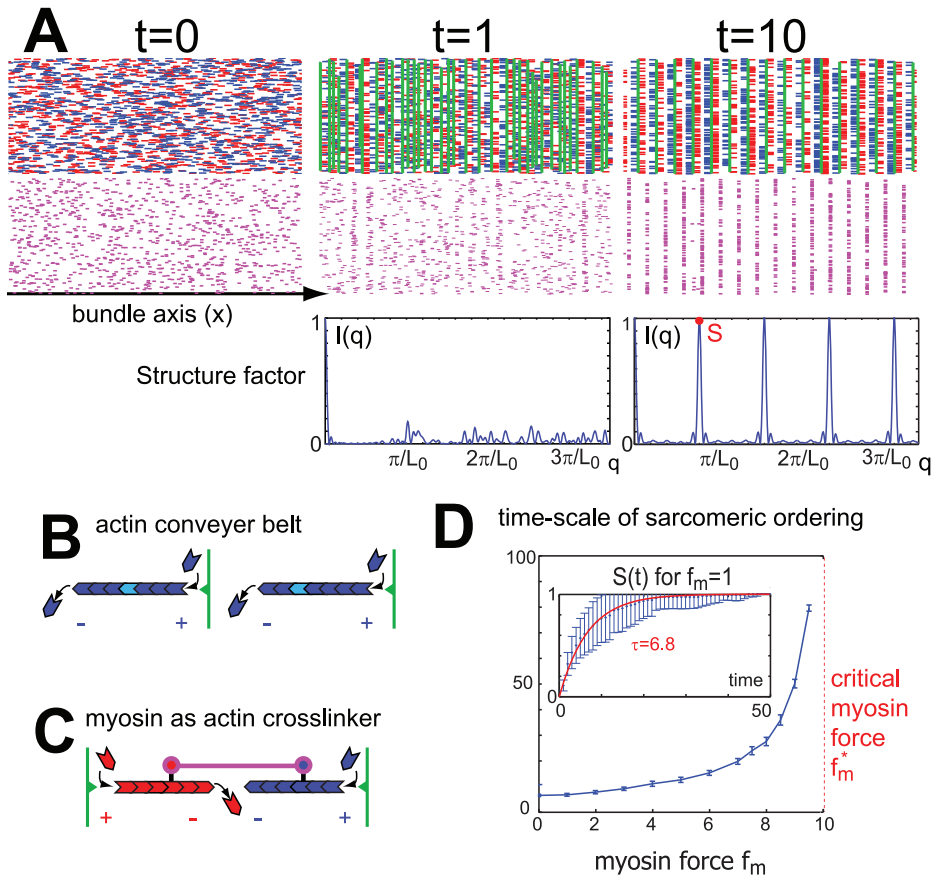

Figure 3. Sarcomeric ordering in the presence of myosin. A. Simulation snap-shots showing the emergence of sarcomeric order in an acto-myosin bundle (single actin filaments: blue and red, myosin filaments: magenta, plus-end crosslinker connecting actin filament plus ends belonging to one cluster : green). Actin filaments can interact if their projections on the bundle axis overlap. Additionally, bipolar myosin filaments (magenta) dynamically attach to actin filaments in a polarity-specific manner, thus acting as a second set of active crosslinkers. Different vertical positions of the filaments are indicated solely for visualization purposes. Initially, filament positions are random ($t=0$). After a transient period during which clusters of crosslinked actin filaments form and coalesce ($t=1$), a stable configuration is established characterized by a periodic pattern of actin clusters interspersed by bands of aligned myosin ($t=10$). To characterize sarcomeric order in these simulated bundles, we compute the structure factor $I(q)$ as defined in the main text (blue curves in lower panel, simulation time $t=1,10$, respectively). The height of the principal Bragg peak (red circle) defines the sarcomeric order parameter S. The active myosin force that tends to oppose sarcomeric ordering was chosen as $f_m=1$, measured in units of $\gamma_a L_0 v_0$. An animated version of this simulation can be found as Video S1 available online as Supplementary Information. **B.** Illustration of the 'actin conveyer belt' mechanism: Actin filaments that are grafted at their plus-end by a processive crosslinker have to polymerize against the crosslinker (that acts as an obstacle) and are pushed backwards in a form of local retrograde flow. Myosin filaments interacting with these treadmilling actin filaments are transported away from the cluster center provided that the actin treadmilling speed exceeds the active myosin walking speed. **C.** Myosin filaments that are attached to actin filaments from two neighboring clusters serve as an active crosslinker and mediate repulsive forces between the two clusters due to the difference in the actin polymerization forces and the myosin active forces, see also SI text S1. **D.** Myosin active force slows-down sarcomeric ordering: The inset shows the time-course of the sarcomeric order parameter $S(t)$ (blue,mean$\pm$s.e.,$n=100$) for $f_m=1$, together with a fit of simulation results to an exponential saturation curve $S_0[1-\exp(-t/\tau)]$ (red) that allows us to extract a time-scale τ of sarcomeric ordering. The main plot shows this time-scale τ as a function of myosin force f_m; τ diverges as f_m approaches a critical value f_m^*. For myosin forces that are larger the critical value f_m^*, sarcomeric order is not established. Instead, myosin forces facilitate the coalescence of crosslinked actin clusters into a small number of very large clusters (not shown), similar to the case shown in figure 2B without friction.
doi:10.1371/journal.pcbi.1002544.g003

the crosslinking Z-band on a time-scale of several minutes [27], which is not included in our minimal model.

Importantly, the proposed plus-end tracking crosslinkers are assumed to be processive, *i.e.* they always remain locally attached to the filament plus-ends, even in the presence of actin treadmilling of the crosslinked filaments, see figure 2A. As a consequence, the center of an actin cluster is subject to polymerization forces of its constituent actin filaments and moves with a velocity v_c that is determined by a local force-balance of cytosolic friction forces. This force balance is spelled out below in the paragraph 'Active motion of a single actin cluster'.

For figure 2 only, a generic friction force $f_{jk}=\zeta L_{jk}(v_j^0-v_k^0)$ for the relative sliding of two actin filaments is introduced, which is proportional to the mutual length overlap L_{jk} of the two filaments. Here, ζ denotes a friction coefficient.

Finally, the motion of actin clusters is determined in each time-step in a self-consistent manner by a balance of forces. We employ periodic boundary conditions with a system size $L_{\rm sys}=40L_0$; a case of static boundary conditions is discussed in the SI text S1. Total filament numbers were $N_a=2000$ for actin filaments and $N_m=1000$ for myosin filaments ($N_m=0$ for figure 2).

Myosin as dynamic actin crosslinker

In the premyofibrils of developing muscle cells as well as in stress fibers of non-muscle cells, the molecular motor myosin II

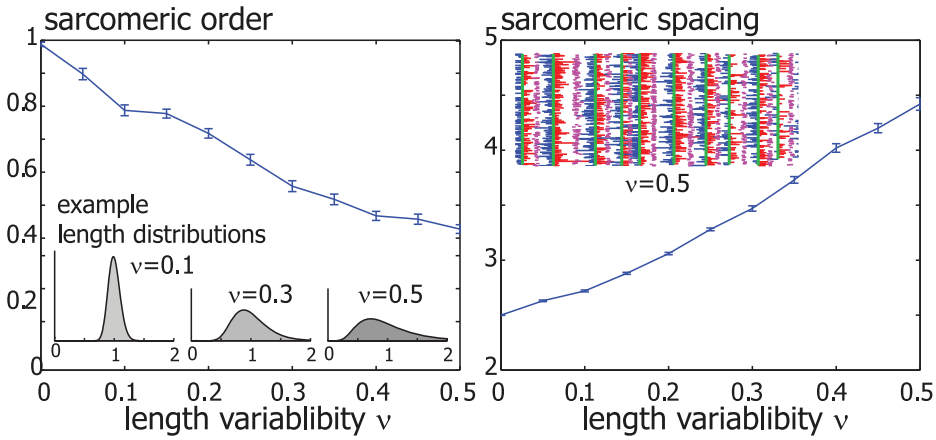

Figure 4. Sarcomeric order despite actin filament length variability. In a modified version of the simulations shown in figure 3, the lengths of individual actin filament were chosen from a unimodular length distribution, see main text. Example length distributions are shown for three values of the length variability parameter ν. Sarcomeric order also evolved in simulated acto-myosin bundles with a distribution of filament lengths, but with a reduced sarcomeric order parameter and increased sarcomere spacing at steady-state (mean $\pm$ s.e.).
doi:10.1371/journal.pcbi.1002544.g004

polymerizes into bipolar filaments of a few hundred nanometers length that have numerous myosin heads at either end [37]. Individual myosin heads change conformations via ATP-dependent cycles, while synchronously attaching to (and pushing on) actin filaments. Despite the low duty ratio of individual myosin heads, the large number of these heads ensures a processive and significant myosin-actin interaction. In our simulations, we employ a coarse-grained description of bipolar myosin filaments of length $L_m = 0.5L_0$, in which the individual myosin heads at the two ends of a myosin filament are described as a pair of 'actin binding sites', see figure 3D. Each of these two actin binding sites can bind one actin filament in a polarity-specific way. Attachment and detachment to actin filaments are described as simple Poisson processes with constant rates $k_{\text{on}} = k_{\text{off}} = v_0/L_0$. Once a myosin filament is attached to an actin filament, we assume a linear force-velocity relation for myosin walking past the actin filament, see also SI text S1 for details. Myosin walking speed is directly related to an active myosin force f_m (that also equals the myosin stall force). While myosin filaments tend to walk towards actin filament plus-ends, a strong backward force acting on the actin filament can push both the actin and myosin filaments in the opposite direction. In our simulations, actin treadmilling and associated polymerization forces indeed cause such a motion of myosin filaments towards actin filament minus-ends.

Active motion of single actin clusters

For sake of illustration, consider an isolated actin cluster that comprises a total number n_+ of filaments of positive orientation that treadmill towards the $x>0$-direction (blue in figures) as well as a number n_- of filaments of negative orientation (treadmilling towards the $x<0$-direction, red in figures). In our deterministic description of filament treadmilling, the monomers of the n_+ filaments with positive orientation all move with the same velocity $v_c - v_0$, whereas those of the n_- filaments of negative orientation all move with velocity $v_c + v_0$. Here v_0 is treadmilling speed and v_c the (yet unknown) velocity of the crosslinking Z-band. The two sets of filaments exert respective friction forces on the cytosol, $f_+ = \gamma_a L_0 (v_c - v_0) n_+$ and $f_- = \gamma_a L_0 (v_c + v_0) n_-$, where L_0 is actin filament length and γ_a a cytosolic friction coefficient per actin filament unit length, see above. By Newton's third law, the counter forces of these cytosolic friction forces act on the Z-band and amount in this case exactly to the polymerization forces of the treadmilling actin filaments. Local force balance at the Z-band, $0 = (-f_+) + (-f_-)$, determines the velocity of this single cluster as $v_c = v_0(n_+ - n_-)/(n_+ + n_-)$.

The structure factor quantifies sarcomeric order

The structure factor is a standard measure used in condensed matter physics to quantify the regularity of periodic order [38]; it is defined as the squared amplitude of the Fourier transformed density-density correlation function. We can adopt the structure factor to quantify sarcomeric order in our simulations: We characterize the crosslinked clusters by their respective plus-ends positions x_j and total filament number n_j. We then define $I(q) = |\sum_j n_j \exp(iqx_j)|^2 / \sum_j n_j^2$. Examples of this structure factor as a function of wave vector q are shown in figure 3A. Periodic order is characterized by a series of very sharp, so-called Bragg peaks. The height S of the principal Bragg peak (red point) defines a sarcomeric order parameter.

Parameter estimates

Our computational model primarily serves as a proof of physical principle. The emergence of striated order in the framework of this model is a robust process that is not sensitive to the parameter choices. A sensitivity analysis can be found in the SI text S1. Since the parameters in the model represent effective quantities (which, in particular, average out transverse degrees of freedom), numerical estimation of these parameters is difficult. Therefore, our simulation results are presented assuming specific ratios of parameters only, without specifying their absolute values in physical units. Nevertheless, we now present a rough guide to these parameter values.

In unstriated stress fibers, actin filament length range from $0.5-2\,\mu\text{m}$, myosin filaments have a length of about $1\,\mu\text{m}$ [39]. Thus, the length-scale L_0, which sets the mean length of actin filaments in our simulations, may be chosen as $\sim 1\,\mu\text{m}$. Actin polymerization speeds of up to about $1\,\mu\text{m/s}$ have been observed *in vitro*, while filopodia protrusion driven by actin polymerization can be as fast as $0.1\,\mu\text{m/s}$, see [40] and references therein. In stereocilia, actin polymerization is highly regulated and polymerization speeds can be as low as $1\,\mu\text{m}/24h$ [41]. While in general the polymerization speed of an actin filament is force-dependent

with a stall force in the pico Newton range [37,42], we assume here a constant mean polymerization speed v_0. The ratio L_0/v_0 sets the primary time-scale of sarcomeric pattern formation in our simulations, and it is shown below that sarcomeric ordering in established within $\tau \sim 10 L_0/v_0$ for typical parameter choices. Experimentally, sarcomeric pattern formation evolves on a time-scale of hours [5], which corresponds to an actin polymerization speed $v_0 \sim 0.1\,\mu\mathrm{m/min}$ in our simulations. This estimated actin polymerization speed would be lower than that in filopodia, but significantly larger than the speed measured *e.g.* in stereocilia.

Myosin filaments may exert pico Newton forces on actin filament at full activation. Decoration of actin filaments with troponin/tropomyosin reduces myosin walking, which would correspond to lower values for the active myosin force f_m in our simulations. Below, we argue that myosin walking towards actin filaments impedes the correct, sarcomeric polarity sorting, which is established in our model by actin treadmilling. The effective friction for an actin filament moving within a dense bundle is presumably dominated by binding-unbinding interactions with the surrounding actin gel as well as integrin-mediated interactions with the substrate. The corresponding effective friction coefficient γ_a is expected to be orders of magnitude larger than the hydrodynamic friction coefficient for motion in water [43], $\gamma_a > 3 \cdot 10^{-3}\,\mathrm{pN\,s/\mu m^2}$. Assuming a friction coefficient for single actin filaments (per unit length) in the range $\gamma_a \sim 0.1 - 10\,\mathrm{pN\,s/\mu m^2}$, we would find for a filament of length $1\,\mu\mathrm{m}$ moving at a speed of $1\,\mu\mathrm{m/min}$ friction forces in the range $1.5 - 150\,\mathrm{fN}$, *i.e.* well below both the stall force of actin polymerization and the buckling force of single actin filaments.

We did not incorporate filament diffusion explicitly in our model, as thermal motion will be small in a dense bundle. Note, however, that dynamic myosin forces with short correlation time can induce stochastic, bidirectional motion of filaments.

Several studies pointed out the effect of integrin-mediated anchorage of Z-lines for myofibrillogenesis [44]: Although, initial I-Z-I complexes did form even in the presence of RNAi against integrin, Z-body stability was apparently reduced and bundle integrity was impaired in these experiments [28]. Presumably, integrins play multiple roles starting with the stabilization of I-Z-I-complexes, which corresponds in our model to a reduced rate of dissociation of single filaments from an actin cluster (see also SI text S1). Secondly, anchorage reduces the mobility of I-Z-I complexes, which would correspond to an increased total friction coefficient of actin clusters. As anchored I-Z-I complexes still showed some residual mobility, anchorage must be dynamic and allow for slippage. Thus, dynamic anchorage affects the effective parameters in our model, but does not change its basic, qualitative features. Finally, stable anchorage at the two terminal ends of an acto-myosin bundle specifies its boundary conditions; a simulation case of static boundary conditions is shown in the SI to mimic a bundle whose terminal ends are grafted by focal complexes to a substrate.

Results

Plus-end crosslinking facilitates formation and growth of I-Z-I clusters

In our simulations, we consider a minimal, one-dimensional model of a bundle of treadmilling actin filaments. Actin filaments with nearby plus-ends can form a stable crosslink by a complex of molecules (that eventually become the Z bodies) that holds the plus-end of the two actin filaments, but still allows for actin polymerization at the plus-end, see section 'The computational model' and figure 2A. Subsequent crosslinking gives rise to the formation of actin clusters that consist of several actin filaments whose respective plus-ends are aligned and which are permanently crosslinked by effective plus-end tracking crosslinkers. Each actin cluster will move as a whole subject to the sum of forces acting on its constituent actin filaments. These crosslinked actin clusters can grow by fusion and eventually self-organize into sarcomeric order, thus representing precursors of the I-Z-I complexes observed during early myofibrillogenesis [45]. To gain basic insight into the process of actin cluster formation and coalescence, we first simulated bundles of treadmilling actin filaments and crosslinks without myosin filaments; the effect of myosin filaments is discussed in the next section. We observe the formation and coalescence of clusters of crosslinked actin filaments, see figure 2B.

In each actin cluster, the constituent actin filaments polymerize at their plus-ends, thereby pushing against the processive cross-linkers of the Z-band. The growing actin filaments themselves move away from the Z-band in a form of 'local retrograde flow'. The polymerization forces exerted by the polymerizing actin filaments on the Z-band are counter-balanced by friction forces that constrain the motion of the actin filaments. Any imbalance in the number of filaments of the two orientations will result in a net polymerization force and thus net motion of the cluster. The collision of two clusters can result in their mutual coalescence and the formation of a larger cluster. If actin filaments slide past each other without any friction, all filaments would eventually coalesce into a small number of very large clusters, see figure 2B. If we assume, however, a hypothetical, effective friction between moving actin filaments, coalescence of actin clusters above a critical size is dynamically impeded and sarcomeric order results.

The arrest of actin cluster coalescence due to our proposed inter-filament friction can be understood on qualitative grounds as follows: The active motion of a single actin cluster is driven by an imbalance of polymerization forces acting on the Z body that can arise from an imbalance between the respective numbers of the constituent filaments of the two different filament orientations. This net polymerization force is balanced by the total friction force of the actin cluster (and possibly additional forces due to interactions with neighboring clusters). Since this total friction is proportional to the total number of filaments in the actin cluster, whereas the net polymerization force (due to statistical imbalance) roughly scales only as the square root of this number, smaller actin clusters move faster than larger clusters. Furthermore, the mutual friction force between two overlapping actin clusters adds a friction term to the force balance that scales as the product of the respective filament numbers and therefore will eventually stall the approach of actin clusters above a certain size. In the more complex case of an actin bundle, the force balance for all actin clusters has to be considered. Friction between sliding actin filaments may be provided by fast, dynamic crosslinking along the entire lengths of the actin filaments by a second set of crosslinkers. Next, we discuss the possibility that myosin filaments serve as such a dynamic actin crosslinker, which mediates an effective repulsion between neighboring actin clusters.

Treadmilling actin filaments act as a conveyor belt that moves myosin to the A-band

We now augment the simple actin bundle model by adding bipolar myosin filaments that can dynamically attach to actin filaments in a polarity-specific way, see figure 3D. The relative motion of actin and myosin filaments is governed by a linear force-velocity relation for myosin walking, see section 'The computational model'. While myosin activity leads to 'walking' of the myosin towards the actin plus-ends, the local retrograde flow of treadmilling actin filaments transports the myosin in the opposite

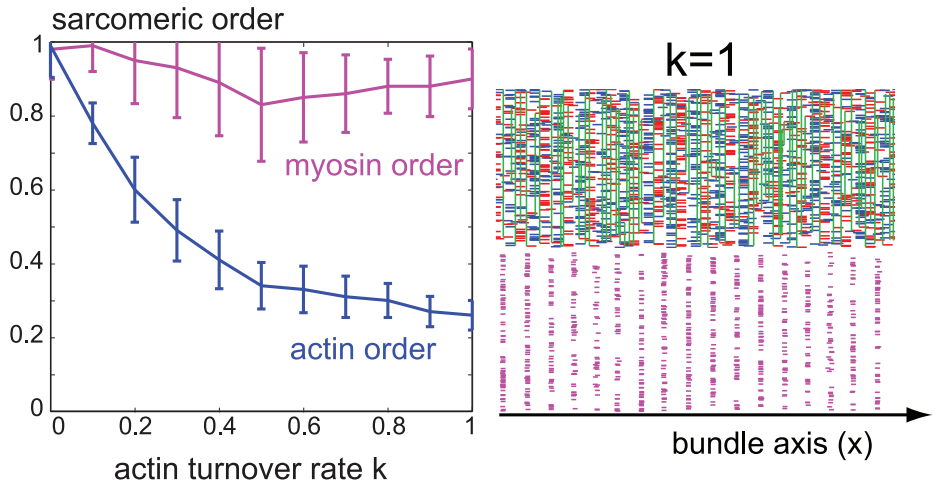

Figure 5. Myosin order despite actin turnover. We devised a minimal model of actin filament turnover, see main text. For simulations as in figure 3, but with actin turnover, the sarcomeric order parameter was found to decrease as a function of actin filament turnover rate (blue curve) as actin turnover impedes the formation of large actin clusters (blue, mean $\pm$ s.e., $n=100$). Surprisingly, an analogously defined order parameter for myosin positions attains significant values even for considerable actin turnover rates. A simulation snap-shot at $t=50$ is shown to the right for actin turnover rate $k=1$ (in units of v_0/L_0).
doi:10.1371/journal.pcbi.1002544.g005

direction as in figure 3A. For the case shown, actin treadmilling outpaces active myosin walking towards actin plus-ends, resulting in highly regular sarcomeric patterns with myosin localized near the actin minus-ends. Any actin filament, which is grafted at its plus-end in a Z-band has to polymerize against this obstacle, and is pushed away from the cluster center in a form of 'local retrograde flow', see figure 3C. For weak active myosin forces and thus slow active myosin walking, myosin filaments attached to such an actin filament are dragged along with this retrograde flow towards the depolymerizing minus-end of the actin filament. This 'actin conveyor belt' not only transports myosin filaments to the future A-band, but also generates an effective repulsion between neighboring I-Z-I clusters mediated by crosslinking actin filaments, which ensures a regular sarcomeric spacing of actin clusters. Stronger active myosin forces drive the myosin towards the actin plus-ends and therefore slow down sarcomeric ordering, see figure 3D. Above a critical force level, active myosin walking dominates actin treadmilling, and a wrong polarity sorting results that localizes myosin at the plus-ends and thus impedes sarcomeric ordering.

Sarcomeric order despite actin length variability

To account for a distribution of actin filament lengths, we simulated bundles comprising actin filaments of different lengths. For simplicity, we chose a static polydispersity for the actin length given by a unimodular distribution of fixed mean length $\langle L\rangle = L_0$ and tunable width $\langle L^2\rangle - L_0^2 = v^2 L_0^2$. Remarkably, sarcomeric ordering occurred even for considerable length variability v, though with a sarcomeric order parameter that decreased monotonically with v, see figure 4. Sarcomeric spacing increased as a function of length variability v, showing that the longest actin filaments set sarcomere spacing. Using an exponential distribution for actin filament length instead of a unimodular distribution resulted in no apparent sarcomeric ordering (not shown). Assuming static filament lengths allows us to study separately the mechanisms that result in actin filament length control and actin turnover, which we now discuss.

Myosin order despite high actin turnover

Actin filament length control and turnover of filaments both depend crucially on the polymerization and depolymerization dynamics of actin filaments. Thus, length control and filament turnover are in principle inseparable. This being said, we nonetheless aimed at isolating the qualitative effect of actin turnover. To this end, we augmented our computational model by including prototypical actin dynamics that differentiates between idealized dynamic regimes of either (i) steady-state treadmilling with constant actin filament length L_0, (ii) 'actin catastrophies' characterized by fast and complete depolymerization of filaments that occur with rate k, and (iii) rapid *de novo* polymerization of new actin filaments [46]. These simple limits are not intended to realistically depict actin dynamics. Rather they allow us to study the qualitative effects of actin filament turnover, without changing the filament length distribution. As expected, actin filament turnover interferes with the formation of large actin clusters and results in reduced sarcomeric order, see figure 5. Surprisingly, myosin is still sorted into regular A-bands even for considerable actin turnover rates. We conclude that partial polarity sorting of actin filaments is sufficient to sort myosin into A-bands. This may provide an explanation for experimental observations in which myosin ordering was observed to precede the formation of large, periodically spaced I-Z-I complexes.

A simple model for actin filament length control

Our simulations suggest that sarcomere spacing is set by the length of actin filaments at early stages of striated ordering. How is actin filament length controlled within a pool of highly dynamic actin filaments? Capping proteins regulate filament polymerization and depolymerization rates. However, on their own, these proteins do not provide a means to tune the average filament length to a set point since they act locally in a manner that is not sensitive to the total length of a filament. Energetically favorable crosslinking or attraction of actin filaments all along their length can result in a unimodular length distribution as this ensures maximal mutual overlap of filaments [47]. However, to allow for filament sliding and sorting, such crosslinking would have to be highly dynamic. Alternatively, severing agents (such as ADF/cofilin-like UNC-60B

[23]) are recruited by actin filaments in a length-dependent manner and can provide a generic feedback mechanism that controls actin filament length [48–50]. We consider a simple implementation of actin filament severing assuming that filaments elongate by polymerization at their plus-end with constant polymerization speed v_0, whereas the minus-end is stable. A generic severing agent can bind with constant rate α anywhere along the filament and cut it there. Since the minus-end facing fragment of a cut actin filament comprises mainly ADP-bound actin monomers and thus is less stable, we assume that this fragment rapidly depolymerizes after severing, see figure 6A.

This simple severing mechanism results in a unimodular length distribution at steady state, see figure 6B as well as SI text S1. For an intuitive explanation for this length control mechanism, note that longer filaments with more monomers have a higher probability to recruit a severing agent within a certain time interval compared with shorter filaments: In this scenario, filaments act as 'binding antennas' for severing agents. Figure 6 shows the emergence of sarcomeric order from an initially unstriated bundle for which actin filaments polymerize and are cut by severing agents.

Discussion

Here, we proposed a simple, generic, and robust mechanism for striated pattern formation in a crosslinked bundle of aligned actin filaments. This physical mechanism of sarcomeric ordering is based on the formation of small actin clusters by the plus-end crosslinking of single actin filaments and the subsequent coalescence of these smaller actin clusters into larger ones, which are reminiscent of the I-Z-I complexes observed during early myofibrillogenesis [45]. This mechanism represents a way to establish cytoskeletal order on length-scales of tens of microns from micron-size building blocks independent of any external scaffolding. Termination of cluster coalescence and stabilization of sarcomeric units requires a repulsive force between actin clusters. In mature myofibrils, the giant protein titin acts like an elastic spring and could serve this function. However, it is questionable if titin could play its role as a spacer between Z-bodies already at these early stages. While the N-terminal domain of titin is involved in early Z-body formation [28], the M-line epitope of titin associated to its C-terminal domain is established only after a delay [51] and ligand binding may be required to stretch the titin protein so that it spans the sarcomere; thus, at early times, titin may not set the initial sarcomere spacing [20]. Here, we studied polymerization forces from polymerizing actin filaments as a possible mechanism to generate repelling forces between actin clusters. A similar mechanism may apply to stress fibers in adherent, non-muscle cells as well as to stress-fiber like structures in developing muscle cells.

The assembly of mature myofibrils in striated muscle cells has been proposed to be a multi-step process [8] that starts with the formation of unstriated, stress fiber-like acto-myosin bundles near the plasma membrane, followed by the establishment of sarcomeric order within these bundles [10], possibly by actin cluster formation and coalescence as proposed here. These striated bundles represent an important intermediate in the assembly of mature myofibrils and are termed nascent myofibrils. Nascent myofibrils can grow by incorporating free actin and myosin filaments in a mechanism of "self-templating". Additionally, they can fuse with each other into a single fiber of increased diameter after aligning their respective periodic patterns [5,52]. Finally, maturation processes and actin length fine-tuning regularizes sarcomeric order resulting in mature myofibrillar "crystals". This myofibrillogenesis pathway represents a succession of hierarchical ordered states. We speculate that the assembly of striated stress

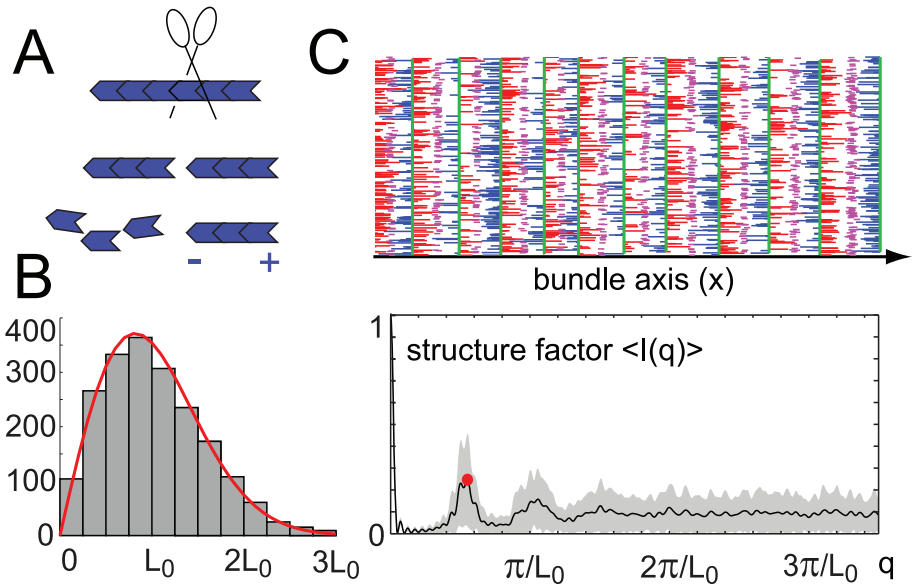

Figure 6. Actin filament length control by severing. A. Filament severing provides a simple physical mechanism for actin filament length control, see main text. In an idealized scenario, an actin filament (blue) binds a severing agent (scissors) with a rate αL that is proportional to its length L at a random position. The filament is then cut at the binding position, and its minus-end facing fragment is subsequently depolymerized. **B.** Actin filament severing results in a unimodular filament length distribution at steady state, see histrogram (gray) and analytical expression (red, see SI text S1). For the severing rate used, $\alpha = 1.5 v_0/L_0^2$, mean filament length $\langle L \rangle = 1.02 L_0$, and filament length variability parameter, $v = 0.52$. **C.** Simulation of an acto-myosin bundle as in figure 3, but with actin filament severing as described in panel A. Shown is a snap-shot of the simulations at time $t = 50$ (actin filaments: blue and red; myosin: magenta; end-tracking crosslinker: green), as well as the averaged structure factor (black curve, gray region indicates mean $\pm$ s.e., $n = 100$).
doi:10.1371/journal.pcbi.1002544.g006

fibers in non-muscle cells may follow a partial sequence of myofibrillar steps. Initial sarcomeric pattern formation in unstriated bundles would be a key step in this pathway and could rely on similar physical mechanisms both in muscle and non-muscle cells.

Experimental visualization of early sarcomeric pattern formation including actin filament length distribution, polymerization dynamics and their associated forces is technically challenging, but may be essential to test theoretical models of sarcomere formation. Little is known about the dynamics of actin filaments at early stages of sarcomeric pattern formation. In mature myofibrils, actin polymerization dynamics has been observed at both the plus- and the minus end [6,29]. These experiments show that actin filaments are highly dynamic even in these apparently stable striated bundles and that Z-bodies may act as plus-end tracking actin crosslinkers. It should be noted that at these late stages, actin filament treadmilling was not observed; thus, actin treadmilling may be limited to the early stages of striated ordering.

In vitro experiments with reconstituted actin stress fibers [53] might serve as an accessible experimental system to study sarcomeric pattern formation and actin polarity sorting. Additionally, filament treadmilling in the presence of crosslinkers is a source of expansive stress and should reduce any contractile prestress in the bundle, or even give rise to an overall expansive stress. This prediction could be tested in future experiments, possibly by laser nano-surgery of unstriated bundles.

Myosin filaments walk towards actin plus-ends. Unless counteracted by other mechanisms, myosin walking would result in a wrong localization of myosin at nascent Z-bodies and thus impair sarcomeric ordering. In our model, actin treadmilling counter-acts myosin walking and transports myosin towards the future M-band, provided active myosin forces are not too strong. It has been suggested that in some species, the early establishment of sarcomeric patterning involves a non-muscle isoform of myosin II, which is later replaced by muscle-specific myosin II [8]. It is tempting to speculate that muscle myosin allows for maximal force generation, whereas non-myosin filaments play a role as structural elements during the early establishment of striated order, for which, according to our model predictions, strong myosin forces could be obstructive. Alternatively, the decoration of actin filaments with tropomyosin may limit myosin walking during the early stages of sarcomeric pattern formation and thus prevent the active myosin forces from disrupting the treadmilling imposed myosin localization as we suggest. This is consistent with a recent study by Rui *et al.*, which showed that sarcomeric pattern formation was impaired in the presence of RNAi against tropomyosin and troponin [28].

In conclusion, we put forward a model that includes a minimal number of generic mechanisms that results in sarcomeric polarity sorting in *in silicio* acto-myosin bundles. We acknowledge the possibility that the mechanism presented here is only partial and that other mechanisms also contribute to sarcomeric pattern formation that can be tested experimentally. In particular, details of our computational model can differ from the genesis of sarcomeres in developing muscle cells: Actin filament buckling as observed in reconstituted *in vitro* systems [12,53] may reduce the myosin mediated repulsion force between neighboring actin clusters. Also, adhesive linkage of nascent Z-bodies to an extracellular substrate could reduce actin cluster motility [7,44]. We believe, however, that our theoretical study helps identify key elements of sarcomeric pattern formation. We propose that the length of sarcomere constituents such as actin filaments must be tightly controlled as it is expected to set sarcomere length at early stages of striated ordering. The emergence of sarcomeric order from the active condensation of actin clusters fits into the general framework of cytoskeletal pattern formation by active self-organization, which provides an alternative to external templating mechanisms.

Supporting Information

Text S1 Supplementary Text S1 provides further details on the computational model used, a sensitivity analysis for the model parameters, a model extension for the case of reversible actin crosslinking, as well as an illustrative mean-field description of actin cluster crosslinking by biopolar myosin filaments.
(PDF)

Video S1 Supplementary Video S1 shows the emergence of sarcomeric order in a simulated, one-dimensional acto-myosin bundle: Single, treadmilling actin filaments are shown in blue and red depending on the direction of their plus-end. At their plus end, actin filaments can become permanently crosslinked by a processive crosslinker that tracks actin plus ends while allowing for plus-end actin polymerization. Additionally, bipolar myosin filaments (magenta) dynamically attach to actin filaments in a polarity-specific manner, thus acting as a second set of active crosslinkers. Different vertical positions of the filaments are indicated solely for visualization purposes. Sarcomeric order in these simulated bundles can be quantified by the structure factor $I(q)$ as defined in the main text (blue curves in lower panel). See also figure 3 in the main text.
(AVI)

Acknowledgments

We thank Anne Bernheim-Groswasser and Dennis Discher for stimulating discussions.

Author Contributions

Analyzed the data: BMF EFF NSG SAS. Contributed reagents/materials/analysis tools: BMF EFF. Wrote the paper: BMF EFF NSG SAS. Designed the computer simulations: BMF EFF. Performed the computer simulations: BMF.

References

1. Huxley AF (1956) Interpretation of muscle striation: Evidence from visible light microscopy. Brit Med Bull 12: 167–70.
2. Alberts B, Bray D, Lewis J, Raff M, Roberts K, et al. (2002) Molecular Biology of the Cell, fourth edition. New York: Garland Science. 1616 p.
3. Peterson LJ, Rajfur Z, Maddox AS, Freel CD, Chen Y, et al. (2004) Simultaneous stretching and contraction of stress fibers in vivo. Mol Biol Cell 15: 3497–3508.
4. Hotulainen P, Lappalainen P (2006) Stress fibers are generated by two distinct actin assembly mechaisms in motile cells. J Cell Biol 173: 383–394.
5. McKenna NM, Johnson CS, Wang YL (1986) Formation and alignment of Z lines in living chick myotubes microinjected with rhodamine-labeled alpha-actinin. J Cell Biol 103: 2163–71.
6. Sanger JW, Wang J, Fan Y, White J, Sanger JM (2010) Assembly and dynamics of myofibrils. J Biomed Biotechnol 2010: 858606.
7. Quach NL, Rando TA (2006) Focal adhesion kinase is essential for costamerogenesis in cultured skeletal muscle cells. Dev Biol 293: 38–52.
8. Sanger JW, Kang S, Siebrands CC, Freeman N, Du A, et al. (2005) How to build a myofibril. J Muscle Res Cell Mot 26: 343–54.
9. Clark KA, McElhinny AS, Beckerle MC, Gregorio CC (2002) Striated muscle cytoarchitecture: an intricate web of form and function. Ann Rev Cell Dev Biol 18: 637–706.
10. Aratyn-Schaus Y, Oakes PW, Gardel ML (2011) Dynamic and structural signatures of lamellar actomyosin force generation. Mol Biol Cell 22: 1330–9.
11. Hosek M, Tang J (2004) Polymer-induced bundling of F actin and the depletion force. Phys Rev E 69: 1–9.
12. Soares e Silva M, Depken M, Stuhrmann B, Korsten M, MacKintosh FC, et al. (2011) Active multistage coarsening of actin networks driven by myosin motors. Proc Natl Acad Sci U S A 108: 9408–13.

13. Walcott S, Sun SX (2010) A mechanical model of actin stress fiber formation and substrate elasticity sensing in adherent cells. Proc Natl Acad Sci U S A 107: 7757–62.
14. Haviv L, Gov N, Ideses Y, Bernheim-Groswasser A (2008) Thickness distribution of actin bundles in vitro. Eur Biophys J 37: 447–54.
15. Claessens MMAE, Semmrich C, Ramos L, Bausch AR (2008) Helical twist controls the thickness of F-actin bundles. Proc Natl Acad Sci U S A 105: 8819–22.
16. Gov NS (2008) Packing defects and the width of biopolymer bundles. Phys Rev E 78: 1–5.
17. Shin H, Drew KRP, Bartles JR, Wong GCL, Grason GM (2009) Cooperativity and Frustration in Protein-Mediated Parallel Actin Bundles. Phys Rev Lett 103: 1–4.
18. Witt CC, Burkart C, Labeit D, McNabb M, Wu Y, et al. (2006) Nebulin regulates thin filament length, contractility, and Z-disk structure in vivo. EMBO J 25: 3843–55.
19. Pappas CT, Krieg Pa, Gregorio CC (2010) Nebulin regulates actin filament lengths by a stabilization mechanism. J Cell Biol 189: 859–70.
20. Gregorio CC, Granzier H, Sorimachi H, Labeit S (1999) Muscle assembly : a titanic achievement ? Curr Opin Cell Biol 11: 18–25.
21. Carroll S, Lu S, Herrera AH, Horowits R (2004) N-RAP scaffolds I-Z-I assembly during myofibrillogenesis in cultured chick cardiomyocytes. J Cell Sci 117: 105–14.
22. Takano K, Watanabe-Takano H, Suetsugu S, Kurita S, Tsujita K, et al. (2010) Nebulin and N-WASP cooperate to cause IGF-1 induced sarcomeric actin filament formation. Science 330: 1536–1540.
23. Ono S (2010) Dynamic regulation of sarcomeric actin filaments in striated muscle. Cytoskeleton 67: 677–92.
24. Zigmond SH, Evangelista M, Boone C, Yang C, Dar AC, et al. (2003) Formin Leaky Cap Allows Elongation in the Presence of Tight Capping Proteins. J Cell Biol 13: 1820–1823.
25. Laurent V, Loisel TP, Harbeck B, Wehman A, Gröbe L, et al. (1999) Role of proteins of the Ena/VASP family in actin-based motility of Listeria monocytogenes. J Cell Biol 144: 1245–58.
26. Salmikangas P, Mykkänen OM, Grönholm M, Heiska L, Kere J, et al. (1999) Myotilin, a novel sarcomeric protein with two Ig-like domains, is encoded by a candidate gene for limb-girdle muscular dystrophy. Hum Mol Genet 8: 1329–36.
27. Stout AL, Wang J, Sanger JM, Sanger JW (2008) Tracking changes in Z-band organization during myofibrillogenesis with FRET imaging. Cell Motil Cytoskeleton 65: 353–67.
28. Rui Y, Bai J, Perrimon N (2010) Sarcomere Formation Occurs by the Assembly of Multiple Latent Protein Complexes. PLoS Genetics 6: e1001208.
29. Skwarek-Maruszewska A, Hotulainen P, Mattila PK, Lappalainen P (2009) Contractilitydependent actin dynamics in cardiomyocyte sarcomeres. J Cell Sci 122: 2119–26.
30. Kruse K, Zumdieck A, Jülicher F (2003) Continuum theory of contractile fibres. Eur Phys Lett 64: 716–722.
31. Zemel A, Mogilner A (2008) Expansion and Polarity Sorting in Microtubule-Dynein Bundles. Prog Theoret Phys Suppl 173: 17.
32. Zemel A, Mogilner A (2009) Motor-induced sliding of microtubule and actin bundles. Phys Chem Chem Phys 11: 4821–4833.
33. Craig E, Dey S, Mogilner A (2011) The emergence of sarcomeric, graded-polarity and spindle-like patterns in bundles of short cytoskeletal polymers. J Phys: Condens Matter 23: 374102 (10pp).
34. Hasson T, Mooseker MS (1994) Porcine myosin-VI: characterization of a new mammalian unconventional myosin. J Cell Biol 127: 425–40.
35. Zumdieck A, Kruse K, Bringmann H, Hyman AA, Jülicher F (2007) Stress generation and filament turnover during actin ring constriction. PloS One 2: e696.
36. Yoshinaga N, Joanny JF, Prost J, Marcq P (2010) Polarity patterns of stress fibers. Phys Rev Lett 105: 3–6.
37. Howard J (2001) Mechanics of Motor Proteins and the Cytoskeleton. Sunderland, MA: Sinauer. 367 p.
38. Chaikin P, Lubensky T (1995) Principles of Condensed Matter Physics. Cambridge: Cambridge UP. 699 p.
39. Cramer LP, Siebert M, Mitchison TJ (1997) Identification of novel graded polarity actin filament bundles in locomoting heart fibroblasts: implications for the generation of motile force. J Cell Biol 136: 1287–305.
40. Peskin CS, Odell GM, Oster GF (1993) Cellular motions and thermal uctuations: the Brownian ratchet. Biophys J 65: 316–24.
41. Rzadzinska AK, Schneider ME, Davies C, Riordan GP, Kachar B (2004) An actin molecular treadmill and myosins maintain stereocilia functional architecture and self-renewal. J Cell Biol 164: 887–97.
42. Footer MJ, Kerssemakers JWJ, Theriot JA, Dogterom M (2007) Direct measurement of force generation by actin filament polymerization using an optical trap. Proc Natl Acad Sci U S A 104: 2181–2186.
43. Berg HC (1993) Random Walks in Biology. Princeton: Princeton UP. 152 p.
44. Sparrow JC, Schöck F (2009) The initial steps of myofibril assembly: integrins pave the way. Nature Rev Mol Cell Biol 10: 293–8.
45. Holtzer H, Hijikata T, Lin ZX, Holtzer S, Protasi F, et al. (1997) Independent Assembly of 1 . 6 Angstrom Long Bipolar MHC Filaments and I-Z-I Bodies. Cell Struct Funct 93: 83–93.
46. Guthardt Torres P, Doubrovinski K, Kruse K (2010) Filament turnover stabilizes contractile cytoskeletal structures. Eur Phys Lett 91: 68003.
47. Biron D, Moses E, Borukhov I, Safran SA (2006) Inter-filament attractions narrow the length distribution of actin filaments. Europhys Lett 73: 464–470.
48. Roland J, Berro J, Michelot A, Blanchoin L, Martiel JL (2008) Stochastic severing of actin filaments by actin depolymerizing factor/cofilin controls the emergence of a steady dynamical regime. Biophys J 94: 2082–94.
49. Gov NS (2007) Theory of the length distribution of tread-milling actin filaments inside bundles. Eur Phys Lett 77: 68005.
50. Edelstein-Keshet L, Ermentrout GB (2001) A model for actin-filament length distribution in a lamellipod. J Math Biol 355: 325–355.
51. Ehler E, Rothen BM, Hämmerle SP, Komiyama M, Perriard JC (1999) Myofibrillogenesis in the developing chicken heart: assembly of Z-disk, M-line and the thick filaments. J Cell Sci 112: 1529–39.
52. Friedrich BM, Buxboim A, Discher DE, Safran SA (2011) Striated acto-myosin fibers can reorganize and register in response to elastic interactions with the matrix. Biophys J 100: 2706–2715.
53. Thoresen T, Lenz M, Gardel ML (2011) Reconstitution of contractile actomyosin bundles. Biophys J 100: 2698–705.

Supporting Information: Sarcomeric pattern formation by actin cluster coalescence

BM Friedrich[1,3,*], E Fischer-Friedrich[2,3], NS Gov[2], SA Safran[1]
1 Department of Materials and Interfaces, Weizmann Institute of Science, Rehovot, Israel
2 Department of Chemical Physics, Weizmann Institute of Science, Rehovot, Israel
3 Present address: Max Planck Institute for the Physics of Complex Systems, Dresden, Germany
∗ E-mail: benjamin.friedrich@weizmann.ac.il

S1 Details of the computational model

S1.1 Algorithm structure

We employ an Euler scheme with fixed time-step $dt = 0.01L_0/v_0$. (In initial simulations, testing smaller time-steps did not change results.) At the beginning of each simulation, both actin and myosin filaments are assigned random positions x_j and $x_{m,k}$, respectively; additionally, a random orientation $\varepsilon_j = \pm 1$ is assigned to actin filaments. At this stage, no crosslinks between actin filaments exist and all myosin filaments are unbound from the actin filaments.

In each subsequent time-step, any two actin filaments whose projections on the x-axis overlap can establish a stable crosslink at their plus-ends with a probability $\rho(|x_j - x_k|)dt = \rho_0 \exp(-|x_j - x_k|/\delta)dt/\delta$ that depends on the distance of the respective plus-end positions, x_j and x_k. Subsequent crosslinking results in the formation of 'actin filament clusters' that consist of many actin filaments with aligned plus-ends. If two actin filaments belonging to two small clusters establish a new crosslink, these two clusters then merge into a single cluster. The x-coordinate of this new cluster is taken as the weighted average of the respective x-coordinates of the two clusters.

In our simulations, an idealized myosin filament with midpoint position x is assumed to have one actin binding site at either end located at $x \pm L_m/2$, where L_m is the length of a myosin filament. Each of these two binding sites can bind to exactly one actin filament in a polarity-specific manner, see figure 3C. (The binding site at $x \pm L_m/2$ binds to an actin filament of orientation $\varepsilon = \pm 1$, respectively.) During a time-step, a free binding site may bind to an actin filament in the range of this binding site with probability $k_{\text{on}}dt$. An occupied myosin binding site may unbind from its actin filament either spontaneously with probability $k_{\text{off}}dt$, or, by forced unbinding, if the depolymerizing minus-end of the actin filament retracts past the binding site.

For the simulations that include actin filament turn-over in figure 5, the number of "actin catastrophies" during a time-step was determined as a Poisson random variable

with mean kN_a, where N_a is the total number of actin filaments in the bundle. A corresponding number of actin filaments was randomly selected and removed from the system. Actin filament severing as employed for figure 6 was similarly implemented.

Furthermore, we employ a continuous description of actin polymerization assuming a constant plus-end polymerization speed v_0. In a more microscopic description not considered here, this would correspond to a plus-end elongation by four monomers during each time-step (using typical values $L_0 \approx 1\,\mu$m for the length of a two-stranded actin filament and $a = 5.5\,$nm for the size of a monomer [43]).

Finally, the individual speeds of actin clusters and myosin filaments inside the bundle are determined in a self-consistent manner by a balance of forces at each actin cluster and myosin filament, respectively, see figure S1. We consider cytosolic friction forces for both actin filaments ($\gamma_a L_j v_j^0$) and myosin filaments ($\gamma_m L_m v_{m,j}$), as well as a linear force-velocity relation for the interaction of bound pairs of actin and myosin filaments, see section S1.4. Actin polymerization at the plus-end is taken into account as an offset $\varepsilon_j v_0$ between the velocity of the actin plus-end $v_j = \dot{x_j}$ and the velocity $v_j^0 = v_j - \varepsilon_j v_0$ by which the individual actin monomers move with respect to the cytosol. The corresponding positions of actin and myosin filaments are updated accordingly in each time-step.

S1.2 Actin filament length

For figures 2, 3, and 5, we assumed a monodisperse distribution for the length of actin filaments, $L_j = L_0$ for all j. An equal polymerization and depolymerization speed v_0 at the plus- and the minus-end, respectively, ensures that filament length does not change in time. For figure 4, the length of individual filaments was also taken to be static, but was drawn from a unimodular length distribution $p(L)$ with mean $\langle L \rangle = \int_0^\infty dL\, L p(L) = L_0$ and variance $\langle L^2 \rangle - L_0^2 = \nu^2 L_0^2$. For $p(L)$, we chose a log-normal distribution with scale parameter $\sigma = \sqrt{\ln(1+\nu^2)}$ and location parameter $\mu = -\sigma^2/2$

$$p(L) = \frac{1}{L\sigma\sqrt{2\pi}} \exp\left[-\frac{(\ln(L/L_0) - \mu)^2}{2\sigma^2}\right]. \tag{S1}$$

Finally, for figure 6, the length of individual filaments changes dynamically with time, see section S1.3.

S1.3 Actin filament length control by severing

We present a simple model for the length control of polymerizing actin filaments, which is employed in a modified version of our computational model presented in figure 6. This simple model idealizes a more sophisticated model discussed in [36–38]. We consider a pool of N_a filaments, which for simplicity are assumed to elongate at their plus-end with a constant polymerization speed v_0, while their minus-ends are stable (possibly due to minus-end capping). Consequently, the length of a filament grows in time, $\dot{L}_j = v_0$.

Additionally, severing agents can bind to a filament with equal probability all along the filament length and cut the filament at the binding position, see figure 6A. Subsequently, the minus-end facing fragment of the cut filament is assumed to depolymerize completely (possibly due to the fact that it consists mainly of ADP-actin), whereas the plus-end facing fragment remains (possibly recruiting a new cap for its minus-end). Let $\alpha\, dL$ denote the rate by which a severing agent binds to a short length segment dL of a filament. Then the total probability that during a short time-interval dt a filament of length L is cut somewhere along its length is $\alpha\, L\, dt$, *i.e.* the overall scission probability is proportional to filament length. A simulation of this mechanism with $N_a = 2000$ actin filament results in unimodular distribution of filament length at steady-state, see figure 6B.

In a mean-field description, the filament length distribution $p(L)$ is found to obey a master equation

$$\frac{\partial}{\partial t} p(L,t) = -v_0 \frac{\partial}{\partial L} p(L,t) - \alpha\, L\, p(L,t) + \alpha \int_L^\infty dl\, p(l,t). \tag{S2}$$

The first term on the right hand side is a convective term that arises from the polymerization speed and describes a flux in probability space due to the elongation of actin filaments by polymerization. The second term is the rate at which filaments of length L are cut into smaller filaments by the severing agent, which decreases the number of filaments of length L. The third term finally represents the rate of accrual of stable, plus-end facing fragments of size L from the scission of longer filaments. The probability that a cut will occur at a distance L from the plus-end of a long filament of length l is α. Equating the left-hand side of equation (S2) to zero, we can solve for the the steady-state length distribution $p_0(L)$ and find

$$p_0(L) = \alpha L / v_0 \exp[-\alpha L^2/(2v_0)]. \tag{S3}$$

The mean filament length $\langle L \rangle$ is determined by a competition of the cutting rate α and the polymerization speed v_0, whereas the normalized length variability ν is independent of both α and v_0

$$\langle L \rangle = \sqrt{\frac{\pi v_0}{2\alpha}}, \quad \langle L^2 \rangle - \langle L \rangle^2 = \nu^2 \langle L \rangle^2, \quad \nu = \sqrt{(4/\pi) - 1} \approx 0.52. \tag{S4}$$

S1.4 Linear force-velocity relation of actin-myosin interaction

We assume a linear force-velocity relation for the active walking of a myosin filament that is attached to an actin filament. If the actin filament (say of orientation $\varepsilon = +1$) is held fixed with zero velocity ($v_a^0 = 0$), this force-velocity relation reads

$$\tilde{\gamma} v_m = f_m + f_{\mathrm{ext},m}, \tag{S5}$$

where v_m is the velocity of the myosin filament, $f_{\text{ext},m}$ an external force acting on the myosin filament and f_m denotes an active myosin force (that also equals the myosin stall force). The actin filament is subject to an opposite force $-f_m$. The coefficient of proportionality $\tilde{\gamma} = \gamma_m L_m + \gamma_{m,a}$ represent a friction coefficient that combines a contribution stemming from a cytosolic friction force $\gamma_m L_m v_m$ for myosin motion relative to the cytosol, and a contribution that effectively describes protein friction of the actin-myosin interaction, $\gamma_{m,a}(v_m - v_a)$, which we assume is proportional to the relative velocity of the myosin with respect to the actin. We use $\gamma_a = \gamma_m$ and $\gamma_{m,a} = 10\gamma_a L_0$. The above force-velocity relation can thus be rephrased in equivalent form as a force balance

$$\gamma_m L_m v_m + \gamma_{m,a}(v_m - v_a^0) = f_m + f_{\text{ext},m}. \tag{S6}$$

This formulation generalizes in a straightforward manner to the case of a moving actin filament. If $f_{\text{ext},a}$ denotes an external force acting on the actin filament of length L_a, we have an analogous force balance for the actin filament

$$\gamma_a L_a v_a^0 - \gamma_{m,a}(v_m - v_a^0) = -f_m + f_{\text{ext},a}. \tag{S7}$$

In the context of our actin bundle simulations, the external force $f_{\text{ext},a}$ is actually zero for free actin filaments. For polymerizing actin filaments grafted in a Z-band, however, $f_{\text{ext},a}$ is non-zero and represents the counter force of the actin polymerization force. Given $f_{\text{ext},a}$ and $f_{\text{ext},m} = 0$, we can self-consistently solve for the myosin and actin velocities, v_m and v_a, respectively, see figure S2. In the absence of external forces, the active myosin force f_m causes the myosin filament to move towards the actin plus-end, while the actin filament itself is pushed backward as a result of a counter-acting force f_m. A strong, backward-directed external force acting on the actin filament, $f_{\text{ext},a} < -\gamma_a/\gamma_{m,a} f_m$, pushes both the actin filament and the myosin filament backwards, $v_a, v_m < 0$, despite the fact that the myosin filament advances relative to the actin filament, $v_m - v_a > 0$.

S2 Model parameters and sensitivity

Table S1 lists reference parameters used for the figures (unless stated otherwise). The parameters marked with an asterisk (L_0, v_0, γ_a) set a characteristic length scale (L_0), time-scale (L_0/v_0), and force-scale ($\gamma_a L_0 v_0$), respectively. All other parameters are defined in a dimensionless manner relative to these scales. We independently varied parameters and determined (non-exclusive) ranges for which robust sarcomeric pattern formation occurred (characterized by a mean sarcomeric order parameter $\langle S \rangle > 0.9$; simulation time $t = 50$).

S3 Myosins crosslink actin clusters

In our model, bipolar myosin filaments can mechanically link neighboring actin clusters by binding to one actin filament from each cluster, respectively. These linker myosin

symbol	meaning	value	range
N_a	number of actin filaments	2000	250-4000
N_m	number of myosin filaments	1000	250-2000
L_0	mean actin filament length	1 ($*$)	n.a.
L_m	myosin filament length	0.5 (L_0)	0.1-1 [a]
L_{sys}	system size	40 (L_0)	20-80
v_0	actin polymerization speed	1 ($*$)	n.a.
γ_a	cytosolic friction coefficient for actin	1 ($*$)	n.a.
γ_m	cytosolic friction coefficient for myosin	1 (γ_a)	0-10
γ_{ma}	friction coefficient for actin-myosin interaction	10 ($\gamma_a L_0 v_0$)	2.5-100
f_m	active myosin force	1 ($\gamma_a L_0 v_0$)	0-9.5 [b]
k_{on}	actin-myosin binding rate	1 (v_0/L_0)	0.05-10
k_{off}	actin-myosin unbinding rate	1 (v_0/L_0)	0-10
δ	range of actin crosslinking	0.05 (L_0)	0.01-0.1
ρ	base rate of actin crosslinking	1 (v_0/L_0)	0.01-1

[a] System size was adapted as $L_{\text{sys}} = 16(2L_0 + L_m)$ to be an integer multiple of the expected sarcomere size.

[b] A simulation time of $t = 250$ was chosen to account for an increased time-scale of sarcomeric ordering.

Table S1. Reference parameters used in simulations.

mediate an effective interaction force between the two clusters: While myosin tends to walk towards actin plus-ends, thus pulling the two clusters closer together as in the sliding filament model of sarcomere contractions, actin treadmilling together with acto-myosin friction mediates an effective repulsion. For a sufficiently high density of actin filaments, the net repulsion force between the two clusters scales with the total number n of linker myosins, $(\gamma_{m,a}v_0 - f_m)n$. Figure S4A shows the number of myosin filaments linking two neighboring actin clusters as a function of the separation distance Δx between cluster centers in simulations with variable actin filament length; this dependence is non-monotonic. Intuitively, this can be understood as follows: For small separation distances, only a small number of myosin filaments happen to be enclosed between two clusters. For large separation distances, however, the number of long actin filaments that can possible engage in a myosin-mediated mechanical link is small. In the following, we will make this reasoning more quantitative. The expected total number of myosin filaments fully enclosed by two cluster centers can be approximated by $c_m(\Delta x - L_m)$, where $c_m = N_m/L_{\text{sys}}$ is the density of myosin filaments in the bundle and $\Delta x > L_m$ the separation distance of the two clusters. Out of this total number of myosin filaments between the two clusters, only a certain fraction will actually bind to two actin filaments at a given time. We can estimate this fraction of linker myosin filaments by formulating a mean-field theory. For this, we consider an idealized scenario of two static actin half-clusters separated by a distance Δx, each of which comprises a number N of actin filaments whose individual lengths are distributed according to some length distribution, $p(L)$, see figure S4B. We characterize the myosin filaments enclosed between the two cluster centers by four different concentration fields of their midpoint positions, according to whether they are not bound to any actin filament ($c_0(x)$), bound to an actin filament from either the left or right cluster only ($c_L(x)$, $c_R(x)$, respectively), or, if they are true linker myosins that are bound to actin filaments from both the left and the right cluster ($c_2(x)$). The dynamics of these concentration fields is governed by convection due to the actin conveyor belt with speed $v_m = (\gamma_{ma}v_0 - f_m)/(\gamma_{ma} + \gamma_m)$, as well as by exchange terms Δ_* due to binding/unbinding kinetics and forced unbinding of myosins that have reached the depolymerizing minus-end of an actin filament

$$\begin{aligned}
\dot{c}_L &= -v_m \nabla c_L - \Delta_{L2} - \Delta_{L0}, \\
\dot{c}_R &= +v_m \nabla c_R - \Delta_{R2} - \Delta_{R0}, \\
\dot{c}_0 &= \qquad\qquad\qquad\qquad + \Delta_{L0} + \Delta_{R0}, \\
\dot{c}_2 &= \qquad\qquad + \Delta_{L2} + \Delta_{R2},
\end{aligned} \tag{S8}$$

where the exchange terms read

$$\begin{aligned}
\Delta_{L0} &= k_{\text{off}} c_L - k_{\text{on}} \Phi(x_L) N c_0 + v_m \frac{p(x_L)}{\Phi(x_L)} c_L, \\
\Delta_{R0} &= k_{\text{off}} c_R - k_{\text{on}} \Phi(x_R) N c_0 + v_m \frac{p(x_R)}{\Phi(x_R)} c_R, \\
\Delta_{L2} &= -k_{\text{off}} c_2 + k_{\text{on}} \Phi(x_R) N c_L, \\
\Delta_{R2} &= -k_{\text{off}} c_2 + k_{\text{on}} \Phi(x_L) N c_R.
\end{aligned} \tag{S9}$$

Here, $x_L = x - L_m/2$, $x_R = \Delta x - x - L_m/2$, and $\Phi(x) = \int_x^\infty dx'\, p(x')$ is the cumulative distribution function of actin filament lengths that counts how many filaments have sizes greater than x. The exchange rate Δ_{L0} characterizes the exchange between the pool of myosin filaments exclusively attached to an actin filament from the left cluster and the pool of free myosin filaments that are not bound to any actin filament: Spontaneous unbinding occurs occurs at a rate $k_{\text{off}} c_L(x)$, while the rate of binding of free myosin filaments with center position x to an actin filament from the left cluster is proportional to the number $\Phi(x_L)N$ of actin filaments that are long enough to extend to position x_L, where x_L is the position of the left binding site of these myosin filaments. The latter rate thus reads $k_{\text{on}} \Phi(x_L) N c_0(x)$. Finally, the third term accounts for forced unbinding of myosin filaments: once a myosin reaches the depolymerizing minus end of its actin track, it 'falls off' the filament to which it was bound. Forced unbinding of myosin filaments occurs with a rate $v_m[p(x_L)/\Phi(x_L)]c_L$ that is proportional to the local proportion $p(x_L)/\Phi(x_L)$ of actin filaments of length $L = x_L$ among those with a length larger than x_L. The other exchange rates are derived similarly. Provided none of the actin filaments extends over the entire cluster distance, myosins are confined to the region between the clusters and a steady state evolves. At steady state, we find

$$c_2(x) \sim \frac{k_{\text{on}} N}{k_{\text{off}}} F_+ \exp\left[\frac{k_{\text{on}} N}{v_m} F_- + \frac{F_-}{F_+}\left(\frac{k_{\text{off}}}{v_m} + G_1\right) - G_2\right] \tag{S10}$$

Here, we used short-hand notation $F_\pm = (1/2)[\Phi(x + L_m/2) \pm \Phi(\Delta x - x - L_m/2)]$ and $G_\pm = (1/2)[p(x+L_m/2)/\Phi(x+L_m/2) \pm p(\Delta x - x - L_m/2)/\Phi(\Delta x - x - L_m/2)]$. Figure S4B shows the analytical solution from eq. S10, revealing the formation of a myosin band in the midzone between the two actin clusters at steady state. Interestingly, this steady state is characterized by a cyclic flux of myosin filaments, see figure S4B: Myosins bound to a blue actin filament are actively transported to the left until they detach either spontaneously or because they have been convected by actin treadmilling to the minus-end of their actin track. Free myosins on the left-side of the two cluster system are more likely to bind to a red filament due the higher local prevalence of these filaments. Once bound to a red actin filament, these myosins are transported to the right by actin treadmilling. This cyclic flux implies a violation of detailed balance and underpins the active nature of the underlying processes. In fact, the steady-state analytical solution from eq. S10 also describes the transient behavior in our simulations of acto-myosin bundles, see figure S4A.

Supporting Information Figures

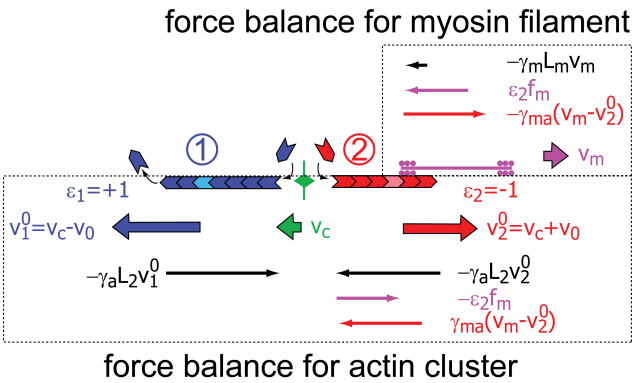

Figure S1. Local force balances determine velocities. Motion of actin filaments parallel to the bundle axis is characterized by respective lab-frame velocities v_j^0 (of the filament monomers). For actin filaments (red and blue) grafted at their plus-end in a crosslinking band (green), these velocities are offset from the velocity v_c of the crosslinking band by $\varepsilon_j v_0$, where $\varepsilon_j = \pm 1$ denotes filament orientation. Moving actin and myosin filaments are subject to friction with the cytosol; black arrows denote the respective friction forces. The mutual interaction of actin and myosin filaments is modeled by a linear force-velocity relation. As detailed in section S1.4, this relation can be also be represented by an active force f_m of actin-myosin interaction acting on the myosin filament (magenta arrow) as well as a protein friction force $-\gamma_{m,a}(v_m - v_j)$ associated with the interaction (red arrow). Corresponding counter forces act on the respective actin track. Force balance for each crosslinked actin cluster, as well as for each individual myosin filament allows us to self-consistently determine the velocities of all actin clusters and myosin filaments, respectively.

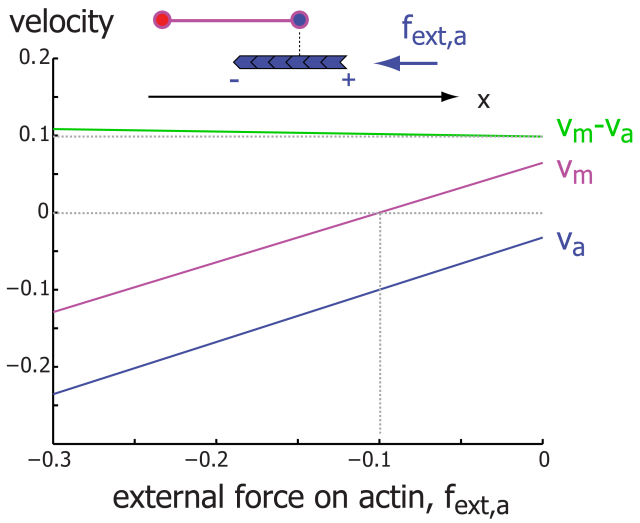

Figure S2. Force-velocity relation of actin-myosin interaction. The walking of a myosin filament (magenta) with respect to an actin filament (blue) is modeled by a linear force velocity relation, see section S1.4. A backward directed force $f_{\text{ext},a}$ acting on the actin filament can push both the actin and the myosin filament backward (in the $-x$-direction). Such forces arise as counter forces of actin polymerization forces in our simulations. In this case, the myosin filament continues to advance with respect to the actin filament as indicated by a positive velocity difference $v_m - v_a > 0$.

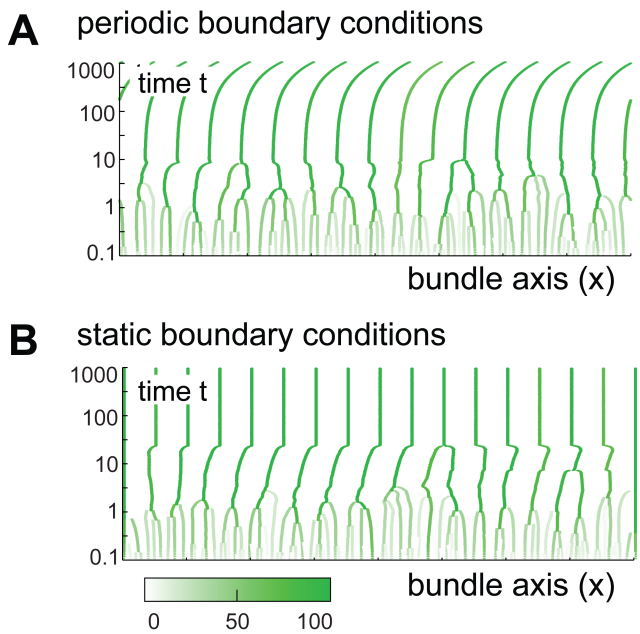

Figure S3. Changing boundary conditions. A. Kymograph of actin cluster formation and coalescence in the presence of myosin for the simulation shown in figure 3. This simulation employed periodic boundary conditions. **B.** Kymograph of actin cluster formation and coalescence in a simulated acto-myosin bundle as in panel A, but for static boundary conditions. Static boundary conditions are realized by inserting two actin half-clusters at the two bundle ends whose positions are fixed throughout the simulation, $x_1 = 0$ and $x_2 = L_{\text{sys}}$, by imposing suitable constraining forces. Each half-cluster comprises $N = 50$ actin filaments of specified polarity at $t = 0$. This mimics bundles that are grafted by focal adhesions at their terminal ends. The color scheme encodes filament number in actin clusters as shown in the color bar.

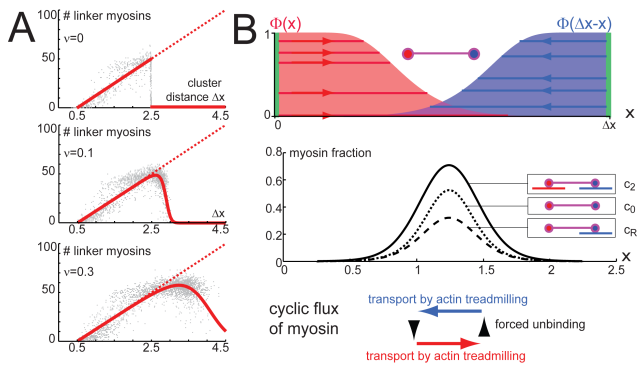

Figure S4. Myosins crosslink actin clusters. A. Myosin filaments mechanically link neighboring actin clusters by binding to one actin filament from each cluster, respectively. The plots show that in simulations of an acto-myosin bundle with variable actin filament length, the number of these linker myosins depends on the distance Δx between actin clusters in a non-monotonic way (gray dots). Also shown is an analytical result for the number of linker myosin derived for a pair of static actin clusters at steady state (red), assuming that the total number of myosins enclosed by the two cluster centers scales as $c_m(\Delta x - L_m)$ where $c_m = N_m/L_{\text{sys}}$ is the density of myosin filaments in the bundle (red dashed curve). Parameters as in figure 4 for different values of the length variability parameter, $\nu = 0,\ 0.1,\ 0.3$; simulation time, $t < 10$. For the mean field theory, we assume $N = 100$ actin filament per half-cluster. **B.** For the analytical theory, we consider an idealized scenario with two static actin half-clusters (with a certain length distribution of actin filaments) as well as a number of myosin filaments enclosed between the two cluster centers, see section S3. Myosin filaments can be either bound to one actin filament from each cluster (no motion due to force balance), be bound to an actin filament from one cluster only (myosin is convected by actin treadmilling), or be unbound. Using a mean field description, we can compute the fractions of myosins in the different binding states at steady state. This steady state is characterized by a cyclic flux of myosin filaments between the different binding states, see main text. Parameters: Actin filament number per half-cluster, $N = 5$ (for illustration purposes); cluster spacing, $\Delta x = 2.5$; actin length variability parameter, $\nu = 0.3$; myosin binding rates k_{on} and k_{off} as in table S1.

Scaling and Regeneration of Self-Organized Patterns

Steffen Werner,[1] Tom Stückemann,[2] Manuel Beirán Amigo,[1,3] Jochen C. Rink,[2]
Frank Jülicher,[1] and Benjamin M. Friedrich[1,*]
[1]*Max Planck Institute for the Physics of Complex Systems, Nöthnitzer Straße 38, 01187 Dresden, Germany*
[2]*Max Planck Institute of Molecular Cell Biology and Genetics, Pfotenhauerstr. 108, 01307 Dresden, Germany*
[3]*Universidad Autónoma de Madrid, Ciudad Universitaria de Cantoblanco, 28049 Madrid, Spain*
(Received 10 November 2014; published 1 April 2015)

Biological patterns generated during development and regeneration often scale with organism size. Some organisms, e.g., flatworms, can regenerate a rescaled body plan from tissue fragments of varying sizes. Inspired by these examples, we introduce a generalization of Turing patterns that is self-organized and self-scaling. A feedback loop involving diffusing expander molecules regulates the reaction rates of a Turing system, thereby adjusting pattern length scales proportional to system size. Our model captures essential features of body plan regeneration in flatworms as observed in experiments.

DOI: 10.1103/PhysRevLett.114.138101 PACS numbers: 87.17.Pq, 05.65.+b, 89.75.Da

Understanding the morphogenesis of a complex multicellular organism from a single fertilized egg poses a fundamental challenge in biology [1,2]. The diversity of shapes of living organisms emerges from biological patterning processes that assign cell fates depending on the spatial position of cells [1]. Patterning processes are remarkably precise and reproducible, despite environmental perturbations and the stochastic nature of fundamental cellular processes such as gene expression [3]. Furthermore, the astonishing regeneration capabilities of certain animals, including flatworms, polyps, salamanders, and newts, require patterning mechanisms that additionally can cope with highly variable initial conditions [4–7]. Both the robust establishment and the scaling of patterns during growth are poorly understood.

The fruit fly *Drosophila melanogaster* has been an important model system to study biological pattern formation and body plan scaling [8–11]. There, specific molecules, called morphogens, are secreted in localized source regions. Morphogens establish long-range concentration profiles by the interplay of transport and degradation. They provide chemical signals away from the source that can regulate patterning and growth [12–19]. Specifically, fly wing development has been extensively studied [13,14,16–18,20]. Quantification of morphogen profiles in the developing fly wing at different stages of development revealed that the morphogen concentration profiles scale with the size of the growing tissue, maintaining an approximately constant shape [16–18,20]. In a minimal description, the characteristic decay length $\lambda = (D/k)^{1/2}$ of these concentration profiles depends on the effective diffusion coefficient D and the degradation rate k [10,14]. It has been proposed that the scaling of these profiles is achieved by a dynamic regulation of the morphogen degradation rate via a chemical signal, called the expander, whose level varies with system size [12,15–18]. Different possible realizations for such mechanisms have been proposed [11,12,15–18,21–23]. These mechanisms rely on prepatterned tissues with specified sources or sinks for morphogens or the expander.

Scaling and regeneration of the entire body plan in the flatworm *Schmidtea mediterranea* challenges scaling mechanisms that rely on prepatterned cues. *Schmidtea mediterranea* can regenerate the complete animal from minute tissue fragments by repatterning the fragment to establish a proportionately scaled body plan [24]. Furthermore, flatworms grow when fed and literally shrink when starving, scaling their body plan proportionally over more than one order of magnitude in length (≈0.5–20 mm for *Schmidtea mediterranea*) [24]. These experimental observations prompt the existence of patterning systems with remarkable self-organizing and self-scaling properties. Recently, chemical signals have been identified whose perturbations have long-range effects on body plan patterning and regeneration. In particular, Wnt signaling, a pathway with conserved roles for developmental patterning, determines head-tail polarity during flatworm regeneration [25–28]. Inspired by these examples of biological pattern formation, we address in this Letter general requirements for the emergence of robust patterns that scale with system size.

The simplest model to spontaneously generate head-tail polarity based on graded concentration profiles of signaling molecules is the classical reaction-diffusion system introduced by Turing [29–31]. However, the resulting patterns do not scale naturally as sketched in Fig. 1, since diffusion

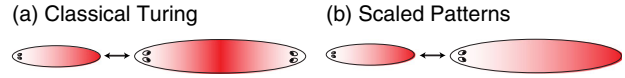

FIG. 1 (color online). Classical Turing patterns show more periodic repeats in larger systems as a result of fixed intrinsic length scales (a), instead of being a scaled-up version of the patterns in small systems (b).

coefficients and reaction rates define fixed characteristic length scales. Here, we extend the Turing model and introduce a self-organized feedback mediated by an expander molecule. This allows the system to robustly scale concentration profiles and source regions over several orders of magnitude of system size. Our model illustrates a general mechanism that could account for essential features of pattern scaling and regeneration observed in biological systems.

Size dependence and multistability of Turing patterns.—We briefly recall the classical Turing framework to highlight the size dependence of its emergent patterns and to introduce the notation used throughout this Letter. We consider a minimal version of the Turing mechanism, which consists of two chemical species (with concentrations A and B) that diffuse with diffusion coefficient D_A and D_B, and interact in a one-dimensional domain of size L with reflecting boundary conditions

$$\partial_t A = \alpha_A P(A,B) - \beta_A A + D_A \partial_x^2 A,$$
$$\partial_t B = \alpha_B P(A,B) - \beta_B B + D_B \partial_x^2 B. \quad (1)$$

We specifically consider linear degradation with rates β_A and β_B and production with rates α_A and α_B, and a switchlike Hill function typical for cooperative and competitive chemical reactions in biological systems:

$$P(A,B) = \frac{A^h}{A^h + B^h}. \quad (2)$$

Equation (2) implies that production is switched on if the activator concentration A exceeds the inhibitor concentration B. The choice of Eqs. (1) and (2) is conceptually equivalent to Turing's original formulation [29], yet particularly suitable for analytical treatment. The diffusion coefficients and degradation rates define two characteristic length scales

$$\lambda_A = \sqrt{D_A/\beta_A}, \qquad \lambda_B = \sqrt{D_B/\beta_B}. \quad (3)$$

The interplay between these length scales and the system size determines the final patterns, as we show next.

Equation (1) possesses a unique homogeneous steady state, which can become unstable with respect to inhomogeneous perturbations [29–31]. For $h \to \infty$, corresponding to a binary source switch $P(A,B) = \Theta(A - B)$, we can analytically solve for all inhomogeneous steady-state patterns of Eqs. (1) and (2). These are indexed by the number m of contiguous sources, defined as regions in which $A > B$, and the number n of source regions touching the system boundaries, see Fig. 2(a). In fact, the (m,n)-pattern can be constructed as the concatenation of $2m - n$ copies of the (1,1)-pattern, which thus serves as a basic building block. The (m,n)-pattern exists only if L exceeds a critical size that linearly increases with mode number $2m - n$ (gray region).

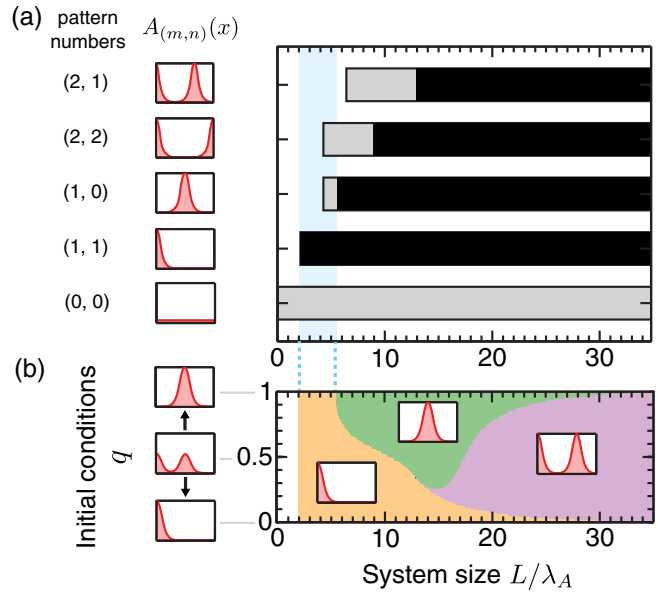

FIG. 2 (color online). Classical Turing patterning implies that in larger systems higher-order patterns form. (a) Steady-state patterns of Eq. (1) are classified by two pattern numbers (m,n): m is the total number of contiguous source regions, while n is the number of source regions touching the system boundaries. Typical profiles of the activator concentration $A_{(m,n)}(x)$ for the (m,n)-pattern are shown in red. Size ranges are shown, where the (m,n)-pattern is linearly stable (black), or exists, but is not stable (gray). In the blue region, the (1,1)-pattern is the only stable pattern. (b) Basins of attraction: final pattern type at steady state as a function of system size on the horizontal axis and initial conditions on the vertical axis. Initial conditions linearly interpolate between the (1,1)- and (1,0)-pattern, i.e., $A(x,t=0) = (1-q)A_{(1,1)}(x) + qA_{(1,0)}(x)$, and analogously for $B(x,t=0)$. Parameters: $D_B/D_A = 30$, $\alpha_B/\alpha_A = 4$, $\beta_B/\beta_A = 2$, $h \to \infty$ (a), $h = 5$ (b).

We numerically find that steady-state patterns become linearly stable only above a second critical size (black region). In large systems, several stable steady states coexist. However, in systems of increasing size, we observed increasingly smaller basins of attraction of patterns with small mode number, rendering these patterns unstable with respect to finite-amplitude perturbations, as exemplified in Fig. 2(b).

The (1,1)-pattern is globally stable only in a limited size range, see Fig. 2(a) (blue region). Next, we show how the introduction of a third reaction species E stabilizes the (1,1)-pattern, irrespective of system size.

Pattern scaling by gradient scaling.—We present a specific example for a general class of minimal feedback mechanisms that yield pattern scaling by adjusting the intrinsic pattern length scales λ_A and λ_B. A third molecular species E, termed the expander, is produced homogeneously, diffuses, and is subject to degradation

$$\partial_t E = \alpha_E - \kappa_E BE + D_E \partial_x^2 E. \tag{4}$$

The Turing system controls the degradation rate of the expander via the inhibitor B. In turn, the expander shall feedback on the Turing system, see Fig. 3(a). We choose a regulation of the degradation rates by the expander (with κ_A, $\kappa_B > 0$)

$$\beta_A = \kappa_A E, \qquad \beta_B = \kappa_B E. \tag{5}$$

We define the relative source size $\ell/L = \langle P \rangle$ and expander-dependent pattern length scales $\lambda_A = (D_A/\langle \kappa_A E \rangle)^{1/2}$ and $\lambda_B = (D_B/\langle \kappa_B E \rangle)^{1/2}$, analogous to Eq. (3). Here, the brackets denote spatial averages over the system.

We numerically find that the source size of steady-state patterns scales with system size over several orders of magnitude, see Figs. 3(b) and 3(c). Concomitantly, we obtain a scaling of the effective Turing length scales $\lambda_A^* \propto L$ and $\lambda_B^* \propto L$, where the asterisk denotes steady state.

We can challenge pattern scaling by perturbations that mimic experiments such as amputations, see Fig. 3(d). Two example trajectories, corresponding to head and tail fragments, respectively, converge to an appropriately rescaled (1,1)-pattern, after a transient overshoot of the source size. Two additional trajectories, simulating uniform injection of the expander, likewise converge to this fixed point. One trajectory [labeled *iv* in Fig. 3(d)] is characterized by the transient formation of a second source.

We observe pattern scaling for a vast parameter range, provided (i) inhibitor diffusion is sufficiently fast (a necessary condition for pattern formation in any Turing system) and (ii) the expander feedback strength falls into an intermediate range, see Fig. 3(e).

Next, we provide insight into how and why scaling works. First, we identify steady states, each of which scales with system size. For the simple case of adiabatically slow expander dynamics, we then show that the (1,1)-pattern is a stable steady state.

The extended Turing system with expander feedback generates steady states, for which the relative source size ℓ^*/L is independent of system size L. This can be shown from Eqs. (1) and (4) at steady state. By spatial averaging, we obtain $0 = \alpha_B \langle P^* \rangle - k_B \langle B^* E^* \rangle$ and $0 = \alpha_E - k_E \langle B^* E^* \rangle$ and hence

$$\frac{\ell^*}{L} = \frac{\alpha_E \kappa_B}{\alpha_B \kappa_E}. \tag{6}$$

In addition, also the pattern length scales λ_A^* and λ_B^* scale with high precision with system size. In the limit of large expander range $[\lambda_E = (D_E/\langle \kappa_E B \rangle)^{1/2} \gg L]$, for which the concentration profile of E is approximately homogeneous, scaling becomes exact. For simplicity, we consider a binary source switch ($h \to \infty$). If the expander level was imposed as constant $E = E_0$, the Turing system would reach one of the (m,n)-patterns discussed above in the absence of expander feedback, with pattern length scales $\lambda_A(E_0)$ and $\lambda_B(E_0)$. The relative source size $f_{(m,n)} = l/L$ of such a pattern depends on E_0 only via the dimensionless ratios $\lambda_A(E_0)/L$ and $\lambda_B(E_0)/L$. Hence, $f_{(m,n)} = f_{(m,n)}(L^2 E_0)$ is a function of $L^2 E_0$. This shows that changing E_0 has

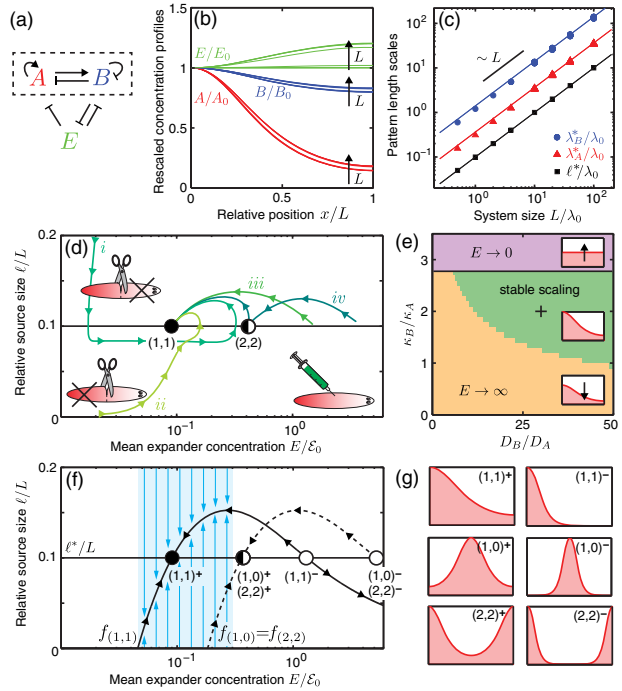

FIG. 3 (color online). Scalable pattern formation in a Turing system with expander feedback. (a) The Turing system and the expander mutually control their degradation rates, resulting in a stable feedback loop. (b) Scaling corresponds to morphogen profiles that collapse as a function of relative position x/L (normalized by respective concentrations A_0, B_0, E_0 at $x = 0$). (c) The feedback self-consistently adjusts the length scales λ_A and λ_B of the morphogen profiles and thus the source size ℓ with system size (symbols: numerical results; lines: analytical solution of Eqs. (1) and (4) at steady state for homogeneous expander concentration and $h \to \infty$). Here, $\mathcal{E}_0 = (\alpha_A/\kappa_A)^{1/2}$ and $\lambda_0 = [D_A/(\mathcal{E}_0 \kappa_A)]^{1/2}$ denote the characteristic concentration and length scales of the system. (d) Example trajectories, mimicking amputation experiments (labeled *i*, *ii*), and uniform, one-time injection of the expander (labeled *iii*, *iv*); all converge to the same stable fixed point, an appropriately scaled (1,1)-pattern. (e) Parameter regions for stable, self-scaling pattern formation (green), and regions of expander divergence (orange, purple). Parameters of panels (a)–(d) indicated by cross. (f)–(g) For adiabatically slow expander dynamics, the system relaxes along the nullclines of the Turing system $f_{(m,n)}$ (shown for $h \to \infty$, $\lambda_E \gg L$). As each nullcline intersects the steady-state condition of Eq. (6) twice, the system possesses two fixed points $(n,m)^+$ and $(n,m)^-$ for each pair (n,m). In the blue region, the (1,1)-pattern is the only stable steady state of the Turing system, compare to Fig. 2, implying that all trajectories must converge to this fixed point. Parameters: $D_B/D_A = 30$, $D_E/D_A = 10$, $\alpha_B/\alpha_A = 4$, $\alpha_E/\alpha_A = 0.4$, $\kappa_B/\kappa_A = 2$, $\kappa_E/\kappa_A = 2$, $h = 5$, $L/\lambda_0 = 10$, unless indicated otherwise.

analogous effects on the relative source size as changing L in the classical Turing system. The same argument also implies that a (m,n)-pattern can only exist above a critical value of E_0, corresponding to the minimum system size for the existence of patterns in Fig. 2(a). Below this critical value, $f_{(m,n)}$ is zero. Above this value, $f_{(m,n)}$ displays a nonmonotonic dependence on E_0, which results from opposing effects of the pattern length scales of the activator and the inhibitor on the source size ℓ, see Fig. 3(f). The intersections of the curves $f_{(m,n)}$ with the constant value ℓ^*/L given by Eq. (6) define the steady states of the full system with expander feedback. For each pattern type (m,n), we find two steady-state patterns, denoted $(m,n)^+$ and $(m,n)^-$, with respective expander levels $E^+_{(m,n)} < E^-_{(m,n)}$, see the black and white circles in Fig. 3(f).

The fact that $f_{(m,n)}(L^2E^*) = \ell^*/L$ is independent of system size L by Eq. (6) implies that also L^2E^* is independent of L for each steady state. We conclude $E^* \propto L^{-2}$ and thus $\lambda_A(E^*) \propto L$, $\lambda_B(E^*) \propto L$, consistent with our numerical results in Fig. 3(c).

We now discuss the stability of the (1,1) pattern in the simple limit of adiabatically slow expander feedback. In this limit, the source size first relaxes to $\ell/L = f_{(m,n)}(L^2E)$ for some (m,n), corresponding to the fast time scale of the Turing system. Then, by Eq. (4), the system moves slowly along this nullcline according to

$$\partial_t E = \alpha_E - \frac{\kappa_E \alpha_B}{\kappa_B} f_{(m,n)}(L^2E). \tag{7}$$

Stability of steady-state patterns requires $\partial_E f_{(m,n)} > 0$, which can be shown to hold only for $E^+_{(m,n)}$, see Fig. 3(f).

Which branch $f_{(m,n)}$ is selected for arbitrary initial conditions by the fast Turing dynamics? This problem is formally equivalent to the stability of (m,n)-patterns in the Turing system without expander feedback as a function of system size L. From the analysis presented in Fig. 2(b), we deduce that the $(1,1)^+$-pattern is the only stable pattern in the blue region, which thus represents a basin of attraction. Numerical analysis shows that the basin of attraction of the $(1,1)^+$-pattern is even larger than the blue region and that this pattern is stable also for nonadiabatic expander dynamics, see the trajectories in Fig. 3(d).

In summary, the scaling mechanism for patterns and sources presented here relies on expander molecules that dynamically adjust the degradation rates of morphogens in a Turing system. Thereby, the expander controls the pattern length scales and the source size of the resulting Turing patterns. The expander concentration is itself dynamic and is regulated by the concentrations of the Turing morphogens. For the feedback introduced here, the relative source size at steady state is always independent of system size, see Eq. (6). We showed that a head-tail polarity pattern with a single source region scales as a function of system size, is stable with respect to perturbations, and regenerates in amputation fragments.

Regeneration of patterns after amputation can be understood as follows. For a head fragment without a source, and hence no inhibitor production, the inhibitor level decreases, which decreases the expander degradation rate. Hence, the expander level increases. For a tail fragment, the inhibitor produced by the source spreads in a smaller system. This implies higher inhibitor levels, which in turn decreases the source size. Only when the relative source size has fallen below its steady-state value does the expander level increase. For head and tail fragments, the increasing expander level increases the degradation rate of the activator and the inhibitor, and thus scales down their pattern length scales.

For a given feedback scheme, the stability of fixed points depends on whether the source is fixed [11,15,21] or dynamic as in our case. For example, two mutually suppressing concentration profiles (here the inhibitor and the expander) would not result in a stable pattern for a fixed source size, but yield a stable scaling pattern in our case, since the expander also effectively expands the source.

The minimal mechanism presented above allows for several generalizations. First, the feedback of the Turing system on the expander level could be likewise implemented via the production rate, e.g., $\alpha_E \propto B$, instead of via the degradation rate $\beta_E = \kappa_E B$. Then, scaling would require $\beta_A \propto 1/E, \beta_B \propto 1/E$, which yields analogous results. As a second possibility for pattern scaling, the feedback in Eq. (5) could also be mediated by A instead of B, provided the expander diffuses sufficiently fast. More generally, similar results also follow for shuttling mechanisms for which E adjusts both the degradation rates and diffusion coefficients of A and B. However, controlling only diffusion is not compatible with self-organized pattern scaling as presented here. Our mechanism relies on a size-dependent amplitude of morphogen profiles, which is lacking for pure diffusion control.

It is interesting to note that the flux $\beta_A A$ has a size-independent amplitude. The spatial profile of this flux could provide a readout of the scaling morphogen profiles independent of their amplitudes.

Conclusion.—Motivated by biological examples of patterns that adjust to organism size [10,11,16–18,20,21], we present a minimal, self-organized patterning system that reliably establishes a head-tail pattern, scaled to match system size for a broad range of initial conditions. We extended a classical Turing system featuring local activation and lateral inhibition by a feedback loop, comprising a third diffusible molecule. The kinetics of this expander depends on the Turing patterns and feeds back on the Turing length scales. Thereby, the expander effectively serves as a chemical size reporter. In contrast to earlier works on gradient scaling [12,15–18,21–23], this mechanism is fully self-organized. In particular, it does not rely on prepatterned sources or sinks.

In size-monitoring systems, as considered here, a key challenge relates to the simple fact that these obviously require long-range communication across the scale of the system. This implies a tradeoff between an upper size limit for scaling, and the time scale of pattern formation. Here, this time scale is set by morphogen diffusion and system size. For example, assuming a maximum diffusion coefficient of 100 $\mu m^2/s$ and a maximum organism size of 20 mm, relevant for the flatworms considered, we infer a patterning time scale of 3–30 days, roughly consistent with the experimental range of 1–2 weeks for the restoration of body plan proportions after amputation [24,26]. Note that transport processes such as active mixing could accelerate morphogen dispersal, and thus allow for faster pattern formation [10]. In the minimal theory formulated here, no expander degradation occurs in the absence of the inhibitor. A basal degradation, independent of the inhibitor, would cap the expander concentration and thus set a lower size limit for scaling.

Our theory provides basic insight into the principles of self-organized pattern scaling and accounts for key qualitative features of scalable patterning during flatworm regeneration and growth. Three important signatures can be associated with the self-organized scaling mechanism introduced here: (i) overall levels of morphogens depend on system size, (ii) morphogen degradation rates depend on system size, and (iii) the source size after amputation can exhibit a nonmonotonic dynamics. These signatures provide explicit testable predictions regarding the regulatory dynamics of candidate patterning pathways such as Wnt signaling during regeneration and growth or degrowth in flatworms. Interestingly, the expression of a Wnt activator (Wnt11-5) indeed displays a nonmonotonic dynamics during regeneration [28], reminiscent of signature (iii). In the future, it will be important to quantify spatial profiles of signaling molecules and degradation rates as a function of system size, which will allow us to test the generic concepts presented here.

We thank L. Brusch, M. Kücken, Y. Quek, A. Thommen, S. Mansour, and S. Y. Liu for stimulating discussions. S. W. and B. M. F. gratefully acknowledge support from the German Federal Ministry of Education and Research (BMBF), Grant No. 031 A 099.

*benjamin.friedrich@pks.mpg.de

[1] L. Wolpert and C. Tickle, *Principles of Development* (Oxford University Press, New York, 2011).
[2] S. F. Gilbert, *Developmental Biology* (Sinauer Associates, Inc., Sunderland, MA, 2014).
[3] L. Abouchar, M. D. Petkova, C. R. Steinhardt, and T. Gregor, J. R. Soc. Interface **11**, 20140443 (2014).
[4] S.-Y. Liu, C. Selck, B. Friedrich, R. Lutz, M. Vila-Farré, A. Dahl, H. Brandl, N. Lakshmanaperumal, I. Henry, and J. C. Rink, Nature (London) **500**, 81 (2013).
[5] B. Galliot and S. Chera, Trends Cell Biol. **20**, 514 (2010).
[6] S. R. Voss, H. H. Epperlein, and E. M. Tanaka, Cold Spring Harbor Protoc., pdb.emo128 (2009).
[7] G. Eguchi, Y. Eguchi, K. Nakamura, M. C. Yadav, J. L. Millán, and P. A. Tsonis, Nat. Commun. **2**, 384 (2011).
[8] *The Development of Drosophila Melanogaster*, edited by M. Bates and A. Martinez Arias, Vol. 1 (Cold Spring Harbor Laboratory Press, New York, 1993).
[9] D. St Johnston and C. Nüsslein-Volhard, Cell **68**, 201 (1992).
[10] T. Gregor, W. Bialek, R. R. de Ruyter van Steveninck, D. W. Tank, and E. F. Wieschaus, Proc. Natl. Acad. Sci. U.S.A. **102**, 18403 (2005).
[11] D. M. Umulis and H. G. Othmer, Development **140**, 4830 (2013).
[12] H. G. Othmer and E. Pate, Proc. Natl. Acad. Sci. U.S.A. **77**, 4180 (1980).
[13] M. Affolter and K. Basler, Nat. Rev. Genet. **8**, 663 (2007).
[14] O. Wartlick, A. Kicheva, and M. González-Gaitán, Cold Spring Harbor Persp. Biol. **1**, a001255 (2009).
[15] D. Ben-Zvi and N. Barkai, Proc. Natl. Acad. Sci. U.S.A. **107**, 6924 (2010).
[16] O. Wartlick, P. Mumcu, A. Kicheva, T. Bittig, C. Seum, F. Jülicher, and M. González-Gaitán, Science **331**, 1154 (2011).
[17] O. Wartlick, P. Mumcu, F. Jülicher, and M. Gonzalez-Gaitan, Nat. Rev. Mol. Cell Biol. **12**, 594 (2011).
[18] D. Ben-Zvi, G. Pyrowolakis, N. Barkai, and B.-Z. Shilo, Curr. Biol. **21**, 1391 (2011).
[19] O. Wartlick, F. Jülicher, and M. Gonzalez-Gaitan, Development **141**, 1884 (2014).
[20] F. Hamaratoglu, A. M. de Lachapelle, G. Pyrowolakis, S. Bergmann, and M. Affolter, PLoS Biol. **9**, e1001182 (2011).
[21] D. Ben-Zvi, B.-Z. Shilo, and N. Barkai, Curr. Opin. Genet. Dev. **21**, 704 (2011).
[22] A. Hunding and P. G. Sørensen, J. Math. Biol. **26**, 27 (1988).
[23] S. Ishihara and K. Kaneko, J. Theor. Biol. **238**, 683 (2006).
[24] P. A. Newmark and A. Sánchez Alvarado, Nat. Rev. Genet. **3**, 210 (2002).
[25] K. A. Gurley, J. C. Rink, and A. Sánchez Alvarado, Science **319**, 323 (2008).
[26] T. Adell, F. Cebrià, and E. Saló, Cold Spring Harbor Persp. Biol. **2**, a000505 (2010).
[27] M. Almuedo-Castillo, M. Sureda-Gómez, and T. Adell, Int. J. Dev. Biol. **56**, 53 (2012).
[28] K. Gurley, S. Elliott, and O. Simakov, Dev. Biol. **347**, 24 (2010).
[29] A. M. Turing, Philos. Trans. R. Soc. London B **237**, 37 (1952).
[30] A. Gierer, Prog. Biophys. Molec. Biol. **37**, 1 (1981).
[31] H. Meinhardt, Cold Spring Harbor Persp. Biol. **1**, a001362 (2009).